Continuous Hydrothermal Flow Synthesis of Optimised Transparent Conducting Oxide Nanoparticles and Thin Films

Dougal P. Howard

A thesis submitted to
University College London
in partial fulfilment of the requirements for the degree of
Doctor of Philosophy

Supervised by Professor Jawwad A. Darr

September 2017

Department of Chemistry
20 Gordon Street
London WC1H 0AJ
United Kingdom

Declaration

I, Dougal P. Howard, confirm that the work presented in this thesis is my own. Where information has been derived from other sources, I confirm that this has been indicated in the work.

Dougal P. Howard

Abstract

This thesis focuses on the synthesis of a variety of different transparent conducting oxide (TCO) nanomaterials using a continuous hydrothermal flow synthesis process, wherein aqueous solutions of chemical precursors were mixed with heated, pressurised water to facilitate nanoparticle formation.

In Chapter 3, a screening investigation was carried out by doping zinc oxide with a number of different elements in order to highlight the most promising systems with regards to electronic conductivity. Of the twenty-four materials tested, zinc oxides doped with aluminium (AZO), gallium (GZO), and silicon (SiZO), Chapters 4 and 5, respectively, were selected for compositional optimisation and further testing. Aluminium and gallium doping and co-doping (AGZO) optimisation resulted in materials of similar conductivity to indium tin oxide (ITO), the industry standard TCO material.

Upon completion of compositional optimisation, ITO and AGZO were synthesised with a citrate coating added in-process (Chapter 6). This aided in the dispersion of the nanoparticles for deposition into thin films by inkjet printing and spin coating; the latter was also carried out with un-coated GZO, AGZO, and SiZO. Preliminary inkjet printed films demonstrated very high conductivity (ITO) or very high transparency (AGZO), but never both in the same film, indicating the promise of the deposition method while requiring further investigation to be carried out. The spin coated films of all four materials were highly transparent and conductive, competitive with the best performing materials so far reported in literature. The AGZO spin coated films in particular, were the most conductive ever reported, superior even to those deposited by the sputtering methods currently used in industry.

List of Publications

Publications related to this work

- **DP Howard**, P Marchand, T Gordon, JA Darr. Sustainable Transparent Conducting Oxide Nanomaterials; Aluminium- and Gallium-Co-Doped Zinc Oxide (AGZO). *Journal of Nanoscience and Nanotechnology*, 16(9):10166-10171, 2016

- **DP Howard**, P Marchand, ID Johnson, CJ Carmalt, IP Parkin, JA Darr. Conducting Al and Ga-doped zinc oxides; rapid optimisation and scale-up. *Journal of Materials Chemistry A*, 4(33):12774-12780, 2016

- **DP Howard**, P Marchand, L McCafferty, CJ Carmalt, IP Parkin, JA Darr. High-Throughput Continuous Hydrothermal Synthesis of Transparent Conducting Aluminum and Gallium Co-doped Zinc Oxides. *ACS Combinatorial Science*, 29:239-245, 2017

- **DP Howard**, P Marchand, CJ Carmalt, IP Parkin, JA Darr. Si-doped Zinc Oxide Transparent Conducting Oxides; Nanoparticle Optimisation, Scale-up and Thin Film Deposition. *Journal of Materials Chemistry C*, 5(34):8796-8801, 2017

Other publications

- M Lübke, **DP Howard**, CF Armer, AJ Gardecka, A Lowe, MV Reddy, Z Liu, JA Darr. High energy lithium ion battery electrode materials; enhanced charge storage via both alloying and insertion processes. *Electrochimica Acta*, 231:247-254, 2017

- M Lübke, D Ning, CF Armer, **DP Howard**, DJL Brett, Z Liu, JA Darr. Evaluating the Potential Benefits of Metal Ion Doping in SnO2 Negative Electrodes for Lithium Ion Batteries. *Electrochimica Acta*, 242:400-407, 2017

- GP Evans, MJ Powell, ID Johnson, **DP Howard**, D Bauer, JA Darr, IP Parkin. Room temperature vanadium dioxide-carbon nanotube gas sensors made via continuous hydrothermal flow synthesis. *Sensors and Actuators B*, in-press (accepted manuscript), 2017

Acknowledgements

Particular thanks are owed to Professor Darr for his guidance for the duration of my research. I have learnt so much under his supervision and benefited immensely from it. Thanks also to my secondary supervisor, Professor Furio Cora, and Professors Carmalt and Parkin for the invaluable feedback they have given me over the years, and to the EPSRC for funding my studentship.

To the various members of the CMTG group: to Pete, Liam, Marco, and Paul for being exactly the post-docs I needed at the time, for the immense support they gave both to me and to the rest of the group, and for all I learned from them. To Eva, Jess, Kalyani, Neel, and Clément for welcoming me into the group and making my Masters project a lot of fun. To Adrian for the Korean fried chicken and karaoke, to Dustin for always being up for another round, to Ian for the crispy doggos, Meggi for the crispy bacon, and to both for being such excellent company in the office over so many years. To the newbies, Carlos, Charles, Chris, and Tom, for coming along for the ride even as the end was in sight.

To the Scanlads, Alex, Ben, and Chris, the Sladies, Mia and Rachel, and David and Felicity, for warming my office, tolerating, abusing and amusing me in equal measure, to share my office with all of them over the years has been an absolute pleasure. To Martin and Oli, and the rest of my gym brethren, Richard, Phil, Zac, Jerzy, and Tom, for making sure my days started the right way, and for pushing me further than I could have gone alone.

To the Jazz folk, Max, Ryan and Sally, Cat, Claire, Sarah, and Mike, for making Tuesdays the highlight of my week. To Mingkang for the years of friendship and support, and for the shell he had me leave behind, and to Mo, Tim, Jimmy, Vicky and Lucy, for the great times we had in undergrad. To Rose and Natalia, for giving me a home when I moved to London. To Anthony, and Simon, and Nick, Becca, Julia, Wini, and the rest of the Oxford crew, who formed me.

To Pub Lyf, those several-times-weekly wonders of human beings, for making my Masters year the best of my life. To Olivia, and Mark, for brightening every single day. To Oliver, Charlotte, Harriet, Leigh, Natalie, Apple and Camellia, for the incredible life they made for me, and the genuine good they all did me, and still do.

And to my parents, Tim and Holly, whose support of my various endeavours has been both ceaseless and profound, and to my often lovely sisters, who grow less and less irritating as time goes on. And to all those dearest of friends who have come and gone, and those who have come and stayed, who have been a source of happiness and (for the most part) sanity, you have my sincere gratitude. To you, and to all those others too numerous to count, who made my life better for being a part of it, I dedicate this.

○ • • •

I am grateful for my family, and for my friends,
for those who shaped me, moulded me, those whose impact I can say
was to help form me into the man I find myself today.

I am thankful for all those who have come into my life,
however briefly, who flitted in and out, or who chose
to stay awhile, especially those who rose
to the challenge of putting up with me, who made me stronger,
who encouraged me to be the best me that I could be,
who pushed and pulled and dragged me on
through all of life's ups and downs, never alone.

For all who joined me at my table,
for accepting me, for choosing to stay awhile
and offering some sort of refuge, some stable
safe haven from the isolation and speed and guile
of the city we are lucky enough to call our home.

Not everyone comes into our lives forever, most
drift in and out, passing through and never
really knowing who or what or why you are the way you are;
Only a very few enter in such a way that even
if tomorrow they were to part, leaving
they'd be leaving on you a work of art,
a mark of the impact they've had along their way,
one that will, for better or worse, always stay.

Such people live with you forever despite
however many thousands of miles and hours of flight
are separating and coming in between a bond
that will remain until the very end, perhaps beyond.

I am grateful to all those who have surrounded me,
for being my friends, and for being my family.
For always greeting me with wine and a smile,
and for letting me be the one to stay awhile.

- D

Contents

List of Figures

List of Tables

List of Abbreviations

AACVD aerosol-assisted chemical vapour deposition

AGZO aluminium and gallium co-doped zinc oxide

APCVD atmospheric pressure chemical vapour deposition

ATO antimony doped tin dioxide

AZO aluminium doped zinc oxide

at% atomic percent

BET Brunauer-Emmett-Teller

BPR back pressure regulator

CHFS continuous hydrothermal flow synthesis

CJM confined jet mixer

CVD chemical vapour deposition

DI deionized

DLS dynamic light scattering

EDS energy dispersive x-ray spectroscopy

E_F Fermi level

EPSRC Engineering and Physical Sciences Research Council

eV electron volt

FTO fluorine-doped tin dioxide

GZO gallium-doped zinc oxide

HOMO highest occupied molecular orbital

ICP-AES inductively coupled plasma atomic emission spectroscopy

IR infrared

ITO indium tin oxide

LED light emitting diode

OLED organic light emitting diode

PLD pulsed laser deposition

PMA poly(methacrylic acid)

PVD physical vapour deposition

SEM scanning electron microscopy

SiZO silicon doped zinc oxide

TCO transparent conducting oxide

TEM transmission electron microscopy

US$ United States dollar

UV ultraviolet

vis visible

XPS x-ray photoelectron spectroscopy

XRD x-ray diffraction

Chapter 1

Literature Review and General Introduction

In this chapter, an overview of transparent conducting oxides (TCOs) is given, including discussions of their optoelectronic properties and how they arise, the applications of TCOs, and the methods by which they are synthesised and deposited as thin films.

1.1 Transparent Conducting Oxides

Transparent conducting oxides (TCOs) are a class of materials that demonstrate the often incompatible properties of high optical transparency and conductivity; this section will outline in detail their properties and key applications, as well as the materials that are predominantly used in them.

1.1.1 Properties of TCO materials

TCOs are present in devices in the form of thin films. This reduces the space they take up in devices, and aids in the optical transparency that is fundamental to many of their uses. The required optical transparency is typically > 80 % across the visible range (400 - 700 nm), and to achieve this a wide, direct optical band gap semiconductor is needed with band gap of 3.1 eV, corresponding to the transmission of visible light.[10] In addition to the gap between the valence band maximum and the conduction band minimum, it is also important that the first allowed transition from the conduction band minimum is also at least 3.1 eV, else already-excited electrons would be able to absorb visible light for further excitation, negating the purpose of the material. Furthermore, such a material requires resistivity values of the order of 10^{-4} Ω cm, and it is the unlikely combination of these two properties, high conductivity and transmittance of visible light, that is so rare and that makes transparent conducting materials so highly sought-after.[11] In determining suitable candidates for these applications, a certain robustness is also required, as chemical or thermal instability would in time contribute to shortened lifespans of the devices in which they are used.

In order to ensure an optically transmissive, intrinsically semiconducting metal oxide is sufficiently conductive, it can be extrinsically doped with an aliovalent element. Lower valency in this element results in *p*-type semiconductivity, wherein the conduction mechanism relies on mobile positive 'holes' in the valence band; higher valency of the element results in *n*-type semiconductivity, in which the conduction mechanism relies on additional, free-moving electrons in the conduction band.

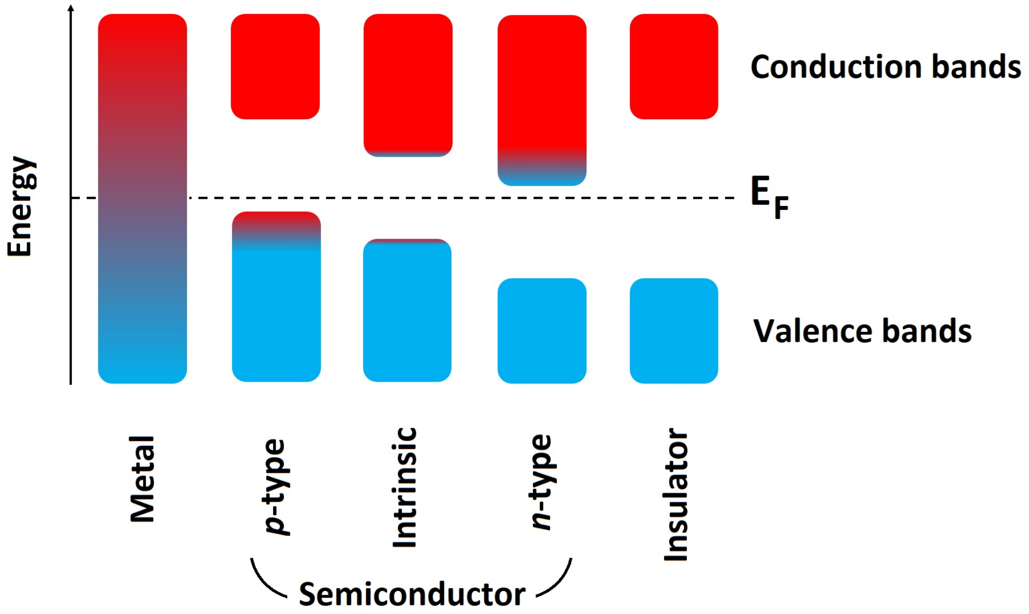

Figure 1.1: Simplified band structures for different types of materials. Valence (filled) bands are shown in blue, conduction (empty) are shown in red, and E_F is the Fermi Energy Level.

A highly simplified diagram showing the valence (blue, filled states) and conduction (red, unfilled states) bands of different types of material classes is shown in Figure 1.1. The wide band gap of insulating materials prevents excitation of electrons due to the large energy distance between the Fermi level (E_F) and either of the band edges, making them non-conductive. Within metallic materials, valence and conduction bands overlap, allowing for the movement of charge carriers and as such they are highly conductive. Semiconducting materials fall into the middle of these two extremes. There is a band gap, so electrons are not as mobile as in metals, however the gap is not prohibitively large. In *p*-type semiconductors, the valence band lies close to the Fermi level. Positive holes are formed in the valence band, which act as mobile charge carriers, balanced by negatively charged, immobile anions, which are shallow acceptors. In *n*-type semiconductors, the conduction band lies near to the Fermi level; additional electrons in this band are mobile and able to carry charge. In this case the charge balance is from immobile, positively charged, shallow donor cations.

Band gaps are visually displayed for several different semiconducting materials in Figure 1.2 (the design of the depiction took inspiration from [12]), with data displayed for In_2O_3,[13] SnO_2,[14] ZnO,[15] Cu_2O,[16] and Si[17]. The deep valence bands of In_2O_3, SnO_2, and ZnO are indicative of *n*-type semiconductivity (which can be further enhanced with doping),[12] and largely prohibit *p*-type semiconductivity, even with extensive doping.[18, 19] Their large electron affinities suggest a preference for electrons rather than holes. The shallower valence bands of Cu_2O and Si indicate that these materials are *p*-type, as their lower ionization potentials suggest an increased preference for holes over free electrons.[13]

Figure 1.3 directly compares the optical band gaps of In_2O_3[13], ITO,[20] SnO_2,[14] ZnO,[15] and TiO_2,[21] four natively *n*-type semiconductors with wide band gaps that can be used as TCOs. Optical band gap size can be significantly affected by doping, as shown by the effect of altering pure In_2O_3 to ITO, 10 at% Sn with respect to 90 at% In, and this can also be taken into account when selecting a TCO material. In this instance, the addition of tin is filling some available

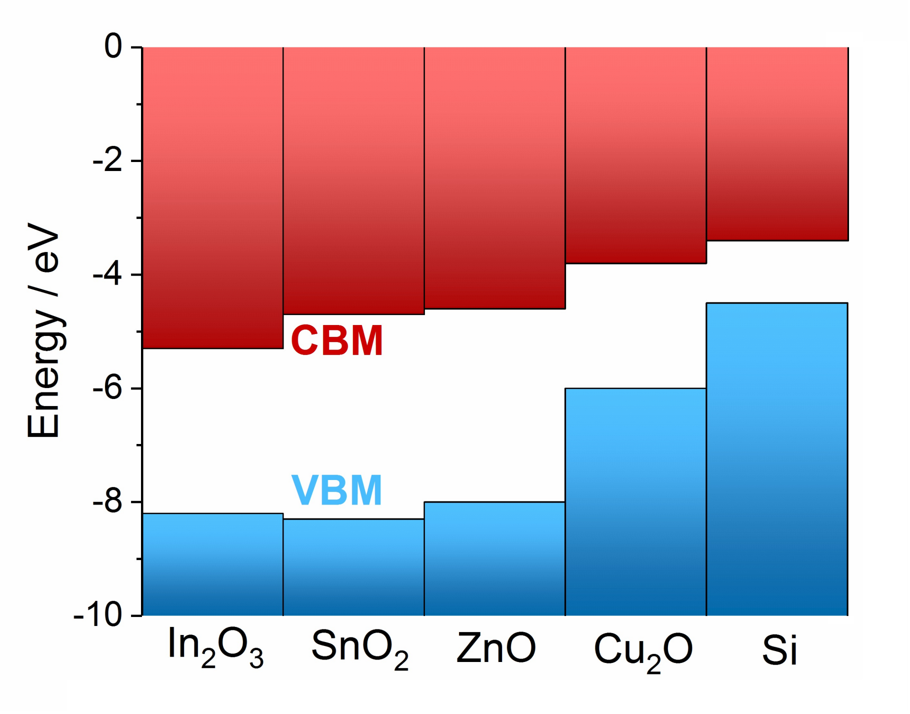

Figure 1.2: Band gap information for five different materials: In_2O_3, SnO_2, ZnO, Cu_2O, and Si. VBM is the valence band maximum, CBM is the conduction band minimum, and their values are relative to the vacuum level, which is set to 0 eV.

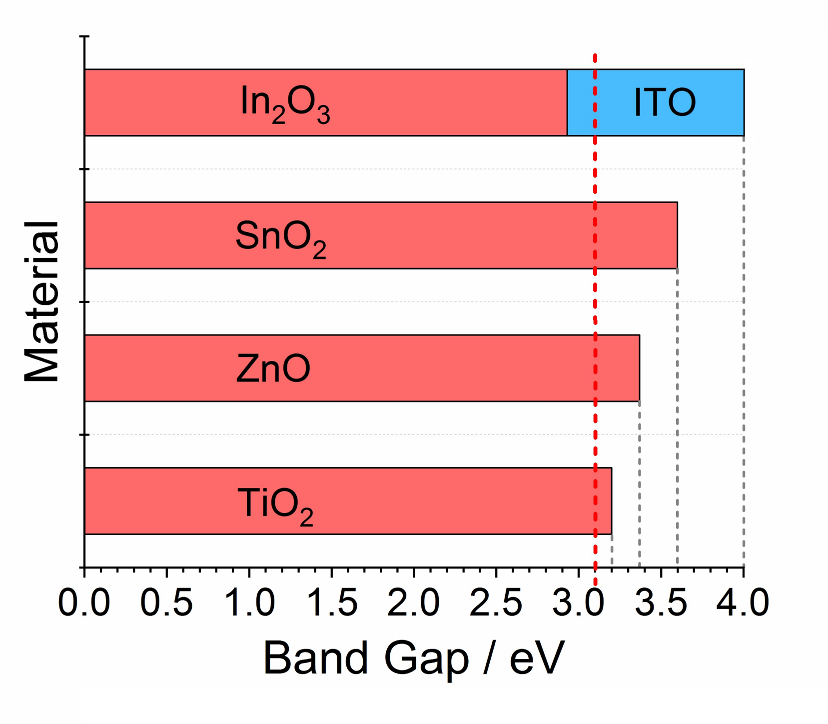

Figure 1.3: Comparison of band gap sizes for In_2O_3 (and ITO), SnO_2, ZnO, and TiO_2.

states in the conduction band, rendering them unavailable for promoted electrons in the valence band, thus the band gap is effectively being increased due to this unavailability of some lower energy conduction band states. This effect is called a Moss-Burnstein shift, which does not affect the fundamental band gap (the energy difference between the VBM and CBM), but does effect the optical band gap, the effective observed band gap of the material. All of these materials can, typically when appropriately doped, demonstrate the high transparency and conductivity required of TCOs. ITO especially is the most conductive of all industrially relevant TCOs,[22] with high physical and chemical stability, which resulted from the 1960's onwards in ITO being the TCO of choice in the vast majority of applications over alternative materials.[23]

The conduction mechanism in ITO is based on both the tetravalent tin on the indium sites, $\mathrm{Sn}_{\mathrm{In}}^{\bullet}$, which theoretically contributes to the carrier concentration according to 3.0 x 10^{20} x C_{Sn} cm^{-3}, where C_{Sn} is the atomic percentage of Sn relative to In, and the presence of oxygen vacancies in the lattice.[24, 25] For pure indium oxide, the oxygen vacancy prevalence is fundamental to the conductivity of the material, contributing as shown in Equation 1.1, using Kröger-Vink notation:

$$\mathrm{O}_{\mathrm{O}}^{\mathrm{x}} \rightarrow V_{\mathrm{O}}^{\bullet\bullet} + 2\mathrm{e}^{'} + \frac{1}{2}\mathrm{O}_2(\mathrm{g}) \tag{1.1}$$

In this notation the subscript denotes the lattice position upon which the element is situated where relevant, and the superscript denotes charge, such that the ' x ' represents neutral charge, the ' • ' represents one positive charge for each present, and the ' $'$ ' represents one negative charge for each present, while V is a vacancy, and i would represent an interstitial site. In this way the oxygen vacancy is a doubly ionised donor, which can donate up to two electrons per defect. Additionally, the presence of these oxygen vacancies facilitates the mobility of O^{2-} through the lattice, contributing to the ionic conductivity of the material, though this is negligible compared to the electronic conductivity.[26]

In an ideal system, the conductivity, σ, carrier concentration, n, and charge carrier mobility, μ, are related by Equation 1.2, where e is electronic charge.

$$\sigma = n\mu e \tag{1.2}$$

Thus, as alluded to above, high carrier concentrations and mobilities lead to higher conductivities. However, μ is proportional to the time between resistive scattering events.[27] In this context, scattering refers to the mechanism by which the non-random directional movement of charge carriers is inhibited, and it follows that the fewer scattering processes present in a material, the higher the possible mobility of the charge carriers.[28] This is visually apparent from the band structures elucidated by computational calculations, in that the curvature of the bands (i.e. the dispersion) is indicative of the mobility of the electron charge carriers such that relatively flat bands across k-vectors show low mobility.[29] It is unfortunate then, that higher charge carrier concentrations increase the propensity for scattering effects, and thus have a negative impact on the mobility of the carriers. Thus the optimisation of the resistivity of the materials is, for the most part, a balancing act between increasing the charge carrier concentration and the mobility, increasing the former as much as possible without inhibiting the latter.[24] For ITO, typical charge carrier concentrations of ca. 10^{21} cm^{-3} are observed, with mobilities of > 30 cm^{2} V^{-1} s^{-1} typically observed in literature reports.[25, 30, 31]

1.1.2 Applications of TCOs

TCOs were first of interest in coating glass for anti-fogging/icing aircraft windscreens and other components that would be negatively affected by the cold temperatures of flight altitude.[32–34] Modern applications of TCOs are prolific, and spread across various electronics industries, principally including organic light-emitting diodes (OLEDs) to enhance optical power output,[35] touchscreens,[23] solar cells (to enable current collection with short carrier diffusion lengths),[36, 37] flat-panel displays,[38] and smart windows,[39] wherein optical properties can be modulated by charge insertion or extraction through a transparent conducting contact. These various technologies have proliferated themselves utterly through modern society; their prevalence and growing indispensability have led to a transparent conductor market the highest-charging analysts estimate to be worth between \$5-10 billion within the next 10 years, of which ITO has comprised 90% as recently as 2013, and is expected to continue to be the most commonly used transparent conducting material for at least the next several years.[40–43]

As an example of a typical TCO application, the following section outlines the schematic of an OLED, and describes how a TCO is incorporated into the device and its purpose.

1.1.2.1 Example application: organic light-emitting diode

Though light emitting diodes (LEDs) have existed in some form for almost a century, OLEDs are a relatively recent invention, with the seminal research paper published in 1987.[35] LEDs consist of a p-n junction (i.e. a junction between a *p*-type and an *n*-type semiconductor), such that activation by application of a voltage across the junction facilitates the recombination of electrons with electron holes, resulting in the emission of visible light. What distinguishes OLEDs from LEDs, is that the emissive layer(s) are comprised of organic materials.

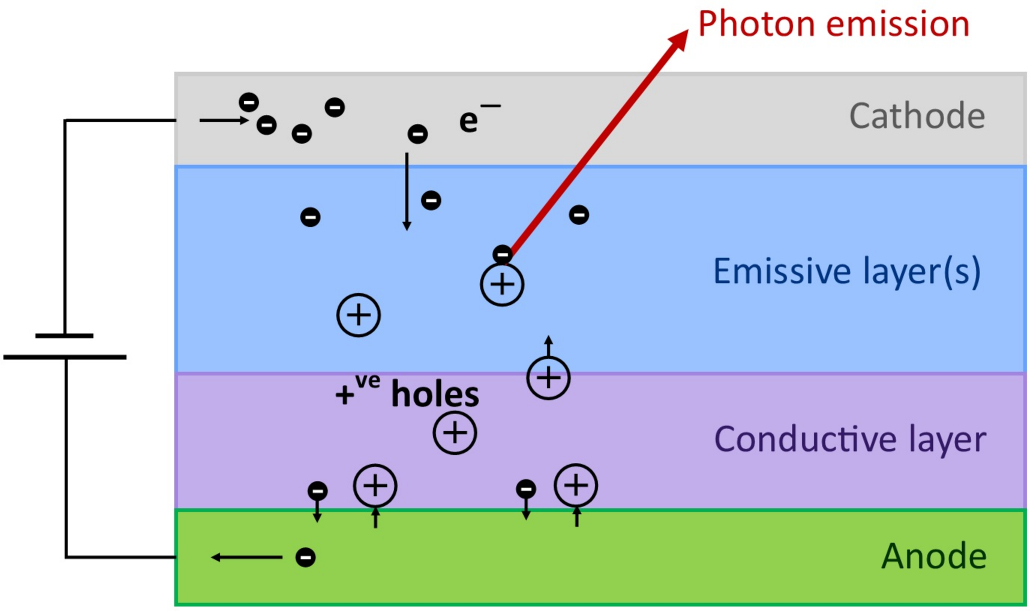

Figure 1.4: Example schematic for an organic light emitting diode.

A schematic is shown in Figure 1.4. Upon activation of the device, electrons are injected to the cathode, typically a reflective metal (to prevent the absorption of emitted photons) such as aluminium, calcium or barium with low work functions that allow the unhindered injection of electrons into the organic emissive layer(s).[44] The holes are injected to the organic conductive layer (also known as the hole transport layer) by the anode, which is typically ITO or an equivalent transparent conducting layer with a work function similar to the energy level of the highest occupied molecular orbital (HOMO) of the organic conducting later, which allows the removal of the HOMO electrons from the organic layer into the TCO, generating mobile holes in the organic layer.[45] These holes can move towards the emissive layer, whereupon they recombine with electrons (from the cathode), emitting visible light photons. Depending on the nature of the organic materials in use in the device, the anode can quite easily be the most expensive component due to the cost of the ITO. As such, replacement of ITO with a cheaper, more sustainable material could dramatically reduce the overall cost of fabricating such devices.

1.1.3 The indium issue

In any application that does not require mechanical flexibility, ITO is the best material for use as a transparent conducting thin film in terms of its properties; it is highly conductive and transmissive, as well as being physically and chemically stable.[22] It is not, however, a sustainable material, in terms of pricing volatility and long-term availability it is unlikely that indium supply will continue to meet demand. ITO films started to gain traction in industry in the 1960's with the emergence or popularisation of various technologies, and the price of the material began its first climb in the 1970's. Figures 1.5 and 1.6 show the price fluctuations of the three most significant metals in TCOs, In, Sn, and Zn, between 1950 and 2015. The former shows best the volatility of the price of indium in the last several decades, from below \$100 kg^{-1} pre-1974, 1984-6, and in 2002, to highs of over \$700 kg^{-1} in 2005 (up to \$946 kg^{-1}), 2006, and 2014.[46] The latter shows the same data, but is adjusted to a logarithmic scale on the y-axis, so as to better compare the price of the three metals.

Indium is sourced exclusively as a by-product from zinc mining operations.[46, 47] The element occurs in such small amounts that dedicated mining operations are impractical; hence the supply of indium faces its greatest worry if the demand for zinc falls. For example, should the automotive industry switch from steel to aluminium car bodies, this would affect the demand for zinc, and thus the mining and production of zinc, which in turn could reduce the amount of indium produced.

Shown in Figure 1.7 is the annual global indium production broken down by country.[47–66] In the last decade, production has been between 500 - 900 tonnes per year, of which the vast majority is produced in China and South Korea. Thus

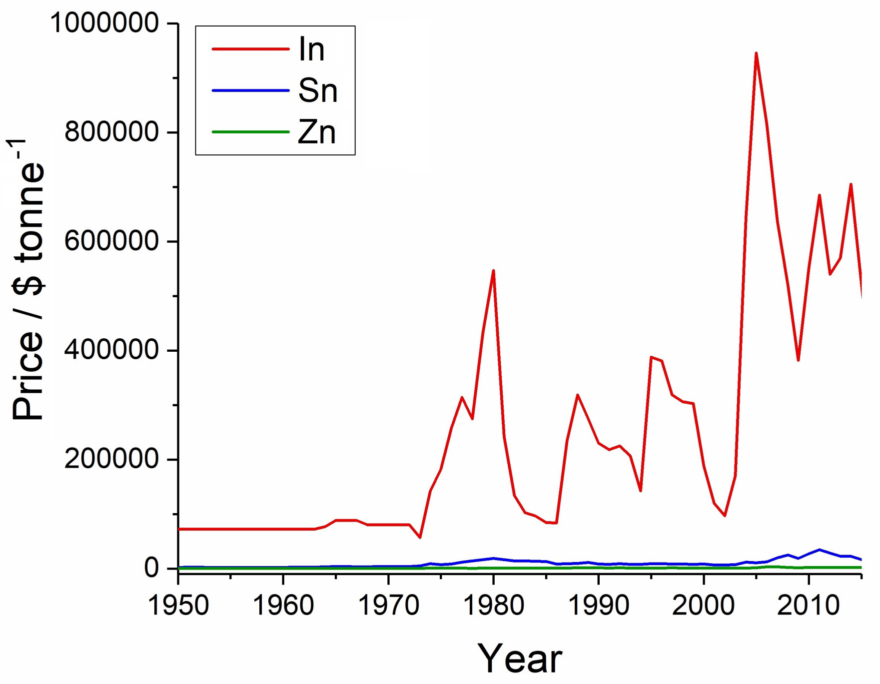

Figure 1.5: Comparison of the prices (in US$ per metric tonne) of In, Sn, and Zn, between 1950 and 2015, using a linear scale.

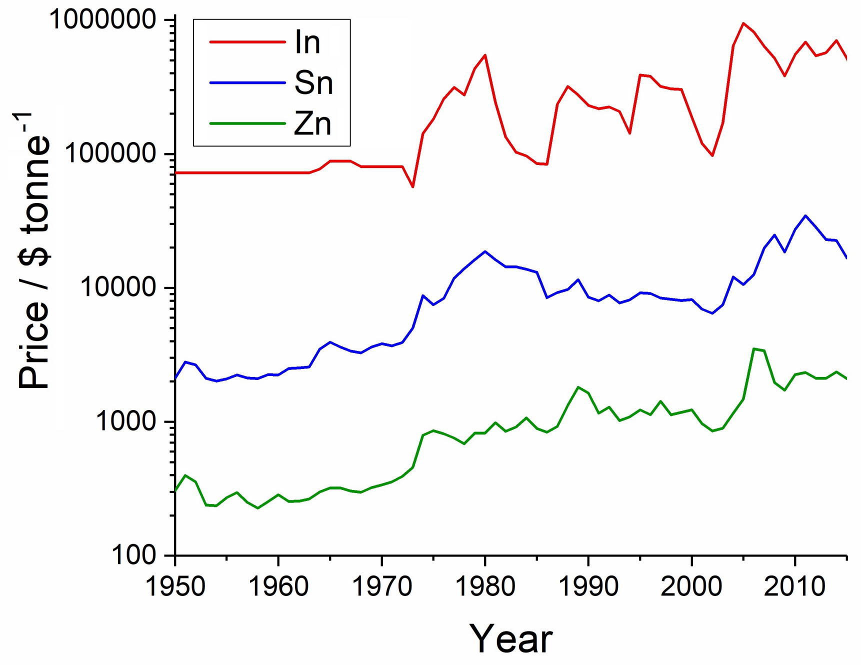

Figure 1.6: Comparison of the prices (in US$ per metric tonne) of In, Sn, and Zn, between 1950 and 2015, using a logarithmic (base 10) scale.

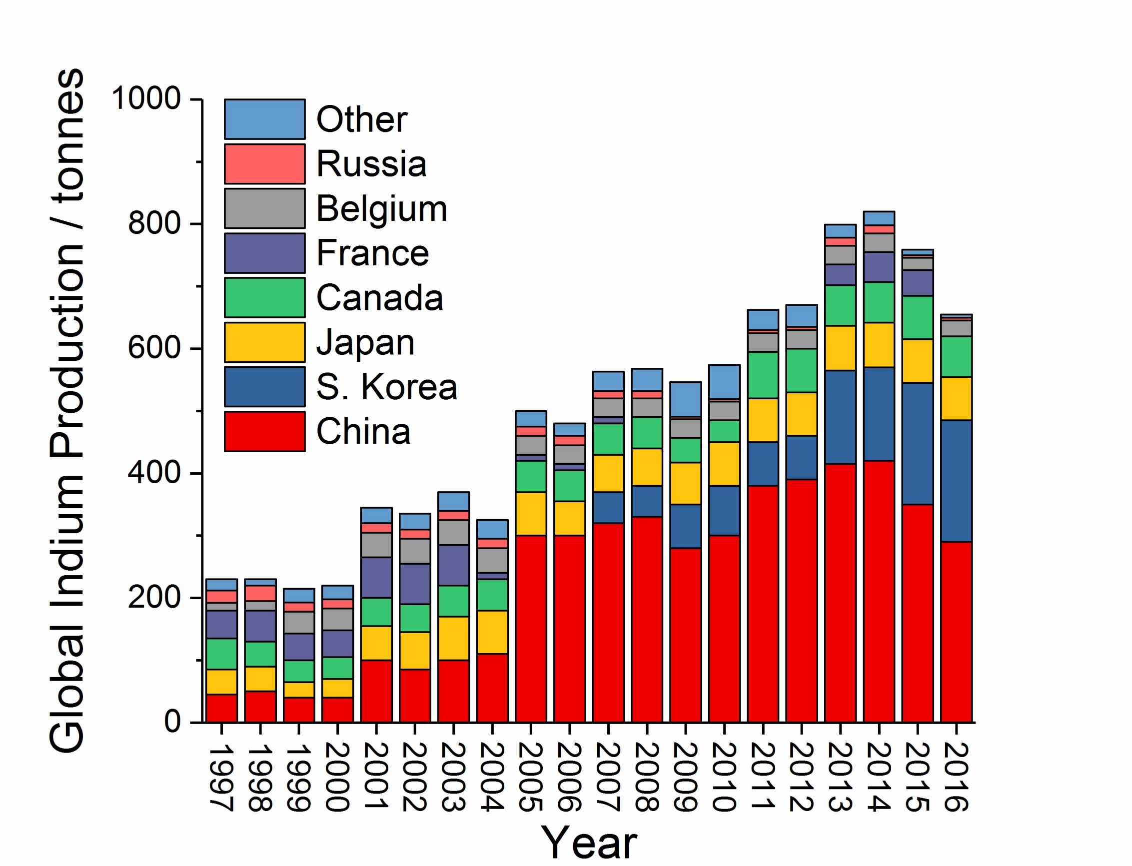

Figure 1.7: World indium production in tonnes broken down by the principal countries producing it, between the years of 1997 and 2016.

there is the potential for sociopolitical issues regarding continued use of indium in industry, in addition to the price volatility and ever-growing demand.

Though not included graphically, the price of indium in 2016 was drastically reduced to as low as \$228 kg^{-1}.[47] This is thought to have been due to the collapse of the Fanya Metal Exchange Co. Ltd. in 2015, resulting in an oversupply of indium and depressed demand for the the metal.[67, 68] Global production was also affected by a fire in November 2015 that damaged the indium production plant at the Auby zinc smelter in France,[69, 70] entirely diminishing France's output.[47]

It is beyond the scope of this Thesis to postulate as to the possible future demand and supply of indium beyond those analytical reports and forecasts already referred to,[40–43] but the aforementioned economic factors have led to the growing need to find cheaper and more sustainable alternatives for indium in technology wherever possible; as such there is both a scientific and industrial imperative to conduct research along the lines of that discussed herein. Most pertinent to this work is thus the requirement to find alternative TCO materials to ITO.

1.2 Promising Replacement Materials

In pursuit of phasing indium out of the TCO industry, there are a number of different potential replacement materials. The two 'host' materials most studied are ZnO and SnO_2. These are both conductive in their own rights, but are improved by introduction of aliovalent dopants. This section discusses the properties of these materials, and the precedent for their use as TCOs.

1.2.1 Tin dioxide

As shown in Figure 1.5, tin tends to be much cheaper than indium, and films based on SnO_2 can be deposited by the same processes as ITO. Thus there is no need to replace the deposition machinery when attempting to replace the material. SnO_2, like In_2O_3, is a natively *n*-type semiconductor, and this native conductivity is again based primarily on the formation of oxygen vacancies,[71] as shown in Equation 1.1 on page 34. The structure is tetragonal rutile, and the band gap is ca. 3.6 eV.[72] It has been postulated for some time that the oxygen vacancies take the form of shallow donor levels near the conduction band.[73] Interstitial tin, Sn_i can also readily form, another source of conductivity, and neither of these are compensated by the formation of V_{Sn} or O_i as might be expected, as these are formed deep in the valence band, leading to a high charge carrier concentration even in the undoped material.[12, 72] Additionally, if the annealing of the material is under reducing conditions, the hydrogen present, though it is possible it could draw out some lattice oxygen, will tend to add hydrogen to the structure, either as H_i, the interstitial, or on the oxygen site, as H_O. In either case, this forms an additional shallow donor level, which can contribute to the conductivity of the material.[12, 73]

Thin films of SnO_2 have been made by a variety of methods, with resistivities as low as 1.1 x 10^{-3} Ω cm for CVD,[74] 1.5 x 10^{-3} Ω cm for films made by magnetron sputtering,[75] and as low as 7.5 x 10^{-4} Ω cm for electron beam evaporation methods,[76] the latter with optical transmittance up to 90 %. Difficulty in effective sintering/annealing has generally prevented SnO_2 from obtaining the levels of resistivity reported for indium or zinc-based materials, the scattering effects from defects and grain boundaries proving deleterious for the electronic properties in many cases, particularly noticeable with increasing film thickness, which inherently causes a greater concentration of these defects to be present in the thin film.[77–79] One potential way around the issues of using polycrystalline material could be to use the amorphous analogue, however despite recent advances and device implementation of amorphous TCO films, these do not tend to exhibit nearly the electronic capabilities of the crystalline materials.[80–83]

In addition to the oxygen vacancies, aliovalent dopants can be introduced to the lattice, most commonly Sb^{5+} onto the Sn^{4+} site, or F^- on the O^{2-} site, i.e. $Sb^{\bullet}_{Sn}$ or $F^{\bullet}_{O}$, respectively, both of which contribute towards the *n*-type semiconductivity of the material. Sb-doped SnO_2, also known as ATO, and F-doped SnO_2, also known as FTO, are the most commonly researched SnO_2-based materials for TCO applications.[71] ATO is analogous to ITO, in that the metal ion is being replaced by a dopant with an oxidation state one higher. Though in some cases, the optical properties are below the standards set for TCOs,[84] films towards the lower end in the order of 10^{-3} Ω cm have been made by sputtering,[78, 85–87], sol gel/spin coating,[84, 88] pulsed laser deposition,[89] and spray pyrolysis.[90, 91] Generally, the reduced conductivity is attributed to low mobilities, caused by the abovementioned effects, often only around 10 cm^2 V^{-1} s^{-1},[84, 90] compared to $>$ 30 cm^2 V^{-1} s^{-1} for ITO.

FTO is actively used in industrial processes as an ITO replacement material, accounting for the second largest share of the TCO market behind ITO itself, in part due to the reduced cost, but also due to the chemical and thermal stability of its electrical properties, though the material is not as conductive as ITO, nor as well suited for patterning or etching.[92] As with ATO, the best films in terms of electrical properties have been deposited by spray pyrolysis,[79, 93–96] as low as 2 x 10^{-4} Ω cm for the resistivity.[94, 96] Sol-gel dip coating methods have obtained resistivities in the order of 10^{-4} Ω cm too,[97] as have CVD processes,[98, 99] though with film growth rates of only a few nm min^{-1}. Up-scaling of similar CVD processes to 100 nm min^{-1} have been carried out, but at a cost of resistivity by some two orders of magnitude.[100]

Though these are the most common SnO_2-based TCO materials, many other dopants have been tested. Tantalum[101, 102] and tungsten[103] doping have achieved resistivities of 2 x 10^{-3} Ω cm when deposited on glass, though by deposition onto a heated Al_2O_3 substrate, the former has been reported to have resistivities as low as 3.5 x 10^{-4} Ω cm.[104] Praseodymium[105] and neodymium[106] have also been tested, with resistivities of 3.7 x 10^{-3} Ω cm and 6.2 x 10^{-3} Ω cm reported, respectively, though the former in conjunction with fluorine doping, which would be expected to further enhance the conductivity.

Introduction of Al, Ga, or In onto the Sn site in the lattice would be superficially expected, by the converse logic to Sb replacing Sn, to result in p-type semiconductivity. And indeed, there are reports that claim precisely that, for In,[107] Ga,[108, 109] and Al.[110] The p-type nature of the conductivity is expressed, by Hall Effect measurements, as producing a positive Hall coefficient, whereas for n-type materials the Hall coefficient is negative. And that is what the aforementioned studies report, specifically a cross-over point at which drastically reduced, p-type semiconductivity is observed (several orders of magnitude increase in resistivity). Though not categorically known to be impossible, the general consensus from recent studies is that p-type SnO_2 is highly unlikely.[12] This is from the computational standpoint of calculating the formation energies of a number of defects, and deducing the likelihood of each being present, and what effect their presence has. It is, from more advanced hybrid density functional theory, concluded that no shallow acceptor levels that are uncompensated will be formed from any likely candidate defects in SnO_2, which would be necessary for p-type semiconductivity to occur,[12] though there do exist less recent computational studies that have concluded that p-type SnO_2 is plausible.[111]

1.2.2 Zinc oxide

Zinc oxide exists predominantly in hexagonal Wurtzite structure, with a band gap ca. 3.4 eV.[19, 112] The mechanism for conductivity differs from that of In_2O_3 or SnO_2 however, in that for ZnO, the V_O defects act as much deeper donor levels than might be conventionally thought.[113] Instead, it tends to be hydrogen impurities that result in the observed n-type conductivity in undoped ZnO. Hydrogen in ZnO is highly atypical; it has been postulated that generally speaking hydrogen acts as an amphoteric impurity in a semiconductor, i.e. it is present as H^+ in a p-type semiconductor, and as H^- in an n-type semiconductor, counteracting the inherent conductivity of the material; the prevailing belief for a time was that in ZnO, hydrogen is always present as H^+, the only form in which it was supposedly thermodynamically stable, and indeed this is the case below the conduction band minimum.[114–116] However a DFT study in 2011 showed that H^- could also be present as a shallow acceptor, with the (+/-) transition for H_i at 0.34 eV above the CBM.[117] Both H_i and H_O have similar formation energies, and while in the lattice the hydrogen will tend to be strongly bound to the lattice oxygen, effectively forming O-H bonds while acting as shallow donors to contribute to the conductivity of the ZnO.[19] Generally speaking, ZnO-based TCO materials can not be patterned as easily due to chemical instability, particularly of Al-doped ZnO, but this sensitivity to both acidic and basic conditions means that wet etching is possible, unlike

ITO, wherein dry etching is necessary.[118]

Again, the introduction of aliovalent dopants has been shown to be highly effective with regards to increasing the conductivity of ZnO, most commonly Al (AZO) and Ga (GZO), but many more have been investigated. ZnO-based materials tend to be slightly less conductive than ITO, and slightly more transparent.[37, 118] It was concerns with the thermal stability of undoped ZnO that led Minami et al. to sputter films of AZO in the early 1980's,[119] achieving resistivities as low as 2 x 10^{-4} Ω cm. Other methods have garnered similarly low resistivities, while still maintaining high optical transparency, including CVD,[120, 121] PLD,[122] and spray pyrolysis.[123] GZO has seen equivalent resistivities (generally slightly higher, but balanced by higher chemical stability than AZO) from magnetron sputtering,[124–126] PLD,[127] and CVD,[128, 129] and the co-doped material, AGZO, has from sputtering achieved similarly conductive thin films.[130–133] The other doped systems explored include zinc oxide doped with silicon,[134–136], indium,[137] tin,[138] niobium,[139] lanthanum,[140] and neodymium,[141] among numerous others. Many of these have quite competitive resistivity and optical properties, however the most promising remain AZO, GZO, and AGZO.[13, 37, 39, 142] The considerable reduction in cost for zinc versus indium, and to a lesser extent versus tin, mean that more expensive dopant elements can be considered, as the low level of these still results in the specific cost of the material being relatively low.

For a fuller description of the different doped zinc oxide systems investigated, see Section 3.2 on page 74. For detailed discussions into AZO, GZO, and AGZO, see Section 4.2 on page 109 and Section 6.2.2 on page 151.

1.3 Deposition Techniques

This section will outline the predominant methods of depositing thin films of TCOs, including physical and chemical vapour techniques, and spin coating and inkjet printing.

1.3.1 Physical vapour deposition methods

Physical vapour deposition (PVD) techniques are the pre-eminent thin film deposition methods employed in the majority of TCO applications. Most commonly used is magnetron sputtering. A highly simplified schematic for such a process is shown in Figure 1.8. Ions (in this case of the in-flowing Ar gas) bombard the target, for example a dense ITO ceramic, and the formed plasma is ejected towards the substrate, guided by electrical and magnetic fields, resulting in a thin film of the target material forming on the substrate. Though the magnetic field helps to direct the formed plasma and moderate thin film growth, inevitably a large proportion of the target will end up on the walls of the chamber.

When one casts their eye over scientific reports of TCO thin films in search of the most conductive films, inevitably magnetron sputtering will dominate the list, particularly with regards to ZnO-based films. For example, the work of Ray et al.[30] and Shigesato et al.,[31, 143] resulting in thin films of ITO deposited by magnetron sputtering all with resistivities $< 2 \text{ x } 10^{-4}$ Ω cm. Examples are prevalent too of thin films of zinc oxide doped with aluminium (AZO),[119, 144–146] gallium (GZO),[124, 125] aluminium and gallium together (co-doped, AGZO),[130–133] and silicon (SiZO),[134, 135, 147] all of which had resistivities in the order of 10^{-4} Ω cm. Magnetron sputtering can be scaled, the technology for deposition is relatively mature, and the resulting films are conductive and transparent.

The other commonly investigated PVD technique is pulsed laser deposition, wherein a high power laser ablates the ceramic target, and the resulting plasma plume condenses into a thin film on the substrate as shown diagrammatically in Figure 1.9.[1] This technique has been shown to be effective in generating conductive films if ITO,[148] AZO,[122] GZO,[127] and SiZO,[136] however the films are seldom as conductive as their sputtered analogues. This process can use an ultra-high vacuum, higher than would be used for sputtering, and uses the Coulombic repulsion and recoil from the target to send the plume towards the substrate, normal to the target orientation.

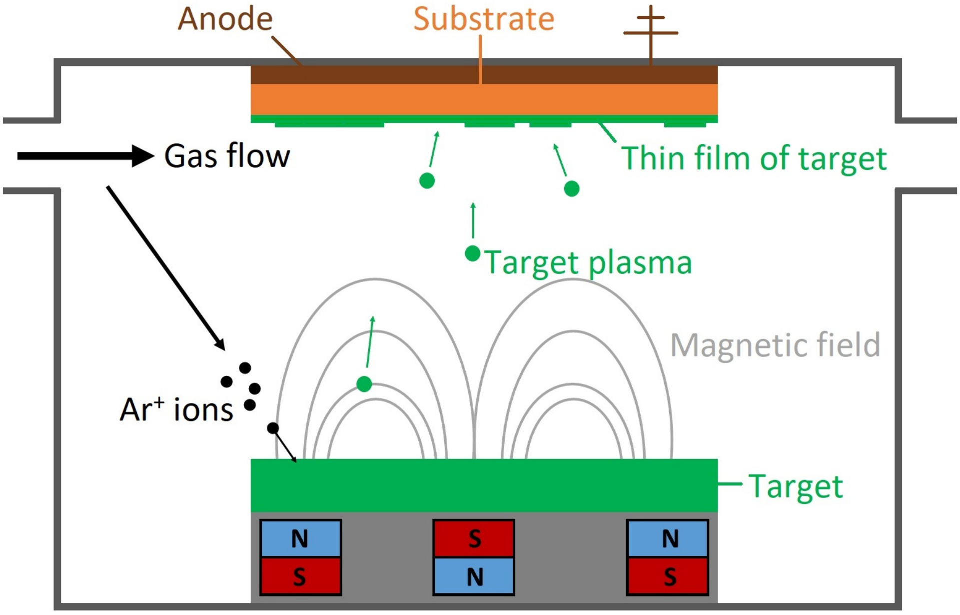

Figure 1.8: Schematic of a simplified magnetron sputtering process.

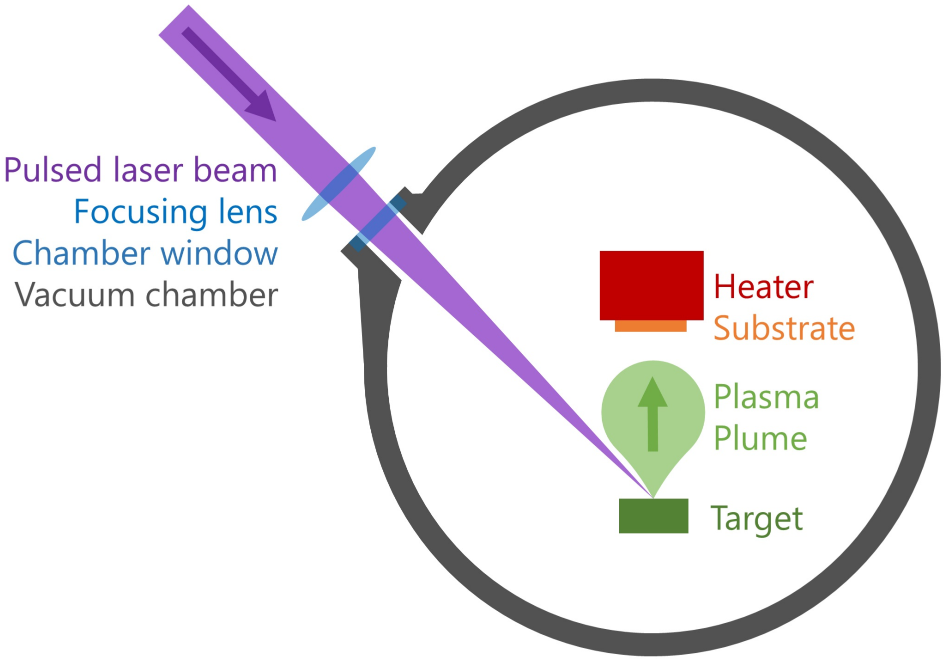

Figure 1.9: Schematic of a simplified pulsed laser deposition process. Adapted from [1]

1.3.2 Chemical vapour deposition methods

Chemical vapour deposition (CVD) methodologies are also widespread when it comes to thin film deposition. In a typical CVD process, volatile organometallic precursors react and/or decompose on the surface of a heated substrate. There is huge variation in the pressures and temperatures used across various CVD techniques, but generally the TCO thin films are now deposited at atmospheric pressure, and particularly for AZO[120, 121] and GZO,[121, 128, 129] some of the most conductive films are deposited using this process. Early CVD depositions were predominantly at reduced pressures,[149] but there is cost and safety benefit to carrying out equivalent processes at atmospheric pressures. An aerosol assisted CVD rig schematic is shown in Figure 1.10. A bubbler of some description is used to generate an aerosol of an organometallic precursor, for example zinc acetylacetonate ($Zn(acac)_2$) as a precursor for ZnO, which would carried into the reaction chamber, the (acac) groups break down on contact with the heated substrate, allowing the formation of the desired thin film, while the decomposition products are extracted.

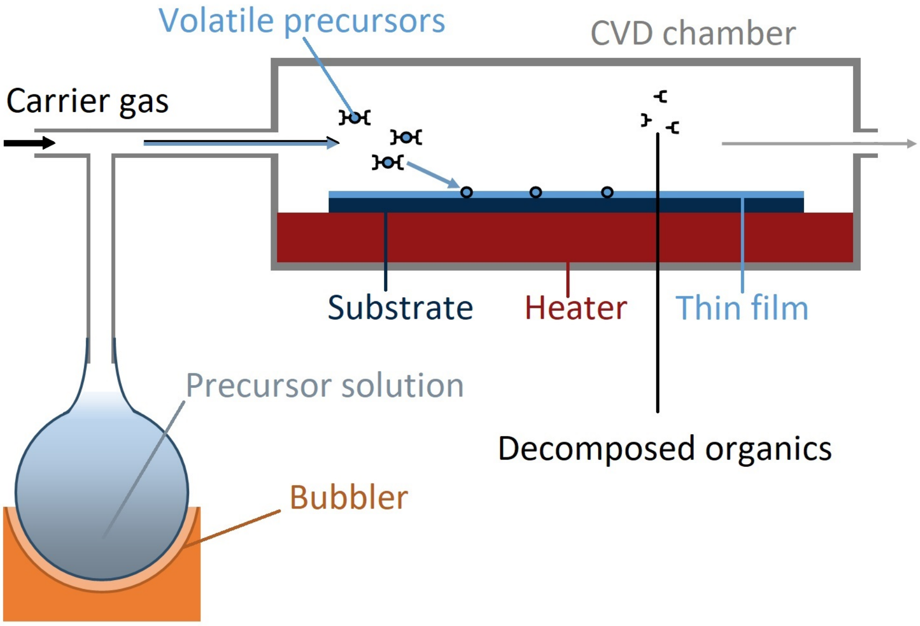

Figure 1.10: Schematic of a simplified aerosol assisted chemical vapour deposition process.

In some ways very similar to CVD, is spray pyrolysis, wherein a typically aqueous precursor solution is sprayed onto a heated substrate, and the product film is formed by hydrolysis reactions. In this case, the distinction between spray pyrolysis and CVD lies in whether or not the solution vapourises before impacting the substrate.[150]

1.3.3 Ink/dispersion-based methods

Inks and dispersions can be made in several ways. With regards to TCOs, the most common method would be via a sol-gel process. The metal precursor(s) are dissolved in a solvent or solvent mixture, heated and stirred, typically with a complexing agent (added after initial nucleation) which facilitates, over time, the formation of a colloidal suspension of the product. 'Ageing' of the solution can take several days before spin coating is carried out. This is typically in a static regime, in that drops are placed on the substrate, which then undergoes rapid spinning, versus dynamic spin coating in which the substrate is already spinning, and the material is dropped onto it.[151–154] TCO thin films have been made by spin coating sol-gel synthesised materials achieving resistivities as low as 6.3 x 10^{-4} Ω cm for ITO,[154] and 3.9 x 10^{-3} Ω cm for AZO.

The alternative is to suspend already-synthesised nanoparticles in a dispersion medium, typically by sonic agitation, and carry out the spin coating before the particles have a chance to settle out, but generally speaking this results in inferior electrical properties.[20, 154]

Inkjet printing is far less reported. In this process, a dispersion of ceramic nanoparticles is used to print thin films by deposition of numerous droplets, placed very precisely, which depending on the wettability of the substrate, and properties of the droplets, can coalesce into a continuous layer, which can in turn be carefully dried of the dispersion medium to leave a consistent film. Heat treatment to anneal this film is necessary to generate the electrical contact and network through the particles. The films tend to be highly transparent, but also highly resistive. As with the re-dispersion of nanoparticles for spin coating, the resulting film is not as conductive as the materials are capable of, whether due to imperfect or ineffectual annealing, dispersion quality or indeed quality of the film itself. Inkjet printed films of ITO have achieved resistivities as low as 3 x 10^{-2} Ω cm (some 100 times higher than required of TCOs) with transparency as high as 87 %.[155] In this study in particular is demonstrated an additional capability of inkjet printing, in that in addition to this film, another was deposited that also had an Ag grid put down, which enhanced the conductivity of the film by approximately two orders of magnitude. The transparency fell to 82%, still within the acceptable range, and due to the precision and small droplet sizes, this required very little expensive silver to achieve. A similarly conductive (sans silver grid) AZO film was deposited by inkjet printing with a transparency of 93 % by Vernieuwe et al.,[156] but the resistivity of 2.5 x 10^{-2} Ω cm is too high for the high transparency to make up for.

1.3.4 Deposition method comparison and summary

Given that the material cost, especially with regards to ITO, is a significant issue in the generation of thin films, using a deposition method that is as efficient as possible is optimal, as waste of material is an additional cost to the process.

Most of the deposition techniques described above do not deposit even a majority of the starting material onto the substrate. This particularly concerns magnetron sputtering, the most commonly used industrial process, wherein as little as 30 % of the target ends up in the film, while the rest coats the walls of the chamber. Much of this can be recovered and is not necessarily permanently lost, but the situation is not ideal. PLD suffers similarly, though to a lesser extent, and CVD too. And it is not only the vapour techniques; spin coating results in much of the dispersion coating the walls rather than the substrate.

Of all the methods, only inkjet printing transfers all of the material into the film. In terms of vehicle-to-substrate transport, it is by far the most efficient, however the electrical properties of the films fall short of the requirements for TCOs. Resistivities in the order of 10^{-2} Ω cm are the best reported thus far, whereas all of the other methods are capable of generating films in the order of 10^{-4} Ω cm. If inkjet printing is to become an industrially viable technique, address of this shortcoming is absolutely essential.

1.4 Synthesis of Nanoparticles

This section aims to outline the specific process by which all of the nanomaterials discussed in this thesis were synthesised, including first a comparison to analogous batch syntheses, then a more detailed discussion as to the nucleation and growth of nanoparticles in a continuous hydrothermal flow synthesis (CHFS) process. Find presently a discussion as to the scientific basis and applications of CHFS; detailed discussion as to how this pertains to the specific TCO materials appears in the introduction sections of each Chapter, where relevant.

1.4.1 Batch synthesis methods versus continuous methods

The distinction between batch and continuous synthesis methods can be distilled as follows: a batch synthesis is a closed process, in that a reaction occurs between a set of reagents under a certain set of conditions, after which the product is separated out and collected, the conditions returned to atmospheric norm. By contrast, a continuous process is not a closed system; it involves the ongoing addition of reagents and removal of products in flow, and subject to the longevity of the machinery involved, and the availability of reagents, a continuous process can be continued indefinitely.

For many syntheses, precise control of temperature and pH, among other properties, is of great importance. Slight variations can, for example in sol-gel processes, lead to significant batch-to-batch variations, a significant issue for an industrial process, in which consistency of particle properties is critical.[157, 158] This and other processes, such as co-precipitation methods, can be very involved, with multiple slow steps required before the end product can be collected.[159] Specifically concerning metal oxides, batch industrial processes, such as the French Process for generating zinc oxide, may involve the use of extreme temperatures (ca. 1000 °C), and as such are very energy-intensive.[160]

Industrial processes for nanoparticle synthesis should ideally satisfy a number of requirements. These include, but are not limited to, the necessity for production of controlled, homogeneous materials with consistent properties for their desired applications, the in-line monitoring of said consistency, lack of needless complexity in the process (single-step processes are ideal), efficiency in energy and resource use, both at research and industrial scale of production, flexibility in reaction parameters to fine-tune particle properties, and perhaps above all should be the safety of the process. This includes the risk to workers from process machinery (and by extension the facility to safely disable said process machinery), as well as from potentially harmful reagents and solvents, and pertinent to this research in particular, from nanoparticles themselves. The long-term health risks are not fully known, but that dry nanoparticles can be inhaled is not in question, merely the potential detriment to the respiratory health of those involved.[159, 161, 162]

In address of these, continuous hydrothermal processes stand tall. Temperature, pressure, pH, concentration, flow rates, and mixing regimes among other parameters are easily controllable, and system/flow properties and dynamics can be calculated precisely should one have a chemical engineer to hand. Monitoring of the process while synthesis is carried out is also possible, and from the point of view of the process scientist carrying out the synthesis, safety precautions and reaction design can allay the majority of concerns. Water is typically the only solvent, and the product is collected as a wet slurry of nanoparticles in water, such that the nanoparticles produced are not in a form that can be inhaled at all.[159] The process is, however, typically carried out at high temperatures and pressures, though at lower temperatures than many industrial batch processes,[159, 160] and though safety precautions can minimise the risk to personnel, no such process can ever be entirely risk-free.

1.4.2 Continuous hydrothermal flow synthesis

Continuous hydrothermal flow synthesis (CHFS) processes, especially those employed herein, principally take advantage of the change in water properties across the supercritical/liquid phase boundary. This is depicted in Figure 1.11, wherein the phase behaviour of water at different temperatures and pressures is depicted.[2] Three points of interest in the graph are denoted by the dashed lines. From left to right, first there is the triple point of water, the point at which (pure) water can exist as solid, liquid, and gas. Second is the boiling point of water at 100 °C and atmospheric pressure, and finally is the critical point. At 22 MPa (218 atmospheres) and 374 °C, water becomes supercritical. Whereas room temperature and pressure water has a density ca. 1000 kg m^{-3}, supercritical water has a density of only 322 kg m^{-3} at the critical point.[163]

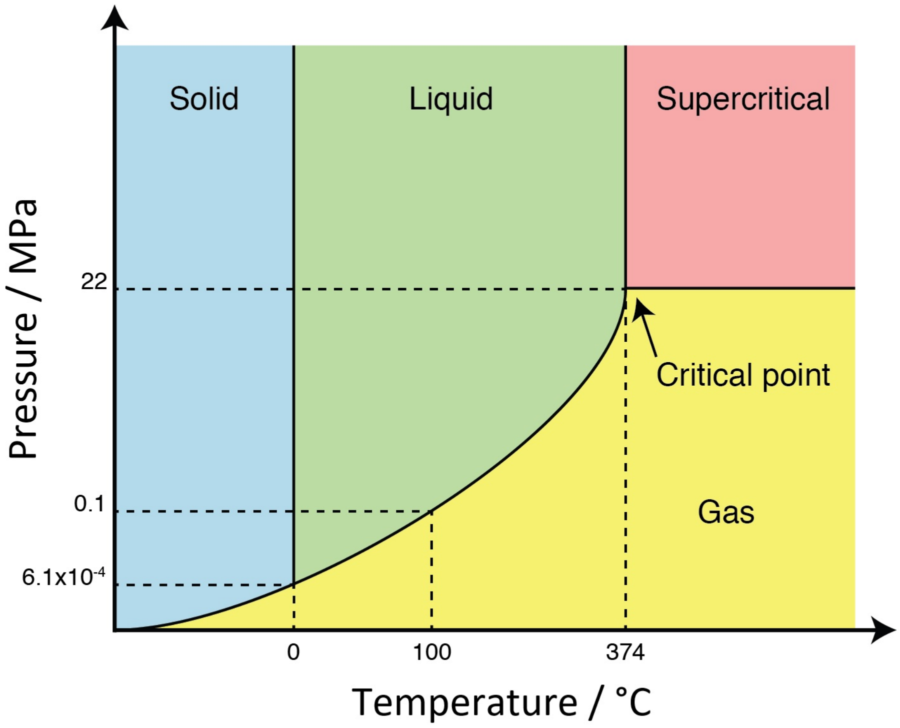

Figure 1.11: Simple phase diagram for water to depict the matter-phase behaviour under different temperatures and pressures. Used with permission from [2].

Another key difference in the properties of liquid versus supercritical water is in the dielectric constant, the measure of its ability to solvate polar species. Room temperature water has a dielectric constant of 80 (the highest of all common solvents), but this falls with higher temperature and pressure, to only 5 at the critical point, primarily due to the breakdown of the extended hydrogen bonding network; in the supercritical phase there is approximately 30 % free monomeric H_2O molecules, and the hydrogen bonding is reduced to ca. 17 % relative to room temperature and pressure water, though still considerably more than would be present in the gas phase. Indeed, supercritical water exists in liquid-like hydrogen bonded clusters dispersed within a gas-like phase, interfaces between other phases no longer exist so there is no surface tension to speak of.[164–166] These changes between liquid and supercritical states do not occur instantaneously upon reaching the critical temperature and pressure, there are significant changes in near-critical (sub-critical) water relative to the liquid phase too, and advantage can be taken of these in a CHFS process.[159, 163]

The precursors for a CHFS reaction are typically aqueous metal salts, for example zinc nitrate as a precursor for zinc oxide. This has a very high solubility in water, 93g per 100 mL of room temperature water,[167] because it is highly polar. This also means that it is not soluble in non-polar solvents, as supercritical water can be classified. Hence if a room temperature solution of zinc nitrate (even very dilute) meets and mixes thoroughly with a stream of supercritical water, it will be in a supercritical, or near-critical state. The solution becomes supersaturated with the zinc nitrate, which will crash out of solution and react with the superheated water around it according to the two-part reaction scheme depicted in Equations 1.3 and 1.4 for a metal nitrate reagent, where the metal is represented by ‘M’. In this case, the nitric acid produced will make the product stream acidic; modifiers such as potassium hydroxide can be added to aid in the nucleation of the metal oxides, and to neutralise or make alkaline the product stream.

$$\mathrm{M(NO_3)_{x\,\mathit{(aq)}}} + x\mathrm{H_2O} \rightarrow \mathrm{M(OH)_{x\,\mathit{(s)}}} + x\mathrm{HNO_3} \tag{1.3}$$

$$\mathrm{M(OH)_{x\,\mathit{(s)}}} \rightarrow \mathrm{MO_{\frac{x}{2}\,\mathit{(s)}}} + \frac{x}{2}\mathrm{H_2O} \tag{1.4}$$

This applies to many metal oxides, though conversion of the hydroxide to the oxide requires that there be sufficient energy, so in some instances, such as in the case of the CHFS synthesis of In_2O_3, the oxide is only formed at mixing temperatures of 400 °C or more; lower temperatures result in the partially converted InO(OH).[28, 168, 169] However, with materials such as CeO_2 and ZrO_2,[170, 171]

NiO,[172] ZnO,[173, 174] and TiO_2,[175] among others, the oxide can be formed at milder temperatures. The applications of CHFS are limited only by what materials can be synthesised. Gas sensing,[176, 177] photocatalysis,[174, 178, 179] lithium ion batteries,[180–183] capacitors[184] and thermochromics[185, 186] are only a small selection of the applications to which CHFS can be lent; for a full and more detailed delve into the field I refer the reader to the review by Darr et al.[159]

With regards to TCO materials, ITO has been made in hydrothermal flow before,[169, 187] but in only one report was subsequently deposited as a thin film, yielding resistivities around 1 x 10^{-2} Ω cm.[168] Other prospective TCO materials have been synthesised by CHFS, including some doped zinc oxides,[174] and niobium-doped titania,[181] however these were not tested for their TCO-related properties, but for photocatalysis and energy storage, respectively.

1.4.3 CHFS as a combinatorial tool

CHFS lends itself very effectively to high throughput, combinatorial screening of different materials, in that by altering the precursor solutions, a large number of samples can be synthesised in a relatively short period of time, for example the high-throughput synthesis of a 66-sample phase diagram of $Ce_xZr_yY_zO_{2-\delta}$ in $<$ 1 day.[170] This is something for which there is no simple analogue for batch synthesis processes, beyond the acquisition and use of 66 autoclaves. Other prevalent combinatorial synthesis methods (non-CHFS) have been in use for up to two decades,[188] including magnetron sputtering,[188–192], pulsed laser deposition,[193–195] molecular beam epitaxy,[196] flame pyrolysis,[197] sol-gel,[198], solid state,[199, 200] and chemical vapour deposition.[201] These have encompassed a variety of technological application research areas, such as superconductors,[188, 193] TCOs,[189–192, 194, 197, 198, 201, 202] photocatalysis,[196, 198] and themoelectrics.[195, 199, 200] These techniques are for the most part geared towards the synthesis of combinatorial libraries in the form of thin films; with the exception of solid state[200] and spray pyrolysis[197] methods, there has been a lack of combinatorial methodology for the production of nanopowders. Given the few examples that so far exist, it is clear that for materials discovery and compositional optimisation, CHFS can be a powerful combinatorial research tool that has yet to be properly applied to the field of TCOs.

1.5 Hypotheses

In this chapter, the fundamentals to the understanding of this thesis were presented. The properties and applications of transparent conducting oxides were discussed, as well as the issues in the field, namely those presented by continued use of indium-based materials, and the consequent requirement not only for more sustainable replacement materials, but also the development, and more prevalent use of increasingly sustainable synthetic and deposition methodologies.

Thus, the hypothesis question of this thesis is as follows:

Can continuous hydrothermal flow synthesis be used to synthesise materials that demonstrate, when deposited as thin films, the optical and electronic properties that are required of transparent conducting oxides in their various applications.

This can be broken down into the following investigative steps:

i. To screen numerous materials synthesised by continuous hydrothermal flow synthesis, in order to determine the systems that demonstrate the most promising electronic properties.

ii. To optimise these most promising systems in terms of the dopant level for maximal conductivity.

iii. To surface-functionalise these optimised materials within the synthetic process, and deposit them as thin films by such methods as spin-coating or inkjet printing, furthermore optimising the processing and heat treatment of the films to obtain as optically transparent, electrically conductive, materials as possible.

Chapter 2

Experimental Methods

2.1 Introduction

This chapter discusses the experimental methods employed throughout this work. Descriptions of the different Continuous Hydrothermal Flow Synthesis (CHFS) setups used are given, followed by descriptions the various techniques used for sample processing and characterisation. The aim of this chapter is to give an overview of synthesis and characterisation methodologies; specific reaction and analysis parameters will be detailed in each corresponding chapter where relevant.

2.2 Synthesis and Cleaning of TCO Nanoparticles via CHFS

The laboratory-scale CHFS reactor was built by Dr C. Tighe, Dr R. Gruar, and Dr N. Makwana, and its development is detailed in the respective theses of the latter two;[203, 204] alteration of the laboratory 3-pump setup to the high-throughput setup was performed by Dr L. McCafferty. The pilot-scale reactor was built by Dr R. Gruar and Dr C. Tighe.[205]

The following sections detail the reactor setups utilised in this work, including 3- and 4-pump laboratory and pilot-scale setups, and the high-throughput setup. All fittings and pipes were made of 316L stainless steel supplied from Swagelok (Kings Langley, UK). Figure 2.1 shows photographs of the pilot-scale (a) and laboratory-scale (b) reactors.

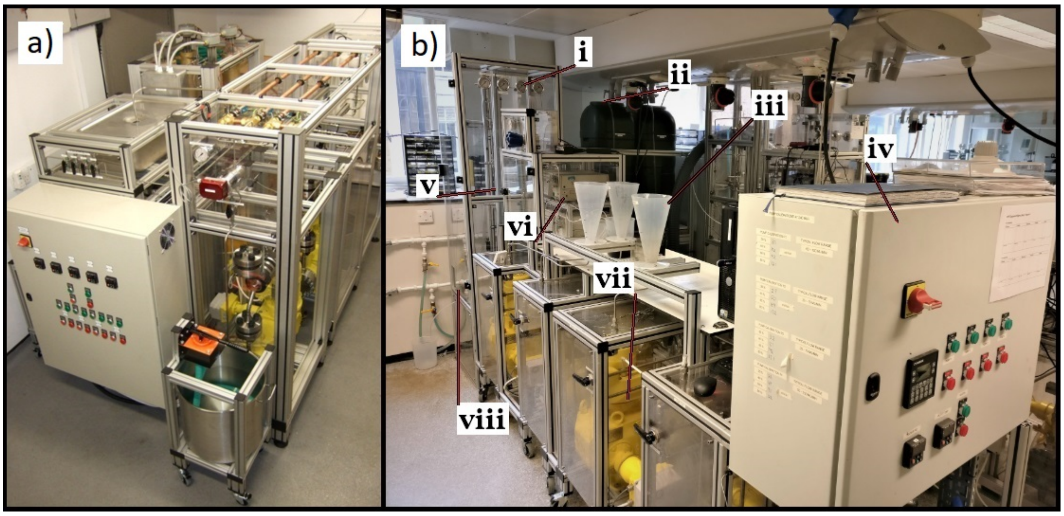

Figure 2.1: a) The pilot-scale CHFS reactor, and b) the laboratory-scale reactor. The labels correspond to i) pressure gauges, ii) deionised water reservoir, iii) the precursor feed vessels, iv) the control module, v) the mixer and chiller setup, vi) the high-throughput setup Gilson pumps, vii) the Milton Roy diaphragm pumps, and viii) the back-pressure regulator (BPR) and outlet.

2.2.1 3-pump setup

Figure 2.2 shows the schematic for the 3-pump CHFS setup. Three identical pressurised diaphragm-pumps (Primeroyal K, Milton Roy, Pont-Saint Pierre, France) were used to supply the three independent precursor feeds. In a typical reaction, P1 supplied the feed of deionised water ($>$ 10 MΩ cm resistivity), which was heated to 450 °C using a custom 7 kW electrical heater (the design of which is detailed in Dr N. Makwana's thesis).[204] Pumps P2 and P3 supplied precursor feeds at room temperature; typically aqueous metal precursor solutions were pumped from P2, and base (and base-soluble precursors) from P3. The precursor feeds from P2 and P3 were mixed in flow in a tee mixer prior to mixing with the supercritical water feed in the confined jet mixer (CJM), at which point the product was rapidly formed in flow. The product feed exiting the CJM mixer was then cooled to ∼40 °C using a pipe-in-pipe heat exchanger. Once cooled, the product slurry passed through a back-pressure regulator (Tescom, model 26-1762-24-194, or Equilibar, model EB1HP2 HF) and was collected in an appropriately sized beaker/vessel depending on the volume being collected.

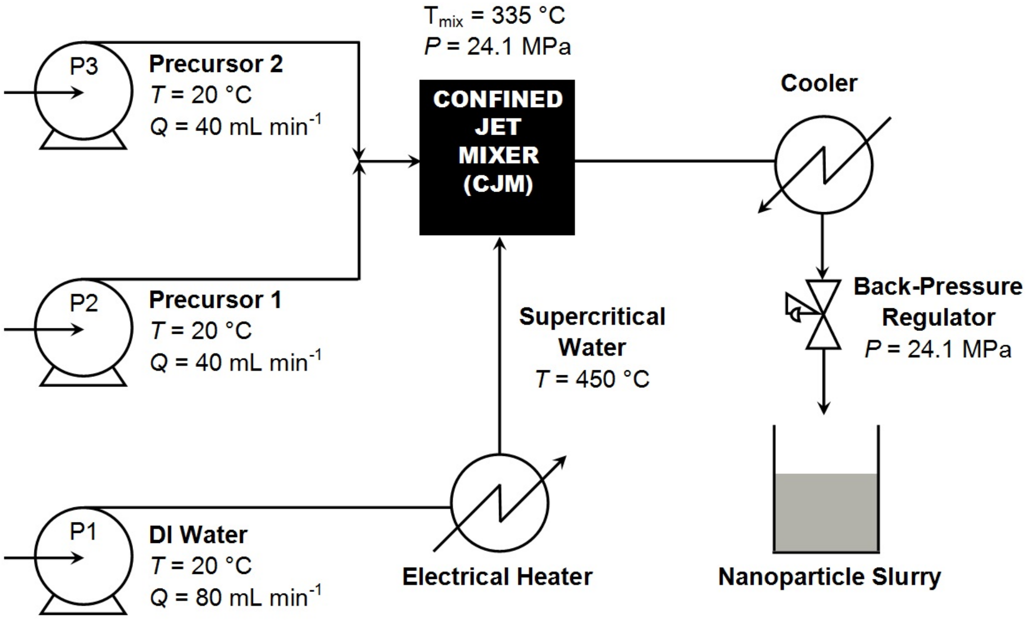

Figure 2.2: Schematic for the 3-pump CHFS setup; P1, P2, and P3 are the diaphragm pumps, *T* stands for the temperature, and *P* stands for the pressure.

Each pump was equipped with a three-way ball valve, with which the inlet could be switched between individual 1 L conical precursor vessels and a communal 200 L reservoir of deionised water to which all pumps were connected. During heat-up, cool-down, and flushing steps, all pumps were fed from the deionised water reservoir, with the feeds from P2 and P3 being switched to the precursor vessels as appropriate. Each pressured line was equipped with a pressure relief valve (Parker HPRV, relief pressure 276 bar), a pressure gauge and a non-return valve assembly before the feed was introduced into the reactor. The pressure relief valves ensured that the pressure in the system did not rise above 276 bar (as would be possible due to blockages in the system), ensuring that the system was safer to operate. The pressure gauges allowed for independent monitoring of the pressure experienced by each pump, and the non-return valve assembly prevented back-flow of the feeds in the event of pump failure.

Flow rates of 80 mL min^{-1} for P1, and 40 mL min^{-1} for each P2 and P3 (a balanced flow rate regime where the total flow rate from P2 and P3 was equal to the flow rate of P1) resulted in a mixing temperature at the CJM of 335 °C.[206] Up-scaling of the process to flow rates of 400 mL min^{-1}, 200 mL min^{-1} and 200 mL min^{-1} for pumps P1, P2 and P3, respectively, was carried out using the pilot-scale CHFS, and five-fold volumetric increase in scale, though also with a mixing temperature of 335 °C.

2.2.2 4-pump setup

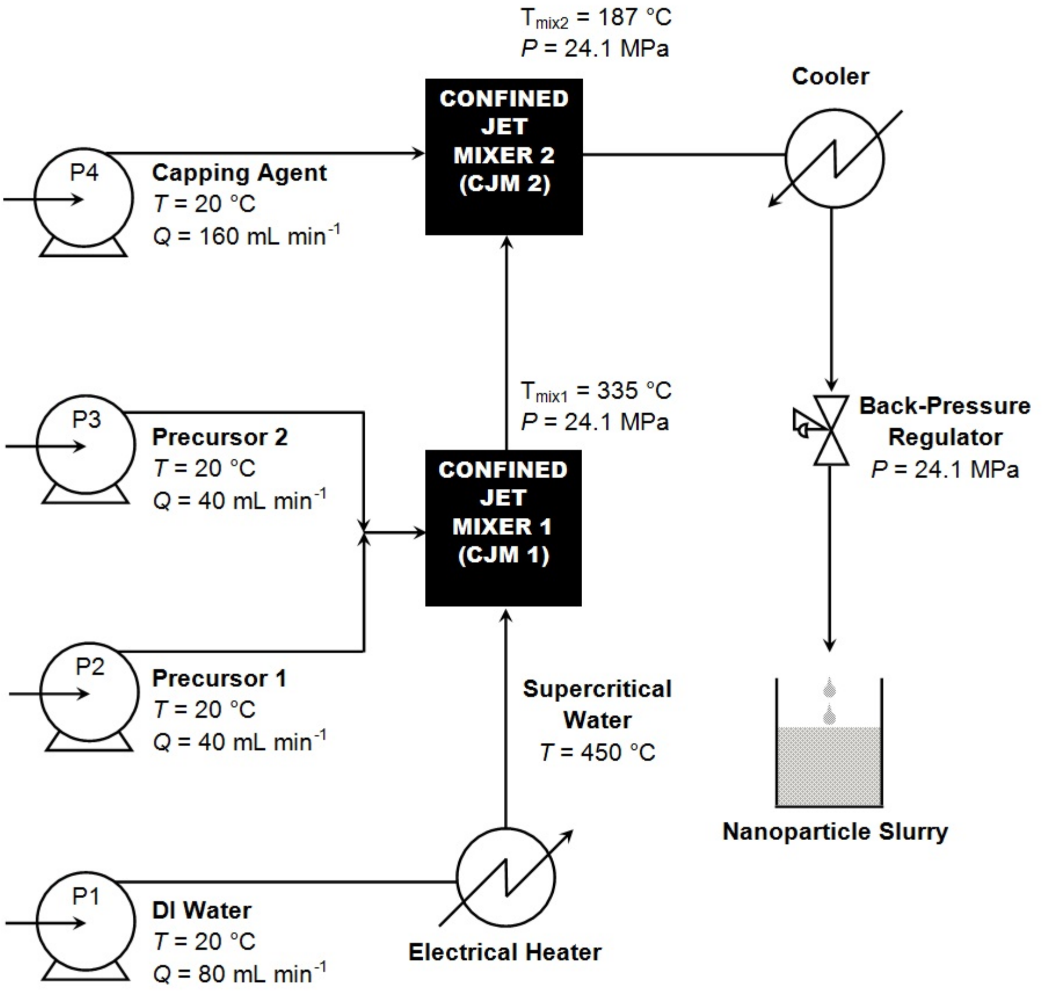

Figure 2.3: Schematic for the 4-pump CHFS setup; P1-4 are the diaphragm pumps, T stands for the temperature, and P stands for the pressure.

Figure 2.3 shows a schematic for the 4-pump setup for a CHFS reactor. Practically, the setup is identical to the 3-pump analogue, with the addition of a second CJM after the first, wherein the product stream comprised of the mixed feeds from P1, P2, and P3, met the room temperature quench feed from P4. This P4 feed contained pure deionised water to curtail particle growth, or sodium citrate solution to act as a capping agent, coating the surface of the newly-formed metal oxide nanoparticles.

In order to maintain a balanced flow rate regime, the flow rate from P4 was equal to the total flow rate of the other pumps, i.e. 160 mL min^{-1}; this resulted in a mixing temperature in the second CJM of 187 °C.

2.2.3 High-Throughput setup

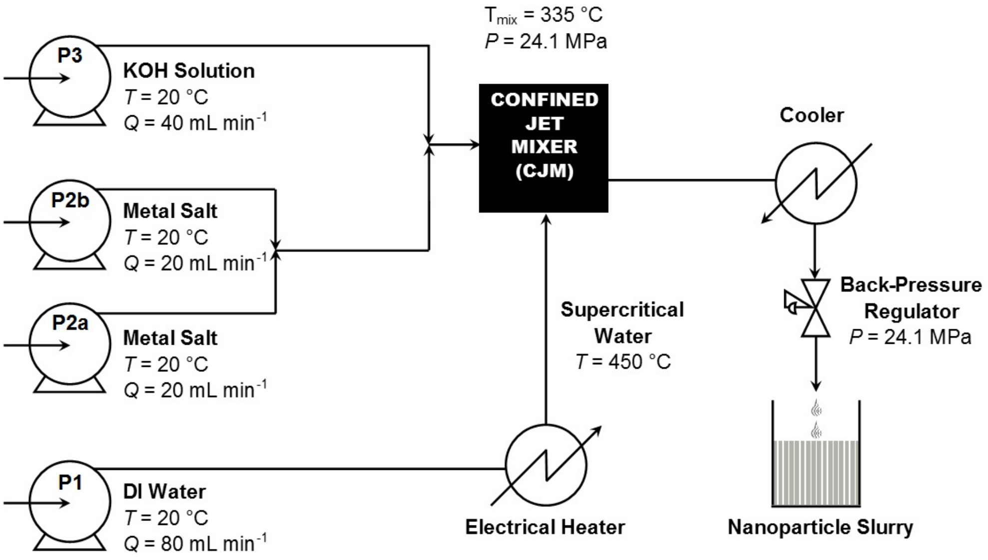

Figure 2.4: Schematic for the high-throughput CHFS setup. P1 and P3 are diaphragm pumps, P2a and P2b are Gilson pumps, T stands for the temperature, and P stands for the pressure.

Figure 2.4 shows the schematic for the high-throughput setup. The setup was identical to that of the 3-pump laboratory-scale setup, but that pump P2 was replaced with two Gilson 305 pumps, labelled P2a and P2b in Figure 2.4. With smaller pipe diameters, less time was required flushing pure deionised water through between each synthesis run to avoid cross-contamination, even with increased precursor concentrations. Thus up to 50 samples could easily be made in less than a day.

2.2.4 Confined Jet Mixer (CJM) design

The design of the CJM is shown in Figure 2.5. The co-current mixer was designed by Darr et al.,[3] in which the two flows (supercritical water and the reagent mixture) were fed co-currently. The pipe-in-pipe setup saw the supercritical water flow through the inner pipe, while the precursor solutions were introduced orthogonal to the water feed. Nanoparticle formation occurred at the point the two feeds mixed, and the reaction products were carried upwards away from the mixing point.

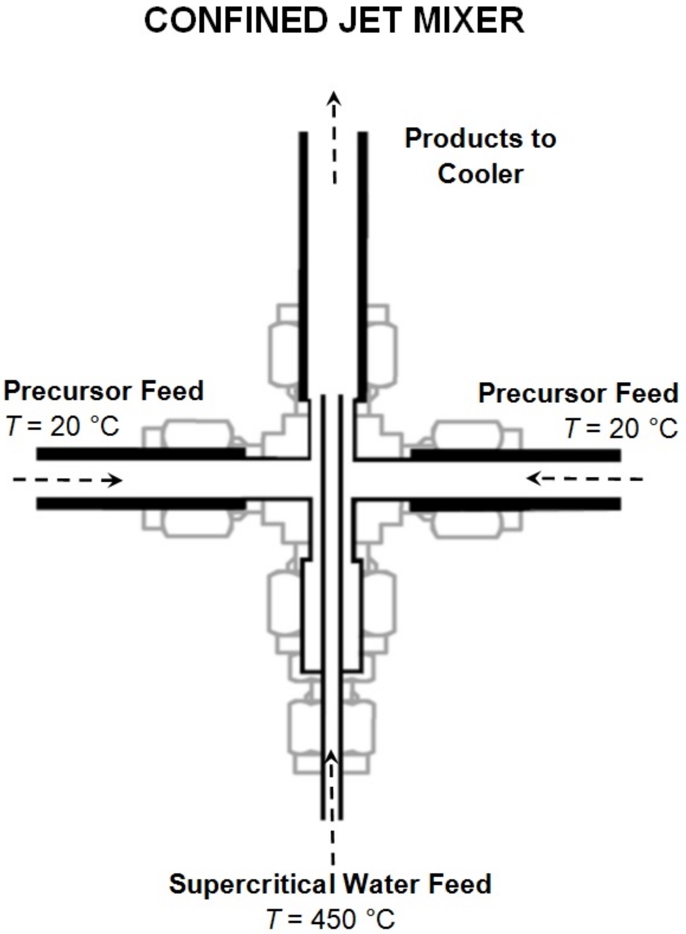

Figure 2.5: Schematic showing the design for the Confined Jet Mixer (CJM) (adapted from [3]).

2.2.5 Cleaning and processing of the as-made slurries

As-prepared samples were collected as particle-laden slurries from the CHFS reactor. Solids were retrieved by centrifugation using a Sigma 4K15 centrifuge at 4500 rpm. If the sample settled readily, centrifugation was carried out using 50 mL Falcon tubes and centrifugation was conducted in the range 5 - 30 minutes depending on how readily the samples settled out. If the sample did not settle, then 500 mL centrifuge buckets were used instead. Un-coated particles were cleaned by washing centrifuged dense pastes with deionised water, agitated, and centrifuged again; this process was repeated until the supernatant measured a conductivity $< 50\ \mu$S as measured using a Hanna Instruments H198311 conductivity meter. Coated particles (which tended to settle less readily) were treated in like manner, but washings were carried out with 20 wt% acetone and 80 wt% deionised water, and each centrifugation step typically took 1 - 3 hours.

After cleaning, samples were in the form of a dense paste, approximately 50-60 wt% solid. Coated samples from which inks were to be made were stored in this form, however the majority of samples were then dried using a Virtis Genesis 35 XL Freeze Drier. This was achieved by first freezing the sample chamber (containing the dense wet pastes) and the condenser unit (which trapped the water) to -40 °C, then implementing a vacuum. Holding the vacuum such that the pressure was < 13 Pa, the temperature of the sample chamber was slowly raised from -40 °C to 25 °C over a period of 24 h. This resulted in free-flowing powders, which were further ground by pestle and mortar, and total yields then measured and calculated.

2.2.6 Precursor materials

All water used in syntheses and subsequent cleaning steps was 10 MΩ deionized water purified using a Millipore Elix Essential water purification system, and the base was potassium hydroxide solution (KOH, Fisher Scientific, Leicestershire, UK). Precursor reagents for each of the desired elements were used as-purchased from the suppliers as detailed in Table 2.1.

Table 2.1: Precursor reagents and supplier information for the synthesis of the compounds discussed in this work. The list is organised alphabetically by element.

Element	**Precursor Compound**
Aluminium	$Al(NO_3)_3.9H_2O$
Cerium	$Ce(NO_3)_4.6H_2O$
Chromium	$Cr(NO_3)_3.9H_2O$
Copper	$Cu(NO_3)_2.H_2O$
Gadolinium	$Gd(NO_3)_3.6H_2O$
Gallium	$Ga(NO_3)_3.H_2O$
Indium	$In(NO_3)_3.H_2O$
Iron	$FeSO_4.7H_2O$
Lanthanum	$La(NO_3)_3.6H_2O$
Magnesium	$Mg(NO_3)_2.6H_2O$
Manganese	$Mn(NO_3)_2.H_2O$
Molybdenum	$(NH_4)_6Mo_7O_{24}.4H_2O$
Neodymium	$Nd(NO_3)_3.6H_2O$
Niobium	$(C_4H_4N)NbO_9.H_2O$
Praseodymium	$Pr(NO_3)_3.6H_2O$
Samarium	$Sm(NO_3)_3.6H_2O$
Silicon	Na_2SiO_3
Tin	$K_2SnO_3.3H_2O$
Titanium	$TiOSO_4.xH_2SO_4.H_2O$
Vanadium	$VOSO_4.H_2O$
Ytterbium	$Yb(NO_3)_3.5H_2O$
Yttrium	$Y(NO_3)_3.6H_2O$
Zinc	$Zn(NO_3)_2.6H_2O$
Zirconium	$ZrO(NO_3)_2.H_2O$

2.3 Physical Characterisation of Powders

The following sections detail the methodologies employed in the characterisation of the powders. These include X-ray diffraction, X-ray photoelectron spectroscopy, transmission electron microscopy, energy dispersive X-ray spectroscopy, Brunauer-Emmett-Teller analysis, thermogravimetric analysis, and atomic emission spectroscopy.

2.3.1 Powder X-ray diffraction (pXRD) and particle size estimation using Scherrer analysis

XRD data were collected using a STOE Stadi P diffractometer in transmission geometry, employing a molybdenum source (Mo-Kα_1 radiation, λ = 0.7093), with a typical data collection range of 2θ = 5 - 35 °. Approximately 0.01 g of sample was mounted between two transparent acetate sheets for analysis.

The 2θ scan range, acquisition time, and step size were dependent on the samples and are detailed in each chapter separately. The phase composition of the samples was determined by comparison to reference patterns available in the Inorganic Crystal Structure Database (ICSD).

Scherrer analysis[8, 9] was carried out on the (100), (002), and (102) peaks, as for Wurtzite ZnO-based samples, these are the three most intense and best defined peaks, positioned at relatively low scattering angles. The method was used for crystallite size *estimation*, not to be taken as accurate values on their own, rather indicative of trends in particle size used in conjunction with BET surface area analysis and TEM particle size analysis. Equation 2.1 shows the calculation used for the Scherrer method, where τ is the lower bound of the estimated crystallite size, K is the dimensionless shape factor taken to be 0.9, λ is the wavelength of the X-ray source used, β is the line broadening at half the maximum intensity for the peak in question, and θ is the Bragg angle.

$$\tau = \frac{K\lambda}{\beta cos\theta} \tag{2.1}$$

2.3.2 X-ray photoelectron spectroscopy (XPS)

X-ray photoelectron spectroscopy was carried out using a Thermo Scientific K-alpha photoelectron spectrometer using monochromatic Al-Kα radiation. Survey scans were collected in the binding energy range 0-1100 eV at a pass energy of 200 eV. Higher resolution scans were recorded for the principle peaks as detailed in the respective chapters concerning them. Peak positions were calibrated using the adventitious carbon 1s peak at 284.7 eV using CasaXPS software, from which XY data was extracted. Samples were prepared by affixing small cuts of double-sided carbon tape to the sample holder, with the powder samples on the up-turned side of the tape.

2.3.3 Transmission electron microscopy and energy dispersive X-ray spectroscopy (TEM/EDS)

Transmission electron microscopy (TEM) was performed using a Jeol 200 kV transmission electron microscope in imaging mode. Samples were dispersed in methanol and drop coated onto 300 mesh carbon-coated copper TEM grids (purchased from Agar Scientific). Image analysis and particle size measurements were carried out using Gatan Digital Microscopy Suite software. Energy Dispersive X-ray Spectroscopy (EDS) analysis was carried out using an Oxford Instruments X-Max^{N} 80-T Silicon Drift Detector (SDD) fitted to the transmission electron microscope and processed using Aztec software.

2.3.4 Inductively couples plasma atomic emission spectroscopy (ICP-AES)

Compositional analysis was carried out on selected samples using inductively coupled plasma atomic emission spectroscopy (ICP-AES). Dilute solutions of the samples were prepared by dissolution in 1% aqueous nitric acid, and analysis was carried out using a Varian 720 ICP-AES in axial configuration equipped with an autosampler. Prior to sample analysis, calibrations were carried out using standards at concentrations of 2.5, 5.0, 7.5, and 10.0 ppm for zinc, and 0.25, 0.5, 0.75, and 1.0 ppm for each Al, Ga, and Si. The measurements and subsequent conversion calculations were carried out by I. Johnson and Dr P. Marchand.

2.3.5 Brunauer-Emmett-Teller (BET) analysis

Brunauer-Emmett-Teller (BET) measurements were carried out on dry powders to ascertain the surface area of the different samples. 0.1 - 0.2 g of powders were weighed out and degassed by heating to 150 °C under a flow of nitrogen gas for $>$ 12 h in glass BET tubes. The samples were re-weighed to ascertain the degassed sample mass, and the tubes affixed to the Micromeritics TriStar II PLUS surface area and porosity analyser, which was used to measure adsorption isotherms and thus calculate the BET surface area.

2.3.6 Thermogravimetric analysis (TGA)

Thermogravimetric analysis (TGA) was performed on a Netzsh STA 449C instrument. TGA was carried out in static air with the samples in aluminium pans at atmospheric pressure. The rate of heating was 10 °C min^{-1}, from room temperature up to a maximum temperature of 600 °C.

2.4 Sample Preparation for Further Analysis

Compositional optimisation was determined by pressing dry powders into discs and performing electrical measurements on them. Optimised compositions were then used to generate thin films, by spin coating and inkjet printing. Methods of preparation of pellets (powders only) and inks (powders and dense wet pastes) are described in the following sections.

2.4.1 Pellet preparation

Approximately 0.5 g of dry powder sample was pressed into a 16 mm diameter, ca. 1 mm thick compact disc using a bench-top hydraulic press (Specac, Orpington, UK), under a force of 50 kN for 5 to 30 minutes, depending on the sample in question. Discs were made in triplicate for each sample. Once pressed, the discs were heat treated in a tube furnace (70 mm internal work tube diameter, Elite Thermal Systems Ltd.) for 3 hours at 500 °C under a 5% hydrogen in nitrogen atmosphere, with an approximate flow rate of 5 cm^3 min^{-1}. Examples of the discs are shown in Figure

2.6.

2.4.2 Ink formulation

Dispersions/inks of the nanoparticles, were required for multiple deposition techniques, including but not limited to spin coating and inkjet printing. These dispersing methodologies are discussed in the following sections.

2.4.2.1 Spin-coating inks

Inks for spin-coating were prepared from dry powders with no surface coatings, or from citrate-coated indium tin oxide dense wet paste. To 1.0 g of dry powder (or equivalent in paste form) was added 4.0 g of dispersing medium (typically 20 wt% ethylene glycol in deionized water). These were mixed by hand using a spatula to ensure that the powder was wetted, then underwent sonic agitation using a sonicating bath (VWR Ultrasonic Cleaner, USC100T) for 30 min. This began the process of breaking up the agglomerates, and cleaned the sample off the spatula, giving a crude dispersion. This was further treated by use of a Branson Digital Sonifier 250 sonicating tip operating at 20% amplitude with a 0.3 s on/off pulse length. The tip was submerged in the dispersion, which was itself held in an ice bath to ensure excessive heating of the dispersion did not occur. Each 2 min sonicating tip treatment (1 min on, 1 min off) was followed by 2 min resting in the ice bath before the next treatment was carried out. Insufficient cooling time resulted in the suspension overheating; this coagulated the formulation, characterised by an irreversible and sudden increase in viscosity. Eight such treatments were carried out, before further sonic agitation of the dispersion in the sonicating bath for 30 min. The dispersions were allowed to rest for up to 1 h before spin coating was carried out.

2.4.2.2 Inkjet printing inks

25 - 30 g inks for inkjet printing were prepared from wet pastes of surface-modified nanoparticles that had been coated with citrate during the synthetic process. A small amount (ca. 0.1 g) of the paste was baked at 300 °C in air using a Carbolite CWF-1300 muffle furnace to ascertain the metal oxide loading (typically 55-60 wt%). An appropriate calculated amount of paste was weighed out, and to it added

Sun Chemical ink vehicle U10197 as the dispersing medium, such that the solid loading was 25 wt%, and the minimum mass of the ink was 25 g. This was agitated using sonication in the abovementioned sonicating bath for 15 minutes before the sonicating tip was used in the manner described above to carry out between 10 and 15 treatments, until the dispersion could in its entirety pass through a 3.1 μm syringe filter (Thermo Scientific).

2.4.3 Ink/Dispersion Analysis Techniques

Dispersion analysis was carried out in the form of dynamic light scattering (DLS) (hydrodynamic diameter and surface zeta potential measurements) and viscometry measurements. Methodologies for these are discussed in the following sections.

2.4.3.1 Dynamic light scattering (DLS) and Zeta potential measurements

DLS and zeta potential measurements were carried out using a Nano Zetasizer ZEN3600 (Malvern Instruments Ltd). Samples were prepared by suspending 10 mg of powder (or equivalent for ink samples) in 100 mL of 5 mM NaCl solution in deionized water.

Particle size distributions were measured at an angle of 173 ° using backscatter geometry. Each size distribution obtained was taken as an average of ten measurements, each lasting 10 seconds. These measurements were carried out in disposable, chemically resistant PMMA cuvettes (Malvern).

Zeta potential measurements were carried out in like configuration, but using disposable folded capillary cells with in-built electrodes (Malvern). The samples as prepared above were adjusted to pH 7, and measurements carried out step-wise either decreasing or increasing the pH to within the stability of the sample in question; 0.1 M and 0.01 M solutions of each HNO_3 and KOH prepared using 5 mM NaCl solution were used to adjust the pH. Each data point was an average of at least ten agreeing measurements (up to 100, depending on the cumulatively calculated standard deviation) after voltage equilibration, and three data points were taken for each pH value for each sample. The mean zeta potentials were then plotted against pH to generate zeta potential curves.

2.4.3.2 Viscosity measurements

Dynamic viscosity of inks/dispersions was measured using a Brookfield DV2T Viscometer. A minimum of 16 mL of ink was required in the vessel, which was fitted with a water jacket through which distilled water set to 25.0 °C flowed to maintain the temperature. A submerged spindle was rotated in the range 1 - 200 revolutions per minute (rpm) to find the maximum value for which the resultant torque was as close to the viscometers measurable limit (displayed as a percentage, i.e. up to 100.0 %) as possible. Data points were collected for a range of speeds (in rpm) up to this maximum, with single point averaging over 30 s to ensure equilibration. Viscosity was measured in cP, centipoise (1 cP = 1 mPa s), and the value obtained closest to 100.0 % torque was taken to be the dynamic viscosity of the sample.

2.4.4 Thin film deposition

Thin films were deposited by spin coating and inkjet printing. These preparatory methodologies, and their subsequent heat treatments, are described below.

2.4.4.1 Spin-coating method

Spin coating was carried out using a Laurell Tech. Corp. WS650MZ-23NPPB spin coater by manually dropping (using 150 mm glass Pasteur pipettes, Fisher Scientific) the prepared dispersion onto float glass substrates (NSG Pilkingtons, UK), spin rates in the range 3000 - 5000 rpm. Between 20 to 100 drops were added to each substrate, depending on the desired film thickness and the material/dispersion in question.

2.4.4.2 Inkjet printing method

Inks prepared with Sun Chemical ink vehicle U10197 as the dispersing medium were printed onto float glass substrates using a Fujifilm Dimatix Materials Printer DMP-2831 with a 10 pL print head. Inks were filtered by syringe sequentially through 3.1 μm, 1.2 μm, 0.7 μm, and 0.45 μm filters, before being loaded into a piezo-based inkjet print cartridge. Prints of 2.0 x 2.0 cm were deposited with a drop spacing of 15 - 20 μm (1270 - 1700 drops per inch), before being dried for 30 min in air at 95 °C to remove the dispersing medium. Proprietary additives were in some cases added to the inks before printing to improve dispersion quality, surface tension, viscosity, or wetting properties of the inks, facilitating a higher quality film. Deposition and proprietary formulation altering was carried out by, or under instruction of Dr M. Pickrell of Sun Chemical Ltd.

2.4.4.3 Heat treatment of thin films

All thin films, deposited by spin coating or inkjet printing methodologies, were heat treated in a tube furnace (100 mm internal diameter work tube, Elite Thermal Systems) at 550 °C for 5 h under a flow of N_2 or Ar (ITO films), or 5% H_2/N_2 (ZnO-based films), with a ramp rate of 5.0 °C min^{-1}.

2.5 Electrical and Optical Characterisation

Methods for the electrical (Hall Effect) and optical (UV/Vis/NIR) characterisation are described below, as well as the methods used to determine film thickness (optical, and side-on SEM), needed to calculate the resistivity of the films.

2.5.1 Hall effect measurements

Heat treated pellets were prepared for Hall measurements by gold-sputtering four electrical contact points onto the surface as shown in Figure 2.6. For heat treated thin films, the electrical contacts were instead added using silver paint (Sigma).

Hall effect measurements were carried out using the Van der Pauw method to determine the bulk resistivity of the materials. The samples (thin film or disc), once mounted onto the sample holder as shown in Figure 2.6, were subjected to an input current of 1 mA and a calibrated magnetic field of 0.58 T using the Van der Pauw probe, as part of an Ecopia HMS-3000 Hall Measurement System; the transverse voltage was then measured. The measurement was repeated by reversing the direction of the magnetic field and the current. Resistivity measurements were made in triplicate for each sample and the mean value and standard deviations were calculated. Between each measurement, the sample was removed and re-mounted to give a fairer representation of the average electrical properties.

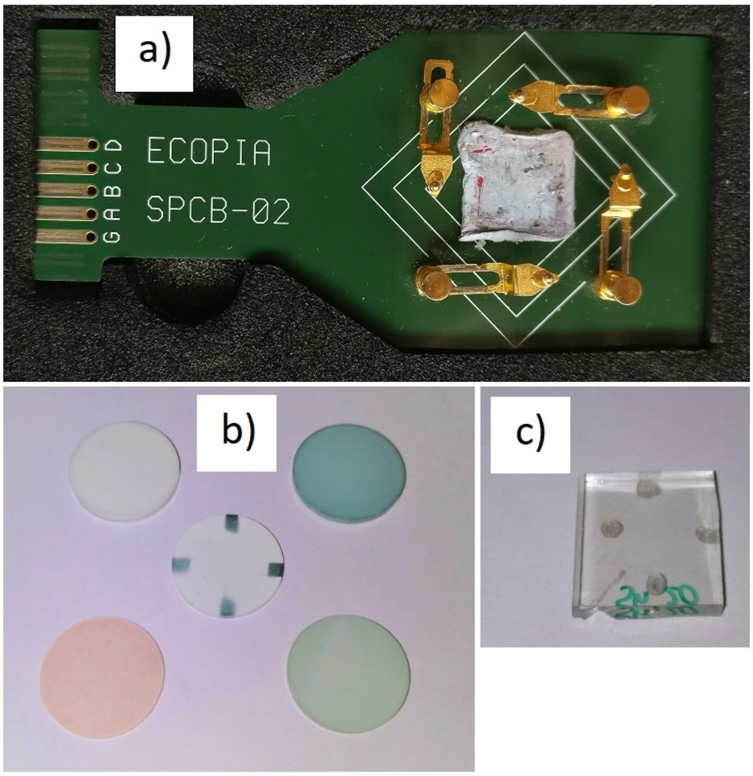

Figure 2.6: a) the Hall Probe mount upon which the sample is loaded, held in place by use of blu-tak, b) a series of heat treated 16 mm pressed discs of varying compositions, with the central disc sporting gold-sputtered electrical contact points, and c) a 10 x 10 mm (approx.) cut shard of a heat treated spin-coated thin film of aluminium and gallium co-coped zinc oxide, with four spots of silver paint added to act as electrical contact points, typical of the size of sample used for Hall Effect measurements on thin films in this work.

2.5.2 UV/Vis/near-IR measurements

Spectra were obtained using a PerkinElmer Lambda 951 UV/Vis/NIR spectrophotometer with an integrating sphere setup and an air background. Samples were measured in the form of thin films prepared by either spin coating or inkjet printing; transmittance, and reflectance measurements were taken in the range 300 - 2500 nm. Average transmission in the visible range was calculated by averaging the transmittance values in the range 400 - 700 nm.

2.5.3 Film thickness measurements

Film thickness was determined predominantly by optical methods, corroborated by side-on scanning electron microscopy (SEM). These methodologies are discussed in the following sections.

2.5.3.1 Ellipsometry

Measurements were carried out using a Filmetrics F20 Thin Film Analyser. Thicknesses were measured at multiple points (typically 8 - 12) on each thin film sample and a mean film thickness calculated. This value was used in the subsequent Hall Effect measurements for the film.

2.5.3.2 Scanning electron microscopy (SEM)

Field emission scanning electron microscopy (FE-SEM) measurements were obtained using a JEOL JSM-6700F microscope with a 5 keV accelerating voltage. Zinc oxide-based samples were gold coated using a sputter coater fitted with a gold target prior to imaging. Images were taken of the surface of the films and in some cases side-on to determine film thickness. Side-on SEM images of inkjet printed ZnO-based films were acquired by Dr P. Marchand.

Chapter 3

Determination of Suitable Dopants for Transparent Conducting ZnO

3.1 Aims

The aim of this chapter is to investigate the identification by synthesis and characterisation of various CHFS-synthesised doped zinc oxides by screening the conductivity of the materials. The electrical testing is carried out by Hall Effect measurements on pressed, heat-treated discs. Physical characterisation is discussed with respect to pXRD (including Scherrer analysis), TEM, and XPS. The benchmark material, ITO, synthesised and tested by the same methods, obtained optimal resistivities of the order of 10^{-3} Ω cm.

3.2 Introduction

For the reasons discussed extensively in Chapter 1, doped zinc oxides are highly desirable as replacement materials for indium tin oxide in applications requiring transparent conducting oxides. The ZnO dopant in question can be immensely variable, though typically the most prevalent in industry and academic research are aluminium[119, 120, 145] and gallium.[128, 129, 207] Many others are well known to benefit the electrical properties of zinc oxide, including post-transition metal elements such as indium,[137] tin,[138] and silicon,[208, 209] transition metals such as iron,[210] manganese,[211, 212] molybdenum,[213] niobium,[139] titanium,[214, 215] vanadium,[216] yttrium,[217] and zirconium,[218] and lanthanides such as lanthanum,[140] neodymium,[141] and ytterbium.[219] Other transition metals such as chromium and copper are known, but full characterisation is limited with respect to the desirable optoelectronic properties pertinent to TCOs. Magnesium is also known in literature, typically as a co-dopant.[220]

Thin films of these materials were generated by a variety of different techniques, including sputtering, atomic layer deposition, and sol gel dip-coating, but never have the majority been made by a continuous hydrothermal flow synthesis, thus all would be considered as part of the screening process. A good number of other elements have been considered for use as TCOs when doped into ZnO that have been excluded for various reasons. Generally speaking the issue is potential harm to the environment, or harmfulness in their handling, or indeed their only water-soluble precursors being inherently damaging to the CHFS process machinery. These include cobalt and nickel,[221] boron,[222] and germanium,[223] among others. Conversely, there were water-soluble precursors to hand for elements such as cerium, gadolinium, prasaeodymium, and samarium, for which there is no literature precedent for doped ZnO TCOs, but based on the chemistry of similar elements (the aforementioned lanthanides for which there *is* literature precedent), it was judged to be worth the effort to include them in the study.

3.3 Experimental Design and Observations

A three-pump, single mixer laboratory-scale CHFS set-up was used (see Experimental chapter, section 2.2.1). With a total metal concentration, [Zn + dopant], of 0.2 M (supplied by pump P2), and pump flow rates of 80, 40, and 40 mL min^{-1} for pumps P1, P2, and P3, respectively, approximately 5 g of product was expected in a collection volume of 1.2 L. Base (KOH) concentration was maintained at twice the metal concentration, 0.4 M, in the feed supplied by pump P3. For a full list of the precursors used, see Table 2.1 in Chapter 2; note that silicon and tin precursors (sodium metasilicate and potassium stannate, respectively) were introduced via pump P3, as they were base soluble, all other dopants were introduced with the zinc precursor via pump P2.

Doping of the respective investigated elements into ZnO had the effect of turning some of the powders from white (as observed for undoped ZnO) to various other colours, as listed in Table 3.1, along with the colours of the corresponding discs made from those powders. All products were collected in the pH range 6-8, with yields of 70 % (± 5 %). Most powders were light in colour, white or off-white, with notable exceptions being those samples doped with Mn, Cu, and Fe, which turned various shades of brown. Pressing of the powders into discs and heat treating in a reducing atmosphere caused many colour changes, for the most part to green or blue (if the colour changed from white at all). ZnO:Cu turned an intense purple, ZnO:Nd turned pink, and ZnO:Fe turned green.

Powder X-ray diffraction (pXRD), transmission electron microscopy (TEM), and X-ray photoelectron spectroscopy (XPS) were used to characterise the powder samples, and Hall Effect measurements were used to determine the electrical properties of the samples as pressed, heat treated discs.

3.4 Dopant Screening Results for Doped Zinc Oxides

This Section describes the electrical and physical analysis results obtained for the various doped powders. First, the Hall Effect resistivity measurements; at this point the testing methodology for screening was new and lacking in refinement, thus electrical results are reported as being within certain ranges (as an order of magnitude). Disc fabrication and heat treatment steps resulted in a relatively low ‘survival rate’, in that two in three discs would break in one of the steps, failing to be tested. Once electrical results were collected from at least five separate discs for each sample, the relative potential of the doped zinc oxides was reasoned for future investigation. Following the electrical results are the characterisation data, including XRD, XPS, and TEM, for all of the materials.

3.4.1 Electrical characterisation for doped zinc oxides

For every material, at least five discs were made that were structurally robust after pressing and heat treating. Electrical contacts were made by sputtering gold contacts, such that the distance between each of the four contact points was typically

Table 3.1: Table summarising the colour of the doped zinc oxide powders and the heat treated discs that resulted, and the pH at which their respective slurries were collected, organised by dopant element.

Dopant	**pH**	**Colour**$_{powder}$	**Colour**$_{disc}$
-	7	white	white
Al	7	pale yellow	green-blue
Ce	8	white	white
Cr	7	pale blue	blue
Cu	6	brown	dark purple
Fe	7	orange	green
Ga	7	pale yellow	green-blue
Gd	7	white	white
In	8	white	blue
La	7	white	pale blue
Mg	7	white	white
Mn	7	brown	dark brown
Mo	6	white	white
Nb	7	white	white
Nd	7	white	pale pink
Pr	7	white	white
Si	8	white	white
Sm	7	white	white
Sn	8	white	white
Ti	6	white	white
V	6	pale grey-blue	dark blue
Y	7	white	white
Yb	7	white	white
Zr	7	white	white

around 5 mm. Readings were taken at least in triplicate for each disc, but due to the fluctuation in results, and judged unreliability in certain cases, the precise figures are not included in their entirety. Rather, for each sample, the best performing disc that obtained a certain order of magnitude in resistivity for at least three readings was taken as the representative of that material, and the orders of magnitude assigned to each.

For the materials that demonstrated conductivity at all, resistivities in the range 10^{-2} to 10^{1} Ω cm were obtained. In order of decreasing resistivity (i.e. least to most promising materials), ZnO doped with Cr and Y had resistivities in the order of 10^{1} Ω cm, ZnO doped with Fe, In, La, Nd, Pr and V had resistivities in the order of 10^{0} Ω cm, ZnO doped with Cu and Si had resistivities in the order of 10^{-1} Ω cm, and finally only ZnO doped with Al and Ga had resistivities in the order of 10^{-2} Ω cm.

Thus the four best dopants with regards to conductivity were judged to be Al, Ga, Cu, and Si, and purely from an electrical standpoint, these were chosen to be the focus of investigation for compositional optimisation (see Chapters 4 and 5). Lagging a further order of magnitude behind these samples were Fe, In, La, Nd, Pr, and V-doped ZnO. These would likely never achieve the resistivities necessary for most TCO applications, but could have been worth subsequent optimisation efforts in the future, though no such were carried out over the course of this project.

3.4.2 Physical characterisation of doped zinc oxides

In the current section, only a representative six samples will have their data shown in various figures, including undoped ZnO for comparison, and ZnO doped with each Al, Ce, Cu, Ga, and Si. Full physical characterisation data (spectra/images/summary tables etc.) and XPS discussion are included at the end of the Chapter in the section titled “Appendix for Chapter 3”, beginning on page 88 for all twenty-four samples; these will be referenced as appropriate in the text in this section.

X-ray diffractometry was carried out for all powder samples. This was principally for the purpose of phase identification, to determine whether any crystalline phases in addition to Wurtzite ZnO were present. Figure 3.1 shows XRD patterns for the selection of six samples, with a reference pattern for ZnO in red.[4] The majority of the samples tested showed phase-pure Wurtzite ZnO structure (see Figures 3.5 and 3.6 on pages 92 and 93, respectively), however in some cases an impurity phase was seen, with peaks denoted by a '*' (see Figure 3.7 on page 94 for all such samples). Due to the low intensity of these peaks, in most cases it was not possible to identify the additional phases present, but in Figure 3.1, the Ce-doped sample has two clear peaks that can be assigned to CeO_2,[224] an indication that the Ce did not go into the ZnO structure. Though no crystalline phases were detected in most samples, this was not an indication in of itself of successful doping, however, as amorphous phases of the various metal oxide or hydroxide species would not necessarily appear in the XRD patterns.

TEM images are shown in Figure 3.2 for the six representative samples, and for all doped zinc oxides in Figures 3.8 to 3.11 in the appendix, on pages 95 to 98, respectively. Particle property data for these, including length and aspect ratio from TEM image analysis (100 particles analysed), as well as Scherrer crystallite size, are included in Table 3.2 on page 107. Due to the generally very broad particle size distribution, the standard deviations were often large. What was more useful from this data were the calculated aspect ratios, which though also suffering from large standard deviations, were still a good indicator as to the propensity of a doped sample to be spheroidal or more rod-like. Dopants such as Al, Fe, and Mn promoted growth along the c-axis, generating more rod-like behaviour, whereas elements such as Si, Ga, or Zr resulted in aspect ratios close to 1, and spheroidal morphologies. Exceptions to this include the particularly ill-behaved Gd, which showed a high aspect ratio of 2.2, indicative of rod-like behaviour, but as can be seen from its TEM image (Figure 3.10a), the sample was generally spheroidal, and the presence of a few rods of excessive proportions drastically affected the statistics. Another generalisation that could be made from looking at the mean TEM particle length, was that the addition of almost any element appeared to increase the particle size

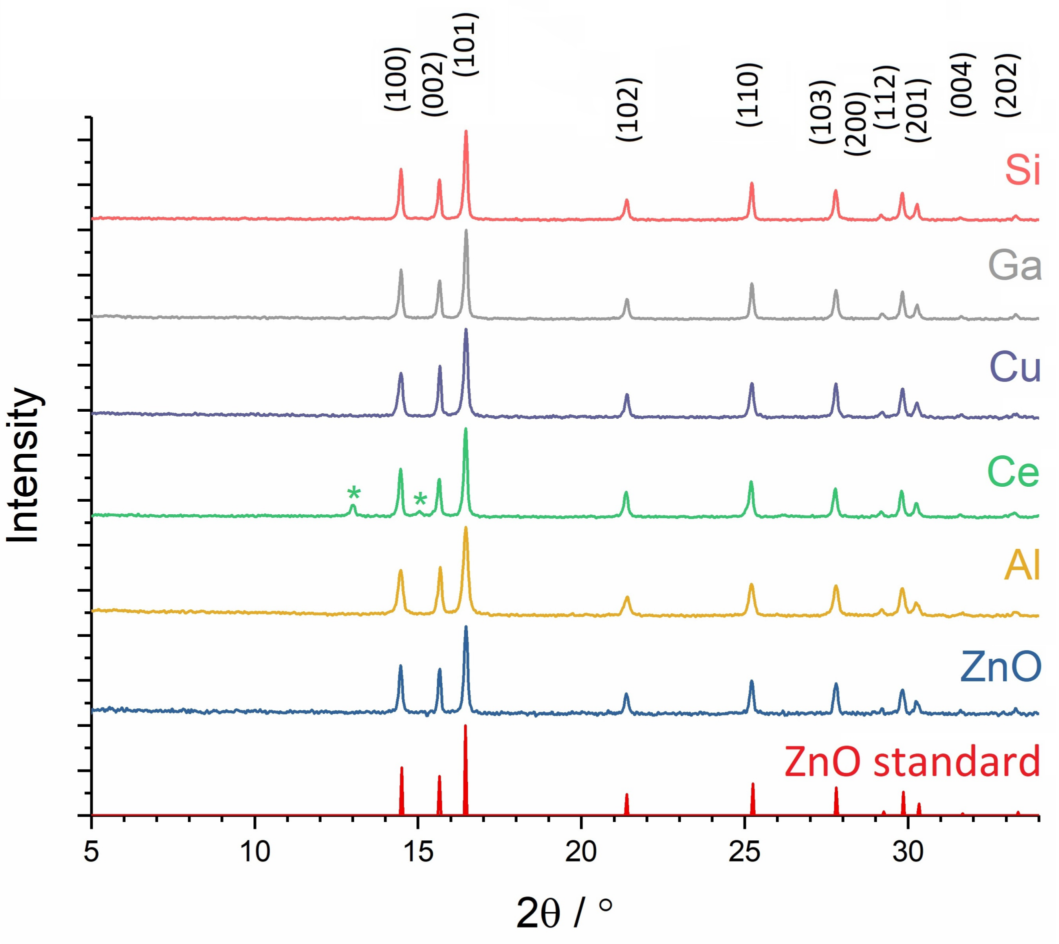

Figure 3.1: XRD pattern for as-synthesised ZnO made by CHFS (black) with a reference pattern for ZnO (red).[4] The measurement was carried out with a molybdenum source, with wavelength λ = 0.7093 Å

versus the undoped material. However the Scherrer crystallite size from XRD data was not greatly altered; thus the lower bound for the crystallite size was generally unchanged (except in the cases of In and Si, which saw a notable decrease from 28 nm to 18 nm for both), but the actual particles observed with TEM were generally larger. Note also that In and Si-doping resulted in two of the narrowest particle size distributions, thus it could generally be stated that those dopant elements that curtail unchecked particle growth of ZnO during continuous hydrothermal flow synthesis result in products with far more controllable and consistent particle sizes.

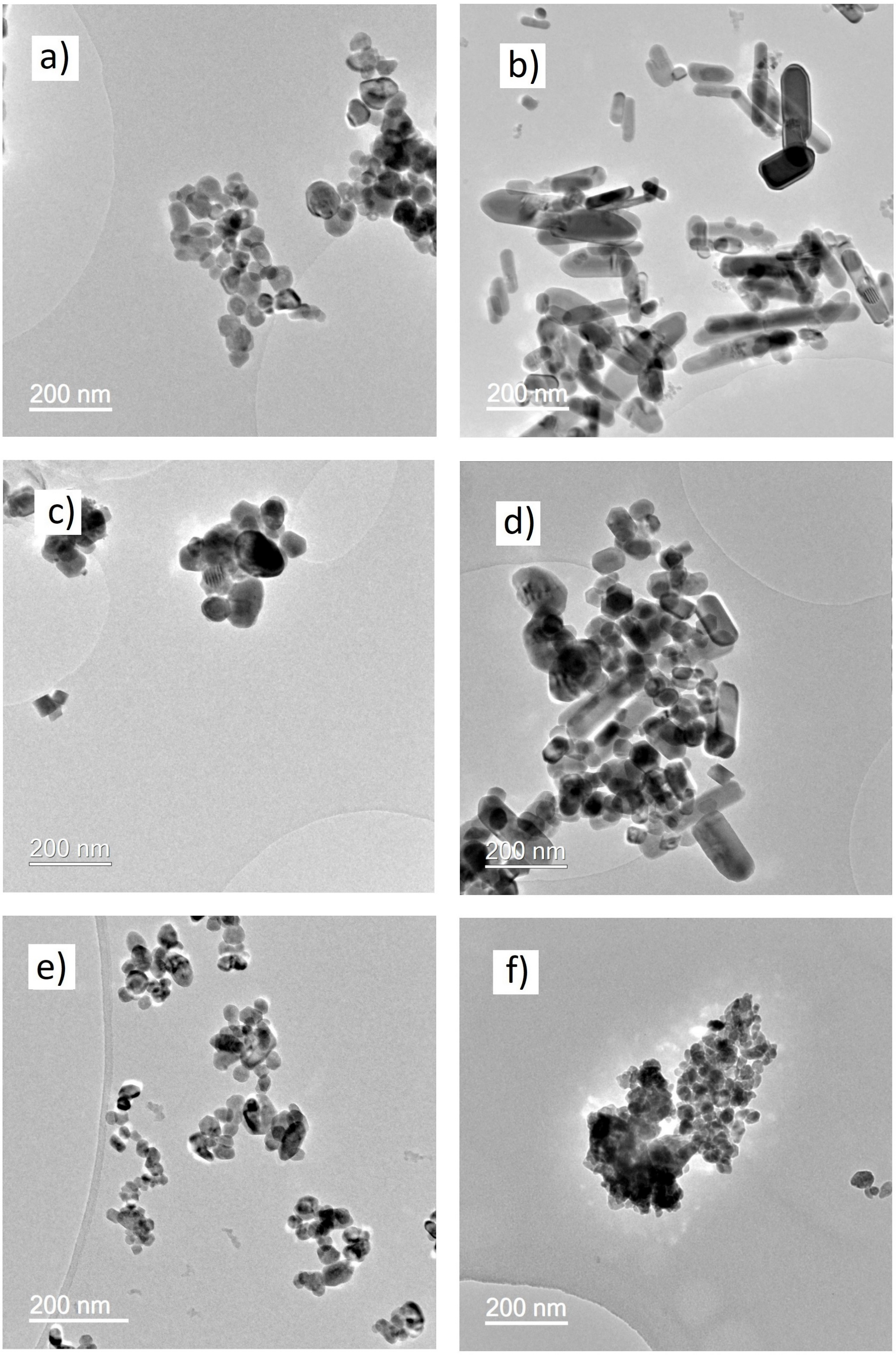

Figure 3.2: TEM images of the six representative samples, including a) undoped ZnO, and ZnO doped with b) Al, c) Ce, d) Cu, e) Ga, and f) Si.

XPS added further complexity in some cases, and provided elucidation in others. Spectra are included in Figures 3.3 and 3.4 of the six representative materials, and in Figures 3.13 to 3.19 in the appendix on pages 99 to 106. Table 3.3 on page 108 summarises the principal XPS data, including the calculated proportion of the dopant present relative to the zinc. In the cases of Mg, Mo, and Yb doped samples, XPS data are not shown as these elements were not detected in their respective scans. Figure 3.12 shows the Zn 2p high resolution scans for the doped samples. The spectra are vertically arranged in increasing binding energy of the $2p_{3/2}$ peak. All samples were calibrated to the carbon 1s peak at 284.7 eV, thus any shift is due to the difference in sample (i.e. the dopant). Undoped ZnO had a binding energy of 1020.6 eV, and the various dopants shifted this up to a maximum of 1021.3 eV, all within a well-known binding energy range for ZnO.[225] Splitting of the doublet was consistent across all samples, at 23.1 eV. All demonstrated the expected form, with the exception of the Ce-doped sample, for which the Zn 2p peaks showed notable asymmetry.

XPS spectra of the metal and oxygen regions are included in Figures 3.3 (undoped, Al-doped and Ce-doped ZnO) and 3.4 (Cu-doped, Ga-doped, and Si-doped ZnO). In particular, note Figure 3.3a, the O 1s region for undoped ZnO, against which the other O 1s spectra can be compared, in which two peaks were observed. The sharper peak around 530 eV was due to the lattice oxygen in ZnO. The broader peak at higher binding energy was due in part to other oxygen environments, including water, oxygen or hydroxyl groups adherent to the surface.[225] In support of the indication from XRD, the Ce 3d XPS spectrum in Figure 3.3e showed the characteristic six peaks of cerium (IV) oxide, a triplet each for the $3d_{5/2}$ and $3d_{3/2}$ orbitals. Fitted with three peaks, the O1s region for the Ce-doped sample was expected to contain three discernible environments; the CeO_2 should have accounted for one, the ZnO for another, and then the broad peak for oxygen-containing surface groups.[226] The indication was that another phase had formed in addition to the ZnO, rather than a single doped material. The O 1s spectrum for the Cu-doped sample (Figure 3.4b) showed an oxygen environment in addition to the lattice oxygen in ZnO, and the strong satellite peaks in the Cu 2p spectrum (3.4a) were diagnostic of Cu(II), hence it could be deduced that CuO was present, not Cu_2O, or Cu metal.[227] The Al 2p (Figure 3.3c), Ga 2p (Figure 3.4c), and Si 2p (Figure 3.4e) regions indicated only a single environment each of Al, Ga, and Si, and the O 1s spectra were markedly similar to that of the O 1s spectrum for undoped ZnO, which taken with the XRD patterns and high conductivity of the samples, suggested that for these three materials, the dopant element was successfully incorporated into the ZnO lattice.

There was generally a large variation across the different samples as to the apparent proportion of the dopant present as calculated from XPS data. For every sample, the dopant to zinc metal in the precursor solution was 2:98 (i.e. always 2 at% dopant), but for some of the materials, the dopant level was as high as 4 or 5 at%, particularly in the cases of Gd, La, Sm, Sn, and Y. In the case that the dopant failed to enter the structure, it was logical that it could have been present (in various forms, for example as CeO_2) at the surface of the ZnO particles, hence a higher dopant level was calculated than expected, as XPS is a surface technique. Similarly, this would be the case for successfully doped materials if there is a high surface segregation of the dopant in the particles. This would have been possible if during particle nucleation, the zinc nucleated first, and the dopant latterly. These figures are included in full in Table 3.3 on page 108.

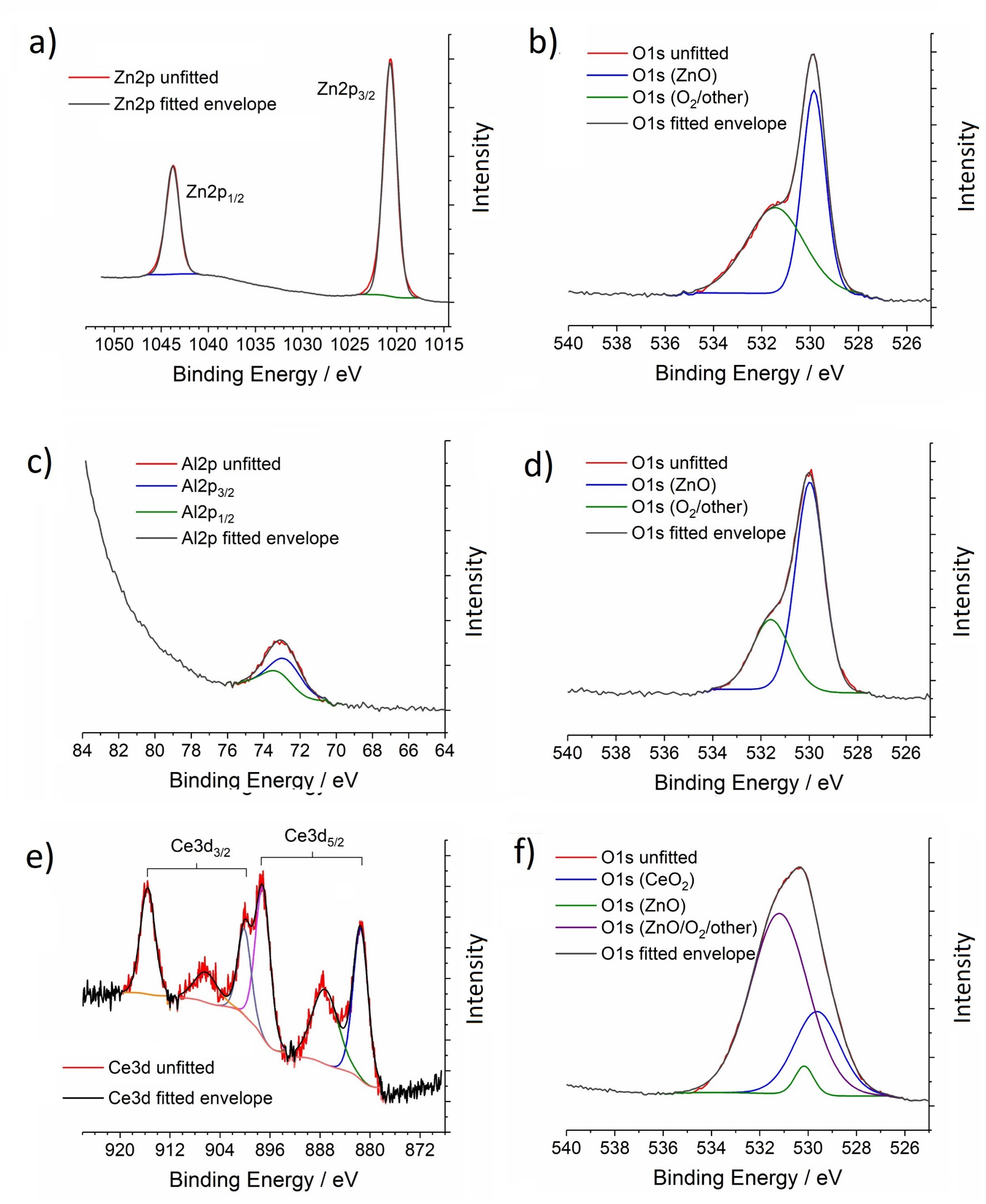

Figure 3.3: XPS spectra of a) the Zn 2p region (in un-doped ZnO), c) the Al 2p region, e) the Ce 3d region, and to the right of each the corresponding O 1s binding energy region.

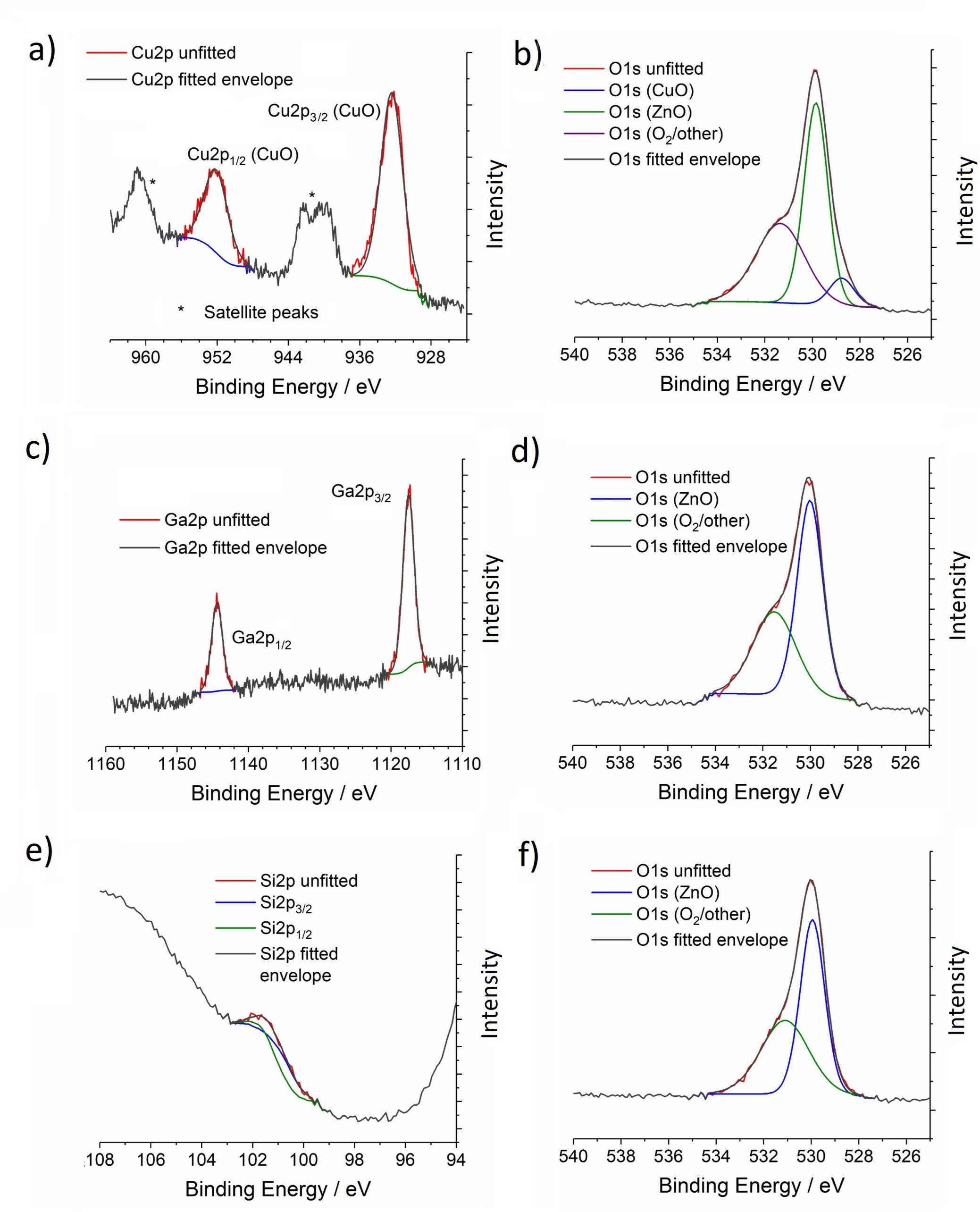

Figure 3.4: XPS spectra of a) the Cu 2p region, c) the Ga 2p region, e) the Si 2p region, and to the right of each the corresponding O 1s binding energy region.

3.5 Conclusions; Promising ZnO:dopant Systems for Further Investigation

ZnO was synthesised via CHFS with an assortment of 24 different dopants, including the undoped material, synthesised under the same conditions (including dopant proportion) for direct comparison. As indicated by XPS and XRD, some elements, such as Al and Ga, were doped successfully into the structure. Others, such as Cu and V, appeared to be partially doped into the ZnO structure, and for some (Ce in particular) there was no evidence of incorporation into the ZnO lattice at all. Morphologies were spheroidal or rod-like for all systems tested, generally with broad, inconsistent particle size distributions (determined by TEM image analysis). The majority demonstrated phase-pure Wurtzite structure by XRD; crystalline impurity peaks were only detected for 5 out of 24 samples.

Generally speaking, inclusion of dopant elements increased the mean particle size versus undoped ZnO and broadened the particle size distribution, but the crystallite size remained approximately consistent across most doped systems, with the notable exceptions of Si- and In-doped ZnO, for which both a drastic decrease in Scherrer crystallite size (from 28 down to 18 nm for both materials), and a significant narrowing of the particle size distribution was observed.

Approximately half of the dopants tested demonstrated some level of conductivity when the powders were tested as pressed, heat treated discs, but of these the only dopants that were judged to be sufficiently conductive for further testing and optimisation were Al, Ga, Si, and Cu. These yielded resistivities of the order of 10^{-2} or 10^{-1} Ω cm; the benchmark material, ITO, synthesised and tested by the same methods obtained resistivities in the order 10^{-3} Ω cm, thus any (unoptimised) materials with resistivities more than two orders of magnitude higher were judged to be inappropriate for further investigation. However, due to the intensely dark colour of the Cu-doped sample, as prepared and then more so post-heat treatment, its promise as a TCO material was judged to be insufficient for further investigation.

Thus the three materials that would be focussed on as ITO-replacement TCO materials were Al-doped ZnO (see Chapter 4), Ga-doped ZnO (see also Chapter 4), and Si-doped ZnO (see Chapter 5). For these, a selection of compositions would need to be synthesised and tested for their electronic properties in order to determine the optimal level of dopant in the doped ZnO system relative to the proportion of zinc. Once this had been established, the optimal samples could be scaled up to semi-industrial scales of synthesis and coated in flow, facilitating the dispersion of the nanoparticles in various media to then be deposited into thin films by spin coating or inkjet printing methods.

Appendix for Chapter 3

This appendix section includes the full characterisation for the dopant screening experiments, including XRD, XPS, TEM, and tables summarising the physical characterisation data. XRD patterns are shown in Figures 3.5 to 3.7, representative TEM images are shown in Figures 3.8 to 3.11, and XPS spectra are shown in Figures 3.12 to 3.19.

Figure 3.12 shows the Zn 2p high resolution scans for the doped samples. The spectra are vertically arranged in increasing binding energy of the $2p_{3/2}$ peak. All samples were calibrated to the carbon 1s peak at 284.7 eV, thus any shift is due to the difference in sample (i.e. the dopant). Undoped ZnO had a binding energy of 1020.6 eV, and the various dopants shifted this up to a maximum of 1021.3 eV, all within a well-known binding energy range for ZnO.[225] Splitting of the doublet was consistent across all samples, at 23.1 eV. All demonstrated the expected form, with the exception of the Ce-doped sample, for which the Zn 2p peaks showed notable asymmetry.

XPS spectra of the metal and oxygen regions are included in Figure 3.13 for undoped, Ce-doped, and Cr doped ZnO and in Figure 3.14 for La-doped, Nb-doped, and Y-doped ZnO. In particular, note Figure 3.13a, the O 1s region for undoped ZnO, against which the other O 1s spectra can be compared, in which two peaks were observed. The sharper peak around 530 eV was due to the lattice oxygen in ZnO. The broader peak at higher binding energy was due in part to other oxygen environments, including water, oxygen or hydroxyl groups adherent to the surface.[225] In support of the indication from XRD, the Ce 3d XPS spectrum in Figure 3.13c showed the characteristic six peaks of cerium (IV) oxide, a triplet each for the $3d_{5/2}$ and $3d_{3/2}$ orbitals. Fitted with three peaks, the O1s region for the Ce-doped sample was expected to contain three discernible environments; the CeO_2 should have accounted for one, the ZnO for another, and then the broad peak for oxygen-containing surface groups.[226] The Cr 2p region in Figure 3.13e showed only a single environment for the chromium, the $2p_{1/2}$ peak overlapping with a Zn Auger peak. Though the conductivity of the sample was indicative of successful doping, it was shown to be incomplete by the appearance of an addition peak in the oxygen spectrum at lower binding energy than the ZnO peak, corresponding to chromium oxide, although the oxidation state of the chromium could not be deduced from the data here, neither in the oxide form nor within the zinc oxide structure.[228]

The La $3d_{5/2}$ binding energy region shown in Figure 3.14a showed peaks characteristic of $La(OH)_3$, supported by the O 1s region, which showed two metal (hydr)oxide peaks; one each could be attributed to $La(OH)_3$ and the other to ZnO.[225, 229, 230] The Nb 3d region shown in Figure 3.14c showed a single niobium oxide environment, the lack of conductivity and over-large peak in the O 1s region indicated the formation of Nb_2O_5.[231] Finally in Figure 3.14 was the yttrium 3d region in Figure 3.14e, in which there were two doublets present, one each for Y_2O_3 (lower binding energy) and $Y(OH)_3$ (higher binding energy). This, coupled with the presence of conductivity in the sample and the single extra peak in the O 1s region (Figure 3.14f) could have indicated that some of the yttrium went into the ZnO structure, while the remainder appeared to form the hydroxide.[232]

Figure 3.15 shows the Gd 4d (a), Mn 2p (c), and Sm 3d (e) regions. Gadolinium showed a single environment (Figure 3.15a), complicated by the presence not only of a satellite peak but also the strongly overlapping Zn 3s peak; the most intense peak present. The O 1s spectrum indicated the possibility of the formation of gadolinium oxide (Gd_2O_3) as a separate phase.[232] In the case of manganese (Figures 3.15c and 3.15d), the spectra were highly diagnostic; a clear peak was seen in the O1s spectrum (Figure 3.15d) at lower binding energy than the one corresponding to ZnO, indicating a separate manganese oxide phase. The single environment seen in the Mn 2p spectrum coupled with a lack of satellite peaks (as would have been seen for MnO) and also lacking the distinctive feature in the Mn $2p_{3/2}$ peak that would have been indicative of MnO_2, suggested that Mn_2O_3 was the species present as the separate phase.[233] The samarium spectra pointed to one environment, but the O 1s spectrum could not be deconvoluted beyond saying that there are likely multiple metal oxide and/or hydroxide species present. This, with the lack of conductivity in the sample, most likely indicated that Sm had not gone into the ZnO structure.

Figure 3.16 shows the Sn 3d (a), Ti 2p (c), and Zr 3d (e) regions. In each case, only a single environment was suggested by the spectra, and the lack of impurity peaks in the XRD patterns could for these materials have suggested that the dopants went into the ZnO structure. However this did not result in conductivity for any of the three;[234–236] formation of additional defects in the structure (e.g. those leading to recombination centres, rendering electrons conductively impotent) could have been to blame.

Figure 3.17 shows the Cu 2p d (a), V 2p (c), and Fe 2p (e) regions. All three resulted in varying degrees of conductivity, and none demonstrated impurities by XRD, which could in itself been used as evidential of successful doping. However, in each there were some points of interest in the XPS spectra. An extra peak in the metal oxide region of the O 1s spectrum (3.17b) of copper indicated another oxygen environment in addition to ZnO, and the strong satellite peaks in the Cu 2p spectrum (3.17a) were diagnostic of Cu(II), hence it could be deduced that CuO was present, not Cu_2O, or Cu metal.[227] There were characteristic peaks in the V 2p spectrum (3.17c) of two oxidation states, (II) and (IV), with the intensity of the latter greatly outweighing that of the former. There was no extra peak in the O1s spectrum (3.17d), but it was likely that partial doping had taken place.[237] Finally, the iron spectrum showed a single environment (Figure 3.17e), with one strong satellite peak. An additional peak appeared in the O 1s spectrum, implying the formation of an iron oxide species, but the oxidation state(s) could not be unequivocally elucidated from this data. The $2p_{3/2}$ peak appeared at 710.0 eV, for which there is precedent for Fe(II) and Fe(III) oxides, however generally speaking it is more likely to be due to FeO from the binding energy position.[226]

Figure 3.18 shows the Pr 3d (a), Nd 3d (c), and In 3d (e) XPS regions. In each case, the O 1s spectra were very similar; one metal oxide peak was seen, along with the broader peak. One environment each for Pr (3.18a) and In (3.18e), coupled with the conductivity of the samples are indicative of the successful doping of these elements. The neodymium spectrum was slightly hampered by the presence of two $3d_{5/2}$ peaks overlapping with the oxygen KLL Auger peak. However, due to the conductivity of the samples, it was probable that some Nd was also successfully doped into ZnO.[238]

Figure 3.19 shows the Al 2p (a), Ga 2p (c), and Si 2p (e) regions. As perhaps could have been anticipated from the three most conductive samples, a single environment each of Al, Ga, and Si were indicated from both the dopant regions and their corresponding O 1s spectra. Data for these and those discussed previously are summarised in Table 3.3.

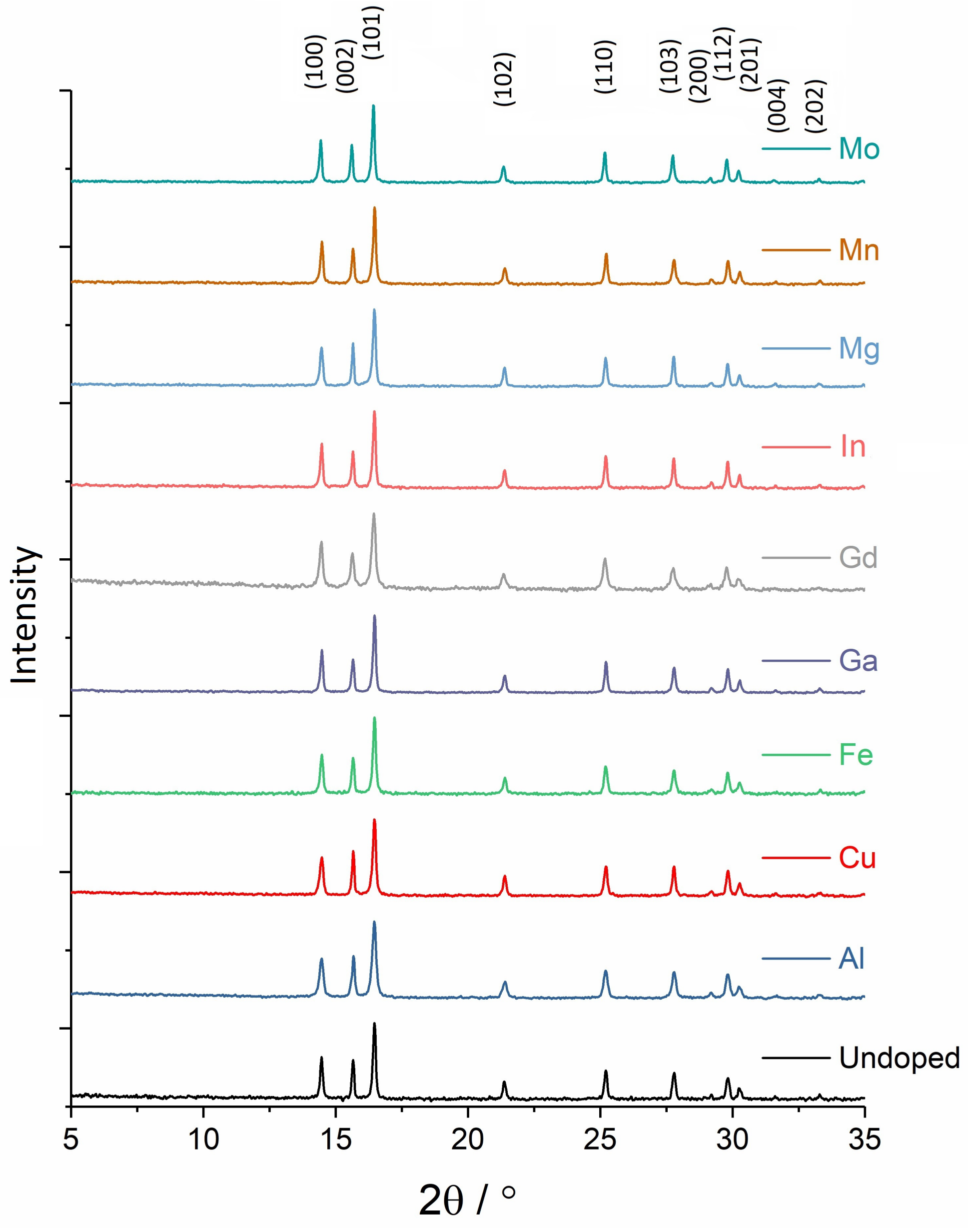

Figure 3.5: XRD patterns for apparently phase-pure doped ZnO samples synthesised by CHFS. The measurement was carried out with a molybdenum source, with wavelength λ = 0.7093 Å.

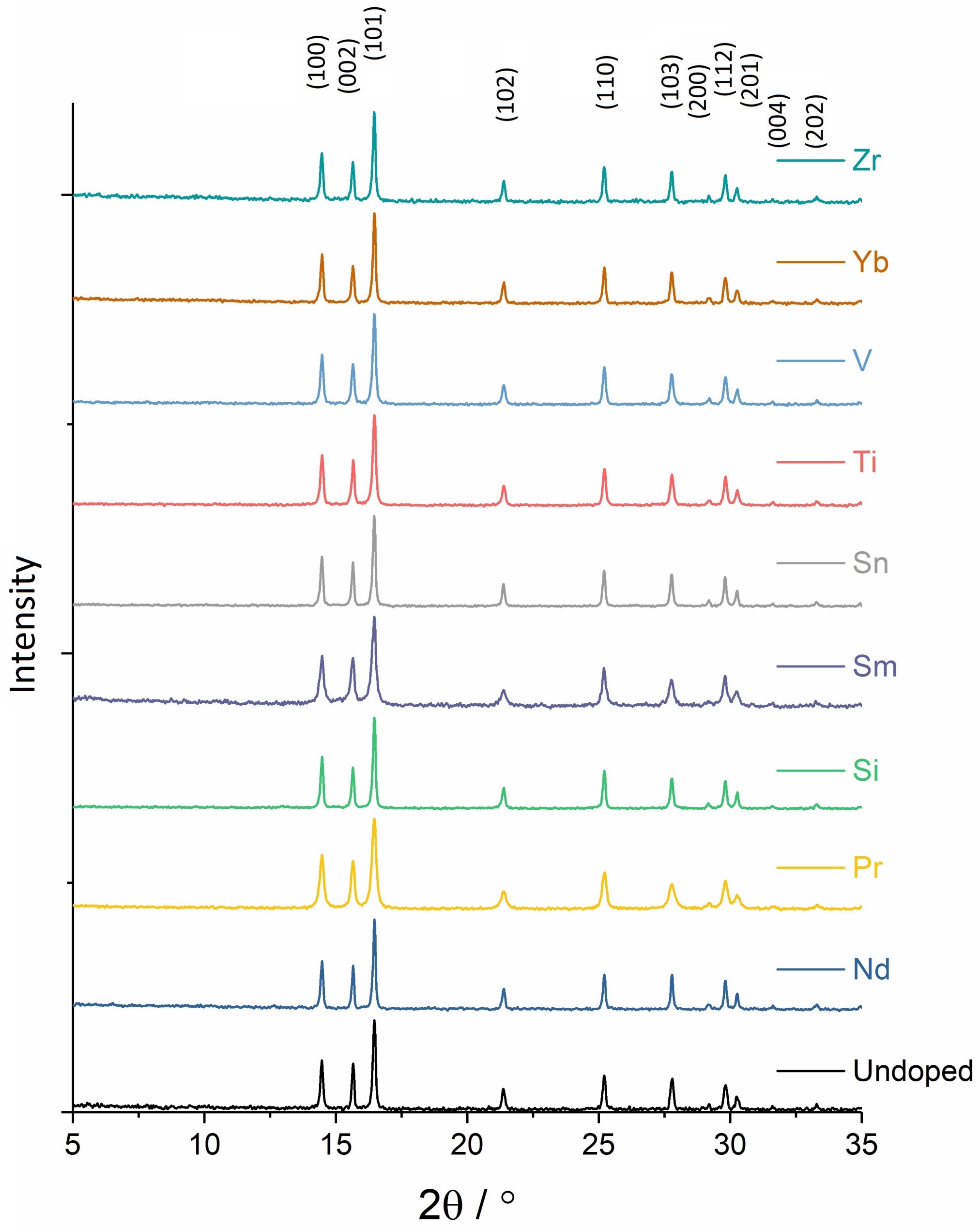

Figure 3.6: XRD patterns for apparently phase pure doped ZnO samples synthesised by CHFS. The measurement was carried out with a molybdenum source, with wavelength λ = 0.7093 Å.

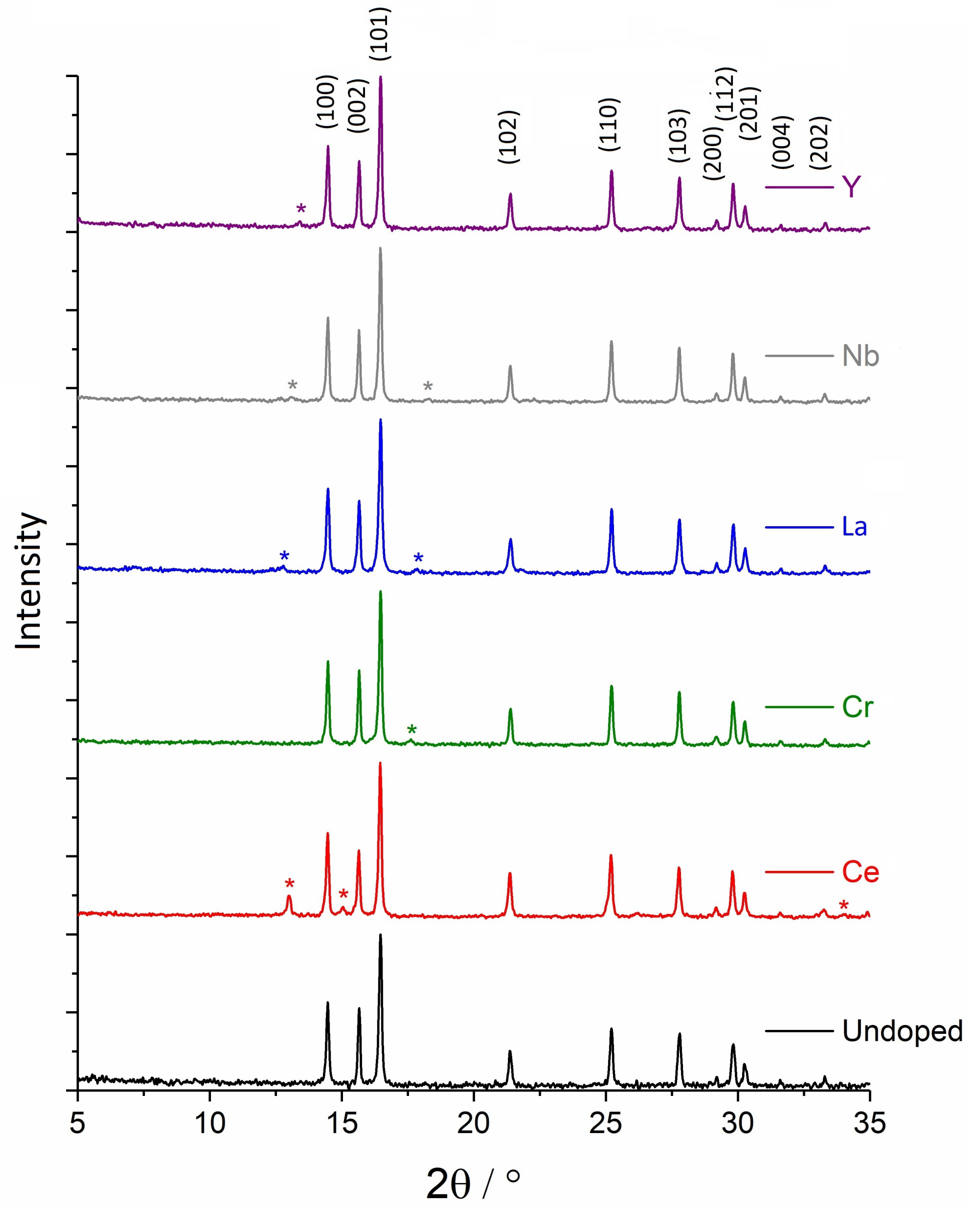

Figure 3.7: XRD patterns for the doped ZnO samples synthesised by CHFS that show clear impurity peaks. The measurement was carried out with a molybdenum source, with wavelength $\lambda = 0.7093$ Å.

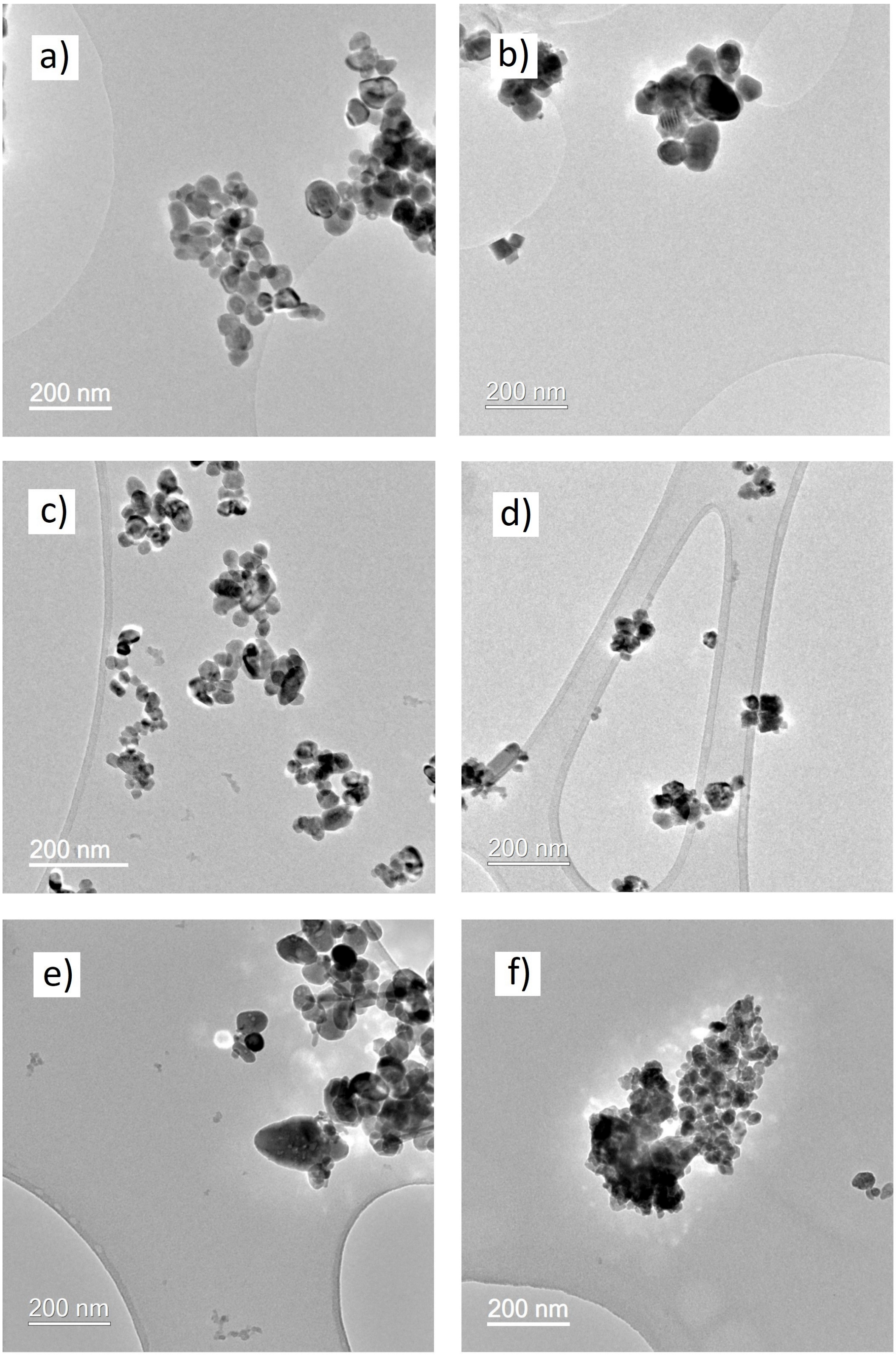

Figure 3.8: Representative TEM images of a) undoped ZnO, b) Ce-doped ZnO, c) Ga-doped ZnO, d) In-doped ZnO, e) Nd-doped ZnO, and f) Si-doped ZnO.

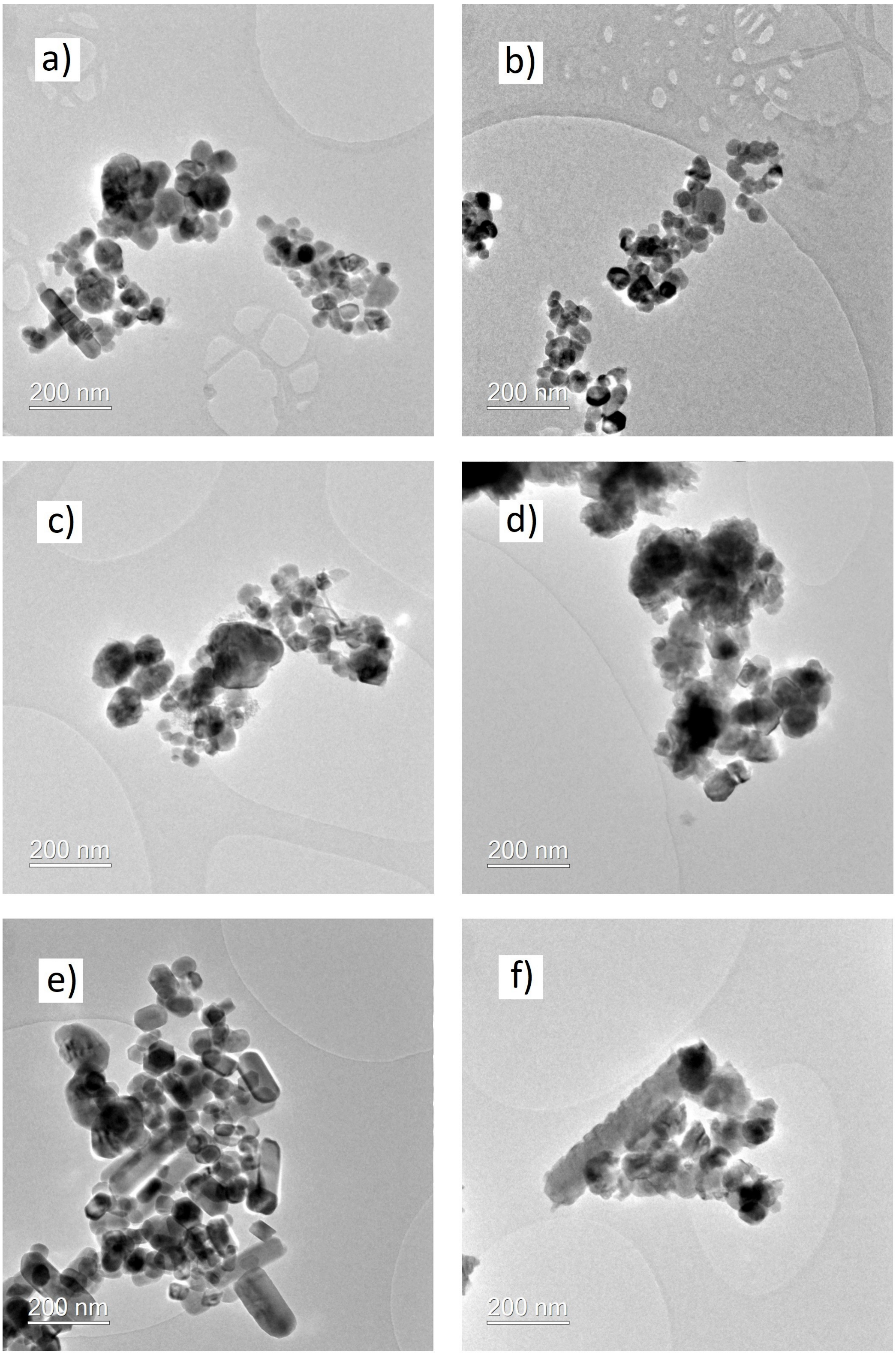

Figure 3.9: Representative TEM images of a) V-doped ZnO, b) Y-doped ZnO, c) Zr-doped ZnO, d) Nb-doped ZnO, e) Cu-doped ZnO, and f) Mo-doped ZnO.

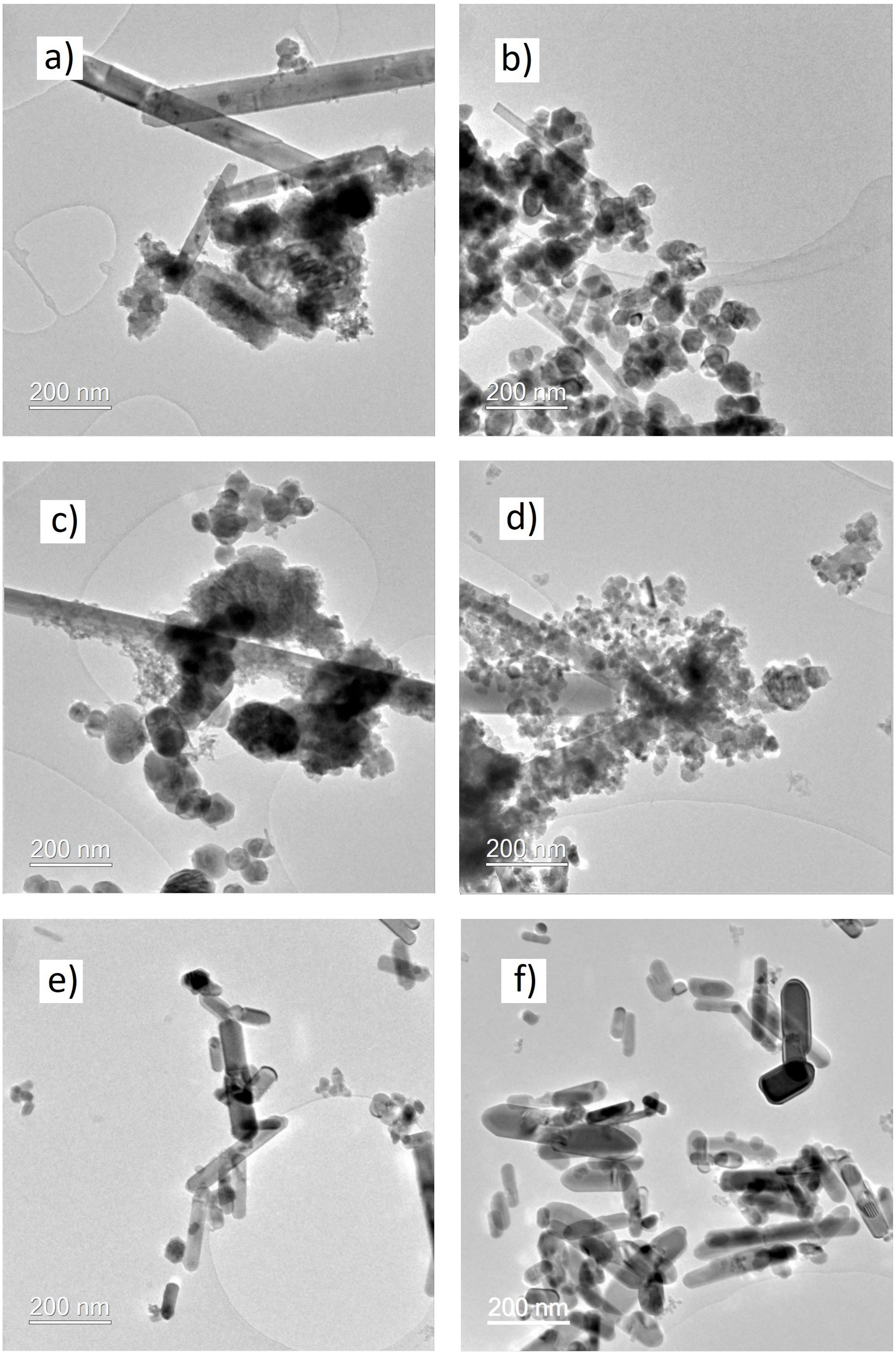

Figure 3.10: Representative TEM images of a) Gd-doped ZnO, b) La-doped ZnO, c) Yb-doped ZnO, d) Sn-doped ZnO, e) Cr-doped ZnO, and f) Al-doped ZnO.

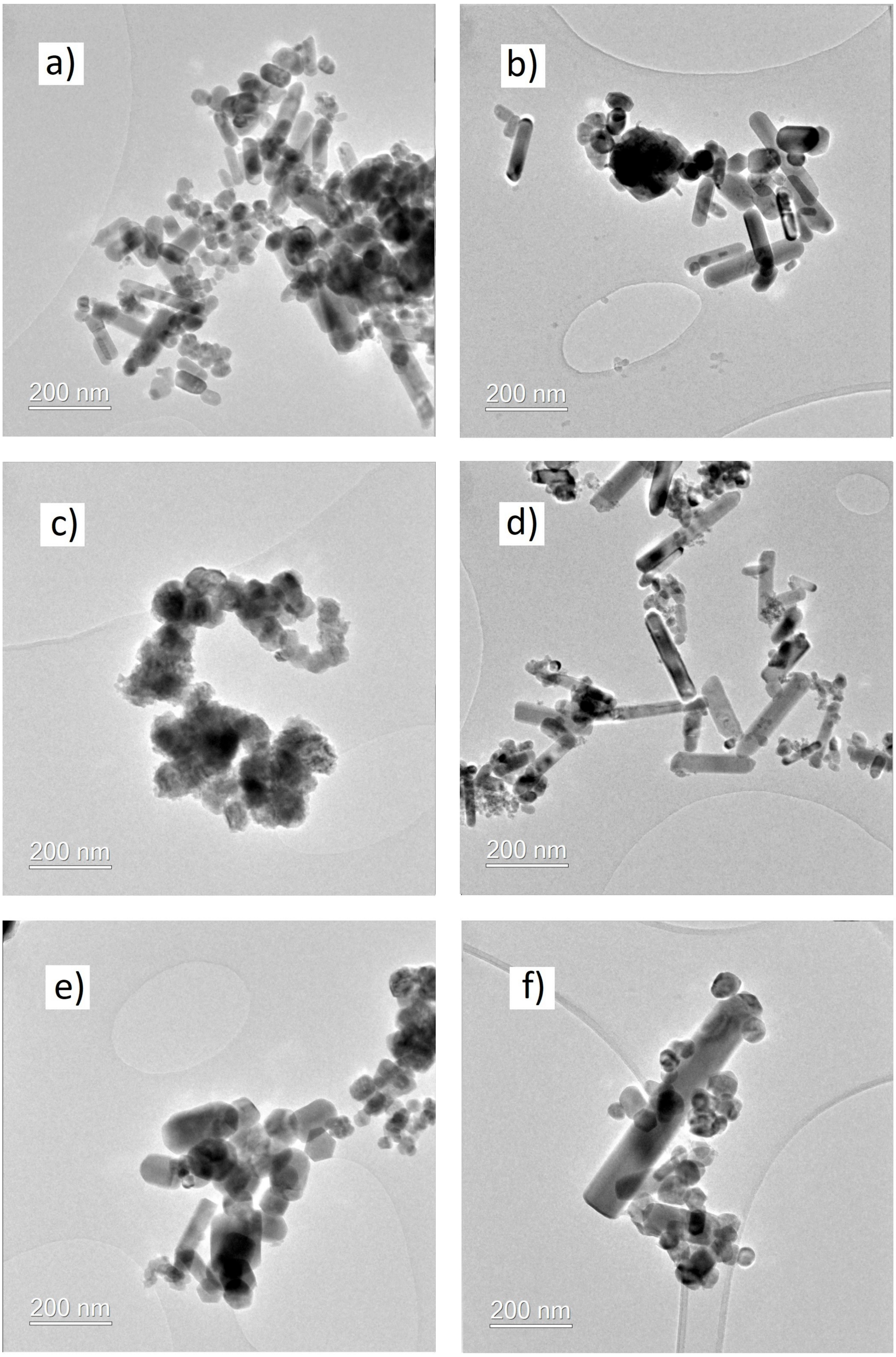

Figure 3.11: Representative TEM images of a) Mn-doped ZnO, b) Pr-doped ZnO, c) Sm-doped ZnO, d) Fe-doped ZnO, e) Mg-doped ZnO, and f) Ti-doped ZnO.

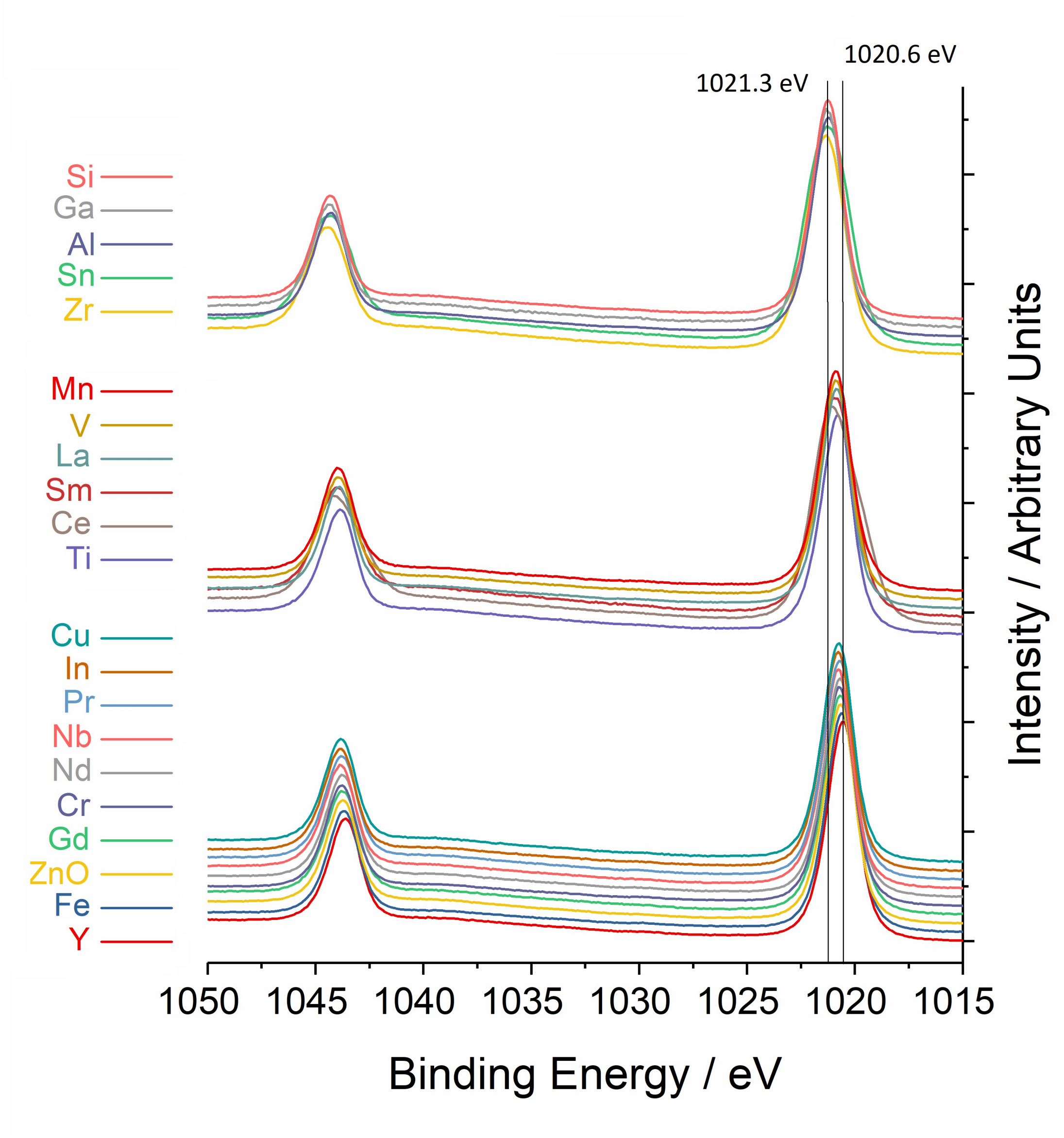

Figure 3.12: XPS spectra of the Zn 2p region for the doped ZnO samples, arranged in increasing binding energies from bottom to top. As per convention, the energy scale increases from right to left.

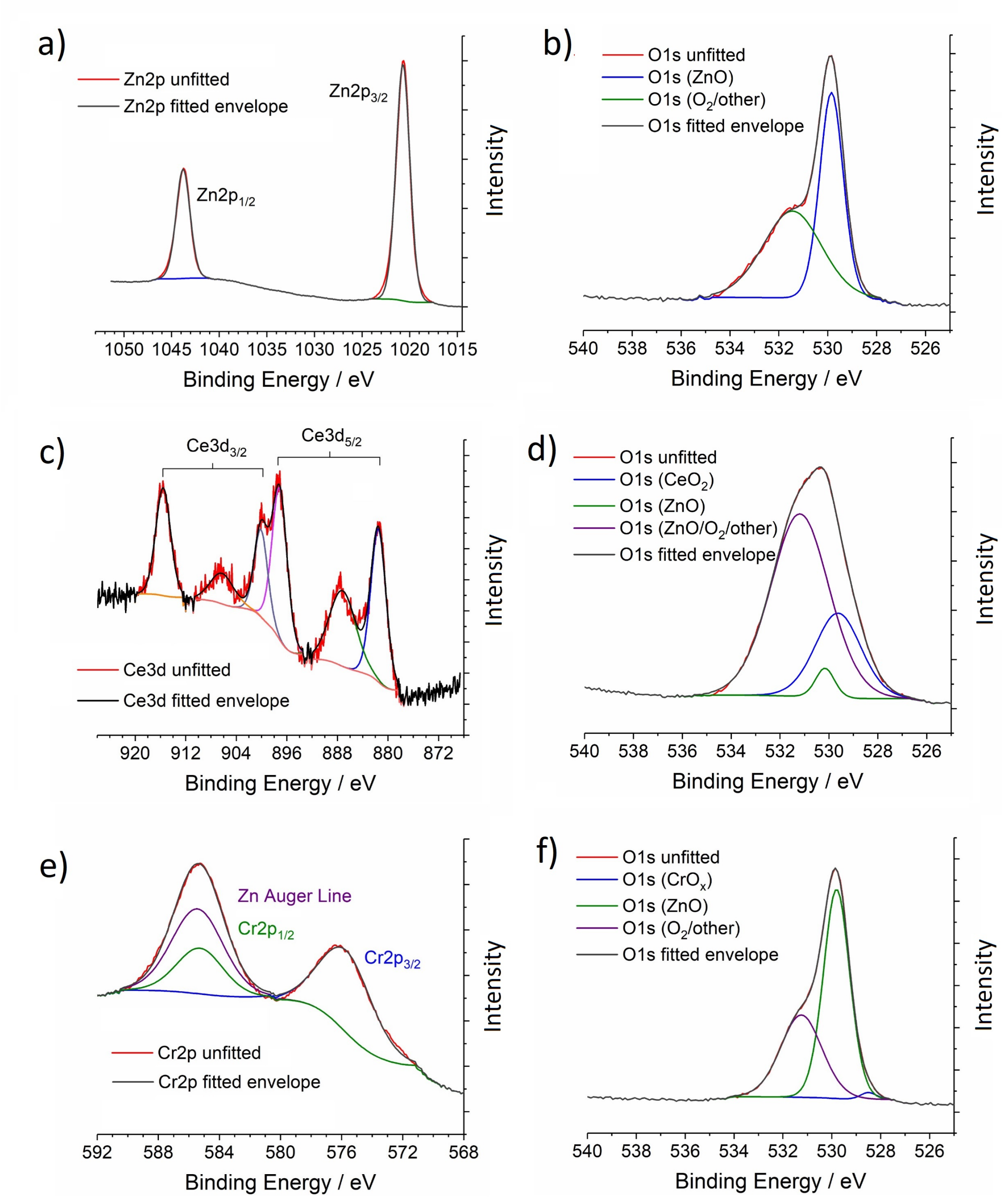

Figure 3.13: XPS spectra of a) the Zn 2p region (in un-doped ZnO), c) the Ce 3d region, e) the Cr 2p region, and to the right of each the corresponding O 1s binding energy region.

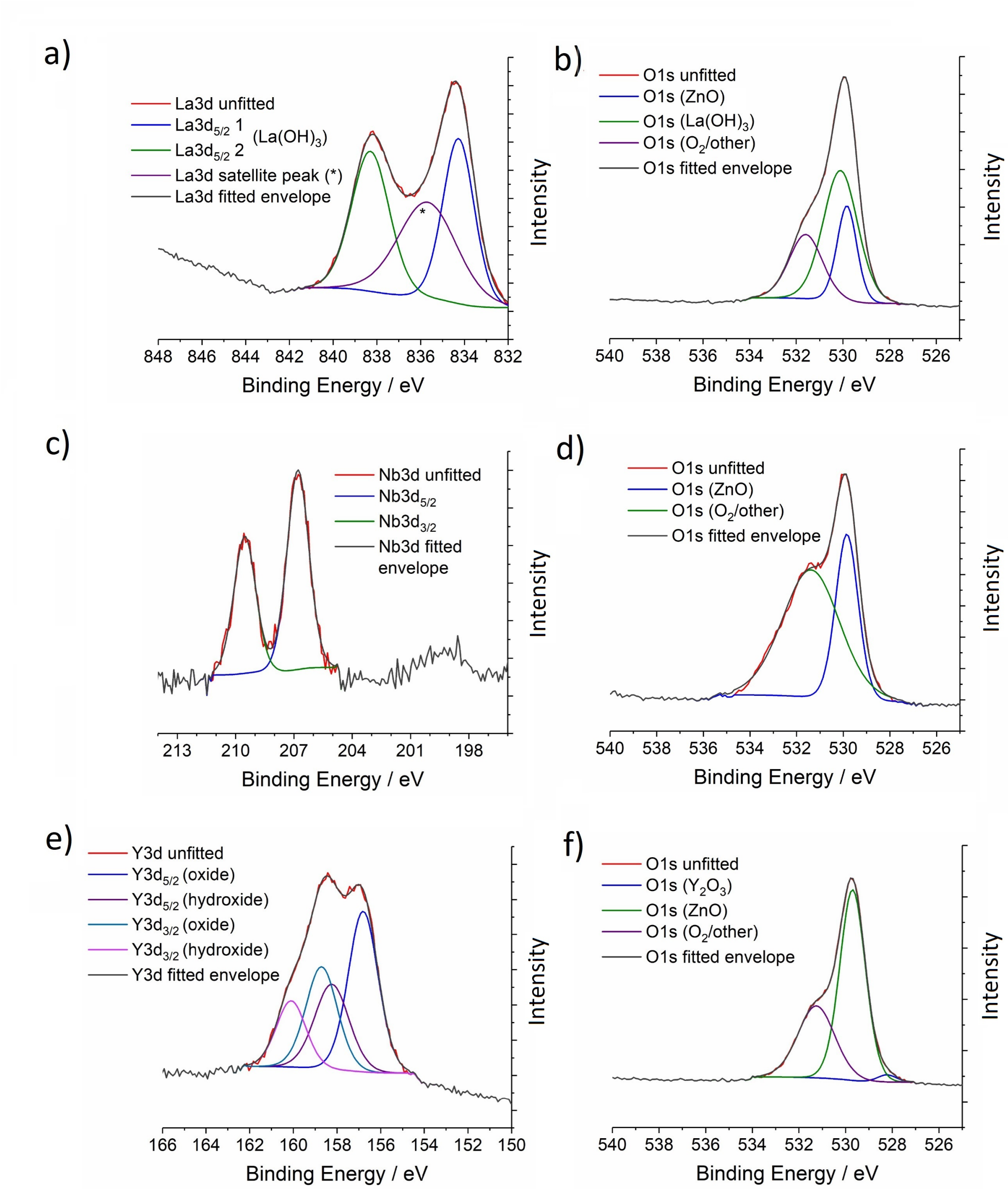

Figure 3.14: XPS spectra of a) the La 3d region, c) the Nb 3d 3d region, e) the Y 3d region, and to the right of each the corresponding O 1s binding energy region.

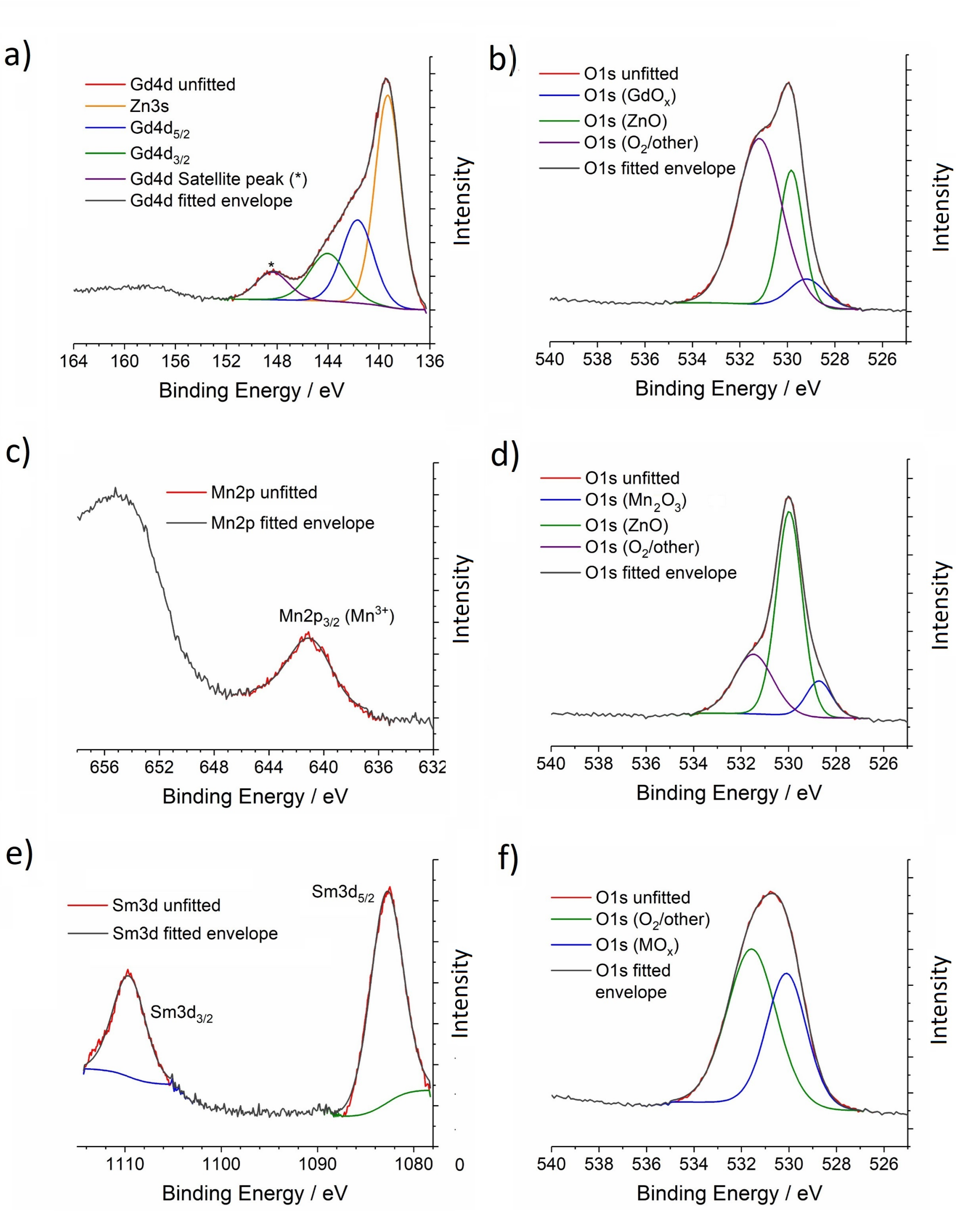

Figure 3.15: XPS spectra of a) the Gd 4d region, c) the Mn 2p region, e) the Sm 3d region, and to the right of each the corresponding O 1s binding energy region.

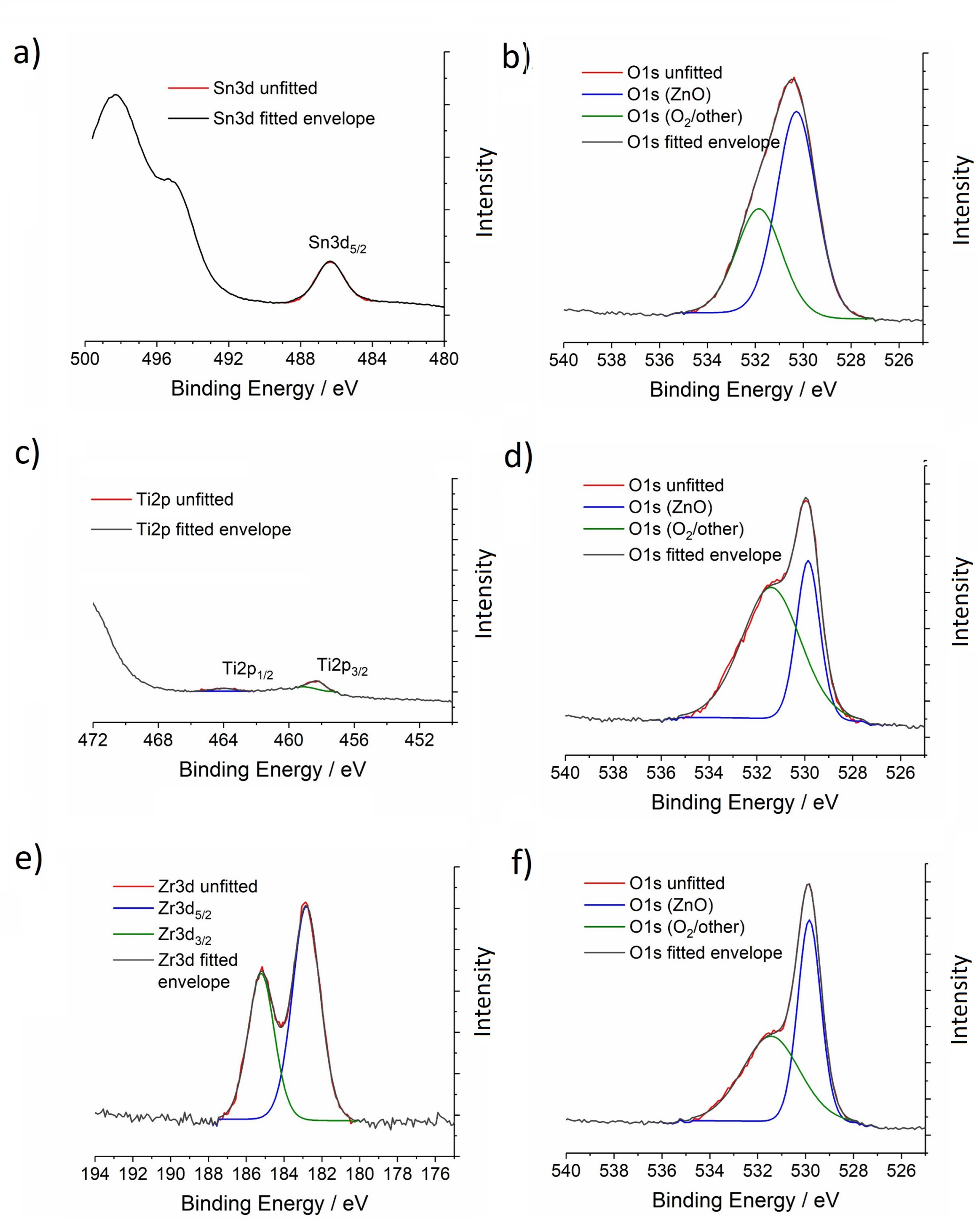

Figure 3.16: XPS spectra of a) the Sn 3d region, c) the Ti 2p region, e) the Zr 3d region, and to the right of each the corresponding O 1s binding energy region.

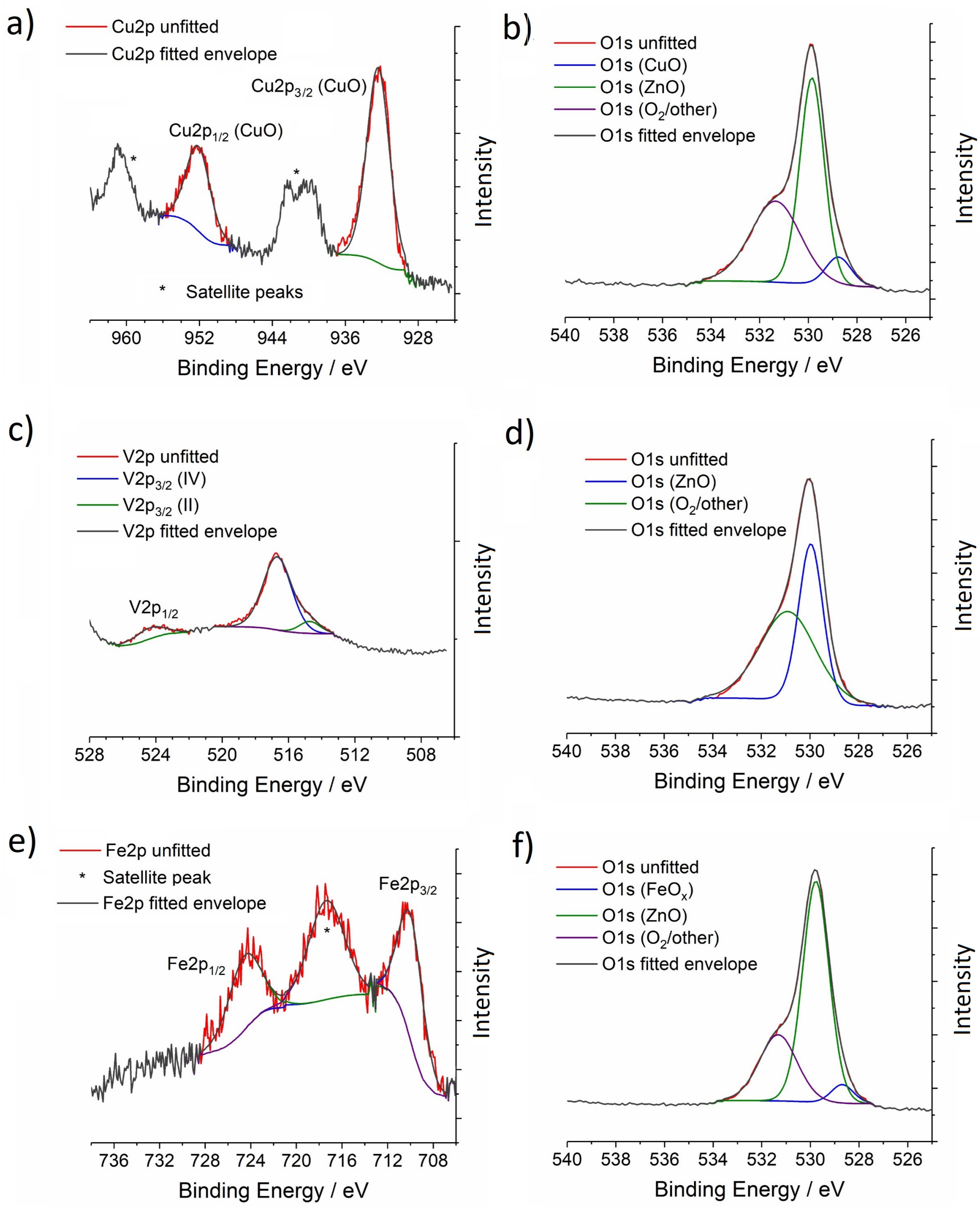

Figure 3.17: XPS spectra of a) the Cu 2p region, c) the V 2p region, e) the Fe 2p region, and to the right of each the corresponding O 1s binding energy region.

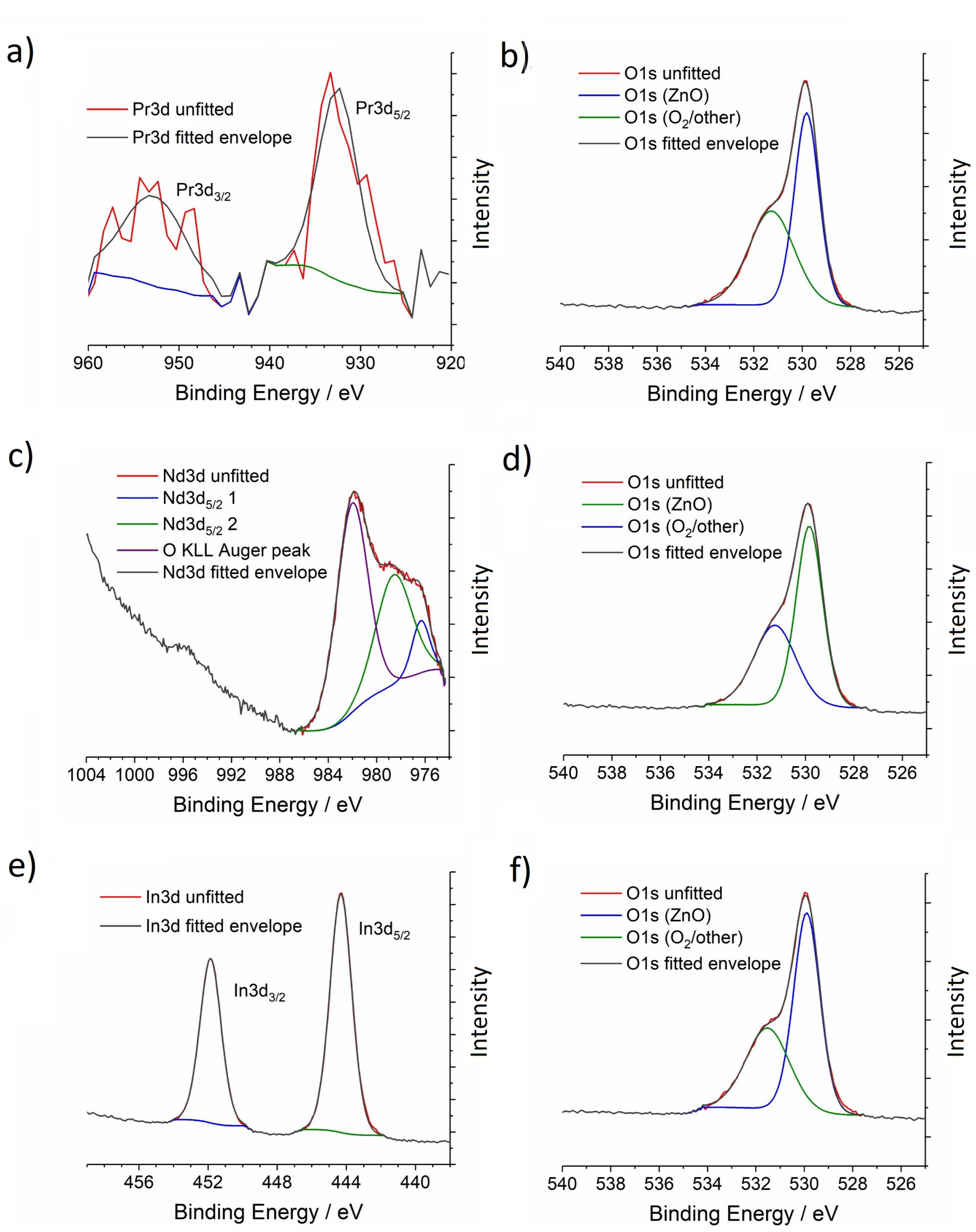

Figure 3.18: XPS spectra of a) the Pr 3d region, c) the Nd 3d region, e) the In 3d region, and to the right of each the corresponding O 1s binding energy region.

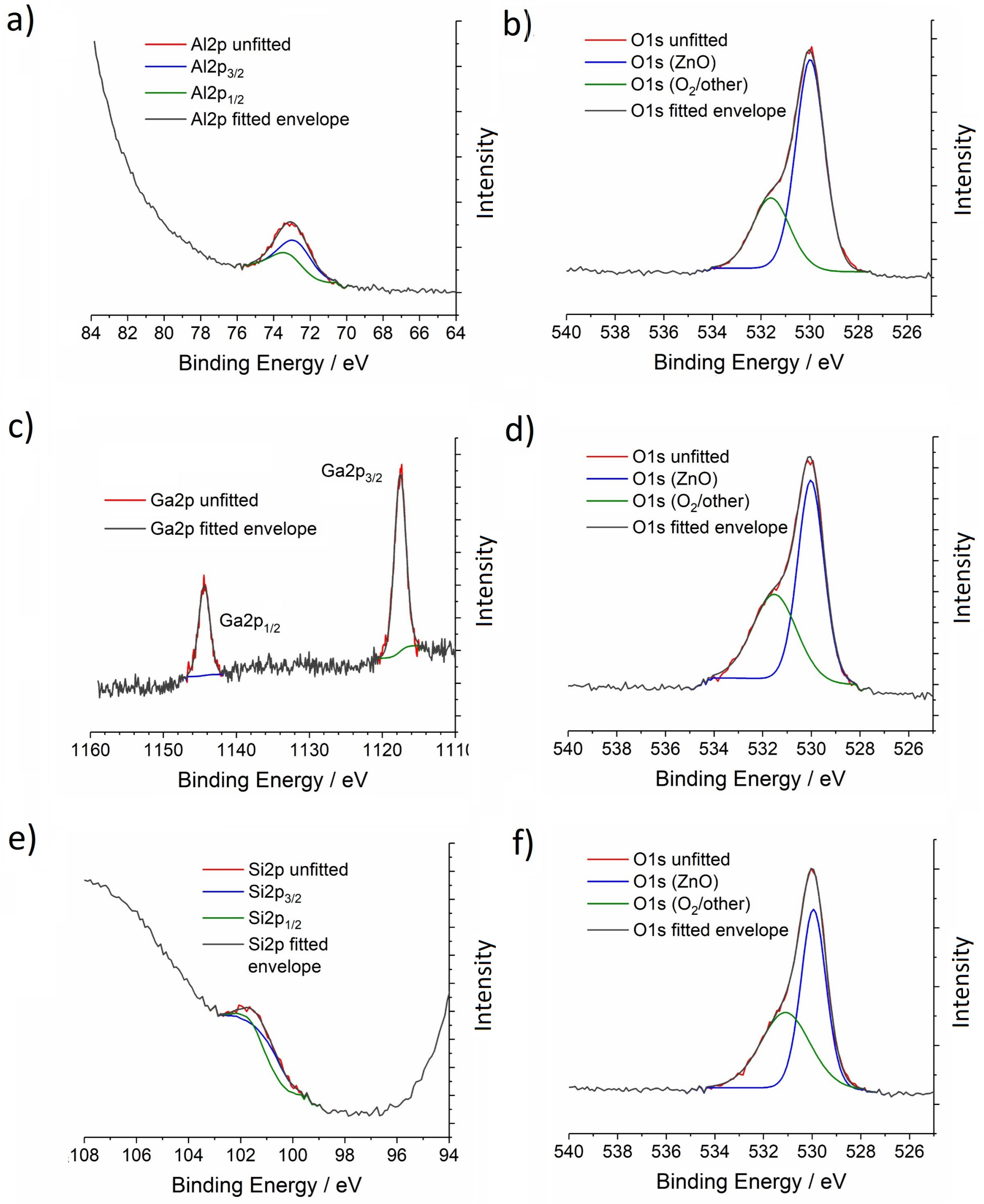

Figure 3.19: XPS spectra of a) the Al 2p region, c) the Ga 2p region, e) the Si 2p region, and to the right of each the corresponding O 1s binding energy region.

Table 3.2: Table summarising key particle size information, including Scherrer crystallite size, mean TEM length (with standard deviation, σ) and aspect ratio (calculated from 100 particles), and corresponding Figure reference for each sample's representative TEM image.

Dopant element	**Scherrer size / nm**	**TEM length / nm**	σ **/ nm**	**TEM aspect ratio**	**Figure reference**
-	28	47	± 25	1.2	3.13a
Al	32	129	± 80	2.9	3.15f
Ce	29	56	± 21	1.3	3.13b
Cr	31	89	± 66	2.6	3.15e
Cu	32	72	± 43	1.5	3.14e
Fe	27	95	± 75	2.6	3.16d
Ga	29	47	± 8	1.1	3.13c
Gd	29	88	± 174	2.2	3.15a
In	22	32	± 15	1.4	3.13d
La	26	88	± 187	2.7	3.15b
Mg	30	67	± 65	1.5	3.16e
Mn	31	57	± 35	1.7	3.16a
Mo	31	84	± 88	1.5	3.14f
Nb	28	74	± 28	1.3	3.14d
Nd	30	45	± 36	1.4	3.13e
Pr	33	49	± 54	1.7	3.16b
Si	18	34	± 10	1.4	3.13f
Sm	31	100	± 97	1.6	3.16c
Sn	18	58	± 172	1.6	3.15d
Ti	31	71	± 84	1.5	3.16f
V	26	50	± 24	1.3	3.14a
Y	26	59	± 34	1.3	3.14b
Yb	30	73	± 202	1.7	3.15c
Zr	29	22	± 30	1.1	3.14c

Table 3.3: Table summarising key XPS data on the doped ZnO samples, including the lower energy orbital binding energies ($n\mathrm{d}_{5/2}$, $n\mathrm{p}_{3/2}$ or 1s), the doublet splitting, and the compositional ratio between zinc and the dopant element, expressed as an atomic percentage of the dopant and based on the detection level of the elements by the instrument. 'D.S.' is the doublet splitting, and 'B.E.' is the binding energy. '*' indicates data could not be acquired.

Dopant (orbital)	**B.E.$_{dop}$ / eV**	**D.S.$_{dop}$ / eV**	**B.E.$_{Zn}$ / eV**	**D.S.$_{Zn}$ / eV**	**Dopant level / at%**	**References**
-	-	-	1020.7	23.1	-	[225]
Al (2p)	73.0	0.4	1021.3	23.1	3.3	[225, 239]
Ce (3d)	881.4	8.0	1020.9	23.1	2.2	[225, 226]
Cr (2p)	575.9	10.0	1020.7	23.1	1.7	[225, 228]
Cu (2p)	932.4	19.9	1020.8	23.1	1.4	[225, 227]
Fe (2p)	710.0	14.3	1020.6	23.1	1.3	[225, 240]
Ga (2p)	1117.6	26.9	1021.3	23.1	1.9	[225, 241]
Gd (4d)	141.6	6.8	1020.7	23.1	5.1	[225, 232]
In (3d)	444.3	7.6	1020.8	23.1	2.0	[26, 225]
La (3d)	834.3 838.2	16.8	1020.9	23.1	4.7	[225, 229] [230, 242]
Mg (1s)	*	*	1021.3	23.1	*	[225]
Mn (2p)	640.9	11.8	1020.9	23.1	2.0	[225, 233]
Mo (3d)	*	*	1021.0	23.1	*	[225]
Nb (3d)	206.9	2.7	1020.8	23.1	1.8	[225, 231]
Nd (3d)	976.2 978.6	*	1020.7	23.1	3.1	[225, 238]
Pr (3d)	932.5	20.0	1020.8	23.1	1.8	[225, 229]
Si (2p)	101.2	0.6	1021.3	23.1	1.8	[225, 243]
Sm (3d)	1082.8	27.2	1020.9	23.1	4.7	[225, 232]
Sn (3d)	486.4	8.5	1021.3	23.1	4.0	[225, 234]
Ti (2p)	458.2	5.8	1020.9	23.1	0.8	[225, 235]
V (2p)	516.7	7.6	1020.9	23.1	3.9	[225, 237]
Y (3d)	157.1	2.1	1020.6	23.1	5.6	[225, 232]
Yb (4d)	*	*	1021.0	23.1	*	[225]
Zr (3d)	182.8	2.4	1021.3	23.1	5.3	[225, 236]

Chapter 4

Al and Ga Doped and Co-Doped Zinc Oxide for Transparent Conducting Oxides

4.1 Aims

Having identified aluminium and gallium doping in zinc oxide (AZO and GZO, respectively) as the most promising doped systems with respect to conductivity, the aim of this chapter is to outline the investigation into the compositional optimisation of AZO and GZO for TCOs as synthesised by continuous hydrothermal flow synthesis (CHFS), on both the laboratory and pilot scales. The effect of co-doping zinc oxide with both aluminium and gallium (usually known as AGZO) was also investigated. In addition to the electrical testing, characterisation including XRD, BET, TEM, XPS, EDS, and ICP-AES is also discussed, to gauge the effect that the different dopant ratios have on the properties of the material.

4.2 Introduction

All three of these materials, AZO, GZO, and AGZO have the same flavour of defect chemistry that gives rise to their improved conductivity over the undoped material. The Al^{3+} or Ga^{3+} will tend to be situated on the Zn^{2+} site, i.e. as $Al^{\bullet}_{Zn}$ or as $Ga^{\bullet}_{Zn}$. In both cases, the dopant acts as a shallow donor; the extra valence electron is loosely bound, and thus is mobile and able to carry charge.[22, 244] These point defects cause a degree of lattice strain; Zn^{2+} has an ionic radius of 0.60 $\AA$, Al^{3+} and Ga^{3+} have ionic radii of 0.39 $\AA$ and 0.47 $\AA$, respectively,[245] and this can lead to mobility issues for the charge carriers at higher dopant levels, counter-balancing the increasing concentration of carriers. The point at which this occurs is difficult to state with certainty, as formation of balancing intrinsic defects can occur, which could trap some of these extra electrons, or inhibition by ionised impurities or scattering effects. As such, not every dopant ion will necessarily contribute its extra electron to the carrier concentration in the material.[11, 244, 246, 247]

Issues with thermal stability of non-stoichiometric (the only way to make it highly conductive) undoped zinc oxide led to Minami et al. experimenting with deposition of AZO for application as a TCO for the first time in 1984.[119] with a little under 2 at% Al, a magnetron-sputtered film demonstrated a marked improvement in thermal stability, and a resistivity of only 1.9 x 10^{-4} Ω cm, and remains among the most conductive AZO films in literature to this day. A great number of other groups have made films of the order of 10^{-4} Ω cm, however, by various deposition methods including magnetron sputtering,[144–146, 248–253] atmospheric pressure[120] and aerosol assisted[121] chemical vapour deposition (APCVD and AACVD, respectively), and pulsed laser deposition (PLD).[122, 254] Other techniques such as spray pyrolysis[123], atomic later deposition (ALD),[255] and inkjet printing[156] and spraying[256] have been explored, but are orders of magnitude higher in terms of resistivity. A summary of the best performing AZO films from literature is included in Table 6.2 in Chapter 6.

GZO was first made by magnetron sputtering in 1990 by Choi et al,[257] though the films displayed resistivities of only ca. 2 x 10^{-3} Ω cm. This was soon improved upon, to the point where films of GZO with resistivities of the order 10^{-4} Ω cm have since been made by sputtering,[124–126, 207, 248, 258, 259] APCVD,[128] CVD,[129], AACVD,[121] and PLD.[127] A tabulated summary for a selection of these materials is included in Table 6.3 in Chapter 6.

Similarly, several AGZO films have been made by sputtering, with resistivities of ca. 10^{-4};[130–133, 248, 253, 260–263] a summary of AGZO film data from literature is included in Table 6.4 in Chapter 6. Section 6.2 of Chapter 6 also expounds upon the additional optoelectronic properties of the materials; this Chapter focuses on comparison of different material compositions primarily by use of their resistivity values.

Though thin films are typically formed by sputtering, the material in the target needs first to be synthesised, in which case the ZnO would most likely have been synthesised for these studies by one of three methods:[112, 160, 264, 265]

- The French (or Indirect) process, wherein metallic zinc is melted in a crucible and vapourised (at ca. 1000 °C), at which point the Zn vapour reacts with oxygen in the air to form ZnO.
- The American (or Direct) process, wherein impure minerals, ores, or composites of zinc undergo carbothermal reduction by heating with a carbon source such as anthracite to produce the zinc vapour, at a similarly high temperature to the French process. Due to the reduced purity of the starting material, the American process also typically results in a lower purity ZnO product.
- Wet chemical process, wherein zinc precursor solutions are used to precipitate the carbonate or hydroxide, which is converted to the oxide by calcining (typically around 800 °C).

Al_2O_3, or alumina, is primarily sourced from the mineral Bauxite, which is typically purified by use of the Bayer Process, adding NaOH to the Bauxite to obtain sodium aluminate, from which pure aluminium hydroxide can be precipitated by seeding. This can then be converted to alumina by calcining at 1100 °C.[266] Gallium oxide (most stably β-Ga_2O_3) can be easily generated from most gallium precursors by simply heating in air or a water environment to several hundred degrees, forming either the oxide or hydroxide phase, which can then be calcined above 600 °C to form highly pure gallium oxide.[267]

In order to generate a sputtering target, or multiple sputtering targets depending on the specific methodology employed, these materials would need to undergo a further annealing step as above, generally >1000 °C.

Benefits of Continuous Hydrothermal Flow Synthesis (CHFS) over such processes are fully discussed in Section 1.4 of Chapter 1, but in brief, CHFS is able to directly deliver ZnO or doped ZnO by a purely hydrothermal (i.e. water as the only solvent) process at drastically lower temperatures than those processes mentioned above, most of which require at least one calcination step at or above 1000 °C. Before the studies outlined in this chapter, no such had been carried out investigating aluminium and gallium doping or co-doping into zinc oxide by CHFS.

4.3 AZO and GZO

This section outlines the investigation into AZO and GZO; the compositional optimisation and scale-up, by means of physical and electrical characterisation.

4.3.1 Experimental design and observations

Initially a three-pump, single mixer laboratory-scale CHFS set-up was used (see Experimental chapter, section 2.2.1). With a total metal concentration, [Zn + Al] or [Zn + Ga], of 0.3 M (supplied by pump P2), and pump flow rates of 80, 40, and 40 mL min^{-1} for pumps P1, P2, and P3, respectively. 8 g of product was expected in a collection volume of 1.2 L, and base (KOH) concentration was maintained at twice the metal concentration, 0.6 M, in the feed supplied by pump P3.

Al and Ga dopant concentrations in the range 0.5 to 6.0 at% (with 0.5 at% increments) were synthesised, such that there were twelve products of each AZO and GZO. With the optimal AZO sample identified as 2.5 at% Al, synthesis of 1.0, 2.0, 2.5, and 3.5 at% Al-doped ZnO was carried out on the pilot scale, wherein the flow rates used were 400, 200, and 200 mL min^{-1} for pumps P1, P2, and P3, respectively (in effect a five-fold volumetric scale-up process). As the optimal GZO sample was at 3.5 at% Ga, 2.0, 3.0, 3.5, and 4.5 at% Ga samples were synthesised on the pilot scale.

Doping of both Al and Ga into ZnO had the effect of turning the powders from white to pale yellow, with the intensity of the colour increasing with dopant level. Ga-doping resulted in more intense colouring than analogous Al doping levels. All samples were collected at pH 7-8, and required three rounds of washing and centrifugation (as detailed in 2.2.5) before freeze-drying. Yields of the collected, dried powder samples were consistently at 80% (±5%). Experimental observations were the same on both the laboratory and pilot scale processes. Upon pressing these yellow powders into discs, the colour significantly intensified, and they turned yellow-green, with more intense green colouring as dopant levels increased. In turn, heat treatment of these green discs resulted in a further colour change to blue, and again the intensity of the colour was dependent on the dopant level.

Powder X-ray diffraction (pXRD), transmission electron microscopy (TEM), energy dispersive X-ray spectroscopy (EDS), X-ray photoelectron spectroscopy (XPS), Brunauer-Emmett-Teller (BET) measurements, and inductively coupled plasma atomic emission spectroscopy (ICP-AES) were used to characterise the powder samples, and Hall Effect measurements were used to determine the electrical properties of the samples as pressed, heat treated discs.

4.3.2 Characterisation

Tables 4.1 and 4.2 show summaries of the characterisation of the 2.5 at% and 5.0 at% samples of each laboratory-scale synthesised AZO and GZO, and the conductively optimal samples of each synthesised on the pilot scale (2.5 at% and 3.5 at% for AZO and GZO, respectively), including surface area, particle size, and elemental compositional analysis.

4.3.2.1 Physical analysis; XRD, TEM, and BET

XRD patterns and excerpts are shown in Figures 4.1 and 4.4; all samples across the compositional space and synthesised on both the laboratory and pilot scales demonstrated phase pure Wurtzite ZnO structure by XRD. Increasing the dopant level for both materials resulted in smaller crystallite size as calculated by the Scherrer method, and up-scaling of the synthesis to the pilot CHFS resulted in a miore sig-

Table 4.1: A summary of the physical analysis results of laboratory and pilot scale AZO samples. Including: initial dopant concentration in the precursor solution, the measured/calculated dopant concentrations by EDS, XPS, and ICP, and particle size from Scherrer[8, 9] and TEM image analysis (average over 250 particles for each sample), and BET surface area.

Material (Scale)	**AZO (lab)**		**AZO (pilot)**
Precursor Al conc. / at%	2.5	5.0	2.5
Al conc. (EDS) / at%	2.3	4.0	2.0
Al conc. (XPS) / at%	3.9	7.2	3.3
Al conc. (ICP) / at%	2.2	4.1	1.9
Scherrer size / nm	34	31	18
Length (TEM) / nm	132 ± 83	187 ± 92	63 ± 40
Width (TEM) / nm	43 ± 14	38 ± 17	32 ± 10
Aspect ratio (TEM)	3.1	4.9	2.0
S.A. (BET) / m^2 g^{-1}	20	27	32

Table 4.2: A summary of the physical analysis results of laboratory and pilot scale GZO samples. Including: initial dopant concentration in the precursor solution, the measured/calculated dopant concentrations by EDS, XPS, and ICP, and particle size from Scherrer[8, 9] and TEM image analysis (average over 250 particles for each sample), and BET surface area.

Material (Scale)	**GZO (lab)**		**GZO (pilot)**
Precursor Ga conc. / at%	2.5	5.0	3.5
Ga conc. (EDS) / at%	2.2	4.8	3.1
Ga conc. (XPS) / at%	3.0	6.1	3.9
Ga conc. (ICP) / at%	2.5	5.5	2.1
Scherrer size / nm	22	21	19
Length (TEM) / nm	44 ± 8	36 ± 9	33 ± 8
Aspect ratio (TEM)	1.1	1.1	1.1
S.A. (BET) / m^2 g^{-1}	26	31	34

nificant decrease in crystallite size, more so in AZO, which saw a fall from 34 nm to only 18 nm, whereas the decrease for GZO was less dramatic, only a slight decrease.

TEM images showed that the morphologies of the two dopant systems were very different; AZO (see Figure 4.2) tended to be more rod-like, and the aspect ratio increased with higher dopant level (4.9 for the 5 at% Al sample versus 3.1 for the 2.5 at% sample). Pilot scale materials, possibly due to the drastically reduced residence time, tended to be less rod-like, and as per the data summarised in Table 4.1, the average particle length was reduced from over 130 nm to only 63 nm for pilot-scale 2.5 at% AZO, with an aspect ratio of 2.0. TEM images of GZO are shown in Figure 4.3; morphology tended to be more spheroidal, with a consistent aspect ratio of 1.1 across all compositions and scales explored. Particle size, consistent with Scherrer calculations, was observed to decrease with increasing dopant level, and more so upon up-scaling of the synthetic process.

BET surface area measurements are more fully tabulated in Table 4.3; increasing the dopant level had the effect of increasing the surface area. Taken together with Scherrer and TEM analysis, the three techniques clearly show the trend of decreasing particle size with higher dopant levels, and also the effect of the pilot-scale synthesis, in the decreased particle size when synthesised at larger scale, particularly for AZO.

4.3.2.2 Compositional analysis; ICP, EDS, XPS

Of the three testing methods for compositional analysis, ICP-AES is by far the most precise and accurate.[268] By virtue of the complete dissolution in acid of the entire sample, the values (accurate to parts per million) are truly representative of the sample. EDS generally agreed with the numbers returned by ICP, and XPS tended to be notably higher, especially for AZO samples. A possible explanation for this could be that the dopants tend to be surface-segregated in the particles, entering the structure after the initial nucleation of ZnO in the reactor. As XPS is a surface-sensitive technique, this could account for the curiously high proportion of (especially Al in

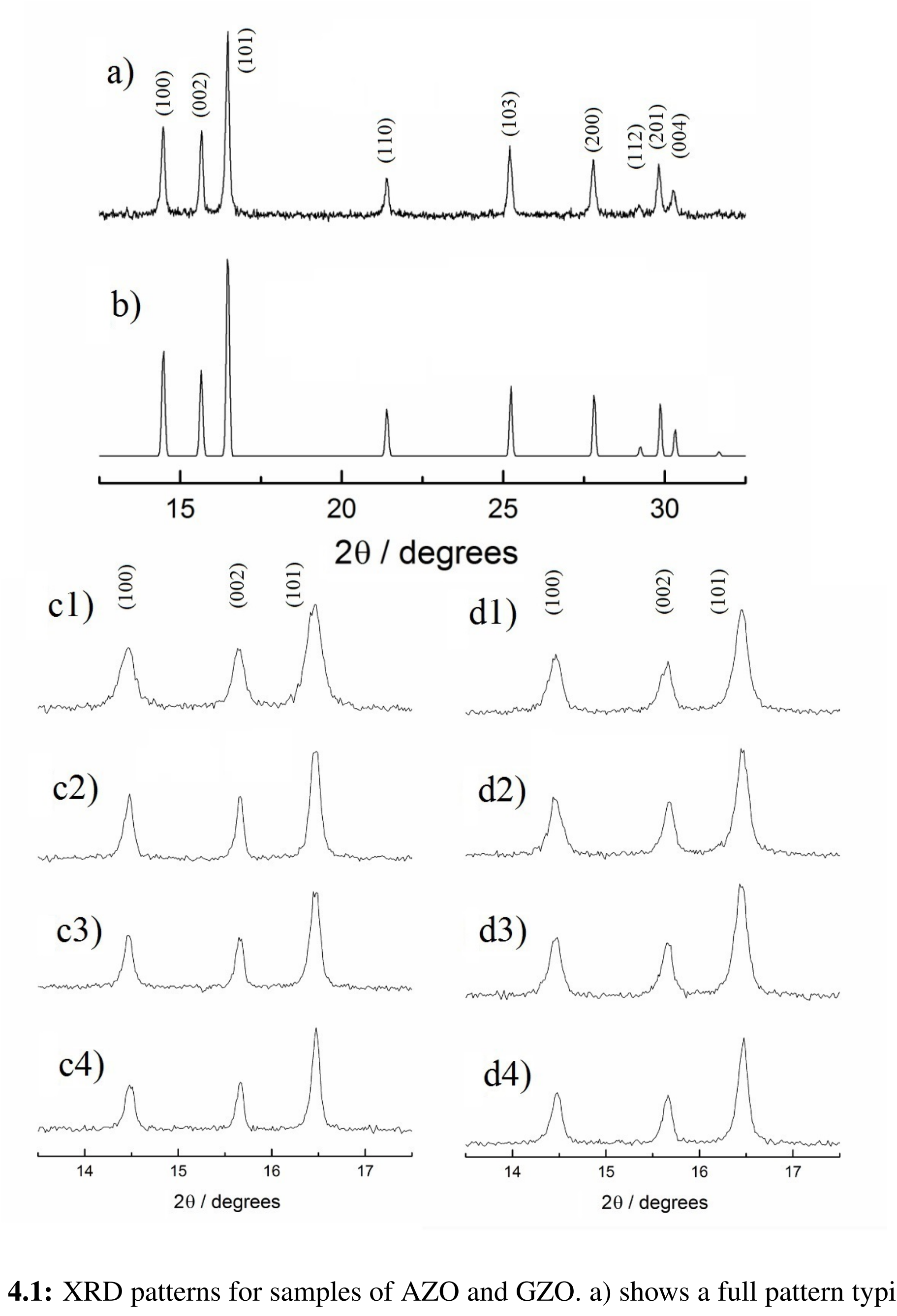

Figure 4.1: XRD patterns for samples of AZO and GZO. a) shows a full pattern typical of the zinc oxides, in this case 1.0 at% AZO. b) shows a standard ZnO pattern.[4] c1) and d1) show peaks in the range 13.5 to 17.5 ° 2θ pilot scale AZO and GZO, c2 - c4) and d2 - d4) show these same peaks for 5, 3, and 1 at% nominal dopant level for each AZO and GZO, respectively, synthesised on the laboratory scale.[5]

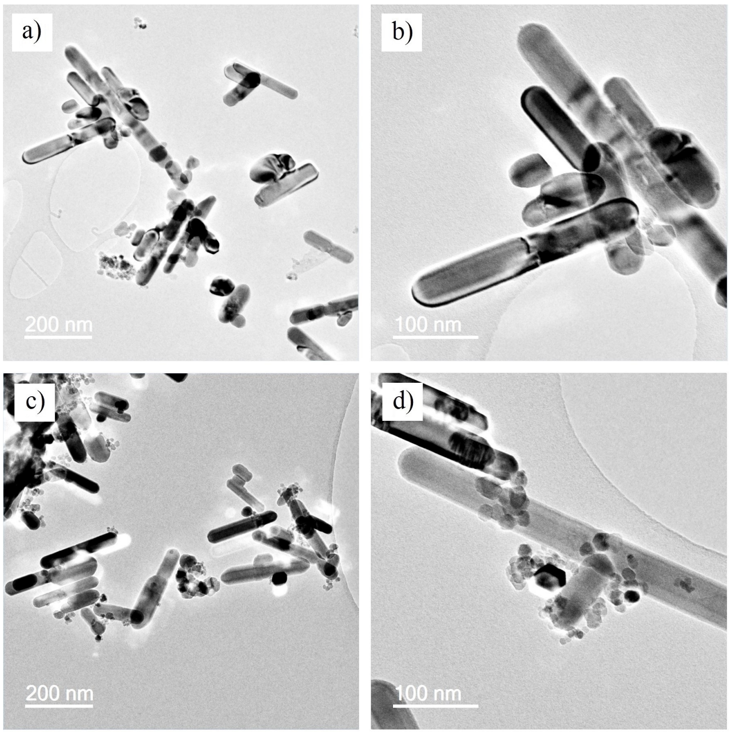

Figure 4.2: TEM images of 2.5 at% AZO (a and b), and 5.0 at% AZO (c and d) made on the laboratory scale CHFS.[5]

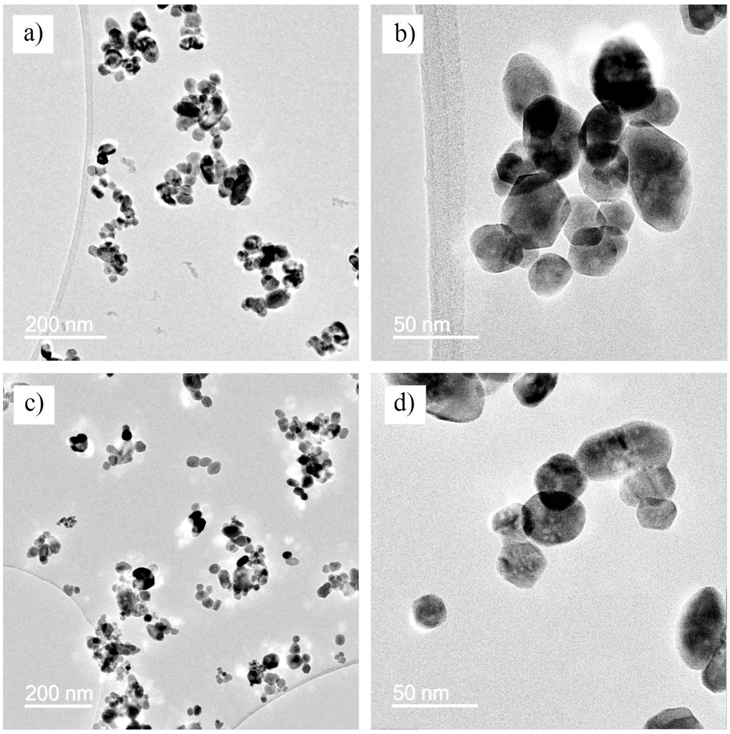

Figure 4.3: TEM images of 2.5 at% GZO (a and b), and 5.0 at% GZO (c and d) made on the laboratory scale CHFS.[5]

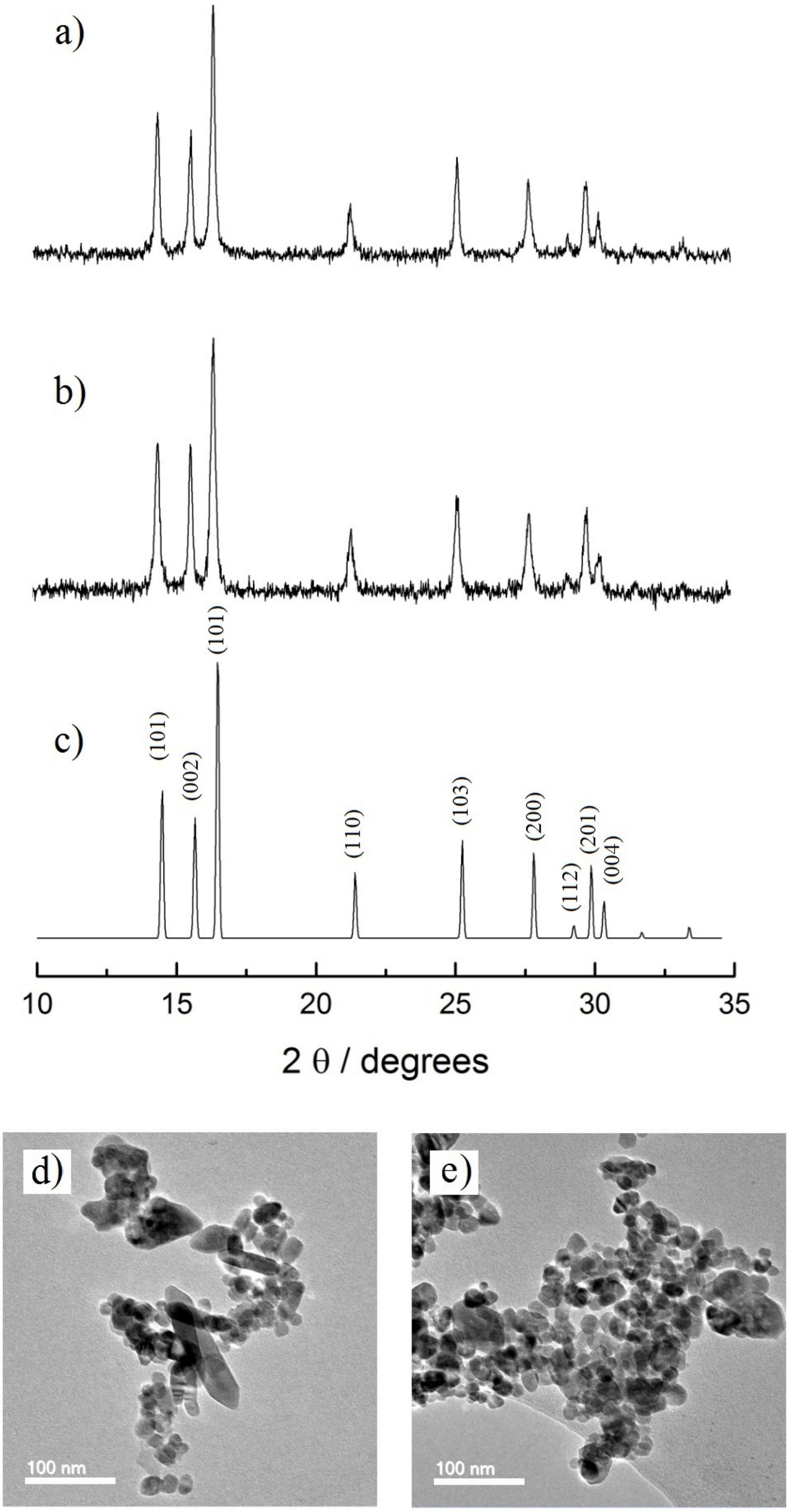

Figure 4.4: a) and b) full XRD patterns for AZO (2.5 at% Al) and GZO (3.5 at% Ga) synthesised on the pilot scale, accompanied by c) the standard reference pattern,[4] and a representative TEM image of each sample in d) and e) for AZO and GZO, respectively.[5]

Table 4.3: Summary of BET surface area data for AZO and GZO samples.

Dopant	dop / at%	Scale	BET Surface Area / m^2g^{-1}
Al	1.0	lab	19
	2.0		20
	3.0		21
	4.0		21
	5.0		22
	6.0		27
	2.5	pilot	32
Ga	1.0	lab	18
	2.0		23
	3.0		27
	4.0		29
	5.0		29
	6.0		30
	3.5	pilot	34

AZO) dopant indicated, whereas EDS and ICP are bulk analysis methods.

The indication from these three techniques is that the uptake of Al into the ZnO lattice is approximately 80% relative to the proportions nominally present in the precursor solutions, and that the uptake of Ga is closer to, or slightly over 100% (over 100% is possible due to the only 80% sample yield; evidential that a fifth of the zinc is not nucleating from solution in the reactor).

XPS data are shown in Figures 4.5 (AZO) and 4.6 (GZO). The AZO spectra indicated a single environment for each aluminium and zinc, with doublet separations of 23.1 eV and 0.4 eV, respectively, consistent with those described in the literature.[239, 241] Likewise the GZO spectra showed a single environment for each Zn and Ga, with doublet separations of 23.1 eV and 27.0 eV, respectively, also consistent with previous literature reports.[241] All high resolution scans (for specific elements) were calibrated to the 184.7 eV C 1s peak, and each set of three doped samples of AZO, and GZO, had their measurements taken in the same session, therefore it can be concluded the small shifts in binding energies were due to the differences between the doped samples themselves, not any outside effects. Consistent for both AZO and GZO are the shift in binding energy of the Zn 2p peaks, such that the laboratory and pilot scale 2.5 at% dopant synthesised materials showed a Zn 2p binding energy that was 0.3 eV lower than then analogous peak for the 5.0 at% dopant materials. Similarly, a 0.2 eV and 0.3 eV (increase) shift was seen when increasing the laboratory-scale dopant level from 2.5 to 5.0 at% for Al and Ga, respectively. It should be noted that the dopant uptake was less efficient for the pilot scale materials (with respect to the nominal dopant concentrations in the precursor solutions) than for the laboratory scale. This is likely due in part to the reduced residence time in the pilot scale process that could have had an effect on the dopant uptake efficiencies.

4.3.3 Electrical testing of discs

This section outlines the electrical testing of all of the laboratory and pilot-scale synthesised products to determine the optimal composition for lowest resistivity. Table 4.7 gives a summary of all resistivities for the various AZO and GZO samples, and the following subsections will show the trends graphically for each system.

4.3.3.1 Aluminium doped zinc oxide (AZO)

Figure 4.7 shows the resistivity trend with increasing Al-content in AZO. After an initial decline (with increasing Al) to a low resistivity of 7.0 x 10^{-3} Ω cm, the resistivity then rose again. The most conductive sample was thus the sample synthesised with 2.5 at% in the precursor solution. This trend appeared to hold on the pilot scale too, however the optimal resistivity at ca. 2.0 to 2.5 at% Al is almost an order of magnitude higher. That the trend held (i.e. a decrease to a minimum resistivity followed by a subsequent increase), implied that there is a factor at play beyond uptake efficiency (as indicated by compositional analysis); leaving a combination of the morphology, particle size, and packing of the particles as possible causes for the inferior pellets.

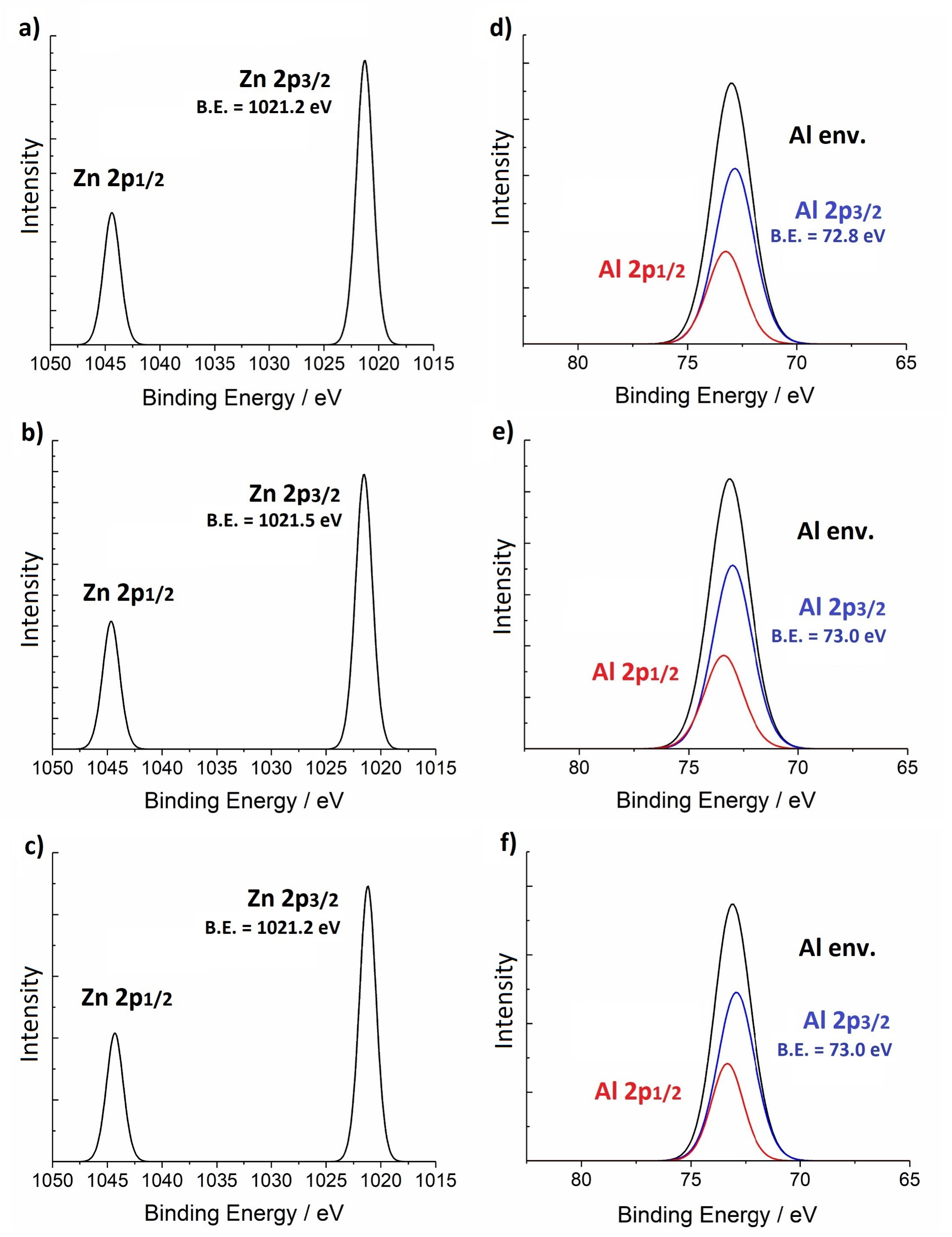

Figure 4.5: XPS spectra for the Zn 2p and Al 2p binding energy regions; a), b), and c) show the Zn 2p binding energy regions for the 2.5 at% AZO (lab scale), the 5.0 at% AZO (lab scale), and 2.5 at% AZO (pilot scale), respectively, and to the right of each is the corresponding Al 2p region, in d), e), and f), respectively.[5]

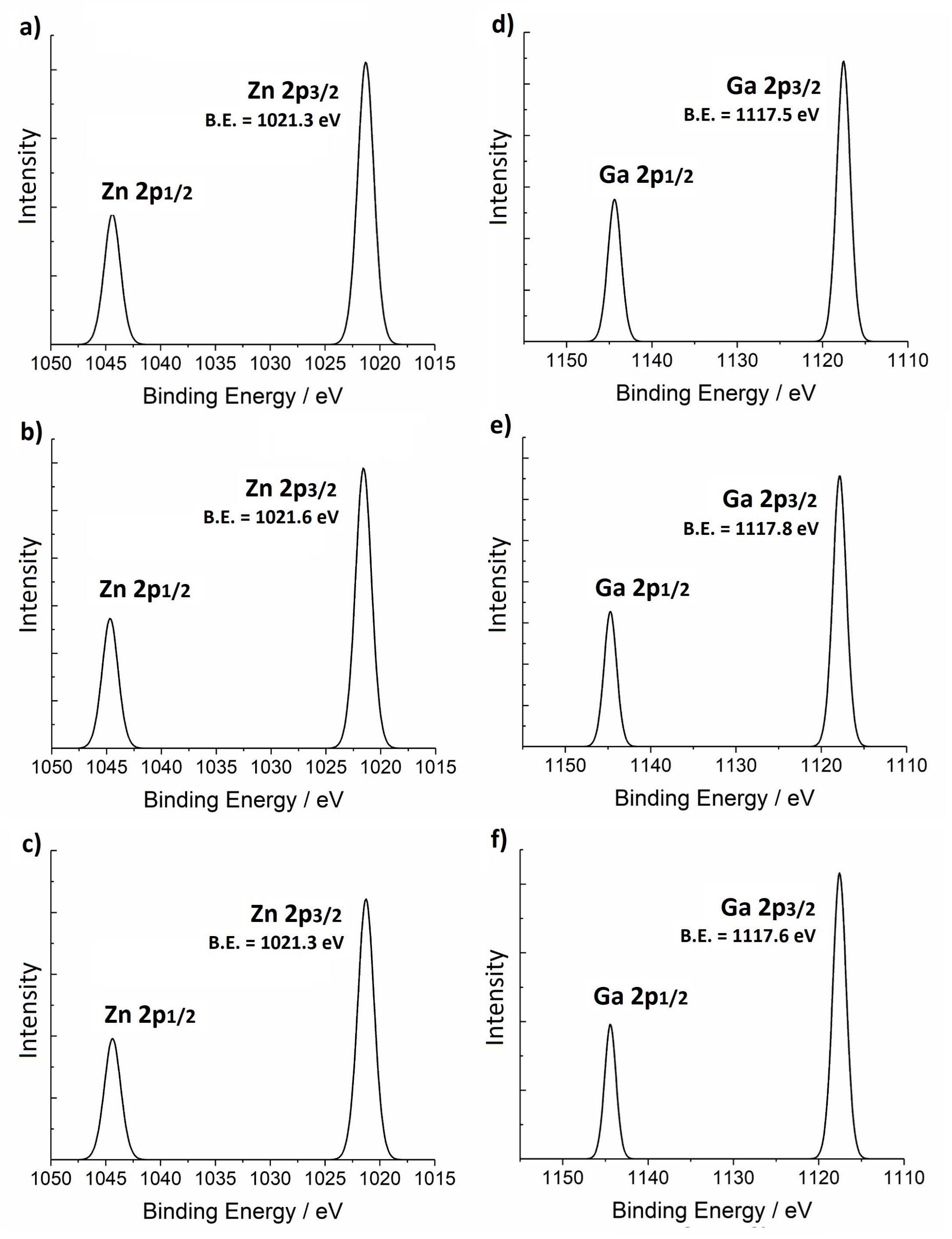

Figure 4.6: XPS spectra for the Zn 2p and Ga 2p binding energy regions; ; a), b), and c) show the Zn 2p binding energy regions for the 2.5 at% GZO (lab scale), the 5.0 at% GZO (lab scale), and 3.5 at% GZO (pilot scale), respectively, and to the right of each is the corresponding Ga 2p region, in d), e), and f), respectively.[5]

Table 4.4: Resistivity data for all of the samples, AZO and GZO, synthesised on both the laboratory and pilot scales. The three best-performing discs of each sample were measured in triplicate, and from these nine resistivity values were averages and standard deviations calculated.

Dopant	**dop / at%**	**Scale**	**Resistivity x 10^{-3} / Ω cm**
Al	0.5	lab	90.7 ± 0.3
	1.0		43.8 ± 1.7
	1.5		21.8 ± 5.3
	2.0		15.8 ± 4.6
	2.5		7.0 ± 3.7
	3.0		22.6 ± 5.9
	3.5		43.7 ± 9.4
	4.0		43.4 ± 16.8
	4.5		47.3 ± 4.3
	5.0		61.2 ± 12.8
	5.5		57.9 ± 3.0
	6.0		95.5 ± 24.7
	1.0	pilot	861.7 ± 0.2
	2.0		60.6 ± 1.0
	2.5		77.2 ± 0.8
	3.5		229.9 ± 5.1
Ga	0.5	lab	33.0 ± 0.1
	1.0		26.1 ± 0.1
	1.5		17.2 ± 0.6
	2.0		21.1 ± 1.5
	2.5		16.8 ± 1.7
	3.0		14.1 ± 6.7
	3.5		9.1 ± 3.1
	4.0		17.4 ± 4.6
	4.5		15.6 ± 5.1
	5.0		13.4 ± 4.2
	5.5		11.7 ± 0.6
	6.0		11.9 ± 1.5
	2.0	pilot	494.2 ± 5.1
	3.0		236.0 ± 0.3
	3.5		47.5 ± 0.3
	4.5		13.0 ± 0.3

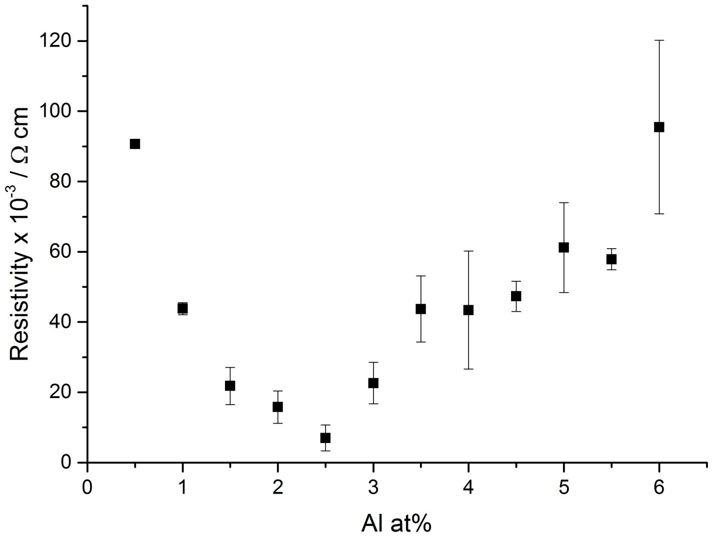

Figure 4.7: Resistivity trend in laboratory scale CHFS-made AZO as tested by Hall Effect measurements on pressed, heat treated discs. Error bars represent the standard deviation in the values.[5]

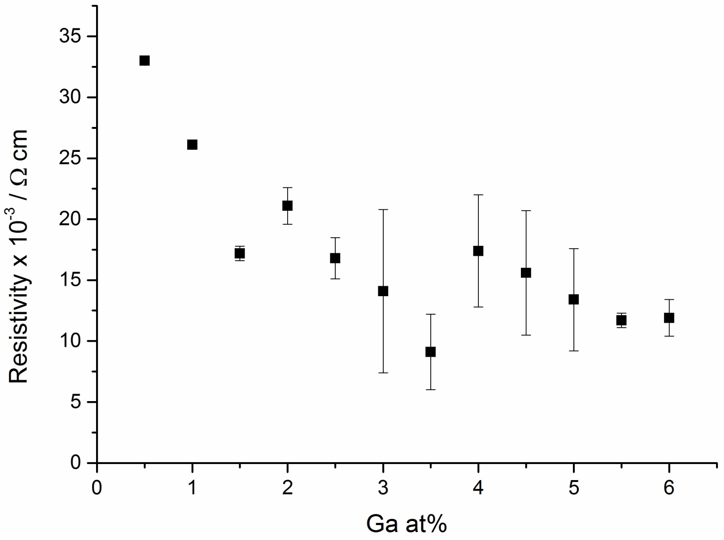

Figure 4.8: Resistivity trend in laboratory scale CHFS-made GZO as tested by Hall Effect measurements on pressed, heat treated discs. Error bars represent the standard deviation in the values.[5]

4.3.3.2 Gallium doped zinc oxide (GZO)

Figure 4.8 shows the resistivity trend with increasing Ga content in GZO. As with AZO, increasing dopant level causes the resistivity to decrease to a minimum of 9.1 x 10^{-3} Ω cm (at 3.5 at% Ga), however unlike with the AZO trend, the subsequent increase in resistivity was not observed. Within error, the resistivity remained approximately constant from 3.5 at% Ga upwards, implying that though additional Ga was not contributing to higher conductivity, neither was it particularly conductivity-inhibiting at the dopant levels being investigated. This was further observed on the pilot scale, wherein increasing the dopant level reduced the conductivity, until by 4.5 at% the resistivity of the pilot-scale powder was 1.3 x 10^{-2} Ω cm, comparable to the laboratory scale material.

4.3.4 Conclusions: AZO

Doping of Al into ZnO was successful; up to 6.0 at%, only a single phase was identified by XRD, and only a single environment was observed for each Zn 2p and Al 2p orbital binding energies. Increasing the dopant level promoted growth along the c-axis, resulting in increasingly rod-like morphology.

The optimal composition as determined by pressing the powder samples into discs and heat treating, pointed to the 2.5 at% AZO sample as being consistently the most conductive. Higher resistivity was observed with both higher and lower dopant levels, above the optimal 7.0 x 10^{-3} Ω cm. This value was close to that of 6.0 x 10^{-3} Ω cm obtained by ITO as synthesised using the same CHFS process,[168] demonstrating the promise of AZO as an ITO replacement material for TCOs. Up-scaling of the synthesis to 330 g h^{-1} resulted in a deterioration of the electrical properties by almost a factor of 10. Rod-like behaviour decreased, as did particle size and dopant uptake, however as the trend observed on the laboratory scale appeared largely to be consistent on the pilot scale (though with fewer data points), the explicit cause of this remains unknown. The most likely reasons could include differences in particle size, packing and agglomeration, altering the resistance of the pellets when pressed.

4.3.5 Conclusions: GZO

Doping of Ga into ZnO was successful; up to 6.0 at% Ga, only a single phase was identified by XRD, and only a single environment was observed for each Zn 2p and Ga 2p orbital binding energies from XPS data. Increasing the dopant level did not alter the morphology, but did decrease particle size. The optimal composition as determined by pressing the powder samples into discs and heat treating, pointed to the 3.5 at% GZO sample as being consistently the most conductive. Higher resistivities were observed with both higher and lower dopant levels, above the optimal 9.1 x 10^{-3} Ω cm. This was also close to the 6.0 x 10^{-3} Ω cm obtained by ITO as synthesised using the same process and the 7.0 x 10^{-3} Ω cm seen in AZO, demonstrating the promise of GZO as an ITO replacement TCO material as made by CHFS. Up-scaling of the synthesis to 330 g h^{-1} resulted in a minor deterioration of the electrical properties, and a shift in the trend to the optimal nominal dopant level (in the precursor solutions) increasing from 3.5 at% to 4.5 at%.

4.4 AGZO: Aluminium and Gallium co-doped Zinc Oxide

4.4.1 Experimental design and observations

The high-throughput set-up was used as described in Section 2.2.3. Twenty compositions were investigated, between 1.0 and 5.0 at% total dopant level, with dopant increments of 0.5 at%. The following naming convention is in use in this section: each sample has been designated (x,y)AGZO, such that x and y are the nominal dopant concentrations in the precursor solutions of Al and Ga, respectively. Thus the sample (1,2)AGZO is the sample made with 1 at% Al, 2 at% Ga, and 97 at% Zn in the precursor solution.

In keeping with the high-throughput nature of the experiment, higher concentration precursor solutions were used than in the previous AZO and GZO experiments; metal concentration, [metal], was 0.5 M, and [KOH] was 1.0 M. 100 mL of each precursor solution was used, such that the 400 mL collected was set to contain approximately 4 g of each sample as dried powder product. Consistent with the observations from the previous AZO and GZO syntheses, increasing the dopant level increased the intensity of the yellow colour in the product slurry and powders, and higher Ga samples had a visibly more intense colour than those with low Ga. Products were collected in $> 80\%$ yield, consistent across the compositional space explored. As with AZO and GZO samples previously, AGZO samples required three cleaning steps in deionised water (as described in Section 2.2.5) before freeze-drying could be carried out. Again, the yellow powders were pressed into green discs, which turned blue upon heat treatment in a reducing atmosphere.

Powder X-ray diffraction (pXRD), transmission electron microscopy (TEM), X-ray photoelectron spectroscopy (XPS), Brunauer-Emmett-Teller (BET) measurements, and inductively coupled plasma atomic emission spectroscopy (ICP-AES) were used to characterise six representative powder samples across the compositional space; (0.5,1.5)AGZO, (1.5,0.5)AGZO, (1,2)AGZO, (2,1)AGZO, (1,3)AGZO, and (3,1)AGZO. Hall Effect measurements (see Section 2.4) were used to determine the electrical properties of all the samples as pressed, heat treated discs.

4.4.2 Physical characterisation; XRD, TEM, ICP and BET

All samples were phase-pure Wurtzite ZnO structure by XRD, as shown in Figure 4.9, and demonstrated broadly similar morphologies as can be seen from representative TEM images in Figure 4.10. Particle size and composition information are summarised in Table 4.5; Scherrer analysis indicated a slight decrease in crystallite size from 17 nm to 16 nm for 4 at% total dopant level, and the mean particle size by TEM image analysis correspondingly showed a slight decrease from 26 nm for 2 at% and 3 at% total dopant level to 23 nm for 4 at% total, and the aspect ratio was consistent across all samples at 1.2 ($\pm$ 0.3). Finally, the BET surface area was also consistently for all samples, around 38 $m^2 g^{-1}$, rising up to 40 $m^2 g^{-1}$ for the highest total dopant level. The similarity across the compositional space implies that any changes observed in the electrical properties of the materials are most significantly due to the compositional differences.

Dopant uptake efficiency was between 70-100 % as indicated from ICP analysis,

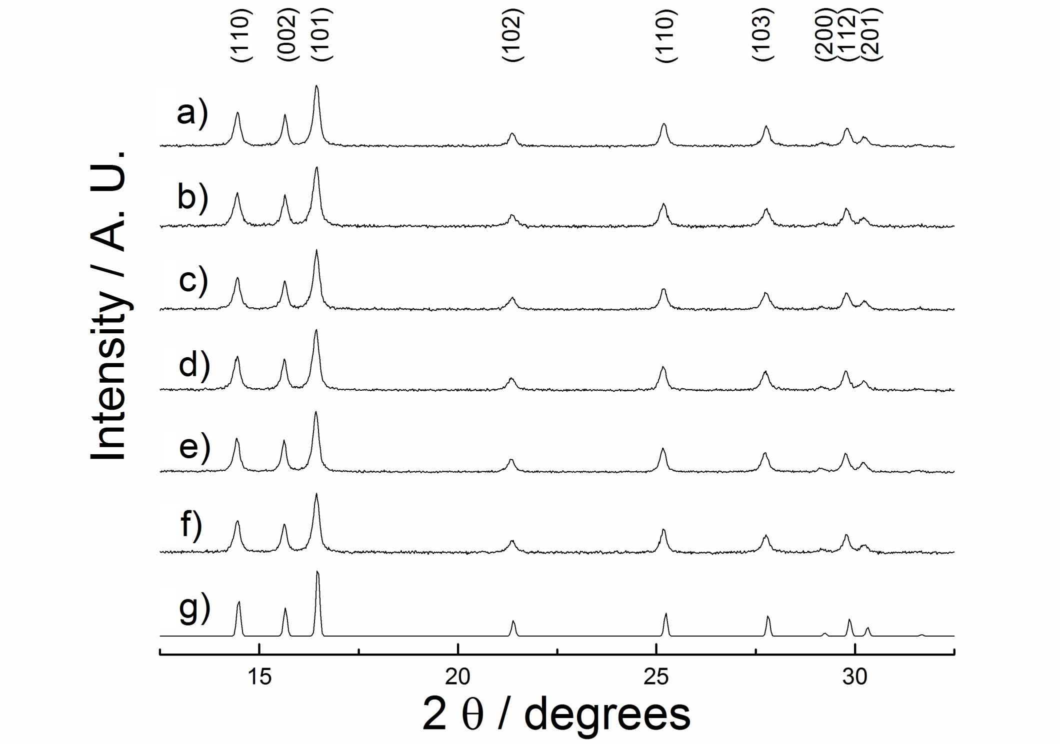

Figure 4.9: XRD data for the six representative AGZO samples, including a) (3,1)AGZO, b) (1,3)AGZO, c), (2,1)AGZO, d) (1,2)AGZO, e) (1.5,0.5)AGZO, f) (0.5,1.5)AGZO, and g) a ZnO reference pattern.[4, 6]

Table 4.5: Physical characterisation data for the six representative samples, including Scherrer calculated crystallite size, mean particle size as calculated from TEM images (300 particles analysed), and BET surface areas.

Sample / Al,Ga	**Scherrer size / nm**	**Mean length (TEM) / nm**	**BET surface area / m^2 g^{-1}**
0.5,1.5	17	26 ± 12	38
1.5,0.5	17	26 ± 16	38
1,2	17	26 ± 12	38
2,1	17	25 ± 12	39
1,3	16	23 ± 10	40
3,1	16	23 ± 10	40

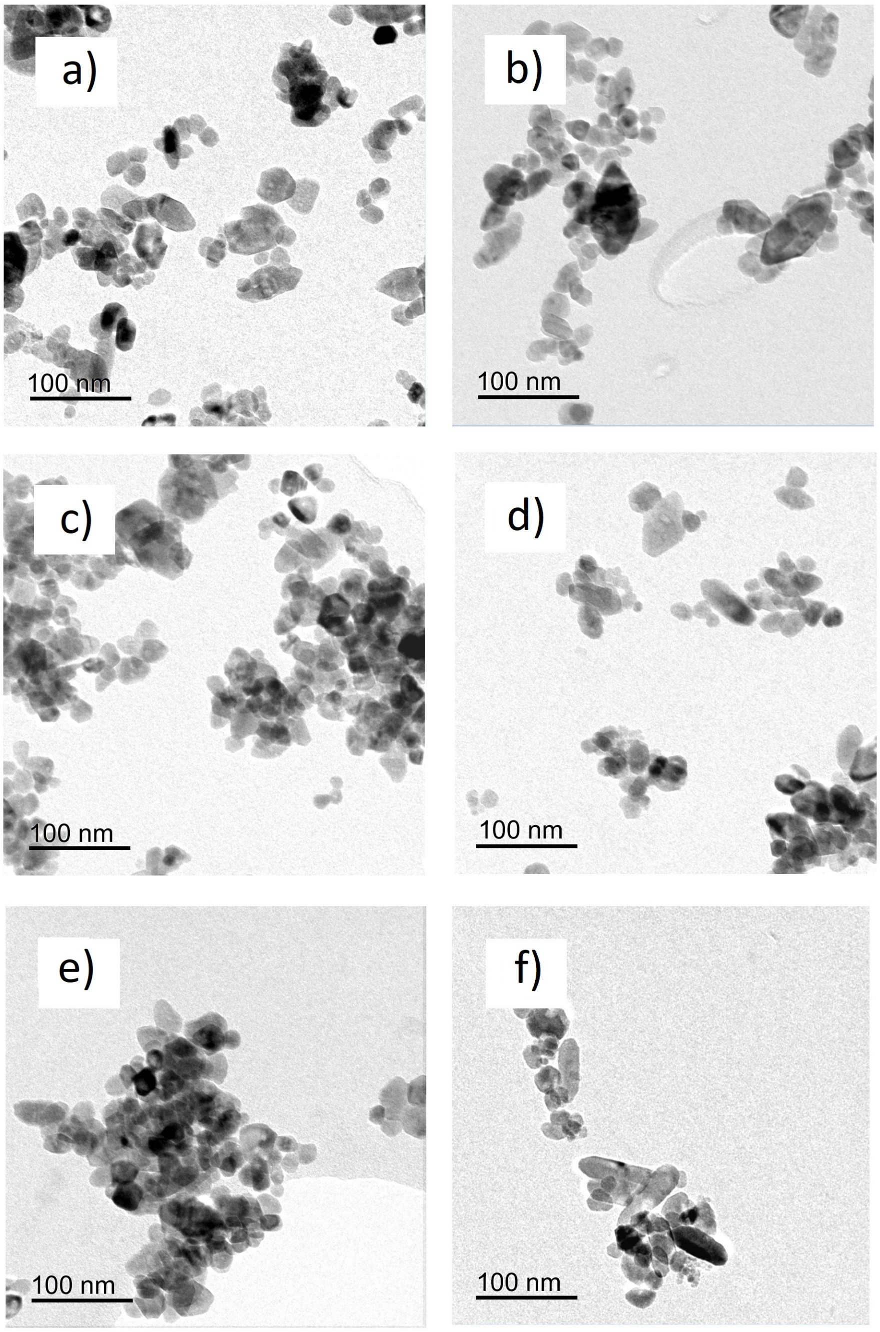

Figure 4.10: TEM images for the six representative AGZO samples, including a) (0.5,1.5)AGZO, b) (1.5,0.5)AGZO, c) (1,2)AGZO, d) (2,1)AGZO, e) (1,3)AGZO, and f) (3,1)AGZO.[6]

Table 4.6: Compositional information as determined by ICP-AES data, in the form of relative atomic percentages of each Zn, Al, and Ga.

Sample / [Al,Ga]	Zn / at%	Al / at%	Ga / at%
0.5,1.5	98.4	0.5	1.1
1.5,0.5	98.6	1.1	0.3
1,2	97.8	0.8	1.3
2,1	97.9	1.4	0.7
1,3	96.6	0.9	2.5
3,1	96.9	2.3	0.8

with lower nominal dopant levels returning proportionally higher uptake. Precise compositional figures are detailed in Table 4.6 as determined by ICP-AES analysis.

4.4.3 Electrical characterisation

Details of the resistivities of all the samples are summarised in Table 4.7, and displayed visually as a point map in Figure 4.11 (as conductivities), and as a resistivity contour map in Figure 4.12. In both cases, data for the singularly doped AZO and GZO systems was included for the added context and data points.

Thus away from the edges of the plots there were three 'islands' of low resistivity, with (1.0,2.0)AGZO, (2.0,2.0)AGZO, and (3.0,1.0)AGZO measuring resistivities of 9.1 x 10^{-3} Ω cm, 9.3 x 10^{-3} Ω cm, and 9.4 x 10^{-3} Ω cm, respectively. These all significantly reduced the material cost versus GZO (by almost halving the Ga contingent, by far the most expensive component), while retaining almost identical resistivities.

4.4.4 Conclusions

AGZO was synthesised by high-throughput CHFS up to 5 at% total dopant level. Physical characterisation revealed minimal variation across the compositional space explored in terms of particle size, surface area and morphology, indicating that changes seen in the electrical properties were primarily due to the elemental compositions. These, as measured by ICP-AES, indicated a good dopant uptake $> 70\%$

Table 4.7: Resistivity data for all of the (x,y)AGZO samples synthesised in this investigation. Emboldened are the three samples that measured a mean below 1 x 10^{-2} Ω cm.

Sample / (x,y)AGZO	**Resistivity x 10^{-3} / Ω cm**
(0.5,0.5)AGZO	32.5 ± 0.3
(0.5,1.5)AGZO	41.9 ± 0.4
(1.0,1.0)AGZO	33.9 ± 0.5
(1.5,0.5)AGZO	35.6 ± 0.4
(0.5,2.5)AGZO	11.4 ± 7.0
(1.0,2.0)AGZO	**9.1 ± 3.6**
(1.5,1.5)AGZO	31.9 ± 0.6
(2.0,1.0)AGZO	35.2 ± 0.4
(2.5,0.5)AGZO	50.5 ± 0.4
(0.5,3.5)AGZO	21.6 ± 0.3
(1.0,3.0)AGZO	16.2 ± 0.2
(1.5,2.5)AGZO	23.8 ± 0.6
(2.0,2.0)AGZO	**9.3 ± 2.3**
(2.5,1.5)AGZO	20.7 ± 8.1
(3.0,1.0)AGZO	**9.4 ± 7.7**
(3.5,0.5)AGZO	52.9 ± 0.3
(0.5,4.5)AGZO	43.4 ± 0.4
(1.0,4.0)AGZO	20.6 ± 0.1
(1.5,3.5)AGZO	20.7 ± 1.1
(2.0,3.0)AGZO	22.4 ± 3.2

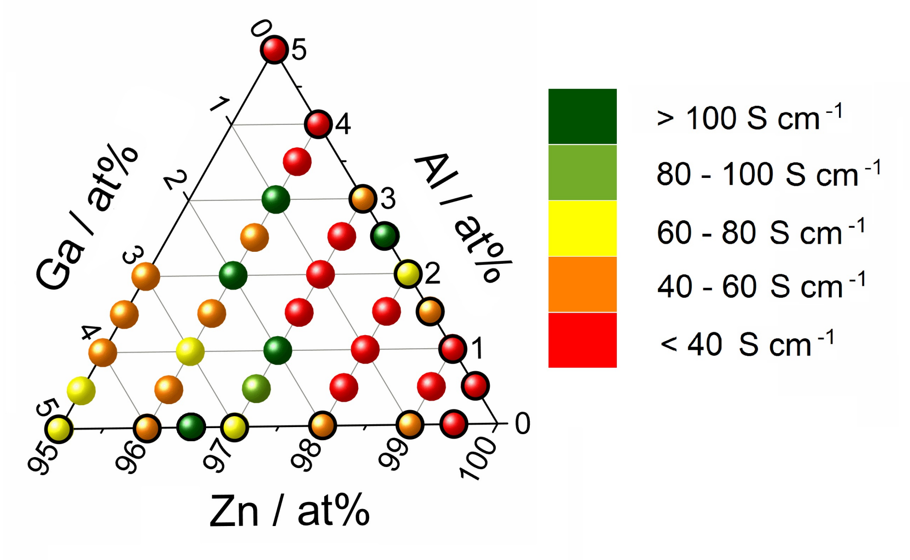

Figure 4.11: Colour point map of the conductivity of the AGZO compositional space explored. Black encircled data points are from AZO and GZO. Green represents high conductivity, and red represents low conductivity. The bottom right apex represents 100 at% Zn, the top apex represents 5 at% Al and 95 at% Zn, and the bottom left apex represents 5 at% Ga and 95 at%.[5, 6]

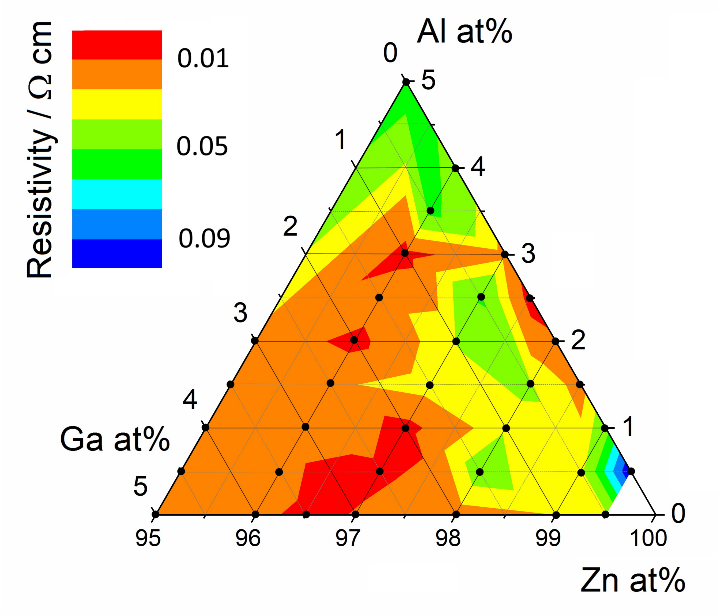

Figure 4.12: Resistivity data ternary contour plot, including several AZO and GZO samples. Data points are marked with a black spot, and the contour is generated using Origin Pro's probability algorithm, wherein red represents the lowest resistivity, and blue the highest. The bottom right apex represents 100 at% Zn, the top apex represents 5 at% Al and 95 at% Zn, and the bottom left apex represents 5 at% Ga and 95 at% Zn.

relative to the nominal precursor solution concentrations, and Hall Effect measurements determined three samples that obtained low resistivities < 1 x 10^{-2} Ω cm; (1.0,2.0)AGZO, (2.0,2.0)AGZO, and (3.0,1.0)AGZO measured resistivities of 9.1 x 10^{-3} Ω cm, 9.3 x 10^{-3} Ω cm, and 9.4 x 10^{-3} Ω cm, respectively, comparable to the singularly doped GZO (9.1 x 10^{-3} Ω cm at 3.5 at% doping level), but not quite as conductive as the best AZO sample (7.0 x 10^{-3} Ω cm).

4.5 Overall Conclusions for AZO, GZO, and AGZO

AZO, GZO, and AGZO were synthesised by CHFS with varying dopant levels in order to determine the optimal composition in terms of electrical conductivity. This was tested by pressing each sample into a pellet and heat treating in a reducing atmosphere, and reproducibility ensured by the pressing of multiple pellets, with multiple readings taken for each pellet before calculating the average and standard deviations. The optimal compositions of each laboratory-scale synthesised (production rate of 60 g h^{-1}) material were as follows: AZO with 2.5 at% Al yielded an average resitivity of 7.0 x 10^{-3} Ω cm, while GZO with 3.5 at% Ga, and AGZO with 1 at% Al and 2 at% Ga both yielded an average resistivity of 9.1 x 10^{-3} Ω cm.

Physical analysis by XRD, BET, and TEM indicated a decrease in particle size with increasing nominal dopant levels in the precursor solutions. Furthermore, colour change and the onset of conductivity in the doped samples relative to un-doped ZnO initially implied that successful doping into the ZnO structure was taking place. These, when taking also into account the single phase observed by XRD, the single environments for the Zn 2p, Al 2p, and Ga 2p XPS peaks, and the compositional analysis by both XPS and ICP, were strongly evidential that these materials, though not in themselves novel, had been synthesised for the first time by CHFS.

For comparison of the electrical properties, the optimal composition of ITO (made with 10 at% Sn) synthesised and tested by the same methods, had a resistivity of 6.0 x 10^{-3} Ω cm.[168] Thus each of the optimal compositions of each AZO, GZO, and AGZO had resistivities very close to that of ITO, indicating their promise as conducting oxide materials when synthesised by CHFS.

Chapter 5

Si Doped and Co-Doped Zinc Oxide for Transparent Conducting Oxides

5.1 Aims

After AZO and GZO, the next most promising system with respect to conductivity was silicon-doped zinc oxide (SZO, or SiZO). The aim of this chapter is thus to investigate the compositional optimisation of SiZO as synthesised by continuous hydrothermal flow synthesis (CHFS), as well as subsequent up-scaling to the pilot-scale CHFS. The effect of co-doping SiZO with either aluminium or gallium is also investigated. In addition to the electrical testing, characterisation including XRD, BET, TEM, XPS, and ICP-AES is also discussed, to gauge the effect that the different dopant ratios have on the properties of the materials.

5.2 Introduction

Silicon is a tetravalent ion, i.e. Si^{4+}, thus when it is present as $Si_{Zn}^{\bullet\bullet}$, as a substitutional defect on a zinc site, it will donate two electrons rather than the single electron donated by trivalent dopant cations such as Al or Ga. Additionally, Si^{4+} is considerably smaller than Zn^{2+}; their ionic radii are 0.26 $\mathring{A}$ and 0.60 $\mathring{A}$, respectively.[245] This has a number of effects; the high charge concentration means that silicon in SiZO will draw oxygen anions to it more effectively than trivalent cation dopants would, and indeed more strongly than the Zn^{2+} in the lattice. Each acts as a point defect, and perturbs the Zn ions closest to it in the Zn plane, generating localised planar defects.[269] This, coupled with the two electrons (charge carriers) contributed by each Si_{Zn} mean that as dopant level increases, the conductivity will be significantly hampered by scattering effects in the lattice, inhibiting carrier mobility, thus the optimally conductive composition of SiZO should have a lower dopant level than seen for AZO, GZO or AGZO.[270] Additionally, upon over-saturation of Si into ZnO, one would expect to see the appearance of additional phases due to the strain on the lattice that the Si ions cause.[269, 270]

Silicon itself is a highly desirable element for incorporation in a ZnO-based TCO film due to a number of factors; comparatively little is needed relative to the equivalent trivalent-doped systems, silicon is highly earth abundant and accessible (second most abundant element in the Earth's crust after oxygen),[271] and has neither the chemical stability issues of AZO, nor the high costs associated with gallium in GZO.[272, 273]

The first calculations on SiZO were carried out by Körner and Elsässer in 2011,[270] to which the conclusion was that substitution of Si onto the Zn sites in the lattice was by far the preferential doping mechanism. Though interstitial silicon was not addressed in that study, in subsequent work by Wu et al.[274] it was shown that Si in either the octahedral or tetrahedral interstitial site has too high a formation energy, at least double that of the substitutional Si_{Zn}, thus the substitutional defect is formed upon Si-doping into ZnO.

Few studies exist in literature in which SiZO thin films are generated and fully characterised in the context of application as TCOs, i.e. with optical and electrical characterisation in tow. That said, from the studies that have been carried out, competitive resistivities, carrier concentrations, charge carrier mobilities, and transmittance properties have been achieved. SiZO thin films have been made by several techniques, including CVD,[275] spray pyrolysis,[276, 277] pulsed laser deposition (PLD),[136, 208, 278] and magnetron sputtering.[134, 147, 279] Of these, sputtered films were the most transmissive, at 90%[134] and 94.5%[147], but PLD and spray pyrolysis techniques also garnered films with $> 80\%$ transmittance across the visible range. The seminal work by Minami et al.[135] was also the first to reach the order of 10^{-4} Ω cm, but many published sputtering and PLD studies managed to match this feat.[134, 136, 147, 208, 278, 279] For a detailed summary of a selection of SiZO thin films deposited by various methods in literature, see Table 6.5 in Chapter 6.

Though thin films are typically formed by sputtering, the material in the target needs first to be synthesised, in which case the ZnO would most likely have been synthesised by one of three methods:[112, 160, 264, 265]

- The French (or Indirect) process, wherein metallic zinc is melted in a crucible and vapourised (around 1000 °C), at which point the Zn vapour reacts with oxygen in the air to form ZnO.
- The American (or Direct) process, wherein impure minerals, ores, or composites of zinc undergo carbothermal reduction by heating with a carbon source such as anthracite to produce the zinc vapour, at a similarly high temperature to the French process.
- Wet chemical processes, wherein zinc precursor solutions are used to precipitate the carbonate or hydroxide, which is converted to the oxide by calcining (typically ca. 800 °C).

In order to generate a sputtering target, these materials would need to undergo a further annealing step as above, likely also $>$1000 °C.

The silicon source could take the form of a single crystal wafer (typical for PLD)[208], or could be used in the form of SiO_2, which could be made top down (it exists in nature as quartz) or bottom-up in the laboratory by a vast number of methods, for example by acidification of solutions of sodium silicate to form a silica gel, then washing, drying, and dehydrating of the gel to form microporous silica; by this method annual global production of silica has exceeded 1 billion kg.[280, 281] In order to generate a sputtering target, these materials would need to undergo a further annealing step as above, likely also $>$1000 °C.

Benefits of Continuous Hydrothermal Flow Synthesis (CHFS) over more conventional synthesis processes are fully discussed in Section 1.4 of Chapter 1. In brief, CHFS should be able to directly deliver ZnO or doped ZnO by a purely hydrothermal (i.e. water as the only solvent) process at much lower temperatures than those processes mentioned above. Before the studies outlined in this chapter, no such had been carried out investigating silicon doping or co-doping into zinc oxide by CHFS.

5.3 SiZO: Laboratory and Pilot Scale Synthesis

This section outlines the investigation into SiZO synthesised on the laboratory (60 g h^{-1}) and pilot (300 g h^{-1}) scales, i.e. the compositional optimisation by means of physical and electrical characterisation.

5.3.1 Experimental design

Initially, a 3-pump, single mixer laboratory-scale CHFS set-up was used (see Experimental chapter, section 2.2.1). With a total [Zn + Si] concentration of 0.3 M (Zn supplied by pump P2, Si supplied by the base feed in pump P3), and pump flow rates of 80, 40, and 40 mL min^{-1} for pumps P1, P2, and P3, respectively, 8 g of product was expected in a collection volume of 1.2 L. Base (KOH) concentration was maintained at twice the [Zn + Si] concentration, 0.6 M, in the feed supplied by pump P3.

Optimal Si dopant level was anticipated to be lower than that of Al or Ga due to the scattering affects alluded to in section 5.2; as such, concentrations of 0.25, 0.5, 1.0, 1.5, 2.0, 2.5, and 3.0 at% Si were investigated. Increasing the Si level had no visible effect on the powders, which remained white for all samples, and the yield remained fairly constant at ca. 79% (± 3%). As seen for AZO, GZO, and AGZO, and as detailed in Section 2.2.5, all samples required three rounds of washing and centrifugation before the supernatant measured negligible conductivity. Powders were still white upon freeze-drying, and remained so after pressing into discs and the subsequent heat treatment.

The optimal composition of 0.25 at% Si was scaled up to the pilot scale CHFS process, with the [Zn + Si] concentration set to 0.5 M and the base (KOH) set to 0.8 M, with flow rates increased to 400, 200 and 200 mL min^{-1} for pumps P1, P2, and P3, respectively, resulting in a production rate (taking yield into account) of at least 300 g h^{-1}.

Powder X-ray diffraction (pXRD), transmission electron microscopy (TEM), X-ray photoelectron spectroscopy (XPS), Brunauer-Emmett-Teller (BET) measurements, and inductively coupled plasma atomic emission spectroscopy (ICP-AES) were used to characterise the powder samples, and Hall Effect measurements were used to determine the electrical properties of the samples as pressed, heat treated discs.

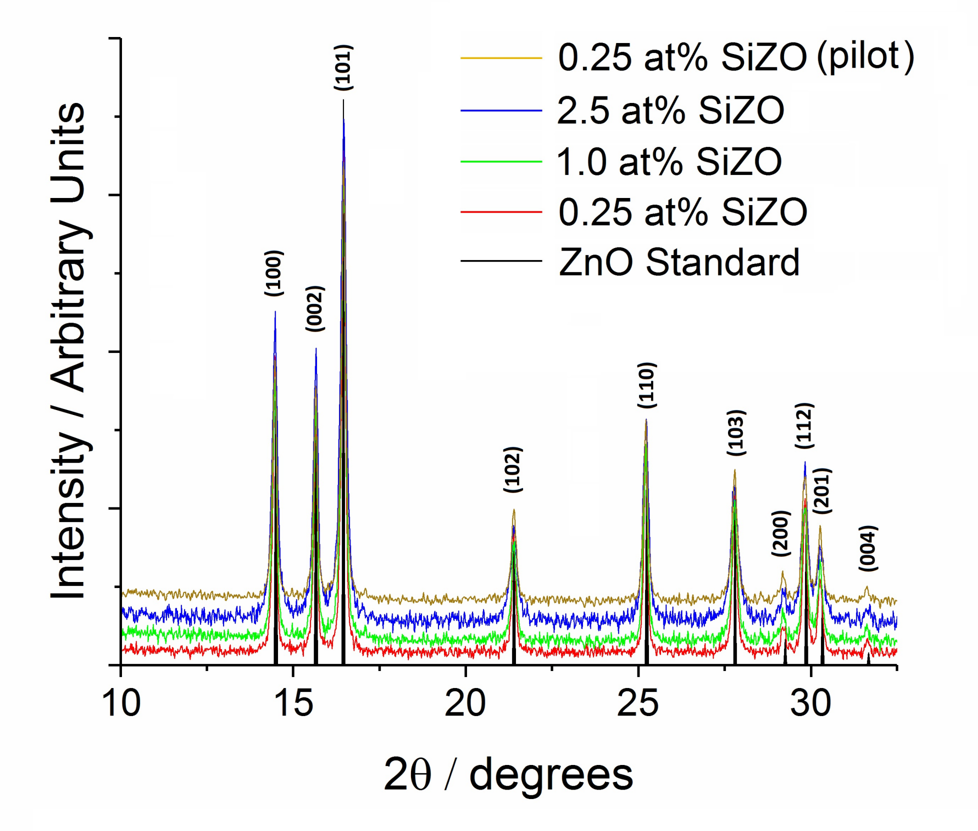

Figure 5.1: XRD patterns of silicon-doped zinc oxide, including samples with 2.5 at% Si (blue), 1.0 at% Si (green), 0.25 at% Si (red for lab-scale and gold for pilot-scale), and a standard ZnO pattern (black).[4, 7]

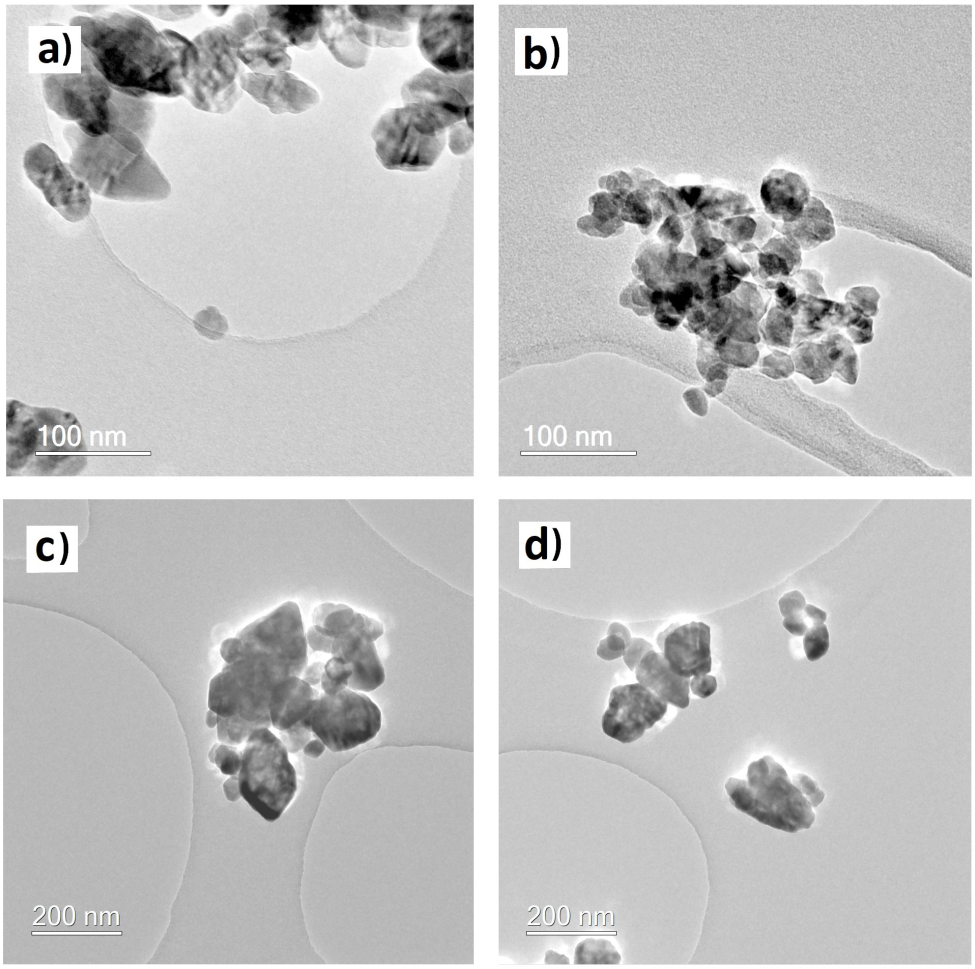

Figure 5.2: TEM images of various SiZO samples as follows: a) and c) show 0.25 at% Si made on the laboratory and pilot scales, respectively, b) shows 2.5 at% Si, and d) shows 1.0 at% Si.[7]

5.3.2 Physical characterisation of SiZO samples

XRD patterns are shown in Figure 5.1 for 0.25 at% Si (laboratory and pilot scale), as well as laboratory scale 0.5, 1.0, and 2.5 at% Si, including a reference pattern for ZnO.[4] As expected, all samples showed phase-pure Wurtzite ZnO structure, though with increasing dopant level, the degree of crystallinity appears (from the noise level in the background) to decrease slightly. A summary of BET, Scherrer analysis, and TEM image analysis for these samples is included in Table 5.1. These indicate that inclusion of a very low (0.25 at%) level of silicon increases the particle size relative to un-doped ZnO, but that further increase results in the particle size decreasing as seen for other systems previously investigated. TEM images are

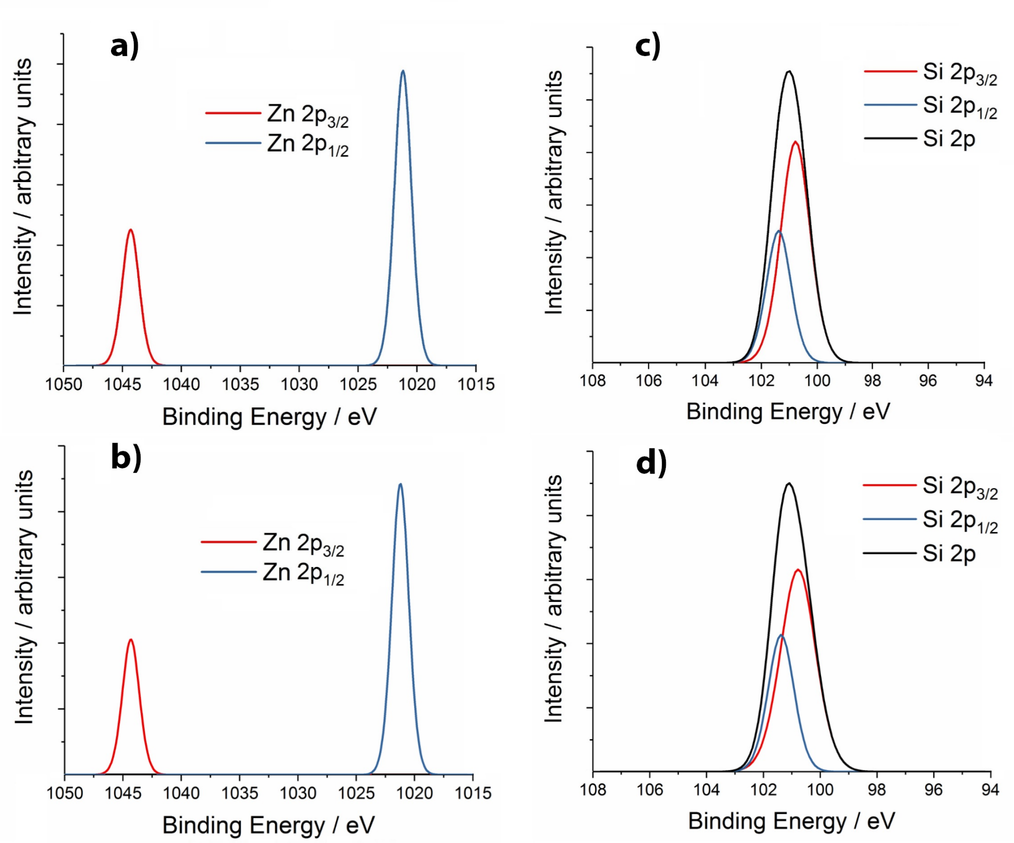

Figure 5.3: XPS spectra for a) and b) the Zn 2p binding energies for the 1.0 and 2.5 at% SiZO samples, respectively, and c) and d) the Si 2p binding energies for the 1.0 and 2.5 at% SiZO samples, respectively, as synthesised using the laboratory scale CHFS.[7]

shown in Figure 5.2; the morphology of the particles was spheroidal with a propensity towards being diamondoid, with higher-Si samples considerably narrowing the particle size distribution. The size decrease was from 83 nm mean particle length for the 0.25 at% Si sample down to 34 nm for the 2.5 at% Si sample, and up-scaling to the pilot scale process resulted in a much smaller decrease in size, from 83 nm to 68, though with a similarly large standard deviation.

Quantitative analysis of XPS spectra of the samples gave a composition of 0.9 and 2.2 at% Si for the nominally 1.0 and 2.5 at% Si samples, respectively, indicated approximately a 90% uptake of the dopant relative to the nominal proportion of Si to Zn in the precursor solutions. XPS spectra for the Zn 2p and Si 2p regions are shown in Figure 5.3 for the 1.0 and 2.5 at% Si-doped samples. Each of the doublets indicates a single environment for each Zn and Si, with the $2p_{3/2}$ peak appearing at

Table 5.1: Summary of characterisation information on 0.25 at% (laboratory and pilot scale), 1.0 at%, and 2.5 at% Si-doped ZnO, including the BET surface area, particle size as calculated using the Scherrer method, and mean particle length and aspect ratio from 300 particles from TEM image analysis.

Sample	**Scherrer size / nm**	**Mean length (TEM) / nm**	**Aspect ratio**	**BET surface area / m^2g^{-1}**
0.25 at% Si	28	82.7 ± 50.7	1.4	12
1.0 at% Si	24	43.8 ± 17.1	1.3	21
2.5 at% Si	17	33.9 ± 13.9	1.3	27
0.25 at% Si (pilot)	26	68.2 ± 37.5	1.4	13

1021.2 eV[241] and 100.8 eV[243] for Zn and Si, respectively, consistent over both samples. Due to the low relative sensitivity factor of Si in X-ray photoelectron spectroscopy, Si 2p analysis of samples below 1.0 at% Si did not show any discernible peaks.

5.3.3 Electrical characterisation

Figure 5.4 shows the trend of resistivity (and conductivity) versus silicon content in the range 0.25 - 3.0 at% Si for SiZO synthesised by CHFS and tested as heat treated, pressed discs. The trend appears almost exponential, with the lowest composition tested (0.25 at% Si) garnering the lowest resistivity of 3.50 x 10^{-2} Ω cm, increasing slowly with dopant level until sharply jumping at 2.5 - 3.0 at% Si, by which point the resistivity is of the order of 10^0, two orders of magnitude higher than that of the optimally conductive sample. The pilot scale 0.25 at% sample measured 3.98 x 10^{-2} Ω cm, very close to that of the analogous sample synthesised on the laboratory scale, indicating a proportionally better scalability of SiZO than seen for AZO and GZO with respect to the electrical properties. Resistivity data for the samples is summarised in Table 5.2 along with the standard deviation in the measurements.

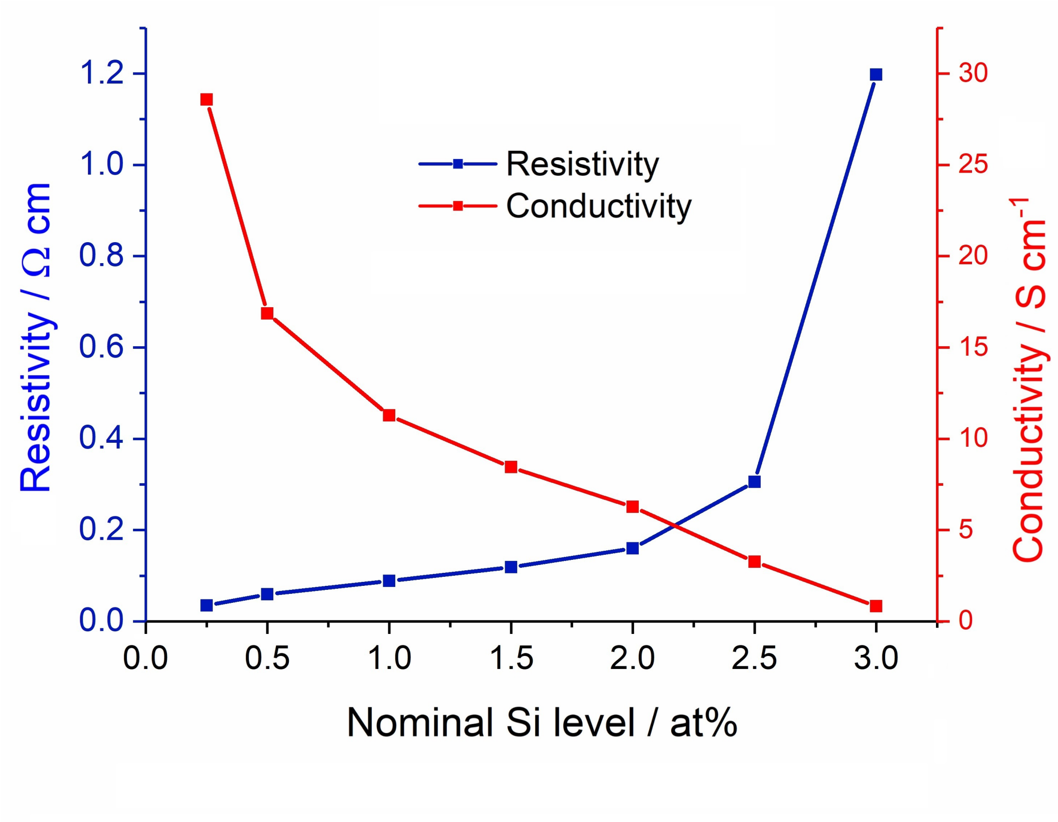

Figure 5.4: Resistivity (blue) and conductivity (red) data for all compositions of SiZO synthesised on the laboratory scale CHFS.[7]

Table 5.2: Summary of the resistivity date for SiZO across the compositional range explored, from 0.25 to 3.0 at% Si, including the standard deviation for each reading.

Sample	**Resistivity x 10^{-2} / Ω cm**
0.25 at% Si	3.50 ± 0.04
0.5 at% Si	5.93 ± 0.65
1.0 at% Si	8.87 ± 0.01
1.5 at% Si	11.84 ± 0.01
2.0 at% Si	15.95 ± 0.47
2.5 at% Si	30.57 ± 0.15
3.0 at% Si	119.73 ± 0.15
0.25 at% Si (pilot)	3.98 ± 0.10

5.3.4 Conclusions

SiZO was synthesised by CHFS in the dopant range 0.25 to 3.0 at% Si. These powders were tested for their resistivity by pressing into discs and subsequent heat treatment, and from Hall Effect measurements the optimally conductive sample was found to be the sample made with 0.25 at% Si, with a resistivity of 3.50 x 10^{-2} Ω cm. This was then synthesised again on the pilot scale process (> 300 g h^{-1}), and was found to retain the electrical properties well; this sample measured a resistivity of 3.98 x 10^{-2} Ω cm. Increase of the dopant level led to a decrease in particle size and an increase in resistivity, and it was also seen that pilot scale synthesis resulted in a slight decrease in particle size and increase in resistivity. There is no indication as to whether the dopant level is directly and solely responsible for the increase in resistivity, or whether particle size is also a significant factor, particularly at low dopant levels where the small change in Si results in a dramatic change in particle size. It is possible that the large particle size resulting from 0.25 at% Si benefits the resistivity by means of reducing the grain boundary effects in the compacts.

5.4 SiZO: Co-Doping Investigation

Though SiZO was among the best materials screened in the experiments discussed in Chapter 3, the optimally conductive sample (ρ = 3.5 x 10^{-2} Ω cm) was still considerably more resistive than the optimal samples of AZO (ρ = 7.0 x 10^{-3} Ω cm), GZO (ρ = 9.1 x 10^{-3} Ω cm), or AGZO (ρ = 9.1 x 10^{-3} Ω cm), by around 4 - 5 times. Thus further experiments were planned to enhance the conductivity of SiZO by co-doping with Al or Ga, SiAZO and SiGZO, respectively.

5.4.1 Experimental design

Synthesis was exactly as carried out previously on the laboratory scale CHFS process for purely Si-doped ZnO. Si was once more introduced into the process with the base feed via pump P3, and Al, Ga, and Zn in various ratios were introduced via pump P2. The samples made were as follows (and as summarised in Table 5.3): 0.25 at% Si with 1.0, 1.5, 2.0, and 3.0 at% of either Al or Ga, and 0.5 at% Si with 1.0, 2.0, and 3.0 at% of either Al or Ga; the remaining at% of each sample

Table 5.3: Summary of particle size data for the co-doped SiZO samples in direct comparison to the singularly doped samples, including BET surface area, and mean particle length and aspect ratio from TEM image analysis.

Si / at%	**Al / at%**	**Ga / at%**	**BET Surface Area / m^2g^{-1}**	**TEM Particle Length / nm**	**Aspect**
0.25	0	0	12	82.7 ± 50.7	1.4
0.25	2	0	20	32.0 ± 17.2	1.4
0.25	0	2	27	30.8 ± 14.5	1.4
0.5	0	0	19	46.1 ± 17.2	1.4
0.5	2	0	26	31.4 ± 16.9	1.5
0.5	0	2	29	24.4 ± 12.9	1.3

consisted of Zn by this nomenclature. No samples were made without Si, as such samples were already investigated as described in Chapter 4.

As was observed for Al- and Ga-doping into ZnO in the previous Chapter, introduction of these resulted in an immediate colour change in the slurries and powders to off-white/yellow depending on the proportion of dopant. Similarly upon pressing of the powders the colour changed to green, then to blue-green after heat treatment. The co-doped samples were characterised by TEM, BET, and Hall Effect measurements on the pressed, heat treated discs.

5.4.2 Characterisation

As previously, all samples were phase pure Wurtzite ZnO as shown in Figure 5.5. Representative TEM images are shown in Figure 5.6 of 2 at% Al or Ga with either 0.25 at% or 0.5 at% Si. Co-doping of the samples resulted in largely more spheroidal (less diamondoid character) particles than purely Si-doped ZnO, with Al-doped samples more rod-like, particularly in the 0.5 at% Si sample, which saw a slight increase in mean aspect ratio of 1.5, compared to typically 1.4 for undoped SiZO. Addition of either Al or Ga resulted in considerable reduction in particle size, as shown from the data summarised in Table 5.3.

A summary of resistivity data for all of the co-doped samples is shown in Table 5.4. Addition of either Al or Ga was shown to improve the electrical properties as

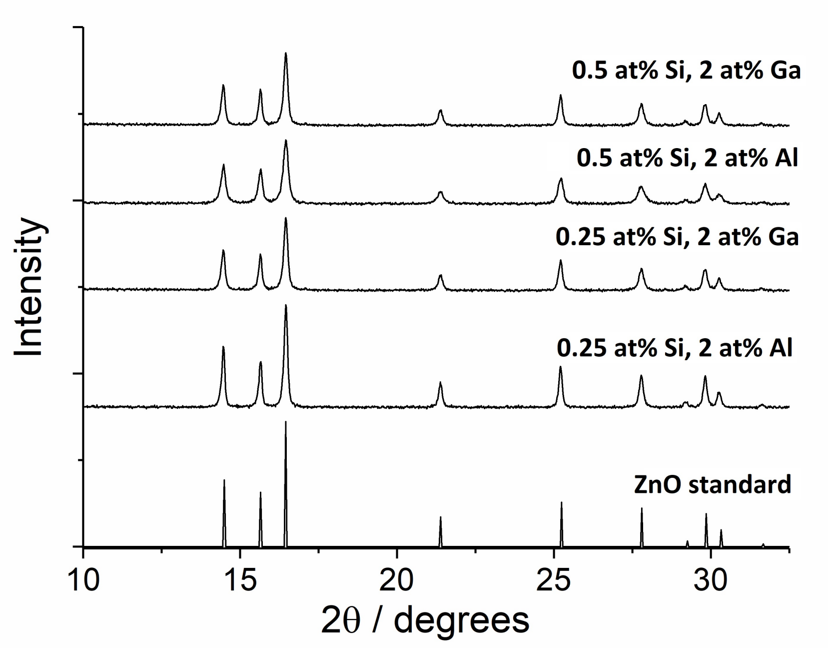

Figure 5.5: XRD patterns for four representative co-doped samples, including the standard pattern for ZnO.

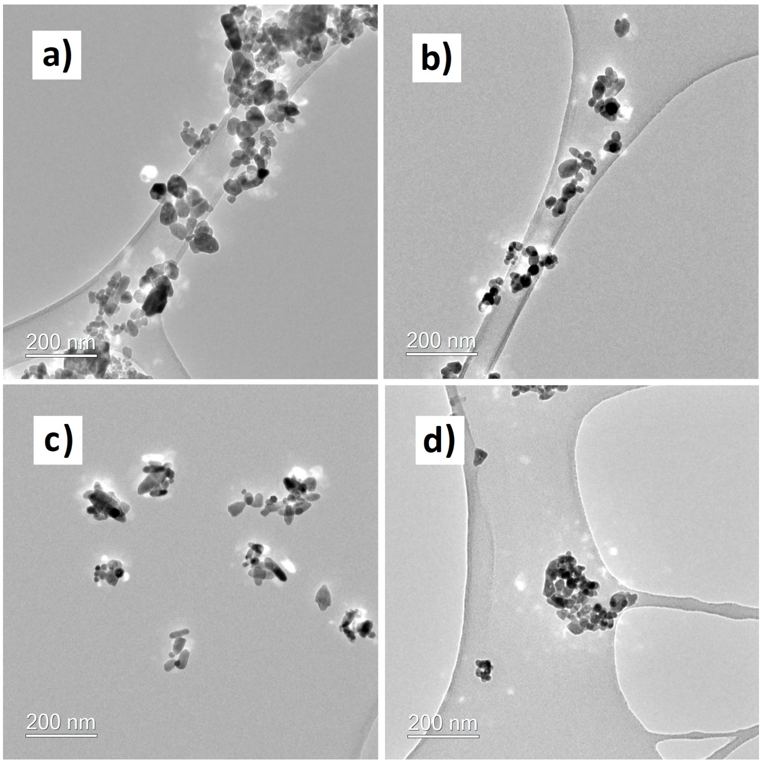

Figure 5.6: TEM images of the Si-co-doped ZnO samples. a) and b) were 0.25 at% Si with 2 at% Al and Ga, respectively, and c) and d) were 0.5 at% Si with 2 at% Al and Ga, respectively.

Table 5.4: Summary of the resistivity data for all co-doped SiZO samples synthesised. In bold are the least resistive samples for each Al- and Ga-(co-)doped SiZO, and in italics are the singularly doped SiZO samples.

Si / at%	**Al / at%**	**Ga / at%**	**Resistivity x 10^{-2} / Ω cm**
0.25	*0*	*0*	*3.50 ± 0.04*
0.25	1	0	1.11 ± 0.35
0.25	**1.5**	**0**	**0.83 ± 0.05**
0.25	2	0	1.16 ± 0.03
0.25	3	0	3.22 ± 0.12
0.25	0	1	2.96 ± 0.05
0.25	**0**	**1.5**	**1.13 ± 0.04**
0.25	0	2	1.75 ± 0.02
0.25	0	3	2.39 ± 0.01
0.5	*0*	*0*	*5.93 ± 0.65*
0.5	1	0	6.94 ± 0.03
0.5	2	0	3.68 ± 0.02
0.5	3	0	5.32 ± 0.03
0.5	0	1	3.14 ± 0.02
0.5	0	2	2.80 ± 0.01
0.5	0	3	5.97 ± 0.52

shown graphically in Figures 5.7 and 5.8 (Al and Ga, respectively). In both cases the optimal sample was that made with 0.25 at% Si and 1.5 at% of Al or Ga, achieving resistivities of 8.3 x 10^{-3} Ω cm and 1.1 x 10^{-2} Ω cm, respectively. In each case, these were very close to the values obtained from purely Al- or Ga-doped ZnO, but reducing the required amount of dopant; in the case of Ga co-doping, the amount of gallium (by far the most expensive component) required was reduced to less than half (from 3.5 at% to 1.5 at%), with only a very small amount of Si required, a negligible cost by comparison. This resulted in a reduction of conductivity of approximately 20%, which in many applications might not discount the material while making it industrially much more viable due to having halved the cost.

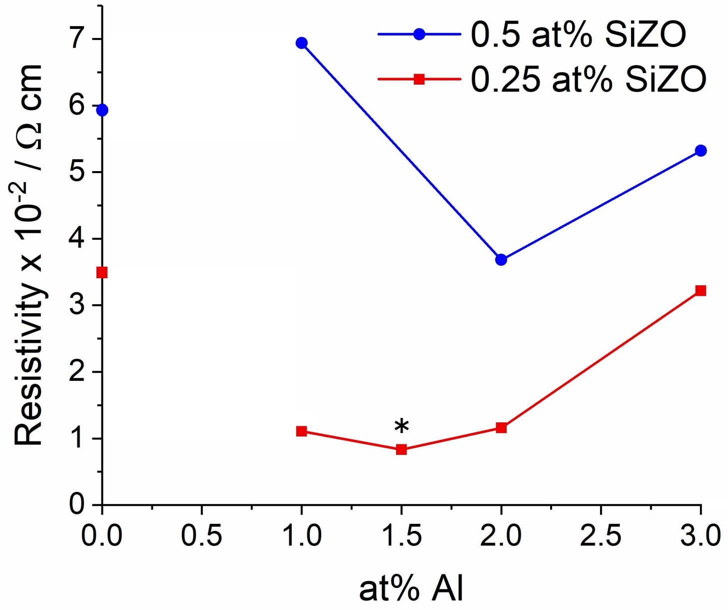

Figure 5.7: Resistivity data for the Al- and Si-co-doped ZnO samples. Those with 0.25 at% Si are in red, those with 0.5 at% Si are in blue. The minimum point (*) represents a resistivity of 8.3 x 10^{-3} Ω cm.

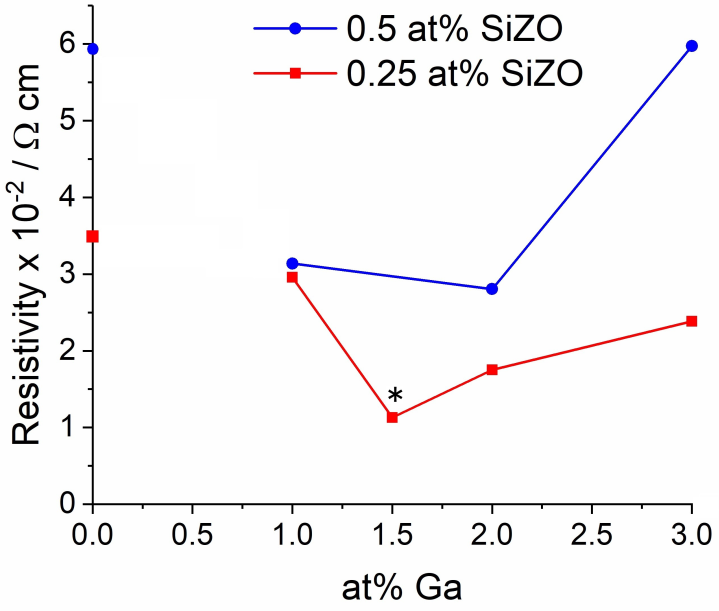

Figure 5.8: Resistivity data for the Ga- and Si-co-doped ZnO samples. Those with 0.25 at% Si are in red, those with 0.5 at% Si are in blue. The minimum point (*) represents a resistivity of 1.13 x 10^{-2} Ω cm.

5.5 Conclusions

Si-doped and co-doped (with Al or Ga) ZnO was synthesised using CHFS and the powders tested by pressing into discs and heat treating. Singularly doped SiZO had the optimal resistivity of 3.5 x 10^{-2} Ω cm at a dopant level of 0.25 at% Si. Doping 1.5 at% Al into this resulted in a decrease in resistivity to only 8.3 x 10^{-3} Ω cm, very close to the optimally conductive AZO sample, which had a resistivity of 7.0 x 10^{-3} Ω cm with 2.5 at% Al. Thus equivalent electrical properties could be obtained but with a 40% reduction in Al (a source of chemical instability in AZO). Similarly, doping with 1.5 at% Ga into the optimally conductive SiZO sample also resulted in a decrease in resistivity, to 11.3 x 10^{-3} Ω cm. This compares well to the optimally conductive GZO sample, which had a resistivity of 9.1 x 10^{-3} Ω cm at a dopant level of 3.5 at% Ga. Thus, again similar resistivity to GZO is seen but with drastically reduced (57% reduction) level of gallium required, more than halving the cost of the material for almost equivalent electrical properties.

Chapter 6

Transparent Conducting Oxide Nanoparticle Ink Formulation and Deposition

6.1 Aims

The principal aim of this chapter is to investigate the deposition of Continuous Hydrothermal Flow Synthesis (CHFS)-made transparent conducting oxide (TCO) nanoparticles onto glass substrates in the form of thin films. This first involves the investigation into the citrate-coating of the nanoparticles, ink formulation, and finally the inkjet printing and spin coating of the optimised materials in order to gauge the effect of depositing the nanoparticles on the optoelectronic properties of the material.

6.2 Introduction

Deposition by inkjet printing would first involve the in-process surface modification of the nanoparticles by inclusion of sodium citrate in the reactor quench feed, coating the particles with citrate. Thus the loading optimisation of citrate is first investigated onto ITO and AGZO (which will henceforth be referred to as cit:ITO and cit:AGZO, respectively, when coated with citrate), followed by deposition by inkjet printing and characterisation of the thin films by optical and electronic means.

Additional deposition by spin coating is also investigated, followed by in-depth optoelectronic characterisation of the thin films, made from cit:ITO, GZO, AGZO, and SiZO. This section outlines the relevant studies so far reported in literature of the deposition of thin films of ITO and ZnO doped with Al, Ga, Al/Ga, and Si, for direct comparison with the films deposited as part of this work, as well as outlining the theory behind surface functionalisation and zeta potential measurements of nanoparticles.

6.2.1 Synthesis and properties of ITO as a TCO

Studies into the deposition of ITO by various methods have generated thin films with resistivities of the order of 10^{-4} Ω cm, including magnetron sputtering,[30, 31, 143, 282] spray deposition[25] and pyrolysis,[283, 284] CVD,[149] dip coating,[285] and spin coating.[154] These films tended to have very high charge carrier concentrations ($> 10^{21}$ cm^{-3}) and reasonable mobilities (> 30 cm^2 V^{-1} s^{-1}), as summarised in Table 6.1, from the last five decades. Almost untested is inkjet printing, the results of which have thus far disappointed in terms of the resistivities, which have been considerably higher than more conventional deposition techniques.[155, 286] That said, optically the inkjet printed films tend to be superior, and inclusion of co-printed Ag grids can decrease the resistivity < 2 x 10^{-4} Ω cm, at a slight cost to the optical light transmittance (82 % vs. 87 %).[155]

ITO has been made in hydrothermal flow before,[169, 187] and a dopant optimisation investigation was recently carried out,[168] which reported the most conductive CHFS-made ITO nanomaterials, 6.0 x 10^{-3} Ω cm as a pressed, heat treated pellet, and spin-coated films of this un-coated material had resistivities ca. 1 x 10^{-2} Ω cm. However, ITO has not been surface-functionalised in-process and subsequently printed. Lu et al. functionalised ITO nanoparticles with hexanoic acid for dispersion in hexane, however the only electrical testing by pressing a thin film indicated resistivity ca. 8 Ω cm, but no printing or other deposition method took place.[169]

Table 6.1: Summary of the properties of a selection of ITO films deposited by various methods, visible light transmittance, resistivity (ρ), charge carrier concentration (n) and mobility (μ), and the corresponding reference. CVD is chemical vapour deposition, DC is dip coating, IP is inkjet printing, MS is magnetron sputtering, RS is reactive sputtering, SC is spin coating, and SP is spray pyrolysis. Included in italics (bottom row) are the figures for the best spin coated ITO film from this work, for comparison.

Deposition Method	**ρ x 10^{-4} / Ω cm**	**n x 10^{20} / cm^{-3}**	**μ / cm^2 V^{-1} s^{-1}**	**Trans. / %**	**Reference**
MS	0.7	27	36	89	[30]
SP	1.3	15	35	-	[25]
MS	1.3	11	43	-	[31]
MS	1.7	8.1	46	-	[143]
SP	2.0	10	30	< 80	[283]
CVD	2.2	-	-	80	[149]
DC	2.5	8.0	27	83	[285]
MS	4.0	10	10	85	[282]
SP	4.8	8.0	16	85	[284]
SC	6.5	7.0	14	85	[154]
IP	300	1.0	1.2	87	[155]
IP	17000	-	-	90	[286]
SC	*0.9*	*28*	*24*	*82*	-

6.2.2 Synthesis and properties of ZnO as a TCO

Aluminium-doped zinc oxide (AZO) was first prepared by Minami et al. in 1984.[119] The investigation was prompted by issues with thermal stability of non-stoichiometric undoped zinc oxide, which was the only way to make the material conductive without dopants present. With a little under 2 at% Al, magnetron-sputtered films of AZO demonstrated a marked improvement in thermal stability, and a resistivity of only 1.9 x 10^{-4} Ω cm, and remains among the most conductive AZO films in literature to this day. A great number of other groups have made films of the order of 10^{-4} Ω cm, however, by various deposition methods including magnetron sputtering,[144–146, 248–253] atmospheric pressure[120] and aerosol assisted[121] chemical vapour deposition (APCVD and AACVD, respec-

Table 6.2: Summary of the properties of a selection of AZO films deposited by various methods, including dopant level, visible light transmittance, resistivity (ρ), charge carrier concentration (n) and mobility (μ), and the corresponding reference. MS is magnetron sputtering, APCVD and AACVD are atmospheric pressure and aerosol assisted chemical vapour deposition, respectively, SP is spray pyrolysis, and IP is inkjet printing.

Deposition Method	ρ x 10^{-4} / Ω cm	n x 10^{20} / cm^{-3}	μ / cm^2 V^{-1} s^{-1}	Dopant level / at%	Trans. / %	Reference
MS	1.9	5.0	25	1.9	85	[119]
APCVD	3.0	8.0	35	0.6	85	[120]
MS	3.4	4.8	38	1.0	78	[144]
MS	3.4	13.0	14	3.2	85	[145]
AACVD	4.2	2.3	65	2.7	81	[121]
MS	4.7	7.5	15	4.0	90	[146]
MS	4.9	8.9	13	4.0	85	[249]
PLD	5.1	6.7	20	-	90	[122]
SP	20.0	0.8	43	1.0	85	[123]
IP	254.0	0.2	11	3.0	93	[156]

tively), and pulsed laser deposition (PLD).[122, 254] Other techniques such as spray pyrolysis[123], atomic later deposition (ALD),[255] and inkjet printing[156] and spraying[256] have been explored, but are orders of magnitude behind in terms of resistivity. Most of the aforementioned studies have however achieved transparencies of 80% or higher, with several surpassing 90% in the visible range.[122, 146, 156, 252, 256] Electron mobilities were variable, though typically in the range 10 - 40 cm^2 V^{-1} s^{-1}, and charge carrier concentrations were in the range 4 - 27 x 10^{20} cm^{-3}, (typically mid-range in the order of 10^{20} cm^{-3}). The vast majority of these materials had dopant levels no higher than 4 at% Al, with the average at 3.4 at% Al. A summary of the best performing AZO films from literature is included in Table 6.2.

GZO was first made by magnetron sputtering in 1990 by Choi et al,[257] though the films managed only resistivities around 2 x 10^{-3} Ω cm. This was improved upon significantly in 1992 by Hu and Gordon, when they made the first GZO thin

Table 6.3: Summary of the properties of a selection of GZO films deposited by various methods, including dopant level, visible light transmittance, resistivity (ρ), charge carrier concentration (n) and mobility (μ), and the corresponding reference. MS is magnetron sputtering, APCVD and AACVD are atmospheric pressure and aerosol assisted chemical vapour deposition, respectively, and SC is spin coating. Included in italics (bottom row) are the figures for the best spin coated GZO film from this work, for comparison.

Deposition Method	**ρ x 10^{-4} / Ω cm**	**n x 10^{20} / cm^{-3}**	**μ / cm^2 V^{-1} s^{-1}**	**Dopant level / at%**	**Trans. / %**	**Reference**
APCVD	2.0	13.5	23	4.3	85	[128]
MS	2.2	24.0	13	4.7	85	[124]
MS	4.0	4.0	22	4.4	85	[125]
CVD	5.0	3.0	15	2.0	85	[129]
MS	5.4	6.5	16	2.6	92	[126]
MS	6.1	1.0	12	5.0	80	[259]
AACVD	6.4	1.9	51	2.5	85	[121]
PLD	7.0	6.8	20	5.0	85	[127]
MS	11.1	3.8	15	0.5	85	[253]
SC	*1.8*	*19.0*	*19*	*3.5*	*83*	-

film with resistivity appropriate for TCO application,[207] at 2.4 x 10^{-4} Ω cm, equalling the best AZO films (using APCVD in place of magnetron sputtering). Other films of GZO with resistivities of the order 10^{-4} Ω cm have since been made by sputtering,[124–126, 248, 258, 259] APCVD,[128] CVD,[129], AACVD,[121] and PLD.[127] These generally display a lower transmission of visible light, with only one exceeding 90% transmission in the visible range,[126] and generally have higher carrier concentrations, similar mobilities, and slightly higher mean dopant levels, around 3.8 at% Ga. A tabulated summary for a selection of these materials is included in Table 6.3.

AGZO is considerably newer in terms of literature presence to AZO and GZO. No fully optoelectronically characterised AGZO thin film was published until 2010, in which effort Kim et al. deposited a film by magnetron sputtering that had a resistivity of 6.8 x 10^{-4} Ω cm. Almost all AGZO films in literature were deposited by magnetron sputtering, and average dopant levels were 2.0 at% Al and 1.2 at% Ga.

Table 6.4: Summary of the properties of a selection of AGZO films deposited by various methods, including dopant level, visible light transmittance, resistivity (ρ), charge carrier concentration (n) and mobility (μ), and the corresponding reference. MS is magnetron sputtering, AACT is aerosol assisted chemical transport, and SC is spin coating. Included in italics (bottom row) are the figures for the best spin coated AGZO film from this work, for comparison.

Deposition Method	**ρ x 10^{-4} / Ω cm**	**n x 10^{20} / cm^{-3}**	**μ / cm^2 V^{-1} s^{-1}**	**(Al, Ga) / at%**	**Trans. / %**	**Reference**
MS	3.0	5.0	42	1.6, 0.9	82	[130]
MS	3.2	2.4	9	0.8, 2.7	<80	[131]
MS	4.5	2.5	10	2.7, 0.3	>90	[132]
MS	4.7	12.0	11	4.3, 2.1	95	[133]
MS	5.7	6.0	29	1.4, 0.3	92	[260]
MS	6.8	4.9	17	-	>85	[262]
MS	7.8	3.9	23	1.6, 0.9	78	[263]
MS	13.0	6.1	10	2.4, 1.3	95	[287]
AACT	57.0	0.7	14	1.5, 1.5	90	[288]
SC	*1.9*	*18.0*	*20*	*2.0, 2.0*	*82*	-

Average transmission was comparable to AZO films and improved on GZO films, as perhaps should have been expected, with several obtaining visible light transmissions above 90%.[132, 133, 260, 287, 288] The carrier concentration is of the same order of magnitude as AZO, a little lower than GZO, and mobilities are generally modest in the range 10 - 30 cm^2 V^{-1} s^{-1}, leading to resistivities generally higher than AZO or GZO films, though still typically of the order of 10^{-4} Ω cm.[130–133, 248, 253, 260–263] A summary of AGZO film data from literature is included in Table 6.4.

Few studies exist in literature in which SiZO thin films are generated and fully characterised in the context of application as TCOs, i.e. with optical and electrical characterisation together. That said, from the studies that have been carried out, competitive resistivities, carrier concentrations, charge carrier mobilities, and transmittance properties have been achieved. SiZO thin films have been made by several techniques, including CVD,[275] spray pyrolysis,[276, 277] pulsed laser deposition

Table 6.5: Summary of the properties of a selection of SiZO films deposited by various methods, including dopant level, visible light transmittance, resistivity (ρ), charge carrier concentration (n) and mobility (μ), and the corresponding reference. MS is magnetron sputtering, PLD is pulsed laser deposition, SP is spray pyrolysis, CVD is chemical vapour deposition, and SC is spin coating. Included in italics (bottom row) are the figures for the best spin coated SiZO film from this work, for comparison.

Deposition Method	**ρ x 10^{-4} / Ω cm**	**n x 10^{20} / cm^{-3}**	**μ / cm^2 V^{-1} s^{-1}**	**Dopant level / at%**	**Trans. / %**	**Reference**
MS	3.3	4.3	15	1.5	90	[134]
MS	3.8	10.0	12	2.0	85	[135]
PLD	3.9	5.9	28	2.0	83	[136]
MS	5.5	5.0	23	3.0	94	[147]
PLD	6.2	2.9	38	1.1	77	[208]
MS	8.7	4.5	16	0.5	>80	[279]
SP	15.0	19.0	-	4.0	87	[277]
SP	37.0	1.7	9	3.0	80	[276]
CVD	200.0	0.3	17	4.0	75	[275]
SC	*24.0*	*1.0*	*11*	*0.25*	*83*	-

(PLD),[136, 208, 278] and magnetron sputtering.[134, 147, 279] Of these, sputtered films were the most transmissive, at 90%[134] and 94.5%[147], but PLD and spray pyrolysis techniques also garnered films with $>$ 80% transmittance across the visible range. The seminal work by Minami et al.[135] was also the first to reach the order of 10^{-4} Ω cm, but all published sputtering and PLD studies managed to match this achievement,[134, 136, 147, 208, 278, 279] with the most conductive film thus far reported by Clatot et al.[134] at 3.3 x 10^{-4} Ω cm. The dopant level varied in these studies, but never exceeded 4 at% Si, and mobilities were around 16 cm^2 V^{-1} s^{-1}. Das et al.[208] reported the highest electron mobility for this material of 38 cm^2 V^{-1} s^{-1}, a feat not since matched. In almost all cases, the carrier concentration was of the order of 10^{20} cm^{-3}, with only one study, Rashidi et al. (spray pyrolysis) exceeding to 10^{21} cm^{-3},[277] and this achieved only by additional incorporation of fluoride into the preparation and deposition methodology. A summary of all of this data is included in Table 6.5 in order of increasing resistivity, along with the corresponding references for further reading.

All of these materials, AZO, GZO, AGZO, and SiZO, have demonstrated electrical and optical properties rivalling (or at least nearing) those of ITO, not only from magnetron sputtering but from several other deposition techniques, to the extent that any of them could be considered as viable replacement materials and worthy of study. This is especially true with regards to using CHFS, as there are very few studies into inkjet printing that show any promise at all (whether with ZnO-based materials, or indeed with ITO itself); typically the films demonstrate excellent optical properties, but with low conductivity.[155, 156, 256, 286] Surface functionalisation of these materials for aid in formulation of inks would be a significant step towards replacing the ubiquitous sputtering techniques currently in use, but there was first the need to elucidate the optimal composition of the materials as made by CHFS, as they had not before been synthesised by such a method before this research. Results of the compositional optimisation are discussed in Chapters 4 (AZO, GZO, and AGZO) and 5 (SiZO), while surface functionalisation and deposition results are discussed further on in this chapter.

6.2.3 Surface functionalisation of nanoparticles using citrate

Efforts toward surface-functionalisation using various different capping agents have been used in coating ceria,[289, 290] various iron oxides,[291–293] silicon,[293] titanium,[294, 295] hafnium,[296] and zirconium dioxides,[297] and gold nanoparticles,[298, 299] among others. The majority of these synthesis methods involve batch processes, but some are continuous, analogous to the methodologies employed in this research. This offers a benefit as coating particles can be introduced at lower temperatures after the initial nucleation of the primary product particles, without risk of organic capping agents thermally decomposing at the elevated temperatures required to synthesise many of the materials in question.[291, 300]

Citrate-coated nanoparticles are desirable in a number of applications, particularly biomedical applications due to citrate's inherent biocompatibility, for example functionalised magnetite nanoparticle synthesis for use in magnetic hyperthermia treatments.[291, 292] This has been demonstrated in hydrothermal flow,[300] however the synthesis of surface-functionalised citrate-coated nanoparticles for application as TCOs has yet to be investigated in literature, though there are a very few articles on other surface modifiers used to disperse TCO nanoparticles including ITO[169] and ZnO.[301]

Citrate was selected as the surface modifier in this instance because of the nature of the desired ink 'product'; the hypothetical ink was to be water-based, as was the synthesis method. As such, the modifier had to be water soluble in reagent form, and hydrophilic when coated onto nanoparticles. Citrate is naturally occurring, inexpensive and has been shown to be effective in this pursuit for other systems.[291, 294, 299, 300] Grafting density of the citrate molecules on the surface of the functionalised nanoparticles can be calculated using Equation 6.1.

$$\sigma = M\frac{(\frac{4}{3}\pi r^3)d(\frac{m_{CA}}{m_{NP}})}{M_{CA}}/4\pi r^2 \tag{6.1}$$

In this equation, σ is the grafting density in molecules per square nanometer (CA nm^{-2}), M is Avogadro's Constant, and m_{CA}/m_{NP} is the ratio of solid mass accounted for by the citrate (versus citrate and metal oxide nanoparticles), which is determined from TGA analysis. M_{CA} is the molecular weight of the capping agent (192.12 g mol^{-1}), d is the density of the metal oxide (assumed to be 7.14 g cm^{-3} for ITO and 5.61 g cm^{-3} for AGZO), and r is the mean radial length across the three axes for each nanoparticle; thus $4\pi r^3$ represents an estimation of the volume of each nanoparticle, which is more accurate the closer the particle is to a perfect sphere. As grafting density is only to be calculated to 1 d.p., the approximation was judged to be acceptable.

For the most part, citrate was used in the form of citric acid in previous reports, however due to the pH sensitivity of ZnO-based materials (particularly at low pH), sodium citrate was used in this study. Its structure is as shown in Figure 6.1. Each of the three (COO)$^-$ groups can be the point of adherence to the surface of nanoparticles, leaving multiple other groups loose, which can then interact with the water molecules in an aqueous medium, facilitating the dispersion of the nanoparticles.[300]

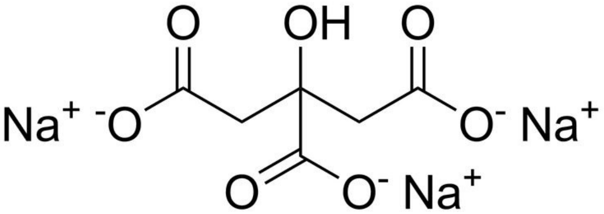

Figure 6.1: The structure of sodium citrate, the citrate precursor used to functionalise the CHFS nanoparticles.

6.2.4 Zeta potential measurements

Zeta potential is a measure of the potential difference between the molecules of the suspending medium adherent to the particles in suspension versus those in the bulk, wherein a greater magnitude of this potential difference is indicative of a more stable suspension. The sign is indicative of the charge on the surface of the particles in suspension, such that positive zeta potentials are observed for particles with net positive charge on the surface, and negative zeta potentials are observed for particles with negative surface charge. For each sample being tested, the zeta potentials should be measured for a number of points across a pH range, which typically generates a reverse S-curve. For every sample there is a pH at which the zeta potential is zero; i.e. the surface charge of the particle is neither positive nor negative; acidification of the solution from this point increases the propensity to positive charge at the surface due to the additional H^+ (or equivalent) ions present, and the addition of alkaline species has the opposite effect, generating negative surface charge on the particles in suspension.[302–304]

Though there are differing accounts as to the exact ranges, generally speaking samples with zeta potentials, $\zeta < |20|$ mV will quickly agglomerate and settle out of suspension, if $|20|$ mV $< \zeta < |40|$ mV then the particles will be fairly stable but will tend to slowly settle out, and for $\zeta > |40|$ mV the suspension tends to be inherently stable.[302–304]

6.3 Citrate-Coated Indium Tin Oxide

This section investigates the coating of ITO with citrate as part of the CHFS process, starting with the optimisation of citrate-loading and continuing with the characterisation of the optimal material. Ink formulation and deposition are detailed in following sections.

6.3.1 Experimental design

Dr P. Marchand et al. previously investigated the compositional optimisation of ITO as synthesised by CHFS, finding that 10 at% Sn relative to 90 at% In gave the lowest resistivity when pressed into a disc and heat treated, with ρ = 6.0 x 10^{-3} Ω cm. Formic acid was used in order to facilitate the formation of oxygen vacancies in the ITO structure.[168, 169] This was included in the indium precursor feed supplied by pump P2. Pump P3 contained the tin precursor and base (KOH), and pump P1 provided the flow of supercritical water as in all previous syntheses. Pump P4 contained aqueous sodium citrate solution at various concentrations, the capping/surface-coating agent. Pumps P1, P2, P3, and P4 had flow rates of 80, 40, 40, and 160 mL min^{-1}, respectively; the mixing temperature in the first mixer was 335 °C, and the mixing temperature in the second mixer was 187 °C, low enough that the citrate ions would not begin to decompose. The indium concentration was 0.09 M, the tin concentration 0.01 M, the formic acid concentration 0.5 M, and the KOH concentration 0.75 M. Citrate:metal ratios of 0, 0.33, 0.67, 1.0, 1.5, and 3.0 were used, the highest citrate concentration a two times excess of citrate versus the metal concentration. Inclusion of citrate had an immediate and drastic effect on the propensity of the slurries to settle out; washing with water and acetone was required for all samples as per the outline in Section 2.2.5, with centrifugation steps up to 3 h per wash. Significant losses of sample during the cleaning steps resulted in final yields of ca. 50 %, though this could have been mitigated by additional time on the centrifuge or improved recovery. The samples were collected at a pH of 8, all a similar colour, very pale blue, indicative of the formation of oxygen vacancies.[168]

6.3.2 Citrate-loading onto ITO investigation

This section outlines the use of zeta potential measurements to gauge the optimal amount of citrate in the ITO synthesis, with regards to the stability of the coated material in aqueous dispersions. The primary method of sample analysis was dynamic light scattering, by which method (see also Section 2.4.3) zeta potential curves were extracted for each material. These are shown in Figure 6.2a, whereas Figure 6.2b shows the comparisons of the different zeta potentials at pH 7 for each sample, the goal being the greatest magnitude of zeta potential, signifying the most stable particles in neutral solution.

As can be seen from the figure, the zeta potential drops sharply on addition of any citrate to the particles, reaching a minimum at a citrate:metal ratio of 1:1. Excess of citrate causes the zeta potential at pH 7 to rise above -30 mV, reducing the effectiveness of the citrate present in preventing agglomeration of the suspended particles. This value of -39.7 mV is indicative of good stability in aqueous media, and it was this material that saw its synthesis scaled up for further characterisation.

6.3.3 Further characterisation of optimal cit:ITO

This section discusses additional characterisation of the 1:1 cit:ITO material, including pre- and post-heat treatment XRD and XPS. As can be seen from XRD in Figure 6.3, the as-synthesised cit:ITO is in fact for the most part InOOH, although some In_2O_3 peaks can also be seen when compared to the reference pattern.[305, 306] The InOOH phase disappeared entirely upon heat treatment of the as-made material (5 h at 550 °C under an Ar atmosphere), leaving phase pure ITO, consistent with previous investigations in the UCL group.[168] This is further supported by XPS as shown in Figure 6.4. The as-prepared material (Figure 6.4a, c, and e) shows clearly two chemical environments for the metals (both In, show in 6.4a, and Sn, in 6.4c). These can be attributed to the oxyhydroxide and oxide phases for the larger and smaller peaks, respectively. Upon heat treating, only a single environment for each metal was observed, consistent with observations from XRD. The $3d_{5/2}$ peaks of 444.9 eV and 486.8 eV for In and Sn, respectively, are consistent with expected

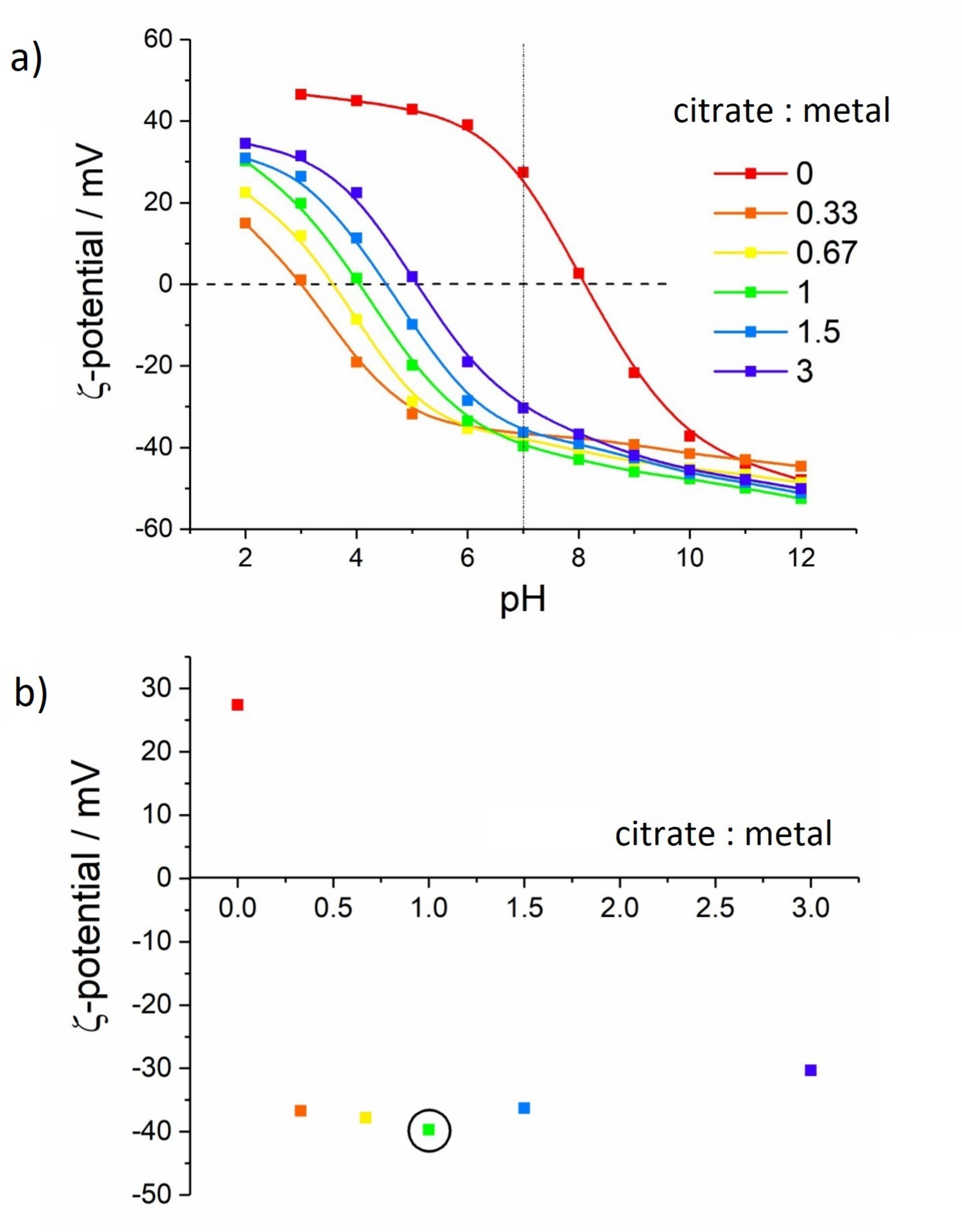

Figure 6.2: a) Zeta potential curves for the ITO samples made with and without citrate in the quench (P4) feed, and b) comparison of the zeta potentials at pH 7 for the different citrate-coated samples. The red curve represent the sample containing no citrate, and then the orange, yellow, green, blue, and indigo curves represent the samples with citrate:metal ratios of 1:3, 2:3, 1:1, 3:2, and 3:1, respectively, and the colour of each point in the lower graph corresponds directly with the curve of the same colour.

binding energies in the literature.[26, 234] Compositional analysis on the 3d regions of both elements indicated a proportion of 89.6 at% In, versus 10.4 at% Sn in the heat treated material.

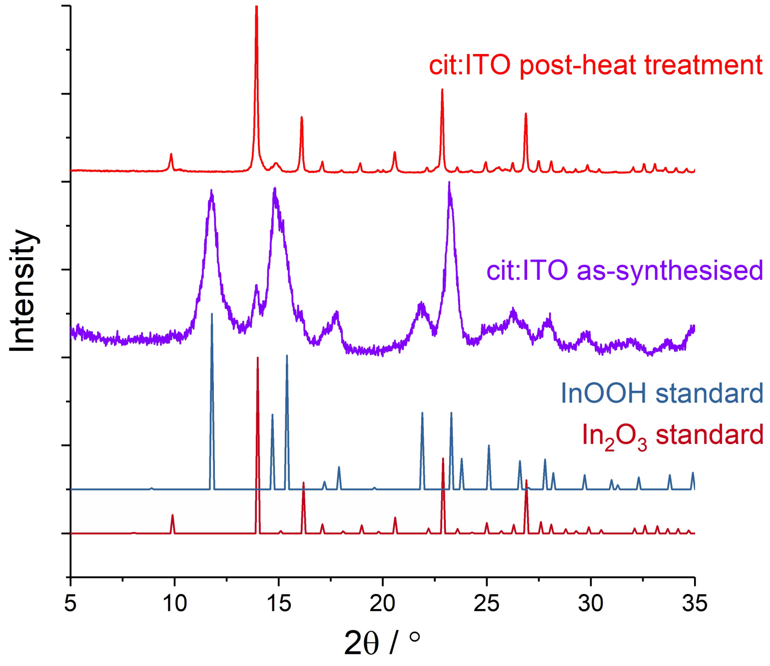

Figure 6.3: XRD patterns of the as-synthesised "ITO" material, with a 1:1 citrate ratio, and the same material after heat treatment. Standard patterns are included for InOOH and In_2O_3. Diffraction was carried out with a Mo source (λ = 0.7093 Å).

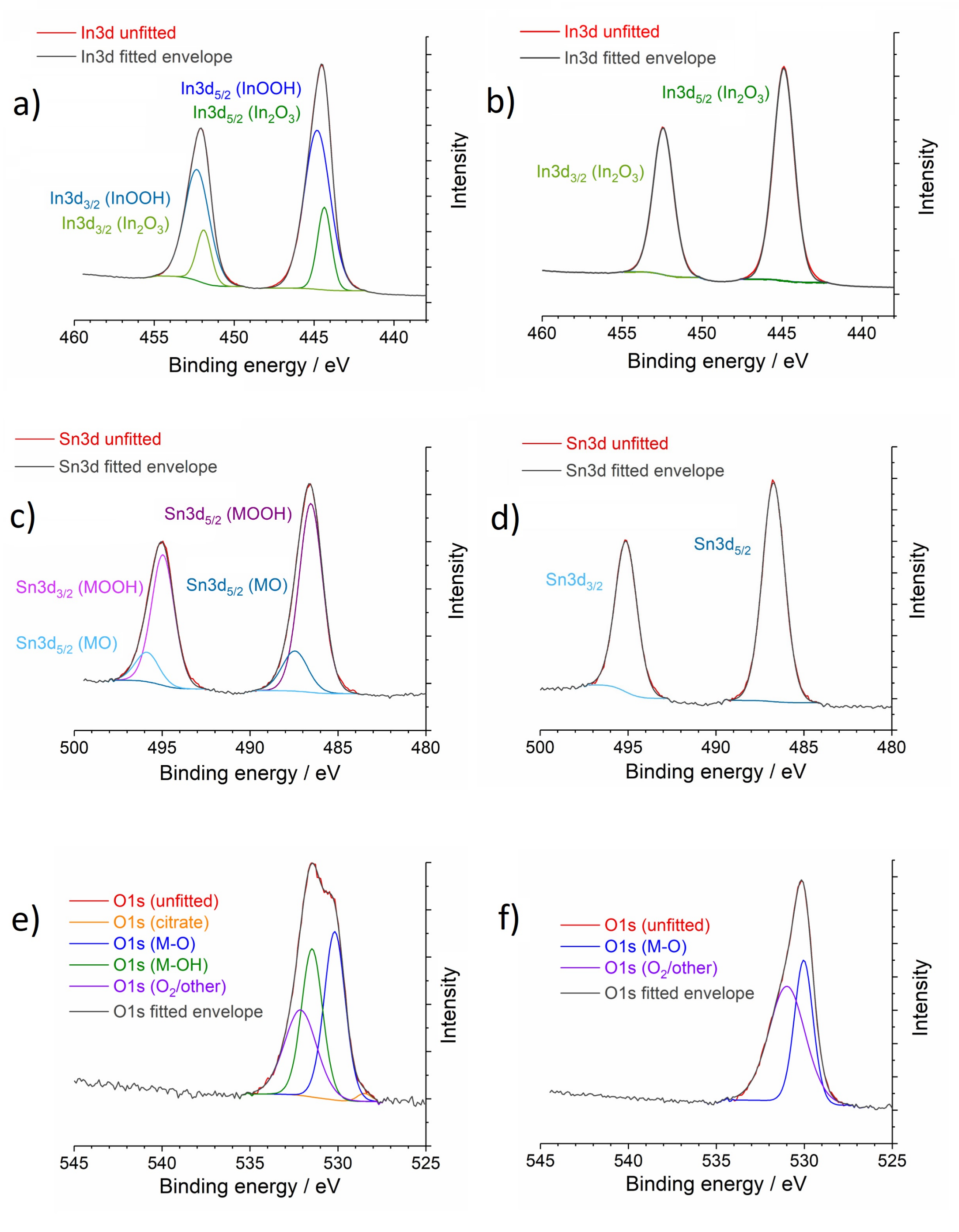

Figure 6.4: XPS spectra for the as-synthesised cit:ITO material, and post-heat treatment, including a) and b) the In 3d region, c) and d) the Sn 3d region, and e) and f) the O 1s region. A reduction in the number of environments is observed between a), c), and e) (as-synthesised) and b), d), and f) (post-heat treatment), as the (Sn-doped) InOOH is converted completely to (Sn-doped) In_2O_3.

6.4 Citrate-coated AGZO

This section investigates the coating of ZnO doped with 2 at% Al and 2 at% Ga (with respect to 96 at% Zn, hereafter referred to simply as "AGZO" in this Chapter) with citrate as part of the CHFS process, starting with the optimisation of citrate-loading and continuing with the characterisation of the optimal material. Ink formulation and deposition is detailed in following sections.

6.4.1 Experimental design

The investigation into the compositional optimisation of Al and Ga co-doped ZnO as synthesised by CHFS took place in 2016,[6, 307] and is detailed in Chapter 4. Over the course of the investigation, three compositions were found to have resistivities below 1 x 10^{-2} Ω cm.[6] These were ZnO doped with (Al at%, Ga at%) of (1.0, 2.0), (2.0, 2.0), and (3.0, 1.0). Of these, the greatest precision of the repeat measurements was with 2 at% each of Al and Ga, the second lowest resistivity sample in the study (ρ = 9.3 x 10^{-3} Ω cm), and as such it was judged to be the best candidate material for the citrate-optimisation study, being cheaper than GZO, and more stable than AZO.

A 4-pump setup was used as described in Section 2.2.2. Pump P1 provided the stream of supercritical water, P2 provided the metal precursors ([Zn + Al + Ga] = 0.3 M), P3 provided the base feed ([KOH] = 0.6 M), and P4 contained various concentrations of aqueous sodium citrate solution. Pumps P1, P2, P3, and P4 had flow rates of 80, 40, 40, and 160 mL min^{-1}, respectively; the mixing temperature in the first mixer was 335 °C, and the mixing temperature in the second mixer was 187 °C. As with the cit:ITO experiments, citrate:metal ratios of 0, 0.33, 0.67, 1.0, 1.5, and 3.0 were used, the highest citrate concentration a two times excess of citrate versus the metal concentration. Similarly to the observations in the cit:ITO experiments, inclusion of citrate had an immediate and drastic effect on the propensity of the slurries to settle out; washing with water and acetone was required for all samples as per the outline in Section 2.2.5, with centrifugation steps up to 1 h per wash; all of the cit:AGZO samples settled more readily than the analogous cit:ITO samples had previously. Yields were higher however, perhaps due in part to the ease of settling of the material, and all samples were obtained in ca. 70% yield by mass.

6.4.2 Citrate-loading onto AGZO investigation

This section outlines the use of zeta potential measurements to gauge the optimal amount of citrate in the ITO synthesis, with regards to the stability of the coated material in aqueous dispersions. The primary method of sample analysis was dynamic light scattering, by which method (see also Section 2.4.3) zeta potential curves were extracted for each material. These are shown in Figure 6.5a, whereas Figure 6.5b shows the comparisons of the different zeta potentials at pH 7 for each sample, the goal being the greatest magnitude of zeta potential, signifying the most stable particles in neutral solution.

As can be seen from the figure, the zeta potential drops sharply on addition of any citrate to the nanoparticle surfaces, reaching a minimum at a citrate:metal ratio of 1:1; however further increase in citrate concentration, differing from the effect observed with cit:ITO, resulted in no change in the zeta potential at pH 7. Thus the 1:1 sample was judged to be the best sample (as it used the minimum amount of citrate for the same result). Its zeta potential at pH 7 was -27.9 mV, indicative of moderate stability, considerably worse than the -39.7 mV obtained for the analogous cit:ITO sample. It should also be noted that the values were less predictable for cit:AGZO; the curves exhibited less of the characteristic s-shape expected, and less of a trend between samples could be identified. This could be due in part to the inherent chemical instability of ZnO-based materials in lower pH environments; derived count rate of the cit:AGZO samples dropped significantly by pH 3 (indicating that the material had most likely started to dissolve), whereas the same effect was not observed for cit:ITO until pH 2. Additionally, reduced efficiency and proclivity of the citrate to bind to the surface could have had an effect.

A visual depiction of the effect of coating ITO with citrate is shown in Figure 6.6, wherein as time passed (up to 3 h), the sample with no citrate settled completely, and samples with increasing citrate loading settled out noticeably slower.

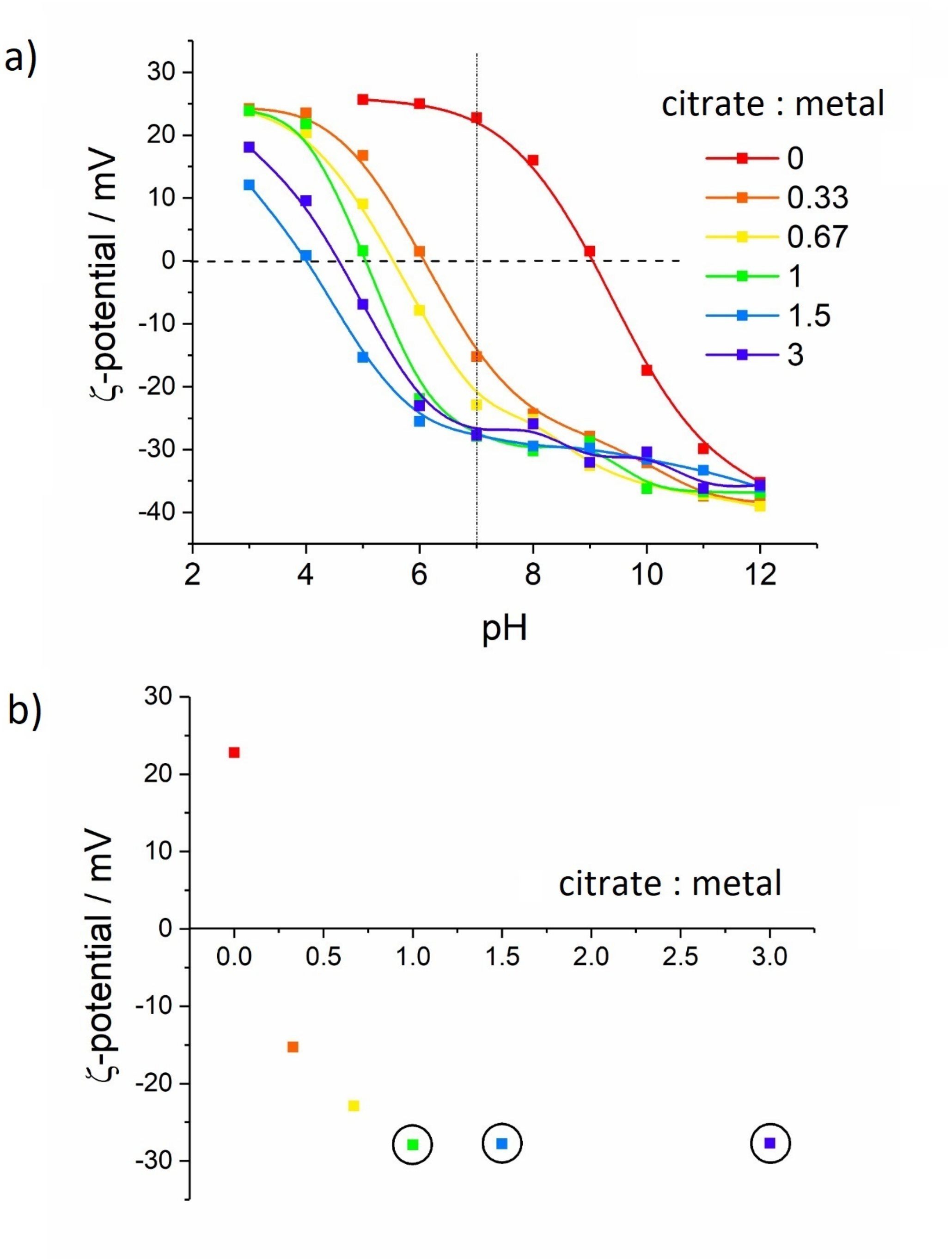

Figure 6.5: a) Zeta potential curves for the AGZO samples made with and without citrate in the quench (P4) feed, and b) comparison of the zeta potentials at pH 7 for the different citrate-coated samples. The red curve represent the sample containing no citrate, and then the orange, yellow, green, blue, and indigo curves represent the samples with citrate:metal ratios of 1:3, 2:3, 1:1, 3:2, and 3:1, respectively, and the colour of each point in the lower graph corresponds directly with the curve of the same colour.

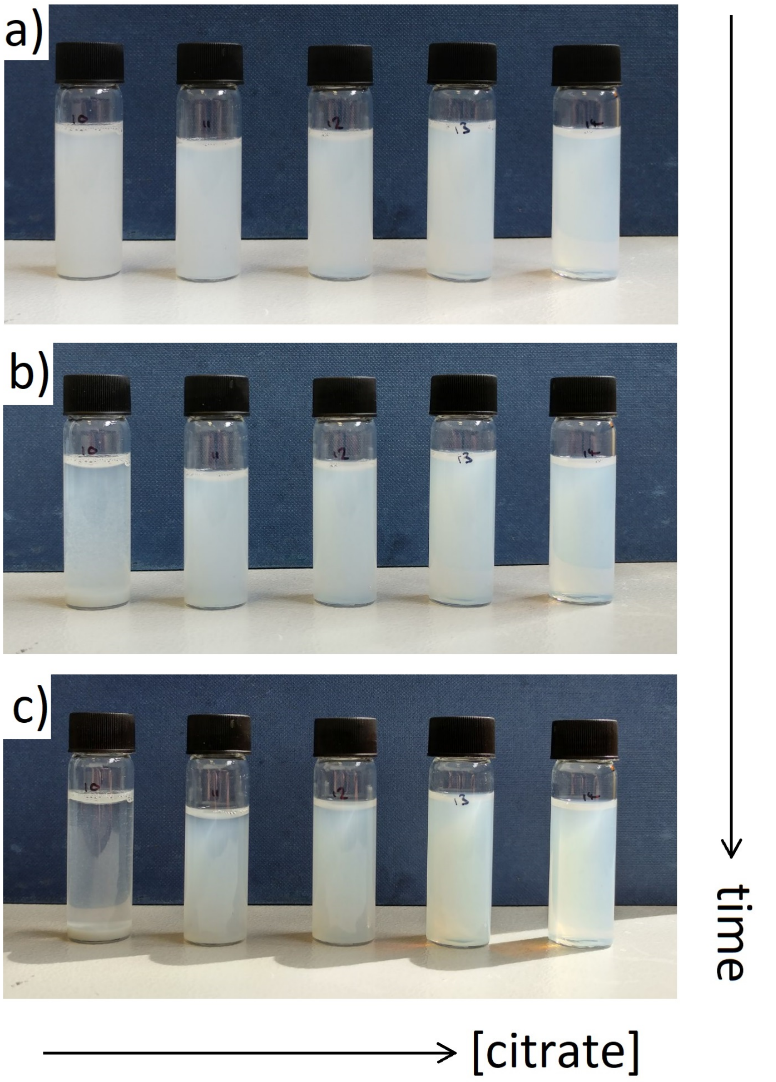

Figure 6.6: A photographic depiction of the settling rate of cit:ITO, with increased citrate loading from left to right. a) is how the as-prepared slurries looked initially, b) shows the slurries after 1 h, and c) shows the slurries after 3 h. These materials were synthesised by Dr P. Marchand, who also took the photographs.

6.4.3 Further characterisation of optimal cit:AGZO

This section discusses additional characterisation of the 1:1 cit:AGZO material, including XRD and XPS. As could be seen from XRD in Figure 6.7, the as-synthesised cit:AGZO was, as for previously synthesised ZnO materials, phase pure Wurtzite structure.[4] However, the Zn 2p and O 1s binding energy regions from XPS (as shown in Figure 6.8) appeared to indicate an additional, smaller chemical environment at higher binding energy, which disappeared upon heat treatment of the material, possibly due to the citrate bound to the surface of the material. The Ga 2p region was largely unchanged, though a decrease in peak intensity could have indicated that upon heat treatment that the gallium became less surface-segregated. The Al 2p region (Figure 6.8e) saw the greatest change; there was no Al detected until after heat treatment.

6.5 Inkjet Printing of cit:ITO and cit:AGZO

This section explores the formulation of the citrate-loaded materials, ITO and AGZO, into inks for inkjet printing. This includes TEM images of the as-prepared materials, TGA-DSC of the pastes, and viscometry measurements.

6.5.1 Further characterisation and ink formulation of cit:ITO and cit:AGZO

Both of the materials, cit:ITO and it:AGZO exhibited very good consistency in particle sizes as measured and calculated from TEM images (see Figure 6.9). cit:ITO typically appeared as 19.4 ± 5.1 nm, with an aspect ratio of 1.2, and cit:AGZO was typically 21.8 ± 4.6 nm, with an aspect ratio of 1.1. This was smaller than observed for the un-coated material, at 1.2 (see Figure 4.10 in Chapter 4), with a considerably narrower particle size distribution, indicating that citrate-coating was of significant benefit in pursuit of particle size control.

When thermogravimetric analysis with differential scanning calorimetry (TGA-DSC) was carried out on dense pastes of the two materials, the graphs as shown in Figures 6.10 and 6.11 were extracted. In both cases, an initial mass loss accompanied by a DSC endotherm (see the regions marked in red) indicated the loss of

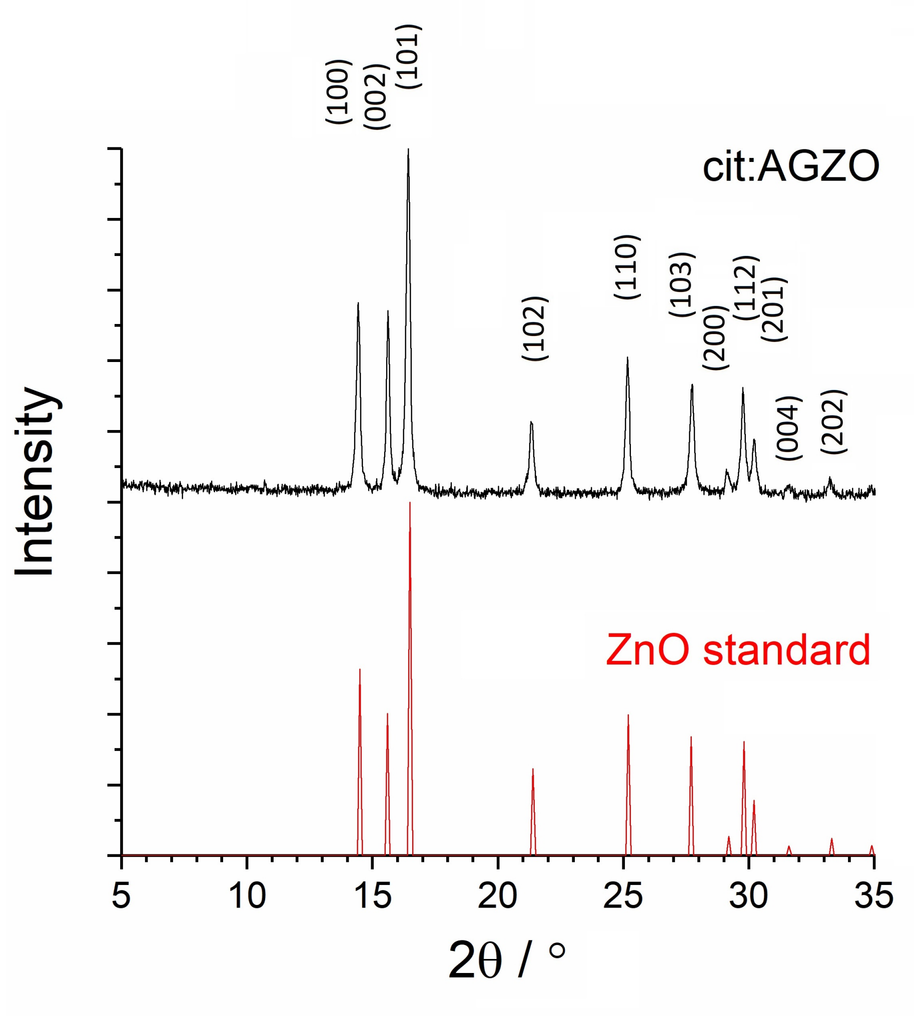

Figure 6.7: XRD patterns of the as-synthesised 1:1 cit:AGZO material, showing phase pure Wurtzite ZnO structure as seen from the ZnO reference pattern included. Diffraction was carried out with a Mo source (λ = 0.7093 Å).

water from the sample, and again for both samples there was another change in mass, this time accompanied by a DSC exotherm (see the regions marked in green), representing the breakdown of the surface-bound citrate molecules. The cit:ITO sample had an additional change not observed for the cit:AGZO sample, in that (as can be seen in the purple region in Figure 6.10) further loss of mass was observed in the temperature range ca. 350 - 400 °C, accompanied by a slight, ill-defined endotherm. This, taking XRD and XPS analysis into account, is most likely indicative of the structural water lost from the indium oxyhydroxide as it was converted to indium oxide. This made extraction of the actual loading of the citrate difficult,

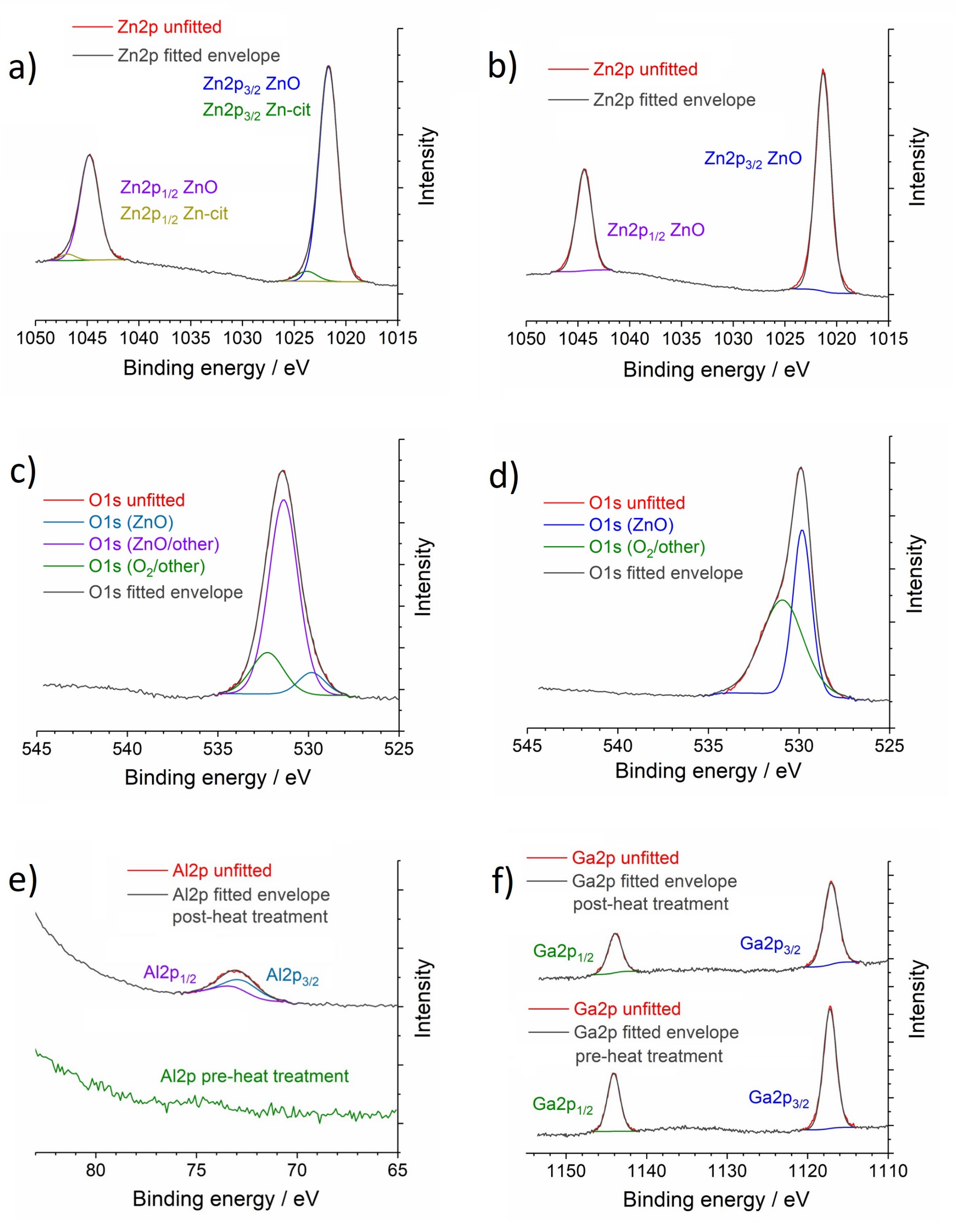

Figure 6.8: XPS spectra for the cit:AGZO material, including a) the Zn 2p region (as-synthesised), b) the Zn 2p region (post-heat treatment), c) the O 1s region (as-synthesised), d) the O 1s region (post-heat treatment), e) the Al 2p region, before and after heat treatment, and f) the Ga 2p region, both before and after heat treatment (lower and upper, respectively).

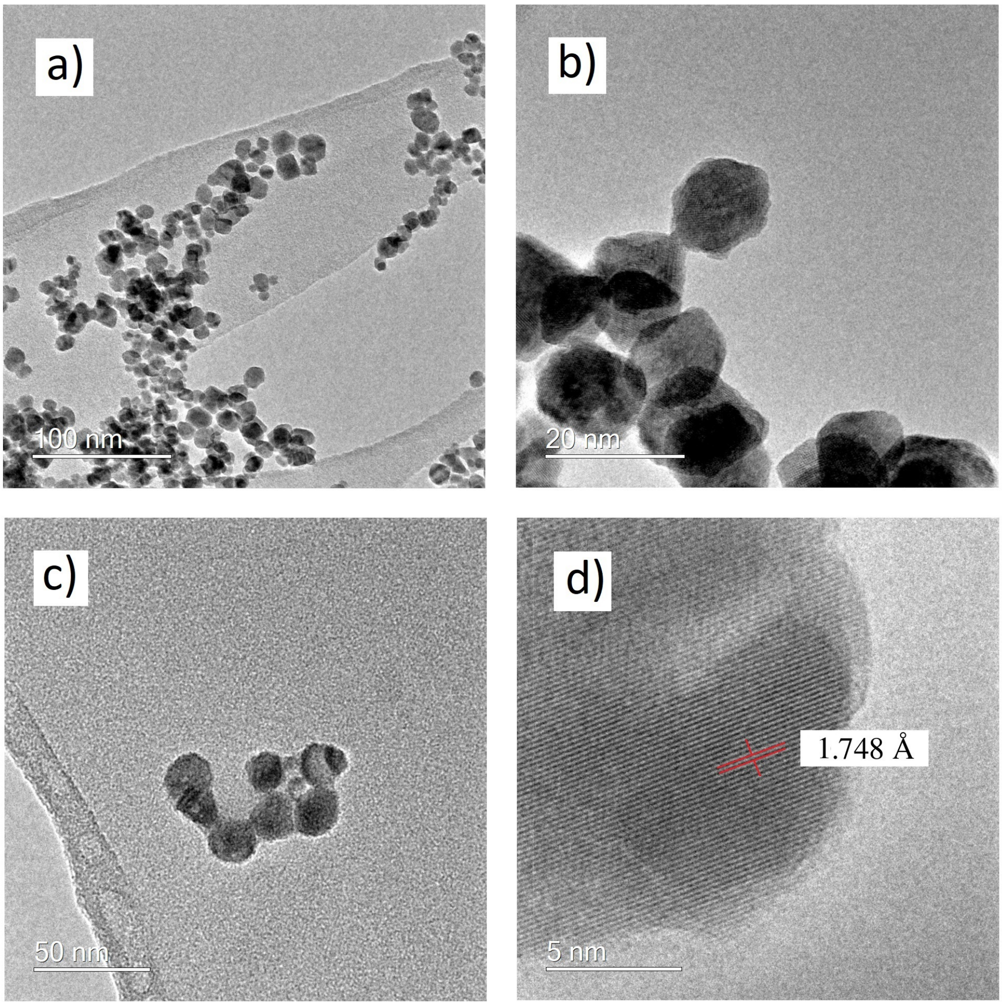

Figure 6.9: TEM images of a) and b) the as-prepared cit:ITO, and c) and d) the as-prepared cit:AGZO. Both materials were made by CHFS according to the procedure outlined in Section 2.2.2

rendering the values as estimates more than calculations. Assuming that the mass change only within the citrate-decomposition exotherm was entirely due to citrate loss, then this accounts for ca. 3.1 % of the mass of the dry sample (i.e. post initial water loss). Citrate accounted for considerably less of the cit:AGZO sample, however, only ca. 1.6 % of the dry mass, approximately half that of the cit:ITO sample. Using Equation 6.1, the grafting density of the citrate was calculated from these to be 2.0 CA nm^{-2} for cit:ITO, and 1.0 CA nm^{-2} for cit:AGZO, based on calculations using particle sized gleaned from TEM image analysis. When compared to the citrate-coated magnetite made previously in CHFS, this had a grafting density of up to 2.6 CA nm^{-2}, so the cit:ITO is very close. However, the density is considerably reduced for the cit:AGZO sample. The reason for this remains unknown, however it suggested a probable reason behind the reduced stability of cit:AGZO in water versus the cit:ITO as measured by DLS.

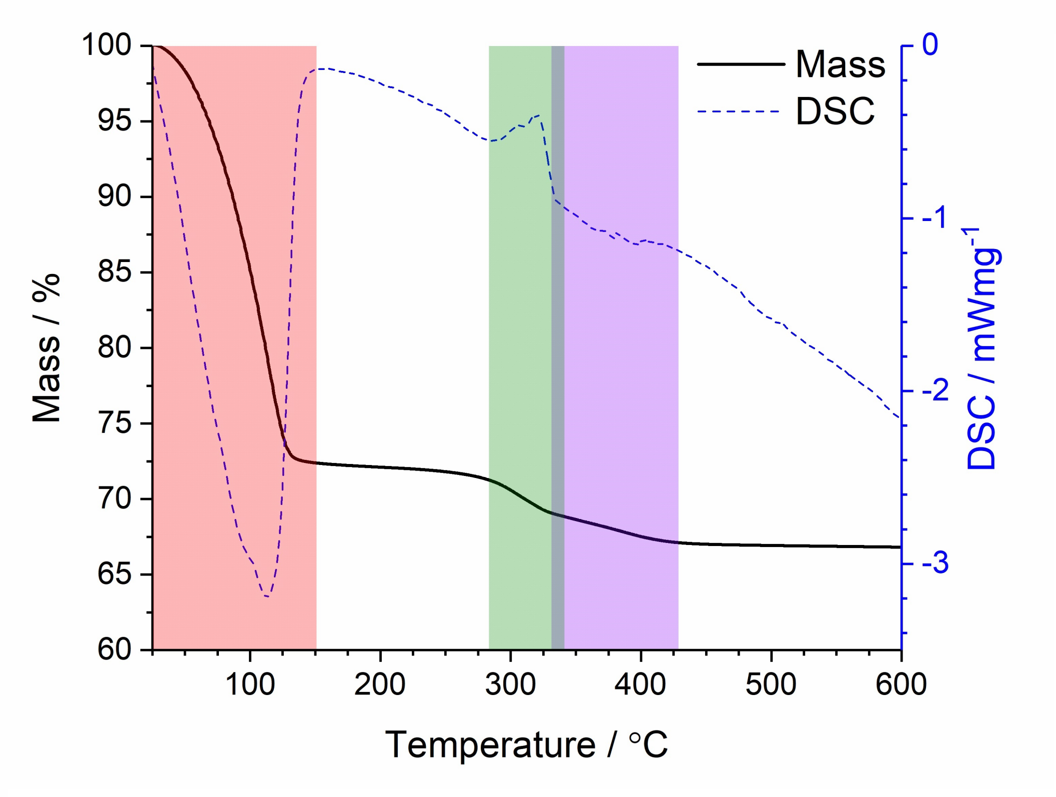

Figure 6.10: Thermogravimetric analysis (TGA) and differential scanning calorimetry (DSC) of the citrate-coated ITO material as a dense wet paste after cleaning of the as-synthesised material. The change in mass is a black solid line, displayed as a percentage loss, while the heat flow from DSC is shown as a blue dashed line.

TGA analysis was important not only with regards to knowing how much citrate was present in each of the samples and the grafting density, but also in determining the solid metal oxide content of the dense pastes to then formulate inks. The ink vehicle was Sun Chemical designation U10197, an approximately 20 wt% ethylene glycol in water-based vehicle with a number of organic additives to lead to improved dispersibility of metal oxide nanoparticles. Note that these additives, and those chemicals added immediately prior to printing to alter the surface tension and viscosity of the inks, are a closely guarded trade secret. Speculation as to their

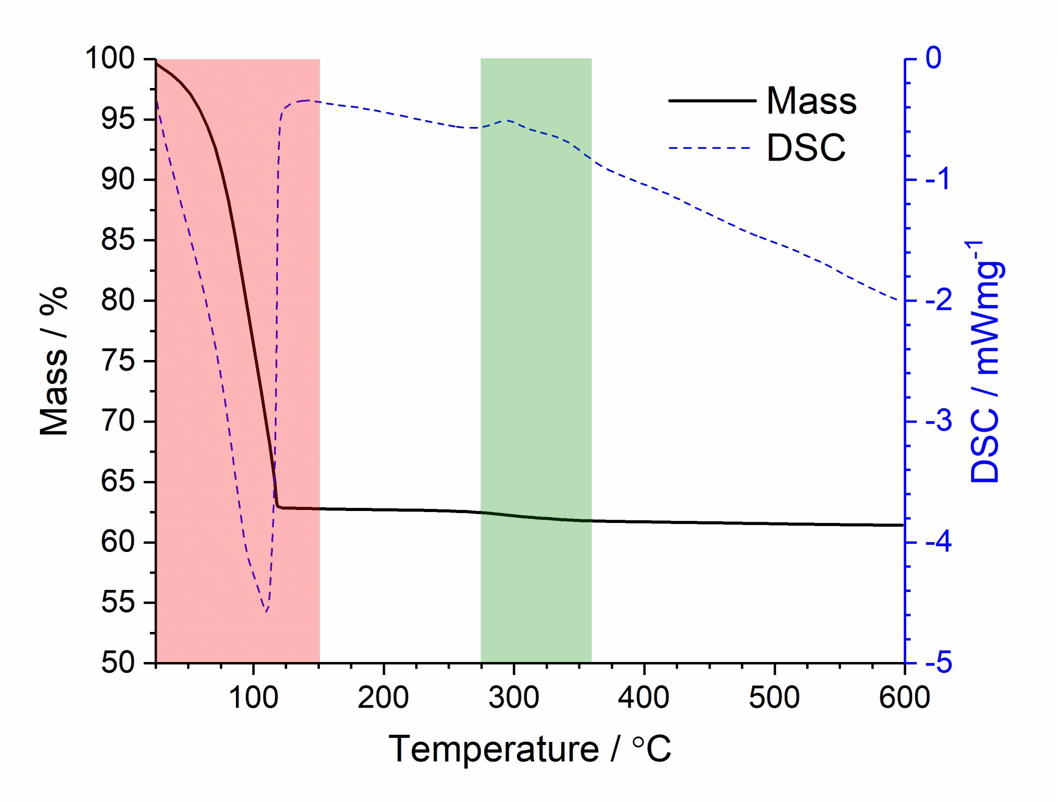

Figure 6.11: Thermogravimetric analysis (TGA) and differential scanning calorimetry (DSC) of the citrate-coated AGZO material as a dense wet paste after cleaning of the as-synthesised material.The change in mass is a black solid line, displayed as a percentage loss, while the heat flow from DSC is shown as a blue dashed line.

identities is beyond the scope of this investigation. The solid metal oxide content of the cit:ITO sample was 66.9 % by mass, and that of the cit:AGZO sample was 61.5 %. Thus to make, for example, a 25 wt% ink of each, 30 g total, to the first would have been added 11.2 g of cit:ITO wet paste and 18.8 g of vehicle U10197, and to the second would have been added 12.2 g of cit:AGZO wet paste and 17.8 g of the ink vehicle. Sonication treatments as described in Section 2.4.2.2 were carried out, resulting in excellent dispersions of the inks, upon which were carried out viscosity measurements.

Figure 6.12 shows a typical dataset for dynamic viscosity readings for a sample at varying shear rates, in this case ink vehicle U10197 with no further additives. From this, the dynamic viscosity of the fluid would be taken as the reading obtained for the highest shear rate for which it was measured (corresponding to the highest percentage torque), for U10197 this was 3.46 cP at a spindle rotation speed of 170 RPM and shear rate 208 s^{-1}. Dynamic viscosity, η (conventionally expressed in centipoise, 1 cP = 1 mPa s), was calculated from the shear rate and shear stress according to equation 6.2, where τ is the shear stress (in N cm^{-2}), and γ is the shear rate (in s^{-1}).

$$\eta = \frac{\tau}{\gamma} \tag{6.2}$$

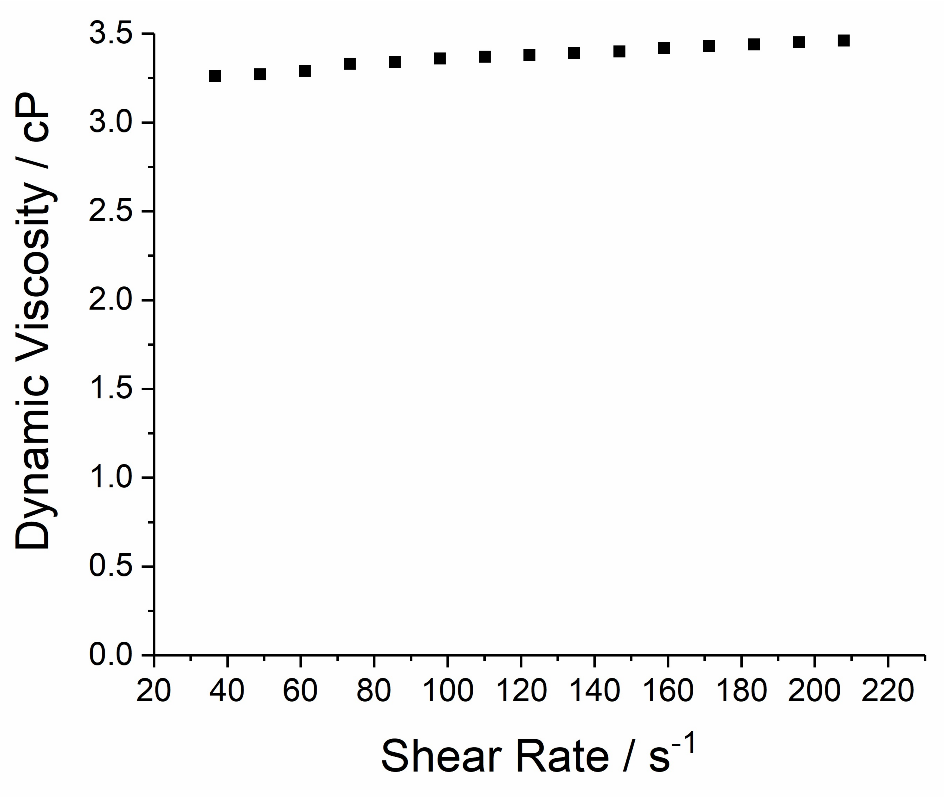

Figure 6.12: An example depiction of the effect of shear rate on the dynamic viscosity, of ink vehicle U10197.

The effect on increasing the mass loading of the inks was, as should have been expected, to increase the viscosity, as shown in Figure 6.13. Loadings of up to 40 wt% cit:ITO in vehicle U10197 were analysed for their dynamic viscosities, which increased exponentially (the linear fitting on the logarithmic plot was calculated to have an adjusted r^2 of 0.99968) from 3.46 cP at 0 wt% (i.e. the vehicle alone), to 6.23 cP at 20 wt% cit:ITO and to a maximum of 11.16 cP at 40 wt%. In all cases,

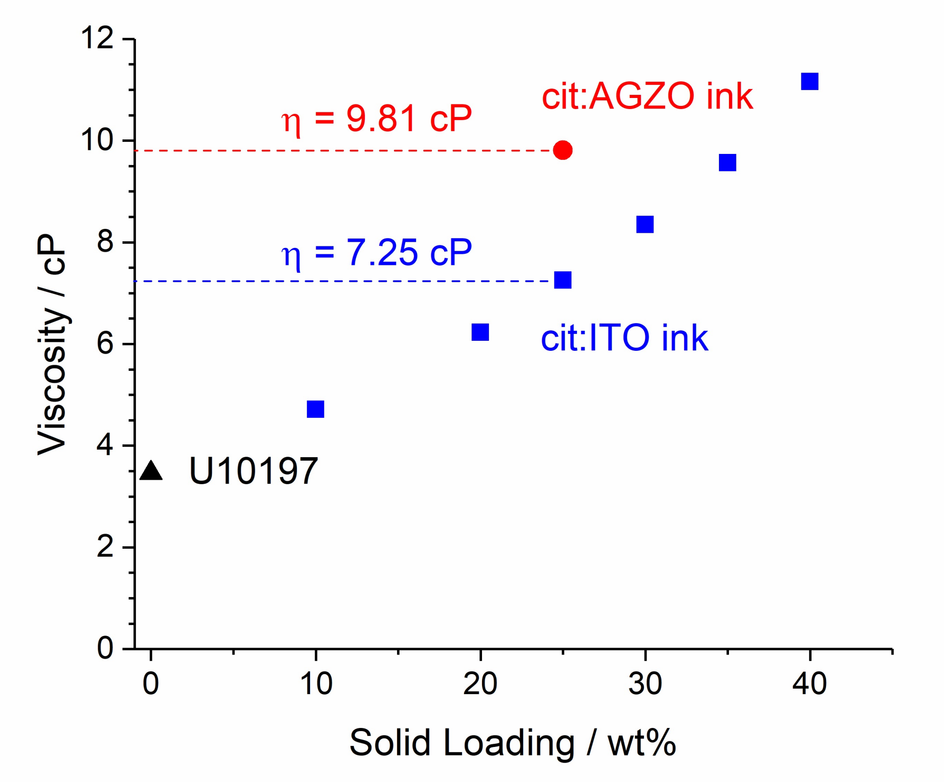

Figure 6.13: The dynamic viscosities of the ink vehicle (U10197), a series of mass loadings of cit:ITO (up to 40 solid wt%), and including the viscosities of the 25 wt% inks of each cit:ITO and cit:AGZO, which were 7.25 cP and 9.81 cP, respectively.

the ink could pass unhindered through a 3.2 μm syringe filter, but only those inks of 30 wt% or less could pass through a 1.2 μm syringe filter without significant blockage from larger agglomerates. Loadings of 35 or 40 wt% were limited to no more than ten separate sonication treatments; further treatments invariably (despite the constant use of an ice bath) led to coagulation of the ink, which could not be reversed or undone.

The desired mass loading for inkjet-printable inks was 25 solid wt%; one for each cit:ITO and cit:AGZO was prepared, and these were couriered to Sun Chemical Ltd., where Dr M. Pickrell and co-workers deposited thin films of each according to the procedure outlined in Section 2.4.4.2.

6.5.2 Inkjet printing results from cit:ITO and cit:AGZO inks

Fewer prints from cit:ITO inks were deposited over the course of the project than of the zinc-based analogues, thus only preliminary results are discussed here, with a good deal more work to be done as part of the investigation. Print quality was inconsistent; many gaps and macro-scale disconnections are clearly visible in the films, as shown in Figure 6.14. The films as-deposited were highly transparent, however were non-conductive. Heat treatments were carried out in H_2/N_2, air, and Ar, and the results are shown in Figure 6.14b, c, and d, respectively, as per the procedure outlined in Section 2.4.4.3. Heat treatment in air resulted in films that were neither transparent, nor conductive. Heat treatment in Ar (as preferred for ITO-based materials)[168] resulted in highly transparent films that were not very conductive; sheet resistances of ca. 25 kΩ were measured by 2-point probe. Heat treatment in a reducing atmosphere resulted in discolouration of the films (see Figure 6.14b) as a result of the burning and inefficient removal of the organic components of the film, principally the citrate bound to the surface of the nanoparticles, but also any components of the ink that were not removed upon drying of the newly-printed film at 90 °C. The resistances plummeted however, to only ca. 40 Ω by 2-point probe, almost a factor of 1000 lower than the films heat treated in Ar. Due to the inconsistency of the film, thickness was impossible to gauge accurately, but could correspond to resistivities around 10^{-3} Ω cm, perhaps as low as the order of 10^{-4} Ω cm depending on the thickness at the point of measuring the resistance.

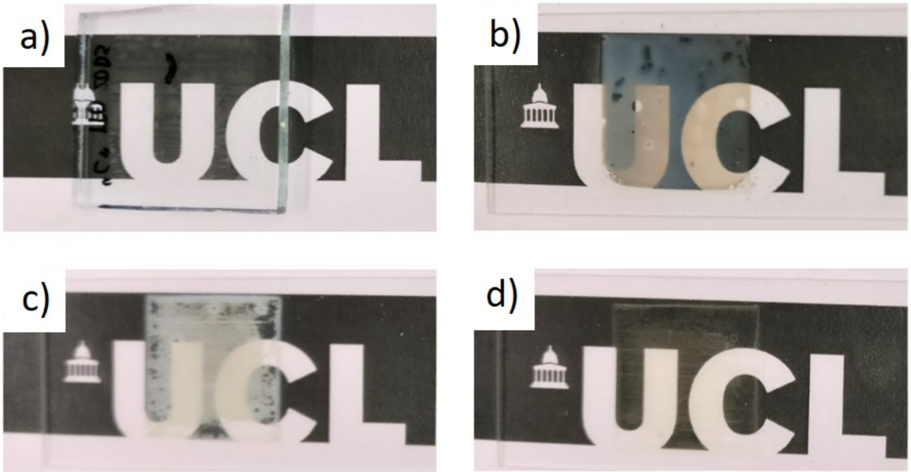

Figure 6.14: Inkjet printed thin films printed from 1:1 cit:ITO inks. a) shows the films as-printed, b) shows the films after heat treatment in 5 % H_2/N_2, c) shows the films after heat treatment in air, and d) shows the films after heat treatment in Ar. All heat treatments were carried out at 550 °C for 5 h onto microscope slides.

Even if the resistivity of the films were to be towards the upper end of the window suggested above, these would still be the most conductive TCO thin films yet deposited by inkjet printing. Further depositions are necessary, and re-formulation of the inks so as to better wet the surface of the glass substrate; this could result in improved, more consistent coverage. An area of relatively even coverage is shown in Figure 6.16 (a and b) of the film shown in Figure 6.14b. In this region, the surface is relatively smooth and featureless, the majority of features can only be seen at X50,000 magnification, but particulates are not easily distinguishable. Returning to the characterisation of the ITO nanoparticles, the relatively un-crystalline (Sn-doped) InOOH appeared to have been annealed especially effectively, forming crystalline ITO with few micro-defects and imperfections in the film, resulting in high conductivity.

Figure 6.15 shows 2 typical inkjet printed films made from cit:AGZO. The as-printed film is non-conductive and has an optical transparency of 80 %. Upon heat treating in a reducing atmosphere (5 % H_2/N_2), the film does not change very much by eye; the transmittance rises to 84 % however, and the film becomes conductive. The lowest resistivities measured for inkjet printed AGZO films are of the order of 10^{-1} Ω cm, considerably higher even than the pressed discs of the material. Deposition of the inks, whether due in part to one or more component of the ink interacting with the ZnO-based nanoparticles, or to the parameters with which the depositions were carried out, did not result in the same conductivity as was seen even in unoptimised inkjet printed ITO. Figure 16 (c and d) shows SEM images of the cit:AGZO film post-heat treatment. More distinct particles were clearly visible than in the ITO analogue, and the surface appeared rougher with cracks and particles. Most notably, many long rodlike needles were visible, up to microns in length, which were not seen at all in TEM images of the nanoparticles after synthesis. Sintering growth appeared to have been preferentially oriented, along the c-axis, possibly accounting in part for a less effective annealing step, and thus a less (electrically) well-connected film and higher resistivity.

Side-on SEM imaging was carried out by Dr P. Marchand on several ZnO-based inkjet printed films, and four representative images are shown in Figure 6.17. Film thickness typically ranged from ca. 1 - 2 μm, and despite some pooling at the edges of the print area (see Figure 6.15), the films were highly regular in thickness.

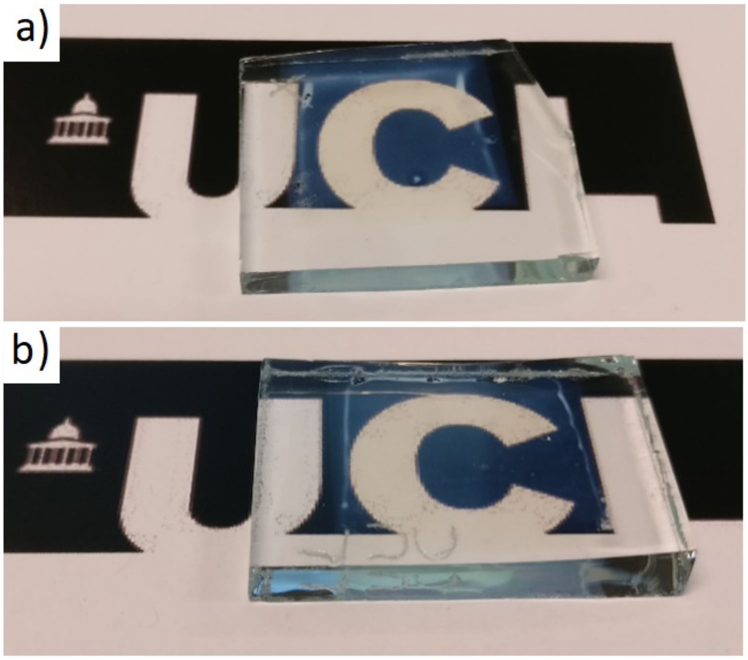

Figure 6.15: Inkjet printed thin films printed from 1:1 cit:AGZO. a) shows an untreated, as-printed film, and b) shows a typical heat treated film. Heat treatments were carried out under 5 % H_2/N_2 at 550 °C for 5 h. The substrate was NSG Pilkington float glass.

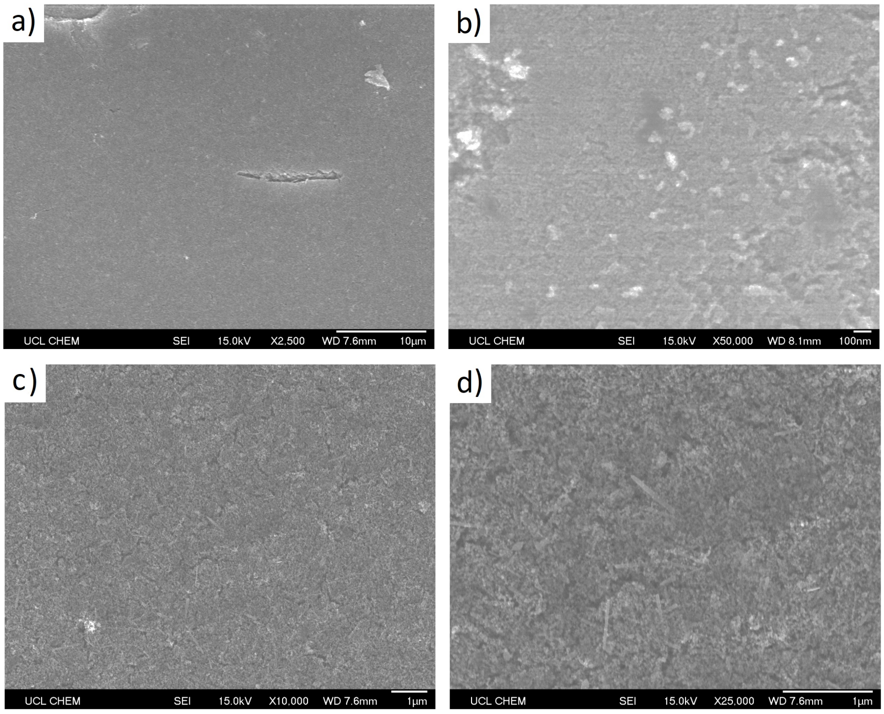

Figure 6.16: SEM images of the surface of a 1:1 cit:ITO inkjet printed film (a and b) and a cit:AGZO inkjet printed film, both heat treated under 5 % H_2/N_2.

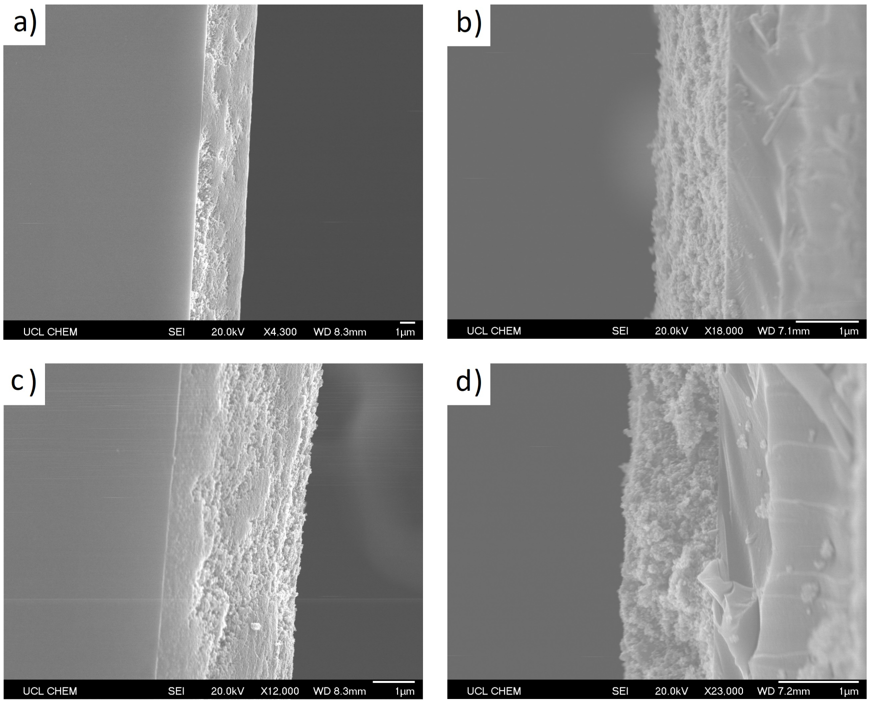

Figure 6.17: Side-on SEM images of inkjet printed films 1:1 cit:AGZO films, to determine thickness. Images were taken by Dr P. Marchand.

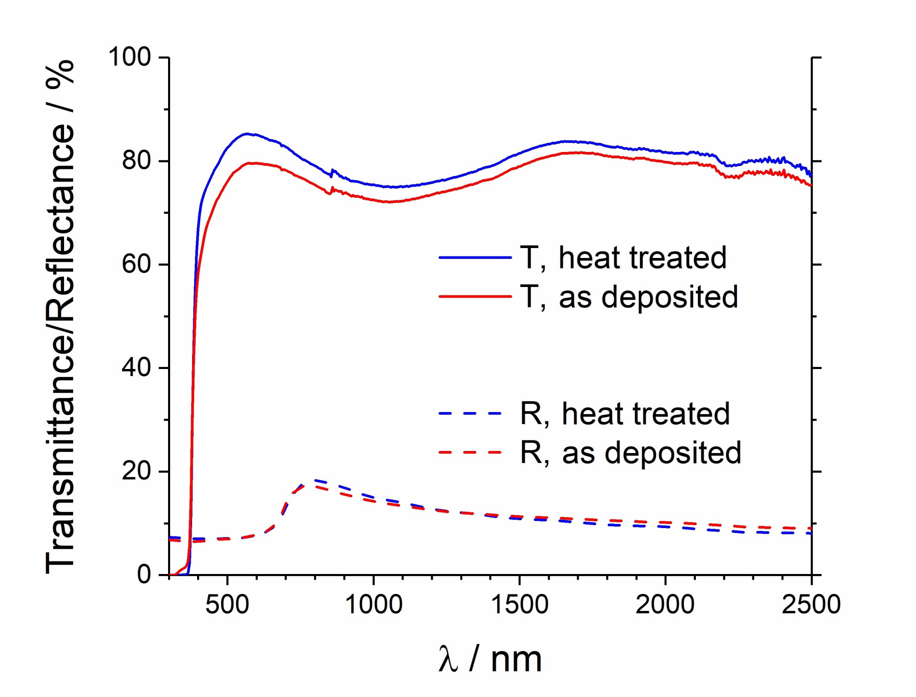

Figure 6.18: UV/Vis/NIR spectra of pre- (red) and post-heat treatment (blue) 1:1 cit:AGZO inkjet printed films, including transmittance, T (solid lines) and reflectance, R (dashed lines) spectra.

6.5.3 Inkjet printing summary and conclusions

Considerably more research is required into the optimisation of inkjet printed TCO films made from inks of CHFS-made coated-nanoparticles, however the results obtained thus far are indicative of immense promise in the area. For both ITO and AGZO, the optimal loading of citrate was obtained by including a 1:1 ratio of citrate to metal in the CHFS process, and this resulted in a 2.0 and 1.0 molecules nm^{-2} surface grafting density for ITO and AGZO, respectively. For both, an endotherm in the DSC indicated the loss of water in the as-prepared paste by ca. 100 °C, and an exotherm indicated the break-down of the surface-bound citrate at ca. 300 °C. The cit:ITO sample experienced a further endotherm due to water loss from the structure as the oxyhydroxide was converted to the oxide in the temperature range ca. 340 - 420 °C.

cit:AGZO printed films were orders of magnitude weaker than industry standards in terms of resistivity (ca. 10^{-1} Ω cm), perhaps due in part to the mode of annealing during heat treatment, which appeared to have preferentially occurred along one axis over the other two, due to the appearance of many rods in the entirely spheroidal as-synthesised nanomaterial. However, the optical properties were as high as needed in most industrial applications, > 80 % post-heat treatment. Even so, without significant improvement in the cit:AGZO printed films' electrical properties, they will remain unsuitable for application as TCO thin films. cit:ITO inkjet printed thin films demonstrated resistivities approaching 10^{-4} Ω cm, depending on the precise thickness of the film in the area tested. This could not be determined with any accuracy or reliability due to the poor coverage and quality of the films. Improved wettability of the ink onto substrates will in future be necessary, as will be improvements in the method of heat treatment so as to avoid the 'burning' observed after the reducing heat treatment, and further investigations into the scaling up of the printing process over larger substrate areas will need to take place before these films could even begin to be implemented industrially. However, if these issues can be addressed, the cit:ITO printed films demonstrate immense promise in the field of TCO thin films.

6.6 Spin Coating of CHFS Nanomaterials

This section investigates the deposition of thin films of CHFS-made nanomaterials by spin coating, including cit:ITO, GZO, AGZO, and SiZO. A considerable amount of work was carried out by N. Kuye in the testing of different dispersing media, and by Dr P. Marchand before her. Some credit is due to both of them in the work subsequently described.

6.6.1 Experimental design and observations

The thin films herein characterised were deposited from dispersions made from 20 wt% cit:ITO, GZO, AGZO, and SiZO in Sun Chemical ink vehicle U10197, dispersed and deposited as described in Section 2.2. Heat treatment of all films was carried out for 5 h at 550 °C, ITO under argon, and ZnO-based materials under 5 % H_2/N_2.

6.6.2 Spin coated films; SEM and optical measurements

Figures 6.19 and 6.20 show SEM images of the spin coated cit:ITO and ZnO-based materials, respectively. Figure 6.19 also includes three representative side-on SEM images, which were used to confirm film thickness as calculated from ellipsometry. As can be seen from the cit:ITO film, it is very similar aesthetically to the inkjet printed film as shown in Figure 6.16. Where it differs significantly is in the thickness. Ellipsometry indicated a thickness of just 90 nm, and this was confirmed from side-on SEM; some regions were slightly thicker, approaching ca. 1 μm, and some were thinner, of the order of a few 10's of nm, however the mean thickness was approximately 100 nm (Figure 6.19c), thus the optical thickness measurements were taken to be accurate for the resistivity measurements and calculations.

The SiZO film was relatively featureless, a smooth film with some small particulate lumps and extrusions as shown from Figure 6.20f. Curiously, the GZO and AGZO films were for the most part smoother still, with much more minor extrusions, but particles were visible of similar size to those of the SiZO. Morphologically, the difference was drastic between the spin-coated AGZO film, and the inkjet printed cit:AGZO film, which should both have annealed similarly, however in the AGZO spin coated film there are very few rods visible, unlike the inkjet printed films, for which rod-like morphology post-heat treatment was the norm (see Figure 6.16d), perhaps indicative that the citrate bound to the surface of the AGZO particles could have been directing the annealing growth of the particles along a particular axis. The films for the ZnO-based materials were too fragile to yield any side-on SEM images; whether due to brittleness of the films themselves, or delicacy in their adhesion to the substrate, no film was ever visible at the cloven edge of the substrate. As such, only the ellipsometry measurements of the thin films gave an indication as to the thickness of the films, but given the apparent accuracy of the technique for the cit:ITO films, the indication that it was an appropriate measure of thickness was reasonably strong. As such, the determined mean thicknesses of the GZO, AGZO, and SiZO spin coated films were 131, 127, and 150 nm, respectively.

UV-Vis-NIR spectra of representative cit:ITO, GZO, AGZO, and SiZO spin coated films are shown in Figures 6.21, 6.22, 6.23, and 6.24, respectively. The cit:ITO (Figures 6.21 and 6.24, respectively) and SiZO films behaved similarly, in that the high transmittance in the visible range fell dramatically at higher wavelengths, i.e. in the near infra-red region of the spectrum. For both of these two films, the reflectance did not rise however, indicating that the materials were absorbing the IR radiation. The GZO film (Figure 6.22) saw the same fall in transmittance in the IR region, but in this case the reflectance increased, indicating that rather than absorbing the IR radiation, the GZO film was reflecting it, a particularly pronounced effect post-heat treatment. The AGZO film (Figure 6.23) behaved similarly to its inkjet printed counterpart (see Figure 6.18), in that the transmittance remained high across the entire range, and the reflectance remained approximately constant, and low. All four of the heat treated films had mean transmittance values across the visible range (400 - 700 nm) above 80 %, as detailed in Table 6.6, with the other optical and electrical characterisation values for the films.

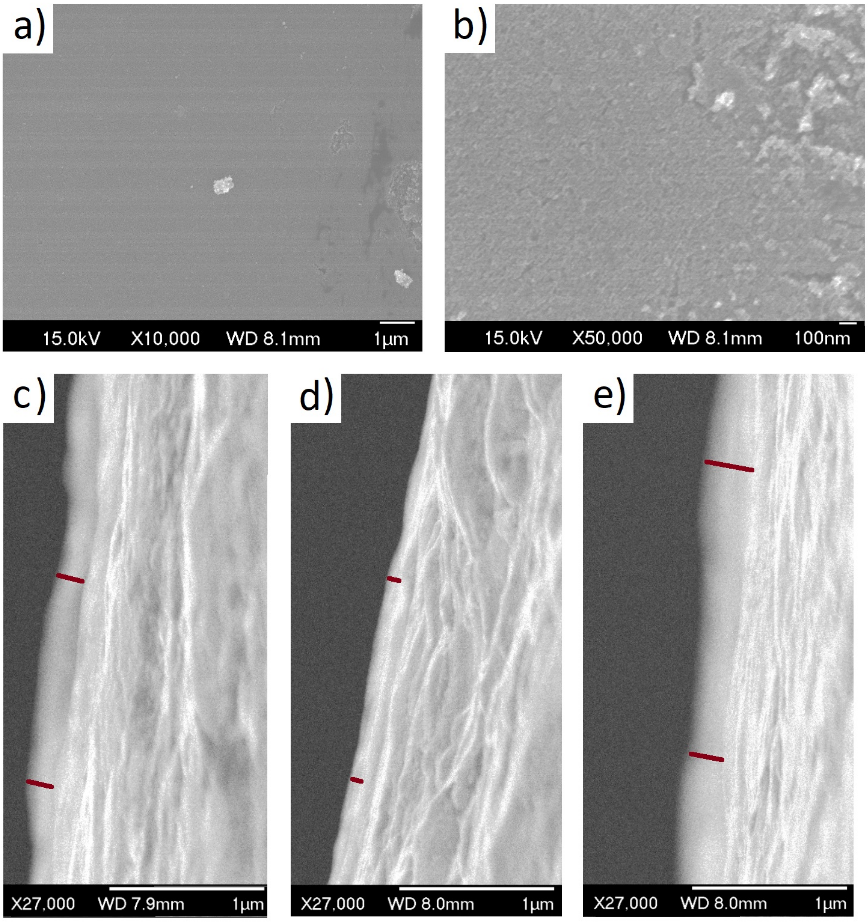

Figure 6.19: SEM images of spin-coated 1:1 cit:ITO films, including surface images (a and b) and side-on (c, d, and e) to gauge thickness.

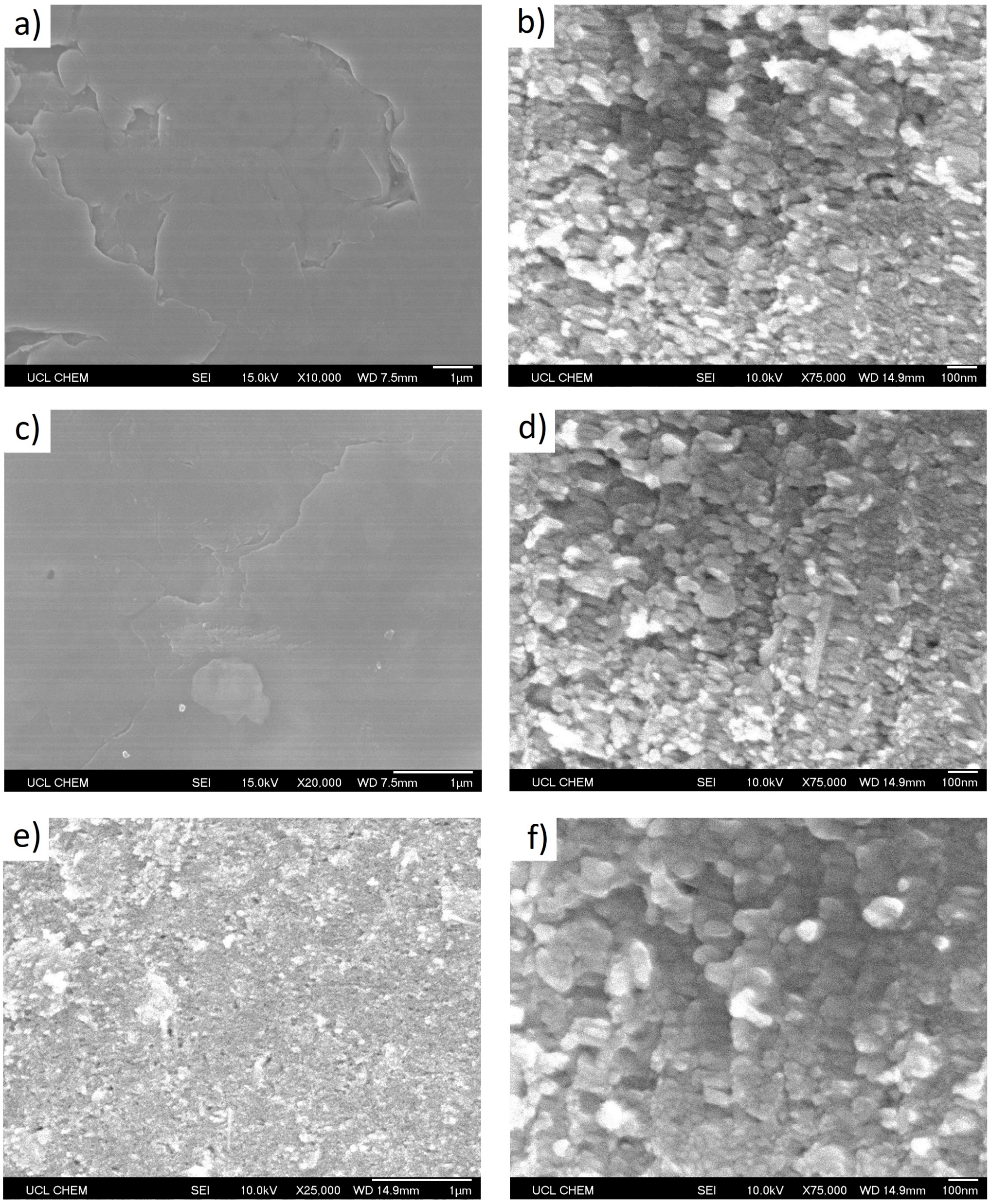

Figure 6.20: SEM images of spin-coated GZO (a and b), AGZO (c and d), and SiZO (e and f) films.

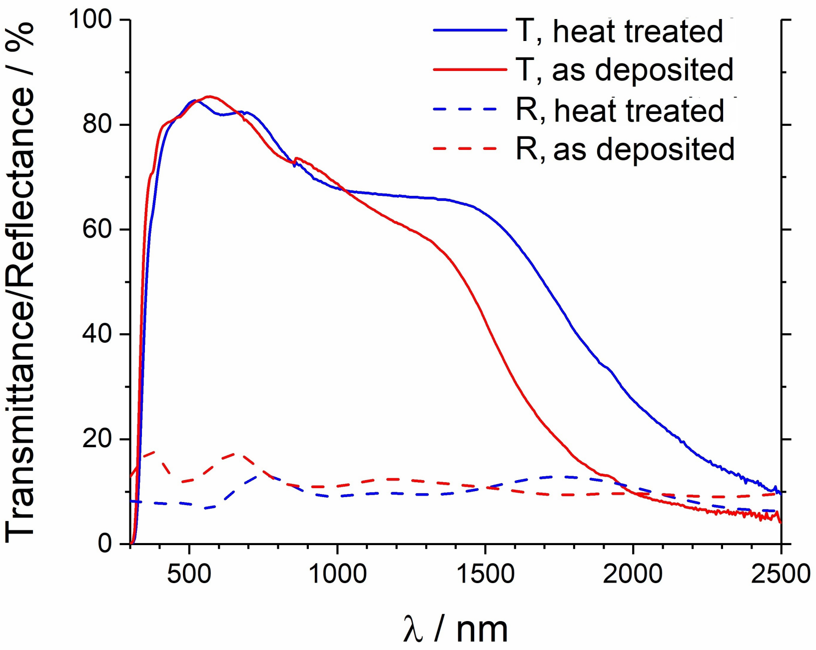

Figure 6.21: UV/Vis/NIR spectra of pre- (red) and post-heat treatment (blue) 1:1 cit:ITO spin coated films, including transmittance, T (solid lines) and reflectance, R (dashed lines) spectra.

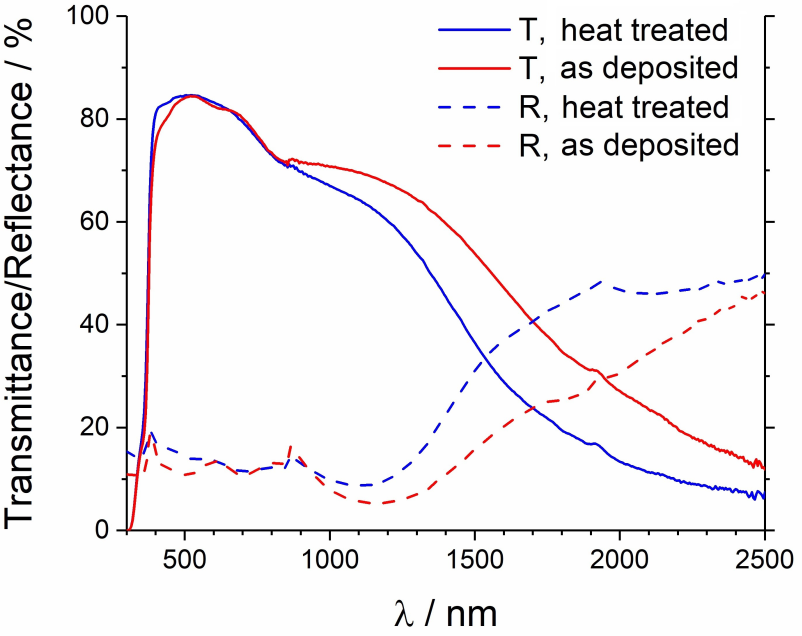

Figure 6.22: UV/Vis/NIR spectra of pre- (red) and post-heat treatment (blue) GZO spin coated films, including transmittance, T (solid lines) and reflectance, R (dashed lines) spectra.

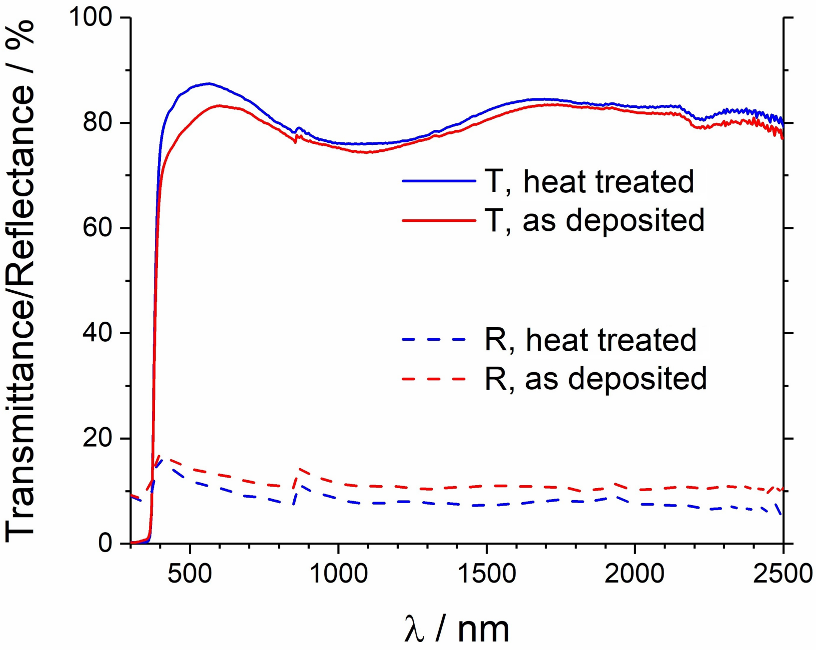

Figure 6.23: UV/Vis/NIR spectra of pre- (red) and post-heat treatment (blue) AGZO spin coated films, including transmittance, T (solid lines) and reflectance, R (dashed lines) spectra.

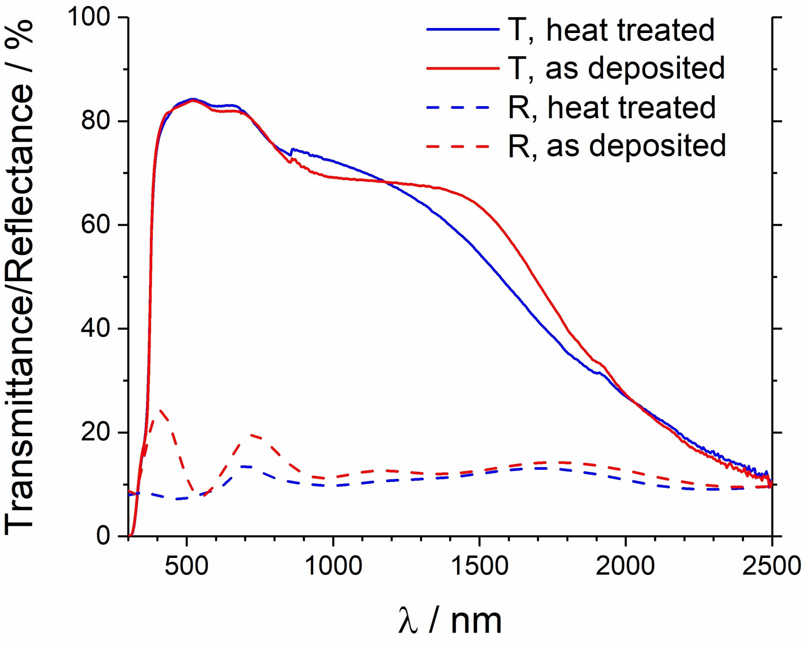

Figure 6.24: UV/Vis/NIR spectra of pre- (red) and post-heat treatment (blue) SiZO spin coated films, including transmittance, T (solid lines) and reflectance, R (dashed lines) spectra.

6.6.3 Spin coated films; electrical measurements

Electrical data is summarised in Table 6.6 with the optical measurements carried out. Resistivity, and charge carrier concentration and mobility values are the mean values from three Hall Effect measurements on the best performing thin film of each material. Note that the four electrical contact points were ca. 8 - 10 mm apart for all four films.

The SiZO film performed adequately enough, resistivity to the lower end of 10^{-3} Ω cm was not as low as for many films deposited by magnetron sputtering[134, 135, 147, 279] or pulsed laser deposition,[136, 208] but given the high transparency, for certain applications it could be acceptable, especially given the very low cost of the material. The mobility value of 11 cm^2 V^{-1} s^{-1} was middling to low, but the charge carrier concentration was around the values the afore-cited studies achieved, just reaching the order of 10^{20} cm^{-3}.

As discussed in Section 6.2, the only thin films of AGZO thus far characterised in literature achieving resistivities of the order of 10^{-4} Ω cm were deposited by magnetron sputtering. Of these, the lowest had a resistivity of 3.0 x 10^{-4} Ω cm.[130] Working under the assumption that the optically measured thickness of the film characterised in this section is accurate, it was more conductive than any thin film of AGZO yet reported, at 1.9 x 10^{-4} Ω cm. The charge carrier mobility of 20.1 cm^2 V^{-1} s^{-1} was towards the higher end of those of the sputtered films, and the carrier concentration is higher than all of them, at 1.7 x 10^{21} cm^{-3}, part of the reason the resistivity is so low.[131–133, 260, 262, 263, 287]

The GZO spin coated film had very similar properties to that of AGZO, a resistivity of 1.7 x 10^{-4} Ω cm, slightly higher carrier concentration, and slightly lower mobility. The mobility was around that seen in previous reports, the concentration higher than most, with only one study measuring one higher.[124] Again, some doubt could be cast that the thickness measurements might not have been accurate as they could not be corroborated by side-on SEM. But again, assuming the thickness measurement to be accurate, the resistivity obtained was superior to the vast majority of the studies reported thus far.[121, 125–129, 249]

Narrowly breaking into the order of 10^{-5} Ω cm, the cit:ITO spin coated film easily meets the industry standard requirements, surpassing all but a few reported studies, and those only based on pre-eminent magnetron sputtering and pulsed laser deposition methods. The mobility of 23.7 $cm^2\ V^{-1}\ s^{-1}$ is not close to the theoretical limits of the material, but the very strong carrier concentration makes up for this limitation, at 2.8 x 10^{21} cm^{-3}. As alluded to already, the film quality post-annealing appears to be a critical factor; a well-packed film consisting of citrate coated particles of mostly amorphous tin-doped indium oxyhydroxide was deposited by spin coating, which annealed and crystallised together, forming a dense, cohesive ITO film, which demonstrated exceptional optical and electrical properties. It is the most conductive TCO thin film deposited from a nanoparticle dispersion, ever. Data for spin coated thin films of this material, and for the other three, are summarised in Table 6.6.

Table 6.6: Summary of the optical and electrical characterisation data for the four spin coated materials; cit:ITO, GZO, AGZO, and SiZO. Data includes transmittance, thickness from ellipsometry, charge carrier concentration (n) and mobility (μ), and resistivity (ρ).

Material	**cit:ITO**	**GZO**	**AGZO**	**SiZO**
Transmittance / %	81.9	83.0	85.2	82.1
Thickness / nm	90	131	127	150
n / cm^{-3} x 10^{21}	2.8	1.9	1.7	0.1
μ / $cm^2\ V^{-1}\ s^{-1}$	23.7	18.8	20.1	11.0
ρ / Ω cm x 10^{-4}	0.94	1.8	1.9	24.3

6.6.4 Spin-coating summary

Spin-coating of the CHFS nanomaterials resulted in thin films with considerably enhanced conductivities, mobilities, and charge carrier concentrations than for the analogous pressed, heat treated discs. The spin coated SiZO film did not perform as well as conventionally deposited films from other reports, with the lowest resistivity measured of 2.4 x 10^{-3} Ω cm, not quite reaching the order of 10^{-4} Ω cm. However, the cit:ITO, GZO, and AGZO spin coated films surpassed the properties (particularly the electrical properties) of the majority of previously reported films by various deposition methods, with resistivities of 0.9, 1.8, and 1.9 x 10^{-4} Ω cm, respectively. In each case these are the most conductive films yet reported for thin films deposited from nanoparticle dispersions, and in the case of the AGZO film, it was the most conductive film of all previous reports, surpassing even the best magnetron sputtered films.[130, 131] Transmittance of all films was over 80 % across the visible range, and thickness was determined by ellipsometry, side-on SEM only used in the case of the cit:ITO film. The ZnO-based films were determined to be 130 - 150 nm thick, the cit:ITO film only 90 nm thick.

6.7 Overall Conclusions

Surface functionalisation of ITO and AGZO was carried out, and in each case the optimal loading of citrate onto the surface was determined to be in a 1:1 ratio with the metal, from zeta potential measurements of the samples, and the cit:ITO had a lower zeta potential at pH 7 than the cit:AGZO (i.e. it was more stable in dispersion). From these materials, inks were formulated and deposited by inkjet printing in collaboration with Sun Chemical (Dr M. Pickrell). cit:AGZO films demonstrated the required optical transparency ($>$ 80 %) required of TCO films, however the resistivity only ever reached ca. 10^{-1} Ω cm, considerably more resistive than required. cit:ITO films suffered in kind; those heat treated in Ar were optically transparent but similarly resistive, and those heat treated in 5 % H_2/N_2 were considerably less transmissive, but demonstrated resistivities nearing 10^{-4} Ω cm; should the optical properties be capable of improvement then cit:ITO inkjet printed films could become industrially viable alternatives to magnetron sputtered films, as almost ubiquitously used in TCO depositions today.

Spin coating of cit:ITO, GZO, AGZO, and SiZO resulted in thin films with highly competitive electrical and optical properties, with resistivities of 9.4 x 10^{-5} Ω cm, 1.8 10^{-4} Ω cm, 1.9 10^{-4} Ω cm, and 2.4 10^{-3} Ω cm, respectively. These values were (comparatively between the materials) in keeping with previous reports testing the materials as pressed, heat treated discs, for which ITO had the lowest resistivity, GZO and AGZO similar but higher, and SiZO five times higher resistivity again.[5–7, 168] These represent, for each of the four materials, the most conductive thin films yet reported for depositions of dispersed nanoparticles by a considerable margin.

Though the spin coating results were very promising indeed, the process is still relatively wasteful; it was one of the aims of the thesis to deposit thin films of the materials by inkjet printing (a zero-waste deposition process) with sufficient optoelectronic properties that the films could be applied as transparent conducting films in industry. This was not achieved; electronically, or optically, every film thus far has failed to reach the benchmarks set. cit:ITO inkjet printed films show the most promise, as they at least appear to have reached the electronic properties required of TCOs, however more work is required in the optimisation of the deposition and heat treatment steps to give more consistent, and indeed transparent, films.

Chapter 7

Conclusions and Outlook

This project had three investigative steps generated by the central hypothesis. First, was to use continuous hydrothermal flow synthesis (CHFS) to identify ZnO-based replacement materials for indium tin oxide (ITO) in transparent conducting oxide (TCO) applications. Then, to optimise the most promising materials in terms of the electronic properties. And finally, to surface-functionalise selected CHFS nanomaterials to facilitate the formulation of stable dispersions and inks, which could then be deposited by such methods as inkjet printing and spin coating.

In pursuit of the first, Chapter 3 discussed the dopant screening experiments, including the synthesis and characterisation of a number of different doped zinc oxides. These were screened as pressed, heat treated discs by performing Hall Effect measurements to determine the bulk resistivity of the materials. As ITO had previously been synthesised, tested and optimised by the same methods, it was used as the benchmark, achieving resistivities as low as 6 x 10^{-3} Ω cm. Of all doped zinc oxides synthesised and tested, only four unoptimised materials obtained resistivities within two orders of magnitude of this. This was judged to be acceptable variance from ITO's electrical properties, as this was a single, arbitrarily chosen composition (2 at% dopant with respect to 98 at% Zn) of each material, and had not yet been optimised. These materials were ZnO doped with Al, Cu, Ga, and Si. Of these, Cu-doping resulted in a material that was dark in colour, black post-heat treatment, marking it inappropriate for use as a TCO, and so the three materials that were highlighted for further investigation as potential ITO replacements were

Al-doped ZnO (AZO), Ga-doped ZnO (GZO), and Si-doped ZnO (SiZO).

Chapter 4 discussed the compositional optimisation of AZO and GZO, finding that the lowest resistivities occurred at dopant levels of 2.5 at% Al and 3.5 at% Ga, respectively, with resistivities of 7.0 x 10^{-3} Ω cm and 9.1 x 10^{-3} Ω cm for AZO and GZO, respectively, both very close to the optimally resistive ITO sample. Further investigation was carried out in the co-doping of these materials (Al- and Ga-co-doped ZnO, AGZO), in an attempt to balance the chemical instability of AZO, and the high costs associated with the use of Ga in GZO. This compositional screening, also included in Chapter 4, indicated that three compositions of AGZO gave similar resistivities to singularly doped GZO, with compositions described as (Al at%,Ga at%)AGZO of (1.0,2.0)AGZO, (2.0,2.0)AGZO, and (3.0,1.0)AGZO obtaining resistivities of 9.1 x 10^{-3} Ω cm, 9.3 x 10^{-3} Ω cm, and 9.4 x 10^{-3} Ω cm, respectively. Of these, the narrowest distribution of measurements (i.e. the most reliable) was of the sample synthesised with 2 at% of each Al and Ga. As such, this material was selected for surface functionalisation experiments as discussed in Chapter 6.

Chapter 5 first conducted the compositional optimisation of SiZO, finding that the most conductive sample made was that with 0.25 at% Si, a considerably lower dopant level than for AZO, GZO, or AGZO. This had a resistivity some four times higher than GZO and AGZO, however, with ρ = 3.5 x 10^{-2} Ω cm. Introduction of Al and Ga as co-dopants improved the electrical properties; in each case the most conductive sample had 0.25 at% Si and 1.5 at% of either Al, or Ga. These materials, SiAZO and SiGZO, obtained resistivities of 8.3 x 10^{-3} Ω cm and 11.3 x 10^{-3} Ω cm, respectively, very close to the singularly doped AZO and GZO materials. Future work to functionalise these and deposit as thin films would be a logical continuation of the project.

Chapter 6 discussed the pursuit of the final project goal, the functionalisation and deposition of CHFS nanomaterials into thin films. Functionalisation was implemented by inclusion of sodium citrate in the CHFS process, introduced at a second mixing point. This quenched particle growth and introduced citrate to the surface of the particles. The two systems for which this was investigated were ITO and AGZO, and for both of these the optimal loading was achieved by a 1:1 ratio of citrate to metal in the CHFS process. From these, cit:ITO and cit:AGZO, were formulated large ink batches, which were deposited by inkjet printing in collaboration with Dr M. Pickrell of Sun Chemical. These films showed promise either optically, or electrically, but never both at the same time in the same film. cit:ITO printed films neared the conductivity requirements of a TCO thin film when heat treated in a reducing atmosphere, perhaps within an order of magnitude (though precise determination of resistivity was not possible due to inconsistent film coverage). This would represent the most conductive injet printed TCO film reported by orders of magnitude, but further depositions and testing are absolutely necessary in the future, as well as improvements to the heat treatment regime so as not to hamper the optical properties of the films. cit:AGZO films were optically and aesthetically superior, however suffered from high resistivities. Formulation optimisation, and improved sintering should be the focus of future research to match the electrical properties required of TCO thin films.

Chapter 6 went on to cover the spin coating of optimised cit:ITO, GZO, AGZO, and SiZO. Each of these films, though the deposition technique was more wasteful than inkjet printing would have been, obtained competitive resistivities, particularly the former three, which showed resistivities of 9.4 x 10^{-5} Ω cm, 1.8 10^{-4} Ω cm, and 1.9 10^{-4} Ω cm, for cit:ITO, GZO, and AGZO, respectively. These are among the most conductive thin films ever reported for any of those materials, particularly significant when noting that this is when compared principally to the sputtering techniques typically used in industrial TCO thin film depositions. When compared to other thin films made from nanoparticle dispersions, these (including the SiZO film, with ρ = 2.4 x 10^{-3} Ω cm) are the most conductive films yet reported by a considerable margin, where comparisons exist at all.

The cit:ITO film was robust, and optimally measured thickness could be corroborated by side-on SEM, however the mechanical strength of the ZnO-based films was lacking. Dropping the film to the floor resulted in significant cracks, and cleaving the substrate destroyed the film to the point that side-on SEM images could not be retrieved for any of the films. It is possible that spin coating of citrate-coated ZnO analogues could aid in the formation of denser, more robust films, and this could be investigated further. Also, as alluded to above, there are other 'optimal materials' for which depositions were not carried out as part of this investigation, including the SiAZO and SiGZO films, and the other optimally conductive AGZO samples. These offer similar solutions to the issues of singularly doped AZO and GZO, by reducing cost and hopefully increasing the chemical stability. Furthermore, this project was limited only to ZnO as the host material. There is precedent for SnO_2 and TiO_2-based materials too; a dopant screen could be carried out for each, followed similarly by compositional optimisation of the most promising materials and finally surface-functionalisation and deposition as thin films.

In conclusion, the goals that were set out in the beginning of the project have broadly been accomplished, though incompletely. There is scope for further research into different dopants (for example, those highlighted in Chapter 3 that were judged insufficiently conductive), different material families altogether, such as SnO_2, and the work as detailed in Chapter 6 would benefit from many more depositions, particularly of the cit:ITO ink by inkjet printing, if the deposition technique is ever to be taken seriously as an industrially viable alternative to magnetron sputtering. Investigations into spin coating of CHFS nanomaterials have demonstrated unequivocally that the materials are capable of exemplary, in some cases unparalleled, optical and electronic properties as thin films. As such they are worth future consideration and experimentation, in order to fully realise their potential, and perhaps through them the potential of the inkjet printing on the whole, in pursuit of a more sustainable, cheaper, and less wasteful technique to generate TCO thin films.

Bibliography

[1] T. Sanders. https://en.wikipedia.org/wiki/File:Diagram_of_pulsed_laser_deposition.png (accessed 31.08.17), 2016.

[2] Clement J. U. Denis. *Nucleation and growth of industrial nanomaterials in a continuous hydrothermal reactor*. PhD thesis, 2016.

[3] J. A. Darr, C. J. Tighe, and R. I. Gruar. Co-current mixer, apparatus, reactor and method for precipitating nanoparticles. U.S. Patent 9,192,901, 2015.

[4] Heinz Schulz and K. H. Thiemann. Structure parameters and polarity of the wurtzite type compounds Sic-2H and ZnO. *Solid State Communications*, 32(9):783–785, 1979.

[5] D. P. Howard, P. Marchand, I. D. Johnson, C. J. Carmalt, I. P. Parkin, and J. A. Darr. Conducting Al and Ga-doped zinc oxides; rapid optimisation and scale-up. *J. Mater. Chem. A*, 4(33):12774–12780, 2016.

[6] Dougal P. Howard, Peter Marchand, Liam McCafferty, Claire J. Carmalt, Ivan P. Parkin, and Jawwad A. Darr. High-Throughput Continuous Hydrothermal Synthesis of Transparent Conducting Aluminum and Gallium Co-doped Zinc Oxides. *ACS Combinatorial Science*, 19:239–245, 2017.

[7] Dougal P. Howard, P. Marchand, Ivan P. Parkin, Claire J. Carmalt, and Jawwad A. Darr. Si-doped Zinc Oxide Transparent Conducting Oxides; Nanoparticle Optimisation, Scale-up and Thin Film Deposition. *Journal of Materials Chemistry C*, 5(34):8796–8801, 2017.

[8] P. Scherrer. Bestimmung der Größe und der inneren Struktur von Kolloidteilchen mittels Röntgenstrahlen. *Nachrichten von der Gesellschaft der Wissenschaften zu Göttingen, Mathematisch-Physikalische Klasse*, 1918:98–100, 1918.

[9] A. L. Patterson. The scherrer formula for X-ray particle size determination. *Physical Review*, 56(10):978–982, 1939.

[10] Klaus Ellmer. Past achievements and future challenges in the development of optically transparent electrodes. *Nature Photonics*, 6(12):809–817, nov 2012.

[11] K Ellmer. Resistivity of polycrystalline zinc oxide films: current status and physical limit. *Journal of Physics D: Applied Physics*, 34(21):3097–3108, 2001.

[12] David O. Scanlon and Graeme W. Watson. On the possibility of p-type SnO2. *Journal of Materials Chemistry*, 39(39):25236–25245, 2012.

[13] P. D C King, T. D. Veal, F. Fuchs, Ch Y. Wang, D. J. Payne, A. Bourlange, H. Zhang, G. R. Bell, V. Cimalla, O. Ambacher, R. G. Egdell, F. Bechstedt, and C. F. McConville. Band gap, electronic structure, and surface electron accumulation of cubic and rhombohedral In2 O3. *Physical Review B - Condensed Matter and Materials Physics*, 79(20):1–10, 2009.

[14] K Reimann and M Steube. Experimental determination of the electronic band structure of SnO2. *Solid State Communications*, 105:649–652, 1998.

[15] A. Mang, K. Reimann, and St Rübenacke. Band gaps, crystal-field splitting, spin-orbit coupling, and exciton binding energies in ZnO under hydrostatic pressure. *Solid State Communications*, 94(4):251–254, 1995.

[16] B. Kramm, A. Laufer, D. Reppin, A. Kronenberger, P. Hering, A. Polity, and B. K. Meyer. The band alignment of Cu 2O/ZnO and Cu 2O/GaN heterostructures. *Applied Physics Letters*, 100(9):094102, 2012.

[17] W. Martienssen and H. Warlimont. *Springer Handbook of Condensed Matter and Materials Data*. 2005.

[18] H.a. Al-Jawhari. A review of recent advances in transparent p-type Cu$_2$O-based thin film transistors. *Materials Science in Semiconductor Processing*, 40:241–252, 2015.

[19] Anderson Janotti, Eric Snow, and Chris G. Van de Walle. A pathway to p-type wide-band-gap semiconductors. *Applied Physics Letters*, 95(17):172109, 2009.

[20] Dilawar Ali, M Z Butt, Iqra Muneer, Farooq Bashir, and Murtaza Saleem. Correlation between structural and optoelectronic properties of tin doped indium oxide thin films. *Optik - International Journal for Light and Electron Optics*, 128:235–246, 2017.

[21] D Reyes-Coronado, G Rodríguez-Gattorno, M E Espinosa-Pesqueira, C Cab, R de Coss, and G Oskam. Phase-pure TiO(2) nanoparticles: anatase, brookite and rutile. *Nanotechnology*, 19(14):145605, 2008.

[22] Roy G Gordon. C riteria for Choosing Transparent Conductors. *MRS Bulletin*, (August):52–57, 2000.

[23] Brian G Lewis and David C Paine. Applications and Processing of Transparent. *MRS Bulletin*, 25(August):22–27, 2000.

[24] R B H Tahar, T Ban, Y Ohya, and Y Takahashi. Tin doped indium oxide thin films: Electrical properties. *Journal of Applied Physics*, 83(5):2631–2645, 1998.

[25] G Frank and H Kostlin. Electrical Properties and Defect Model of Tin-Doped Indium Oxide Layers. *Applied Physics A*, 27:197–206, 1982.

[26] John C C Fan and John B Goodenough. Xray photoemission spectroscopy studies of Sndoped indiumoxide films. *Journal of Applied Physics*, 48(8):3524–3531, 1977.

[27] P. P. Edwards, A. Porch, M. O. Jones, D. V. Morgan, and R. M. Perks. Basic materials physics of transparent conducting oxides. *Dalton Transactions*, (19):2995, 2004.

[28] D. Feng and G. Jin. Transport Properties. In *Introduction to Condensed Matter Physics: Volume 1*, pages 199–231. World Scientific, 2005.

[29] David O. Scanlon and Graeme W. Watson. Undoped n -Type Cu 2 O: Fact or Fiction? *The Journal of Physical Chemistry Letters*, 1(17):2582–2585, sep 2010.

[30] Swati Ray, Ratnabali Banerjee, N. Basu, A. K. Batabyal, and A. K. Barua. Properties of tin doped indium oxide thin films prepared by magnetron sputtering. *Journal of Applied Physics*, 54(6):3497–3501, 1983.

[31] Yuzo Shigesato, Satoru Takaki, and Takeshi Haranoh. Electrical and structural properties of low resistivity tin-doped indium oxide films. *Journal of Applied Physics*, 71(7):3356–3364, 1992.

[32] H A Mcmaster. Conductive coating for glass and method of application, 1947.

[33] M S Tarnopol. Indium oxide coating on a silicious base, 1954.

[34] J. F. Wager, D. A. Keszler, and R. E. Presley. Applications. In *Transparent Electronics*, chapter 3, pages 39–56. Springer, Boston, MA, 2008.

[35] C. W. Tang and S. A. Vanslyke. Organic electroluminescent diodes. *Applied Physics Letters*, 51(12):913–915, 1987.

[36] C. G. Granqvist. Solar energy materials - Overview and some examples. *Applied Physics A Solids and Surfaces*, 52(2):83–93, 1991.

[37] P D C King and T D Veal. Conductivity in transparent oxide semiconductors. *Journal of physics. Condensed matter : an Institute of Physics journal*, 23(33):334214, aug 2011.

[38] Tadatsugu Minami and Toshihiro Miyata. Present status and future prospects for development of non- or reduced-indium transparent conducting oxide thin films. *Thin Solid Films*, 517(4):1474–1477, 2008.

[39] Claes G. Granqvist. Electrochromics for smart windows: Oxide-based thin films and devices. *Thin Solid Films*, 564:1–38, aug 2014.

[40] NanoMarkets. Transparent Conductor Markets 2014-2021. Technical report, 2014.

[41] Allied Market Research. Transparent Conductive Films Market by Technology (ITO on PET, ITO on Glass, Non ITO oxides, Silver Nanowires, Graphene, Carbon Nanotube, Metal Mesh, Micro fine Wire, PEDOT) and Application (Smart Phones, Tablets and tablet PCs, Notebooks, All-in-one PCs,. Technical report, 2014.

[42] Research and Markets. Transparent Conductive Films (TCF) 2017-2027: Forecasts, Markets, Technologies. Technical report, 2017.

[43] Touch Display Research Inc. ITO-Replacement Report, January 2016. Technical report, 2016.

[44] R. H. Friend, R. W. Gymer, A. B. Holmes, J. H. Burroughes, R. N. Marks, C. Taliani, D. D. C. Bradley, D. A. Dos Santos, J. L. Bredas, M. Logdlund, and W. R. Salaneck. Electroluminescence in conjugated polymers. *Nature*, 397(6715):121–128, 1999.

[45] L Ke, P Chen, R.S. Kumar, and A.P. Burden. Indium-tin-oxide-free organic light-emitting device. *IEEE Transactions on Electron Devices*, 53(6):1483–1486, 2006.

[46] T. D. Kelly and G. R. Matos. Historical statistics for mineral and material commodities in the United States (2016 version): U.S. Geological Survey Data Series 140 (date accessed: 06/06/2017), 2016.

[47] Amy C. Tolcin. U.S. Geological Survey, Mineral Commodity Summaries, January 2017. Technical report, 2017.

[48] Robert D. Brown Jr. U.S. Geological Survey, Mineral Commodity Summaries, January 1998. Technical report, 1998.

[49] Robert D. Brown Jr. U.S. Geological Survey, Mineral Commodity Summaries, January 1999. Technical report, 1999.

[50] Robert D. Brown Jr. U.S. Geological Survey, Mineral Commodity Summaries, January 2000. Technical report, 2000.

[51] Robert D. Brown Jr. U.S. Geological Survey, Mineral Commodity Summaries, January 2001. Technical report, 2001.

[52] Robert D. Brown Jr. U.S. Geological Survey, Mineral Commodity Summaries, January 2002. Technical report, 2002.

[53] John D. Jorgenson. U.S. Geological Survey, Mineral Commodity Summaries, January 2003. Technical report, 2003.

[54] John D. Jorgenson. U.S. Geological Survey, Mineral Commodity Summaries, January 2004. Technical report, 2004.

[55] Michael W. George. U.S. Geological Survey, Mineral Commodity Summaries, January 2005. Technical report, 2005.

[56] James F. Carlin Jr. U.S. Geological Survey, Mineral Commodity Summaries, January 2006. Technical report, 2006.

[57] James F. Carlin Jr. U.S. Geological Survey, Mineral Commodity Summaries, January 2007. Technical report, 2007.

[58] Amy C. Tolcin. U.S. Geological Survey, Mineral Commodity Summaries, January 2008. Technical report, 2008.

[59] Amy C. Tolcin. U.S. Geological Survey, Mineral Commodity Summaries, January 2009. Technical report, 2009.

[60] Amy C. Tolcin. U.S. Geological Survey, Mineral Commodity Summaries, January 2010. Technical report, 2010.

[61] Amy C. Tolcin. U.S. Geological Survey, Mineral Commodity Summaries, January 2011. Technical report, 2011.

[62] Amy C. Tolcin. U.S. Geological Survey, Mineral Commodity Summaries, January 2012. Technical report, 2012.

[63] Amy C. Tolcin. U.S. Geological Survey, Mineral Commodity Summaries, January 2013. Technical report, 2013.

[64] Amy C. Tolcin. U.S. Geological Survey, Mineral Commodity Summaries, February 2014. Technical report, 2014.

[65] Amy C. Tolcin. U.S. Geological Survey, Mineral Commodity Summaries, January 2015. Technical report, 2015.

[66] Amy C. Tolcin. U.S. Geological Survey, Mineral Commodity Summaries, January 2016. Technical report, 2016.

[67] Peter Koven. Collapsing Fanya Metal Exchange in China raises concerns about minor metals, 2015.

[68] Lucy Hornby. Head of Fanya metals scheme arrested in China, 2016.

[69] Nyrstar. ”Results Release Nyrstar H1 2016 EN”. Technical report, 2016.

[70] James Heyward. Fire breaks out at Nyrstar’s Auby indium plant, 2015.

[71] Thomas O Mason, Steven P Harvey, Kenneth R Poeppelmeier, Klaus Ellmer, Robert Kykyneshi, Jin Zeng, David P Cann, Mamoru Mizuhashi, Hideo Hosono, Claes G Granqvist, Yuzo Shigesato, Hiromichi Ohta, Timothy J Coutts, David L Young, Timothy a Gessert, Art Sleight, David S Ginley, John D Perkins, David C Paine, Burag Yaglioglu, Joseph Berry, J Robertson, B Falabretti, Nanostructured Tcos Zno, and Dana C Olson. *Handbook of Transparent Conductors*. 2011.

[72] Çetin Klç and Alex Zunger. Origins of coexistence of conductivity and transparency in SnO2. *Physical Review Letters*, 88(9):955011–955014, 2002.

[73] S. Samson and C. G. Fonstad. Defect structure and electronic donor levels in stannic oxide crystals. *Journal of Applied Physics*, 44(10):4618–4621, 1973.

[74] Masahiko Kojima, Hisao Kato, Atsuo Imai, and Akira Yoshida. Electronic conduction of tin oxide thin films prepared by chemical vapor deposition. *Journal of Applied Physics*, 64(4):1902–1905, 1988.

[75] I. H. Kim, J. H. Ko, D. Kim, K. S. Lee, T. S. Lee, J. h. Jeong, B. Cheong, Y. J. Baik, and W. M. Kim. Scattering mechanism of transparent conducting tin oxide films prepared by magnetron sputtering. *Thin Solid Films*, 515(4):2475–2480, 2006.

[76] Ratnabali Banerjee and Debajyoti Das. Properties of tin oxide films prepared by reactive electron beam evaporation. *Thin Solid Films*, 149(3):291–301, 1987.

[77] Takamitsu Isono, Takeshi Fukuda, Koji Nakagawa, Reo Usui, Ryohei Satoh, Eiji Morinaga, and Yu Mihara. High Conductivity SnO2 Thin Films for Flat Panel Displays. *SID Digest*, 37(1):1874–1877, 2006.

[78] Hong-Lei Ma, Xiao-Tao Hao, Jin Ma, Ying-Ge Yang, Jie Huang, De-Heng Zhang, and Xian-Gang Xu. Thickness dependence of properties of SnO 2 : Sb films deposited on flexible substrates. *Applied Surface Science*, 191:313–318, 2002.

[79] E. Shanthi, A. Banerjee, V. Dutta, and K. L. Chopra. Electrical and optical properties of tin oxide films doped with F and (Sb+F). *Journal of Applied Physics*, 53(3):1615–1621, 1982.

[80] Hideo Hosono, Naoto Kikuchi, Naoyuki Ueda, and Hiroshi Kawazoe. Working hypothesis to explore novel wide band gap electrically conducting

amorphous oxides and examples. *Journal of Non-Crystalline Solids*, 198-200:165–169, 1996.

[81] Kenji Nomura, Hiromichi Ohta, Akihiro Takagi, Toshio Kamiya, Masahiro Hirano, and Hideo Hosono. Room-temperature fabrication of transparent flexible thin-film transistors using amorphous oxide semiconductors. *Nature*, 432(7016):488–492, 2004.

[82] G.S. Collins, T. Kachnowski, N. Benczer-Koller, and M. Pasternak. Application of the Mossbauer effect to the characterization of an amorphous tin-oxide system. *Physical Review B*, 19(3):1369, 1979.

[83] Madambi K. Jayaraj, Kachirayil J. Saji, Kenji Nomura, Toshio Kamiya, and Hideo Hosono. Optical and electrical properties of amorphous zinc tin oxide thin films examined for thin film transistor application. *Journal of Vacuum Science & Technology B: Microelectronics and Nanometer Structures*, 26(2):495, 2008.

[84] Ha-Rim An, ChangYeoul Kim, Sung-Tag Oh, and Hyo-Jin Ahn. Effect of sol-layers on Sb-doped SnO2 thin films as solution-based transparent conductive oxides. *Ceramics International*, 40(1):385–391, jan 2014.

[85] J. Montero, J. Herrero, and C. Guillén. Preparation of reactively sputtered Sb-doped SnO2 thin films: Structural, electrical and optical properties. *Solar Energy Materials and Solar Cells*, 94(3):612–616, mar 2010.

[86] J. Montero, C. Guillén, C. G. Granqvist, J. Herrero, and G. a. Niklasson. Lithium intercalation in sputter deposited antimony-doped tin oxide thin films: Evidence from electrochemical and optical measurements. *Journal of Applied Physics*, 115(15):153702, apr 2014.

[87] Hong Lei Ma, Xiao Tao Hao, Jin Ma, Ying Ge Yang, Jie Huang, De Heng Zhang, and Xian Gang Xu. Thickness dependence of properties of SnO2:Sb films deposited on flexible substrates. *Applied Surface Science*, 191(1-4):313–318, 2002.

[88] T. R. Giraldi, M. T. Escote, M. I B Bernardi, V. Bouquet, E. R. Leite, E. Longo, and J. A. Varela. Effect of thickness on the electrical and optical properties of Sb doped SnO2 (ATO) thin films. *Journal of Electroceramics*, 13(1-3):159–165, 2004.

[89] Shihui Yu, Linghong Ding, Chuang Xue, Li Chen, and W.F. Zhang. Transparent conducting Sb-doped SnO2 thin films grown by pulsed laser deposition. *Journal of Non-Crystalline Solids*, 358(23):3137–3140, dec 2012.

[90] Seung-Yup Lee and Byung-Ok Park. Structural, electrical and optical characteristics of SnO2:Sb thin films by ultrasonic spray pyrolysis. *Thin Solid Films*, 510(1-2):154–158, 2006.

[91] H. S. Randhawa, M. D. Matthews, and R. F. Bunshah. SnO2 films prepared by activated reactive evaporation. *Thin Solid Films*, 83(2):267–271, 1981.

[92] Huiyong Liu, V. Avrutin, N. Izyumskaya, Ü Özgr, and H. Morkoç. Transparent conducting oxides for electrode applications in light emitting and absorbing devices. *Superlattices and Microstructures*, 48(5):458–484, nov 2010.

[93] B R Marathe, M G Takwale, and V G Bhide. Structural Properties of SnO2:F Films Deposited by Spray Pyrolysis Technique. *Thin Films*, 164:261–264, 1988.

[94] M Thirumoorthi and J Thomas Joseph Prakash. Effect of F doping on physical properties of (211) oriented SnO2 thin films prepared by jet nebulizer spray pyrolysis technique. *Superlattices and Microstructures*, 89:378–389, 2016.

[95] Boubaker Benhaoua, Soumaia Abbas, Achour Rahal, Atmane Benhaoua, and M.S. Aida. Effect of film thickness on the structural, optical and electrical properties of SnO2: F thin films prepared by spray ultrasonic for solar cells applications. *Superlattices and Microstructures*, 83:78–88, 2015.

[96] Mejda Ajili, Michel Castagné, and Najoua Kamoun. Optik Spray solution flow rate effect on growth , optoelectronic characteristics and photoluminescence of SnO 2 : F thin films for photovoltaic application. *Optik - International Journal for Light and Electron Optics*, 126(7-8):708–714, 2015.

[97] Quang-Phu Tran, Jau-Shiung Fang, and Tsung-Shune Chin. Properties of fluorine-doped SnO2 thin films by a green solgel method. *Materials Science in Semiconductor Processing*, 40:664–669, 2015.

[98] Nuruzzaman Noor, Clair K. T. Chew, Davinder S. Bhachu, Matthew R. Waugh, Claire J. Carmalt, and Ivan P. Parkin. Influencing FTO thin film growth with thin seeding layers: a route to microstructural modification. *J. Mater. Chem. C*, 3(36):9359–9368, 2015.

[99] Tadashi Ishida, Osamu Tabata, Jung Il Park, Sung Ho Shin, Hiroyuki Magara, Shigeharu Tamura, Shoichi Mochizuki, and Toshiyuki Mihara. Highly conductive transparent F-doped tin oxide films were prepared by photo-CVD and thermal-CVD. *Thin Solid Films*, 281-282(1-2):228–231, 1996.

[100] Michael J. Powell, Dominic B. Potter, Rachel L. Wilson, Jawwad A. Darr, Ivan P. Parkin, and Claire J. Carmalt. Scaling aerosol assisted chemical vapour deposition: Exploring the relationship between growth rate and film properties. *Materials & Design*, 129(May):116–124, 2017.

[101] Shoichiro Nakao, Yasushi Hirose, Tomoteru Fukumura, and Tetsuya Hasegawa. Carrier generation mechanism and effect of tantalum-doping in transparent conductive amorphous SnO2 thin films Carrier generation mechanism and effect of tantalum-doping in transparent conductive amorphous SnO 2 thin films. *Japanese Journal of Applied Physics*, 53(05FX04):1–5, 2014.

[102] Mirko Weidner, Joachim Brötz, and Andreas Klein. Sputter-deposited polycrystalline tantalum-doped SnO2 layers. *Thin Solid Films*, 555:173–178, 2014.

[103] Shihui Yu, Lingxia Li, Zheng Sun, Haoran Zheng, Helei Dong, Dan Xu, and Weifeng Zhang. Characteristics of Transparent Conducting W-Doped SnO ₂ Thin Films Prepared by Using the Magnetron Sputtering Method. *Journal of the American Ceramic Society*, 98(4):1121–1127, 2015.

[104] Shoichiro Nakao, Naoomi Yamada, Taro Hitosugi, Yasushi Hirose, Toshihiro Shimada, and Tetsuya Hasegawa. Fabrication of highly conductive Ta-doped SnO2 polycrystalline films on glass using seed-layer technique by pulse laser deposition. *Thin Solid Films*, 518(11):3093–3096, mar 2010.

[105] Shaohang Wu, Yantao Li, Jinsong Luo, Jie Lin, Yi Fan, Zhihong Gan, and Xingyuan Liu. Pr and F co-doped SnO transparent conductive films with high work function deposited by ion-assisted electron beam evaporation. *Optics express*, 22(4):4731–7, feb 2014.

[106] G. Turgut, E. Sonmez, and S. Duman. Evaluation of an Nd doping effect on characteristic properties of tin oxide. *Materials Science in Semiconductor Processing*, 30:233–241, 2015.

[107] Zhenguo Ji, Zhenjie He, Yongliang Song, Kun Liu, and ZhiZhen Ye. Fabrication and characterization of indium-doped p-type SnO2 thin films. *Journal of Crystal Growth*, 259(3):282–285, 2003.

[108] Chien-Yie Tsay and Shan-Chien Liang. Fabrication of p-type conductivity in SnO2 thin films through Ga doping. *Journal of Alloys and Compounds*, 622:644–650, 2015.

[109] M S Anwar, Faheem Ahmed, Si Nae Heo, Keun Young Park, and Bon Heun Koo. Indication of room temperature ferromagnetism in highly transparent and conductive Ga-doped SnO2 thin films. *Thin Solid Films*, 547:137–140, 2013.

[110] C.E. Benouis, M. Benhaliliba, Z. Mouffak, a. Avila-Garcia, a. Tiburcio-Silver, M. Ortega Lopez, R. Romano Trujillo, and Y.S. Ocak. The low re-

sistive and transparent Al-doped SnO2 films: p-type conductivity, nanostructures and photoluminescence. *Journal of Alloys and Compounds*, 603:213–223, 2014.

[111] Abhishek Kumar Singh, Anderson Janotti, Matthias Scheffler, and Chris G. Van De Walle. Sources of electrical conductivity in SnO2. *Physical Review Letters*, 101(5):1–4, 2008.

[112] Claus F. Klingshirn. ZnO: Material, physics and applications. *ChemPhysChem*, 8(6):782–803, 2007.

[113] Anderson Janotti and Chris G. Van De Walle. New insights into the role of native point defects in ZnO. *Journal of Crystal Growth*, 287:58–65, 2006.

[114] M. D. McCluskey and S. J. Jokela. Sources of n-type conductivity in ZnO. *Physica B: Condensed Matter*, 401-402:355–357, 2007.

[115] Sukit Limpijumnong, Luke Gordon, Maosheng Miao, Anderson Janotti, and Chris G. Van De Walle. Alternative sources of p-type conduction in acceptor-doped ZnO. *Applied Physics Letters*, 97(7):072112, 2010.

[116] Anderson Janotti and Chris G. Van De Walle. Oxygen vacancies in ZnO. *Applied Physics Letters*, 87(12):1–3, 2005.

[117] Mao Hua Du and Koushik Biswas. Anionic and hidden hydrogen in ZnO. *Physical Review Letters*, 106(11):1–4, 2011.

[118] David S. Ginley and Clark Bright. Transparent Conducting Oxides. *MRS Bulletin*, 25(08):15–18, 2000.

[119] Tadatsugu Minami, Toshihiro Miyata, Tadatsugu Minami, Hirotoshi Sato, Kouichi Tomura, Masaru Ohnishi, and Michio Yoshizawa. Highly Conductive and Transparent Aluminum Doped Zinc Oxide Thin Films Prepared by RF Magnetron Sputtering. *Japanese Journal of Applied Physics*, 23:280–282, 1984.

[120] Jianhua Hu and Roy G Gordon. Textured aluminum-doped zinc oxide thin films from atmospheric pressure chemical-vapor deposition Textured aluminum-doped deposition zinc oxide thin fil s from atmospheric pressure. *Journal of Applied Physics*, 71:880–890, 1992.

[121] S. Kuprenaite, T. Murauskas, A. Abrutis, V. Kubilius, Z. Saltyte, and V. Plausinaitiene. Properties of In-, Ga-, and Al-doped ZnO films grown by aerosol-assisted MOCVD: Influence of deposition temperature, doping level and annealing. *Surface and Coatings Technology*, 271:156–164, dec 2015.

[122] Tudor Coman, Daniel Timpu, Valentin Nica, Catalin Vitelaru, Alicia Petronela Rambu, George Stoian, Mihaela Olaru, and Cristian Ursu. Sequential PLD in oxygen/argon gas mixture of Al-doped ZnO thin films with improved electrical and optical properties. *Applied Surface Science*, 418:456–462, 2017.

[123] A. F. Aktarazzuman, G. I. Sharma, and L. K. Malhotra. ELECTRICAL, OPTICAL AND ANNEALING CHARACTERISTICS OF ZnO:AI FILMS PREPARED BY SPRAY PYROLYSIS. *Thin Solid Films*, 198:67–74, 1991.

[124] Gui-Gen Wang, Jie Zeng, Jie-Cai Han, and Li-Yi Wang. Highly transparent and conductive Ga-doped ZnO films with good thermal stability prepared by dual-target reactive sputtering. *Materials Letters*, 137:307–310, dec 2014.

[125] P.K Song, M Watanabe, M Kon, A Mitsui, and Y Shigesato. Electrical and optical properties of gallium-doped zinc oxide films deposited by dc magnetron sputtering. *Thin Solid Films*, 411(1):82–86, 2002.

[126] a.S. Pugalenthi, R. Balasundaraprabhu, V. Gunasekaran, N. Muthukumarasamy, S. Prasanna, and S. Jayakumar. Effect of thickness on the structural, optical and electrical properties of RF magnetron sputtered GZO thin films. *Materials Science in Semiconductor Processing*, 29:176–182, jan 2015.

[127] G.a. Hirata, J. McKittrick, T Cheeks, J.M. Siqueiros, J.a. Diaz, O Contreras, and O.a. Lopez. Synthesis and optelectronic characterization of gallium doped zinc oxide transparent electrodes. *Thin Solid Films*, 288(1-2):29–31, 1996.

[128] Ha-Rim An, Hyo-Jin Ahn, and Jeong-Woo Park. High-quality, conductive, and transparent Ga-doped ZnO films grown by atmospheric-pressure chemical-vapor deposition. *Ceramics International*, 41(2):2253–2259, mar 2015.

[129] B. M. Ataev, A. M. Bagamadova, A. M. Djabrailov, V. V. Mamedov, and R A Rabadanov. Highly conductive and transparent Ga-doped epitaxial ZnO films on sapphire by CVD. *Thin Solid Films*, 260(1):19–20, 1995.

[130] Ke Zhu, Ye Yang, and Weijie Song. Effects of substrate temperature on the structural, morphological, electrical and optical properties of Al and Ga co-doped ZnO thin films grown by DC magnetron sputtering. *Materials Letters*, 145:279–282, 2015.

[131] Xiaoyan Du, Jin Li, and Xiaofang Bi. The role of Ga partial substitution for Al in the enhanced conductivity of transparent AZO thin film. *Journal of Alloys and Compounds*, 698:128–132, 2017.

[132] Jia Liu, Weijia Zhang, Dengyuan Song, Qiang Ma, Lei Zhang, Hui Zhang, and Leng Zhang. Investigation of aluminum gallium co-doped zinc oxide targets for sputtering thin film and photovoltaic application. *Journal of Alloys and Compounds*, 575:174–182, 2013.

[133] Shang-Chou Chang. Post-annealed gallium and aluminum co-doped zinc oxide films applied in organic photovoltaic devices. *Nanoscale Research Letters*, 9(1):562, 2014.

[134] J. Clatot, M. Nistor, and a. Rougier. Influence of Si concentration on electrical and optical properties of room temperature ZnO:Si thin films. *Thin Solid Films*, 531:197–202, mar 2013.

[135] Tadatsugu Minami, Hirotoshi Sato, Hidehito Nanto, and Shinzo Takata. Highty Conductive and Transparent Silicon Doped Zinc Oxide Thin Films Prepared by RF Magnetron Sputtering. *Japanese Journal of Applied Physics*, 25(Part 2, No. 9):L776–L779, 1986.

[136] Vladimir L. Kuznetsov, Alex T. Vai, Malek Al-Mamouri, J. Stuart Abell, Michael Pepper, and Peter P. Edwards. Electronic transport in highly conducting Si-doped ZnO thin films prepared by pulsed laser deposition. *Applied Physics Letters*, 107(23), 2015.

[137] Anil Singh, Sujeet Chaudhary, and Dinesh K. Pandya. On the temperature dependence of mobility in hydrogenated indium-doped ZnO thin films. *Acta Materialia*, 77:125–132, sep 2014.

[138] F. Z. Bedia, A. Bedia, M. Aillerie, N. Maloufi, and B. Benyoucef. Structural, Optical and Electrical Properties of Sn-doped Zinc Oxide Transparent Films Interesting for Organic Solar Cells (OSCs). *Energy Procedia*, 74:539–546, 2015.

[139] Muying Wu, Shihui Yu, Lin He, Geng Zhang, Dongxiong Ling, and Weifeng Zhang. Influence of oxygen pressure on the structural, electrical and optical properties of Nb-doped ZnO thin films prepared by pulsed laser deposition. *Applied Surface Science*, 292:219–224, feb 2014.

[140] H.-Y. He, J.-F. Huang, J. Fei, and J. Lu. La-doping content effect on the optical and electrical properties of La-doped ZnO thin films. *Journal of Materials Science: Materials in Electronics*, 26:1205–1211, 2014.

[141] A. Douayar, P. Prieto, G. Schmerber, K. Nouneh, R. Diaz, I. Chaki, S. Colis, A. El Fakir, N. Hassanain, A. Belayachi, Z. Sekkat, A. Slaoui, A. Dinia, and M. Abd-Lefdil. Investigation of the structural, optical and electrical properties of Nd-doped ZnO thin films deposited by spray pyrolysis. *Eur. Phys. J. Appl. Phys.*, 61(1):10304, 2013.

[142] Andreas Stadler. Transparent Conducting OxidesAn Up-To-Date Overview. *Materials*, 5(12):661–683, apr 2012.

[143] Yuzo Shigesato and David C. Paine. A microstructural study of low resistivity tin-doped indium oxide prepared by d.c. magnetron sputtering. *Thin Solid Films*, 238(1):44–50, 1994.

[144] P.J.M. Isherwood, N. Neves, J.W. Bowers, P. Newbatt, and J.M. Walls. High quality aluminium doped zinc oxide target synthesis from nanoparticulate powder and characterisation of sputtered thin films. *Thin Solid Films*, 566:108–114, sep 2014.

[145] Tadatsugu Minami, Hidehito Nanto, and Shinzo Takata. Optical Properties of Aluminum Doped Zinc Oxide Thin Films Prepared by RF Magnetron Sputtering. *Japanese Journal of Applied Physics*, 24(8):605–607, 1985.

[146] Kun Ho, Kimki Cheol, and Dae Young Ma. Structural , electrical and optical properties of aluminum doped zinc oxide films prepared by radio frequency magnetron sputtering Structural , electrical and optical properties of aluminum doped zinc oxide films prepared by radio frequency magnetron sput. *Journal of Applied Physics*, 81:7764–7772, 1997.

[147] Qin Hua, Wang Ligang, Liu Ruijin, and Yuan Wenfeng. Influence of target substrate distance on the properties of transparent conductive Si doped ZnO thin films. *Optik - International Journal for Light and Electron Optics*, 125(15):3902–3907, aug 2014.

[148] H. Kim, J. S. Horwitz, G. P. Kushto, Z. H. Kafafi, and D. B. Chrisey. Indium tin oxide thin films grown on flexible plastic substrates by pulsed-laser deposition for organic light-emitting diodes. *Applied Physics Letters*, 79(3):284–286, 2001.

[149] J Kane and H P Schweizer. Chemical vapor deposition of transparent electrically conducting layers of indium oxide dopet with tin. *Thin Solid Films*, 29:155–163, 1975.

[150] K. L. Chopra, S. Major, and D. K. Pandya. Transparent conductors-A status review. *Thin Solid Films*, 102(1):1–46, 1983.

[151] M Vishwas, K Narasimha Rao, K V Arjuna Gowda, and R P S Chakradhar. Influence of Sn doping on structural, optical and electrical properties of ZnO thin films prepared by cost effective sol-gel process. *Spectrochimica acta. Part A, Molecular and biomolecular spectroscopy*, 95:423–6, sep 2012.

[152] Xu Liu, Kaimeng Pan, Weibo Li, Dan Hu, Shuyang Liu, and Yude Wang. Optical and gas sensing properties of Al-doped ZnO transparent conducting films prepared by solgel method under different heat treatments. *Ceramics International*, 40(7):9931–9939, aug 2014.

[153] R. Jothi Ramalingam, T. Radika, and Hamad A. Al-Lohedan. Preparation and surface characterization of nanodisk/nanoflower-structured gallium-doped zinc oxide as a catalyst for sensor applications. *Chinese Journal of Catalysis*, 37(8):1235–1241, 2016.

[154] N. Al-Dahoudi and M. A. Aegerter. Comparative study of transparent conductive In2O3:Sn (ITO) coatings made using a sol and a nanoparticle suspension. *Thin Solid Films*, 502(1-2):193–197, 2006.

[155] Myun Sung Hwang, Bong Yong Jeong, Jooho Moon, Sang Ki Chun, and Jihoon Kim. Inkjet-printing of indium tin oxide (ITO) films for transparent conducting electrodes. *Materials Science and Engineering B: Solid-State Materials for Advanced Technology*, 176(14):1128–1131, 2011.

[156] Kenny Vernieuwe, Dieter Cuypers, Christine E A Kirschhock, Kristof Houthoofd, Henk Vrielinck, Johan Lauwaert, Jonathan De Roo, Isabel Van Driessche, and Klaartje De Buysser. Thermal processing of aqueous AZO inks towards functional TCO thin films. *Journal of Alloys and Compounds*, 690:360–368, 2017.

[157] A. E. Danks, S. R. Hall, and Z. Schnepp. The evolution of solgel' chemistry as a technique for materials synthesis. *Mater. Horiz.*, 3(2):91–112, 2016.

[158] A. Feinle, M. S. Elsaesser, and N. Hüsing. Solgel synthesis of monolithic materials with hierarchical porosity. *Chem. Soc. Rev.*, 45(12):3377–3399, 2016.

[159] J. A. Darr, J. Zhang, N. M. Makwana, and X. Weng. Continuous Hydrothermal Synthesis of Inorganic Nanoparticles; Applications and Future Directions. *Chem Rev*, in press:1–141, 2017.

[160] Agnieszka Kolodziejczak-Radzimska and Teofil Jesionowski. Zinc oxide-from synthesis to application: A review. *Materials*, 7(4):2833–2881, 2014.

[161] Eleonore Fröhlich and Sharareh Salar-Behzadi. Toxicological assessment of inhaled nanoparticles: Role of in vivo, ex vivo, in vitro, and in Silico Studies. *International Journal of Molecular Sciences*, 15(3):4795–4822, 2014.

[162] Shahnaz Bakand, Amanda Hayes, and Finance Dechsakulthorn. Nanoparticles: a review of particle toxicology following inhalation exposure. *Inhalation Toxicology*, 24(2):125–135, 2012.

[163] D. P. Fernández, Y. Mulev, A. R H Goodwin, and J. M H Levelt Sengers. A Database for the Static Dielectric Constant of Water and Steam. *Journal of Physical and Chemical Reference Data*, 24(1):33–70, 1995.

[164] Hitoshi Ohtaki. Effects of temperature and pressure on hydrogen bonds in water and in formamide. *Journal of Molecular Liquids*, 103-104(SPEC.):3–13, 2003.

[165] G. Galli and D. Pan. A closer look at supercritical water. *Proceedings of the National Academy of Sciences*, 110(16):6250–6251, 2013.

[166] Ph Wernet, D. Testemale, J. L. Hazemann, R. Argoud, P. Glatzel, L. G.M. Pettersson, A. Nilsson, and U. Bergmann. Spectroscopic characterization of microscopic hydrogen-bonding disparities in supercritical water. *Journal of Chemical Physics*, 123(15), 2005.

[167] Kirk-Othmer. *Encyclopedia of Chemical Terminology 4th Ed.* John Wiley and Sons, New York, NY, 1995.

[168] Peter Marchand, Neel M Makwana, Christopher J Tighe, I Gruar, Ivan P Parkin, Claire J Carmalt, and Jawwad a Darr. High-Throughput Synthesis , Screening and Scale- Up of Optimised Conducting Indium Tin Oxides . High-Throughput Synthesis , Screening and Scale-Up of Optimised Conducting Indium Tin Oxides . The combination of low electrical resistivity and high optical t. *ACS Combinatorial Science*, 18:130–137, 2016.

[169] Jinfeng Lu, Kimitaka Minami, Seiichi Takami, Masatoshi Shibata, Yasunobu Kaneko, and Tadafumi Adschiri. Supercritical Hydrothermal Synthesis and In situ Organic Modification of Indium Tin Oxide Nanoparticles Using Continuous- Flow Reaction System. *ACS Applied Materials & Interfaces*, 4:351–354, 2012.

[170] Xiaole Weng, Jeremy K Cockcroft, Geoffrey Hyett, Martin Vickers, Paul Boldrin, Chiu C Tang, Stephen P Thompson, Julia E Parker, Jonathan C Knowles, Ihtesham Rehman, Ivan Parkin, Julian R G Evans, and Jawwad a Darr. High-throughput continuous hydrothermal synthesis of an entire nanoceramic phase diagram. *Journal of combinatorial chemistry*, 11(5):829–834, 2009.

[171] Raul Quesada-Cabrera, Xiaole Weng, Geoff Hyett, Robin J H Clark, Xue Z Wang, and Jawwad a Darr. High-throughput continuous hydrothermal synthesis of nanomaterials (part II): unveiling the as-prepared CexZryYzO2-δ phase diagram. *ACS combinatorial science*, 15(9):458–63, sep 2013.

[172] J. F. K. Cooper, a. Ionescu, R. M. Langford, K. R. a. Ziebeck, C. H. W. Barnes, R. Gruar, C. Tighe, J. a. Darr, N. T. K. Thanh, and B. Ouladdiaf. Core/shell magnetism in NiO nanoparticles. *Journal of Applied Physics*, 114(8):083906, 2013.

[173] Liang Shi, Anu Naik, Josephine B M Goodall, Christopher James Tighe,

Robert Ian Gruar, Russell Binions, Ivan Paul Parkin, and Jawwad a Darr. Highly Sensitive ZnO Nanorods and Nanoprism based NO2-Gas Sensors ; Size and Shape Control using a Continuous Hydrothermal Pilot Plant Highly Sensitive ZnO Nanorods and Nanoprism based NO 2 -Gas Sensors ; Size and Shape Control using a Continuous Hydrothe. *Langmuir*, 29(2):10603–10609, 2013.

[174] Josephine B. M. Goodall, Derek Illsley, Robert Lines, Neel M. Makwana, and Jawwad a. Darr. StructurePropertyComposition Relationships in Doped Zinc Oxides: Enhanced Photocatalytic Activity with Rare Earth Dopants. *ACS Combinatorial Science*, 17:100–112, 2015.

[175] Zhice Zhang, Sonal Brown, Josephine B.M. Goodall, Xiaole Weng, Kathryn Thompson, Kenan Gong, Suela Kellici, Robin J.H. Clark, Julian R.G. Evans, and Jawwad a. Darr. Direct continuous hydrothermal synthesis of high surface area nanosized titania. *Journal of Alloys and Compounds*, 476(1-2):451–456, may 2009.

[176] Sofia Elouali, Leanne G Bloor, Russell Binions, Ivan P Parkin, Claire J Carmalt, and Jawwad a Darr. Gas sensing with nano-indium oxides (In2O3) prepared via continuous hydrothermal flow synthesis. *Langmuir : the ACS journal of surfaces and colloids*, 28(3):1879–85, jan 2012.

[177] Gwyn P. Evans, Michael J. Powell, Ian D. Johnson, Dougal P. Howard, Dustin Bauer, Jawwad A. Darr, and Ivan P. Parkin. Room temperature vanadium dioxidecarbon nanotube gas sensors made via continuous hydrothermal flow synthesis. *Sensors and Actuators B: Chemical*, 2017.

[178] Kathryn Thompson, Josephine Goodall, Suela Kellici, John a. Mattinson, Terry a. Egerton, Ihtesham Rehman, and Jawwad a. Darr. Screening tests for the evaluation of nanoparticle titania photocatalysts. *Journal of Chemical Technology & Biotechnology*, 84(11):1717–1725, nov 2009.

[179] Josephine B. M. Goodall, Suela Kellici, Derek Illsley, Robert Lines,

Jonathan C. Knowles, and Jawwad a. Darr. Optical and photocatalytic behaviours of nanoparticles in the TiZnO binary system. *RSC Advances*, 4(60):31799, jun 2014.

[180] Ian D. Johnson, Mechthild Lübke, On Ying Wu, Neel M. Makwana, Glen J. Smales, Husn U. Islam, Rashmi Y. Dedigama, Robert I. Gruar, Christopher J. Tighe, David O. Scanlon, Furio Corà, Dan J L Brett, Paul R. Shearing, and Jawwad A. Darr. Pilot-scale continuous synthesis of a vanadium-doped LiFePO4/C nanocomposite high-rate cathodes for lithium-ion batteries. *Journal of Power Sources*, 302:410–418, 2016.

[181] Mechthild Lübke, Juhun Shin, Peter Marchand, Dan Brett, Paul Shearing, Zhaolin Liu, and Jawwad A Darr. Highly pseudocapacitive Nb-doped TiO 2 high power anodes for lithium-ion batteries. *Journal of Materials Chemistry A*, 3(45):22908–22914, 2015.

[182] Mechthild Lübke, Dougal Howard, Ceilidh F. Armer, Aleksandra J. Gardecka, Adrian Lowe, M.V. Reddy, Zhaolin Liu, and Jawwad A. Darr. High energy lithium ion battery electrode materials; enhanced charge storage via both alloying and insertion processes. *Electrochimica Acta*, 231:247–254, 2017.

[183] Mechthild Lübke, Ding Ning, Ceilidh F. Armer, Dougal Howard, Dan J.L. Brett, Zhaolin Liu, and Jawwad A. Darr. Evaluating the Potential Benefits of Metal Ion Doping in SnO 2 Negative Electrodes for Lithium Ion Batteries. *Electrochimica Acta*, 242:400–407, 2017.

[184] Dustin Bauer, Alexander J Roberts, Noriyoshi Matsumi, and Jawwad A Darr. Nano-sized Mo- and Nb-doped TiO 2 as anode materials for high energy and high power hybrid Li-ion capacitors. *Nanotechnology*, 28(19):195403, 2017.

[185] Michael John Powell, P Marchand, C J Denis, J C Bear, J A Darr, and I P Parkin. Direct and continuous synthesis of VO 2 nanoparticles. *Nanoscale*, 7(44):18686–18693, 2015.

[186] Raul Quesada-Cabrera, Michael J Powell, Peter Marchand, Clément J Denis, Francesco Di Maggio, Jawwad A Darr, and Ivan P Parkin. Scalable Production of Thermochromic Nb-Doped VO2 Nanomaterials Using Continuous Hydrothermal Flow Synthesis. *Journal of Nanoscience and Nanotechnology*, 16(9):10104–10111, 2016.

[187] Zhen Fang, Hassane Assaaoudi, Roderick I L Guthrie, Janusz A. Kozinski, and Ian S. Butler. Continuous synthesis of tin and indium oxide nanoparticles in sub- and supercritical water. *Journal of the American Ceramic Society*, 90(8):2367–2371, 2007.

[188] X.-D. Xiang, Xiaodong Sun, Gabriel Briceno, Yulin Lou, Kai-An Wang, Hauyee Chang, William G. Wallace-Freedman, Sung-Wei Chen, and Peter G. Schultz. A Combinatorial Approach to Materials Discovery. *Science*, 268:1738–1740, 1995.

[189] J D Perkins, J A del Cueto, J L Alleman, C Warmsingh, B M Keyes, L M Gedvilas, P A Parilla, B To, D W Readey, and D S Ginley. Combinatorial studies of Zn-Al-O and Zn-Sn-O transparent conducting oxide thin films. *Thin Solid Films*, 411:152, 2002.

[190] J D Perkins, J L Alleman, and National Renewable. Discovery and Optimization of In-Zn-Sn-O BasedTransparent Conductors By Combinatorial and Pulsed Laser Deposition Approaches. *Conference Record of the 29th IEEE Photovoltaic Specialists Conference*, pages 1126–1129, 2002.

[191] Matthew P. Taylor, Dennis W. Readey, Charles W. Teplin, Maikel F A M Van Hest, Jeff L. Alleman, Matthew S. Dabney, Lynn M. Gedvilas, Brian M. Keyes, Bobby To, Philip A. Parilla, John D. Perkins, and David S. Ginley. Combinatorial Growth and Analysis of the Transparent Conducting Oxide ZnO/In (IZO). *Macromolecular Rapid Communications*, 25(1):344–347, 2004.

[192] Samuel S. Mao and Paul E. Burrows. Combinatorial screening of thin film materials: An overview. *Journal of Materiomics*, 1(2):85–91, 2015.

[193] M. Murakami, Y. Matsumoto, M. Nagano, T. Hasegawa, M. Kawasaki, and H. Koinuma. Combinatorial fabrication and characterization of ferromagnetic Ti-Co-O system. *Applied Surface Science*, 223(1-3):245–248, 2004.

[194] J. D. Perkins, M. P. Taylor, M. F A M Van Hest, C. W. Teplin, J. L. Alleman, M. S. Dabney, L. M. Gedvilas, B. M. Keyes, B. To, D. W. Readey, A. E. Delahoy, S. Guo, and D. S. Ginley. Combinatorial optimization of Transparent conducting oxides (TCOS) for PV. *Conference Record of the 31st IEEE Photovoltaic Specialists Conference*, pages 145–147, 2005.

[195] M. Watanabe, T. Kita, T. Fukumura, A. Ohtomo, K. Ueno, and M. Kawasaki. Combinatorial synthesis and high throughput evaluation of thermoelectric power factor in Mg-Si-Ge ternary compounds. *Applied Surface Science*, 254(3):777–780, 2007.

[196] Akira Nakayama, Eiji Suzuki, and Takashi Ohmori. Development of high throughput evaluation for photocatalyst thin-film. *Applied Surface Science*, 189:260–264, 2002.

[197] Min Kim, Samson Lai, and Richard M. Laine. Combinatorial Nanopowder Synthesis Along the ZnO-Al 2 O 3 Tie Line Using Liquid-Feed Flame Spray Pyrolysis. *Journal of the American Ceramic Society*, 94(10):3308–3318, oct 2011.

[198] S. J. Henderson, J. a. Armstrong, a. L. Hector, and M. T. Weller. High-throughput methods to optically functional oxide and oxide?nitride materials. *Journal of Materials Chemistry*, 15(15):1528, 2005.

[199] R. Funahashi, S. Urata, and M. Kitawaki. Exploration of n-type oxides by high throughput screening. *International Conference on Thermoelectrics, ICT, Proceedings*, 2002-Janua:219–222, 2002.

[200] Wei Wang and Jinhui Wang. Development of MnZn ferrites by combinatorial synthesis and high throughput screening method. *Journal of Alloys and Compounds*, 463(1-2):112–118, 2008.

[201] Nicholas P. Chadwick, Emily N. K. Glover, Sanjayan Sathasivam, Sulaiman N. Basahel, Shaeel a. Althabaiti, Abdulrahman O. Alyoubi, Ivan P. Parkin, and Claire J. Carmalt. Photo-activity and low resistivity in N/Nb Co-doped TiO 2 thin films by combinatorial AACVD. *J. Mater. Chem. A*, 4:407–415, 2016.

[202] J.D. Perkins, C.W. Teplin, M.F.a.M van Hest, J.L. Alleman, X. Li, M.S. Dabney, B.M. Keyes, L.M. Gedvilas, D.S. Ginley, Y. Lin, and Y. Lu. Optical analysis of thin film combinatorial libraries. *Applied Surface Science*, 223(1-3):124–132, 2004.

[203] Robert I. J. Gruar. *Synthesis and characterisation of nanomaterials produced using laboratory and pilot scale continuous hydrothermal flow reactors*. PhD thesis, 2013.

[204] Neel M. Makwana. *Photoactive and UV Attenuating Nanomaterial and Heterojunction Devices*. PhD thesis, 2016.

[205] Robert I Gruar, Christopher J Tighe, and Jawwad A Darr. Scaling-up a Con fi ned Jet Reactor for the Continuous Hydrothermal Manufacture of Nanomaterials. *Industrial & Engineering Chemistry Research*, 52:5270–5281, 2013.

[206] W. Wagner and A. Pruß. The IAPWS Formulation 1995 for the Thermodynamic Properties of Ordinary Water Substance for General and Scientific Use. *Journal of Physical and Chemical Reference Data*, 31(2):387–535, 1999.

[207] Jianhua Hu and Roy G Gordon. Atmospheric pressure chemical vapor deposition of gallium doped zinc oxide thin films from diethyl zinc, water, and triethyl gallium. *Journal of Applied Physics*, 72:5381–5392, 1992.

[208] a K Das, P Misra, and L M Kukreja. Effect of Si doping on electrical and optical properties of ZnO thin films grown by sequential pulsed laser deposition. *Journal of Physics D: Applied Physics*, 42(16):165405, aug 2009.

[209] Dan Hu, Xu Liu, Shaojuan Deng, Yongjun Liu, Zhipeng Feng, Bingqian Han, Yan Wang, and Yude Wang. Structural and optical properties of Mn-doped ZnO nanocrystalline thin films with the different dopant concentrations. *Physica E: Low-dimensional Systems and Nanostructures*, 61:14–22, jul 2014.

[210] Mohammad F. Al-Kuhaili, Sardar M.A. Durrani, Ayman S. El-Said, and R. Heller. Influence of iron doping on the structural, chemical, and optoelectronic properties of sputtered zinc oxide thin films. *Journal of Materials Research*, 31:3230–3239, 2016.

[211] H. T. Cao, Z. L. Pei, J. Gong, C. Sun, R. F. Huang, and L. S. Wen. Preparation and characterization of Al and Mn doped ZnO (ZnO: (Al, Mn)) transparent conducting oxide films. *Journal of Solid State Chemistry*, 177(4-5):1480–1487, 2004.

[212] Huafu Zhang, Hanfa Liu, Chengxin Lei, Changkun Yuan, and Aiping Zhou. Tungsten-doped ZnO transparent conducting films deposited by direct current magnetron sputtering. *Vacuum*, 85(2):184–186, 2010.

[213] I. Soumahoro, S. Colis, G. Schmerber, C. Leuvrey, S. Barre, C. Ulhaq-Bouillet, D. Muller, M. Abd-lefdil, N. Hassanain, J. Petersen, a. Berrada, a. Slaoui, and a. Dinia. Structural, optical, spectroscopic and electrical properties of Mo-doped ZnO thin films grown by radio frequency magnetron sputtering. *Thin Solid Films*, 566:61–69, sep 2014.

[214] Do-Joong Lee, Ki-Ju Kim, Soo-Hyun Kim, Jang-Yeon Kwon, Jimmy Xu, and Ki-Bum Kim. Atomic layer deposition of Ti-doped ZnO films with enhanced electron mobility. *Journal of Materials Chemistry C*, 1(31):4761, 2013.

[215] Kristin Bergum, Per-Anders Hansen, Helmer Fjellvåg, and Ola Nilsen. Structural, electrical and optical characterization of Ti-doped ZnO films grown by atomic layer deposition. *Journal of Alloys and Compounds*, 616:618–624, dec 2014.

[216] Shuhei Okuda, Takuya Matsuo, Hiroshi Chiba, Tatsuya Mori, and Katsuyoshi Washio. Conductive and transparent V-doped ZnO thin films grown by radio frequency magnetron sputtering. *Thin Solid Films*, 557:197–202, apr 2014.

[217] Xiaofei Han, Kunhee Han, and Meng Tao. Low Resistivity Yttrium-Doped Zinc Oxide by Electrochemical Deposition. *Journal of The Electrochemical Society*, 157(6):H593, 2010.

[218] Maoshui Lv, Xianwu Xiu, Zhiyong Pang, Ying Dai, and Shenghao Han. Transparent conducting zirconium-doped zinc oxide films prepared by rf magnetron sputtering. *Applied Surface Science*, 252(5):2006–2011, 2005.

[219] Chih Hsien Cheng, Wei Lun Hsu, Chun Jung Lin, Yi Hao Pai, and Gong Ru Lin. Performance of highly transparent and stable zinc oxide co-doped thin-film by aluminum and ytterbium. *IEEE/OSA Journal of Display Technology*, 10(10):786–792, 2014.

[220] Wei-Sheng Liu, Wei-Ku Chen, Shen-Yu Wu, and Kuang-Po Hsueh. Improved Crystal Quality of Transparent Conductive Ga-doped ZnO Films by Magnesium Doping Through Radio-Frequency Magnetron Sputtering Preparation. *Journal of the American Ceramic Society*, 97(2):473–480, feb 2014.

[221] G. Vijayaprasath, R. Murugan, G. Ravi, T. Mahalingam, and Y. Hayakawa. Characterization of dilute magnetic semiconducting transition metal doped ZnO thin films by solgel spin coating method. *Applied Surface Science*, 313:870–876, sep 2014.

[222] H. Zhu, Y. Feng, L. Zhang, B. Lai, T. He, D. Liu, Y. Wang, J. Yin, Y. Ma, Y. Huang, H. Jia, and Y. Mai. Investigation of the stability of boron-doped

zinc oxide films grown by low-pressure chemical vapor deposition. *Physica Status Solidi (a)*, 209(7):1259–1265, jul 2012.

[223] Makoto Arita, Mayu Yamaguchi, and Masataka Masuda. Electrical and Optical Properties of Germanium-Doped Zinc Oxide Thin Films. *Materials Transactions*, 45(11):3180–3183, 2004.

[224] Chunman Ho, Jimmy C Yu, Tszyan Kwong, Angelo C Mak, and Sukyin Lai. Morphology-Controllable Synthesis of Mesoporous CeO 2 Nano- and Microstructures. *Chemistry of Materials*, 17:4514–4522, 2005.

[225] B.R. Strohmeier and D.M. Hercules. Characterization of the Interaction Zinc Ions and y-Alumina. *Journal of Catalysis*, 86:266–279, 1984.

[226] E Paparazzo, G M Ingo, and N Zacchetti. Xray induced reduction effects at CeO2 surfaces: An xray photoelectron spectroscopy study. *Journal of Vacuum Science & Technology A: Vacuum, Surfaces, and Films*, 9(3):1416–1420, 1991.

[227] G. Moretti, G. Fierro, M. Lo Jacono, and P. Porta. Characterization of CuOZnO catalysts by Xray photoelectron spectroscopy: Precursors, calcined and reduced samples. *Surface and Interface Analysis*, 14(6-7):325–336, 1989.

[228] B. Wichterlova, L. Krajcikova, Z. Tvaruzkova, and S. Beran. Chromium Ions in Zeolites. *Journal of the Chemical Society, Faraday Transactions I*, 80(I):2639–2645, 1984.

[229] D D Sarma and R Rao. Xpes Studies of Oxides of Second-and Third-Row Transition Metals Including Rare Earths*. *Journal of Electron Spectroscopy and Related Phenomena*, 20:25–45, 1980.

[230] A M De Asha and R M Nix. Interaction of Carbon Dioxide with Oxidised La / Cu (111). *Journal of the Chemical Society, Faraday Transactions*, 91(20):3611–3617, 1995.

[231] V. I. Nefedov, Y. V. Salyn, A. A. Chertkov, and L. N. Padurets. The x-ray electronic study of the distribution of electron density in transition element hydrides. *Zhurnal Neorganicheskoi Khimii*, 19(6):1443–1445, 1974.

[232] Y Uwamino, T Ishizuka, and H Yamatera. X-ray photoelectron compounds spectroscopy of rare-earth. *Journal of Electron Spectroscopy and Related Phenomena*, 34:67–78, 1984.

[233] V. Di Castro and G. Polzonetti. XPS study of MnO oxidation. *Journal of Electron Spectroscopy and Related Phenomena*, 48(1):117–123, 1989.

[234] R. O. Ansell, T. Dickinson, A. F. Povey, and P. M A Sherwood. Quantitative use of the angular variation technique in studies of tin by X-ray photoelectron spectroscopy. *Journal of Electron Spectroscopy and Related Phenomena*, 11(3):301–313, 1977.

[235] A P Dementjev, O P Ivanova, L A Vasilyev, A V Naumkin, D M Nemirovsky, and D Y Shalaev. Altered layer as sensitive initial chemical state indicator*. *Journal of Vacuum Science & Technology A: Vacuum, Surfaces, and Films*, 12(2):423–427, 1994.

[236] S Sinha, S Badrinarayanant, and A P B Sinha. INTERACTION OF OXYGEN WITH Zr76Fe24 METGLASS: AN X-RAY PHOTOELECTRON SPECTROSCOPY STUDY. *Journal of the Less-Common Metals*, 125:85–95, 1986.

[237] Thomas Lindblad, Bernd Rebenstorf, and Zhi-guang Yan. Characterization of vanadia supported on amorphous A1PO4 and its properties for oxidative dehydrogenation of propane. *Applied Catalysis A: General*, 112:187–208, 1994.

[238] C. J. Powell. Recommended Auger parameters for 42 elemental solids. *Journal of Electron Spectroscopy and Related Phenomena*, 185(1-2):1–3, 2012.

[239] I. Olefjord, H. J. Mathieu, and P. Marcus. Intercomparison of surface analysis of thin aluminium oxide films. *Surface and Interface Analysis*, 15(11):681–692, 1990.

[240] E. Paparazzo. XPS and Auger Spectroscopy Studies on Mixures of the Oxide SiO2, Al2O3, Fe2O3, and Cr2O3. *Journal of Electron Spectroscopy and Related Phenomena*, 36:269–279, 1985.

[241] Gunnar Schön. Auger and direct electron spectra in X-ray photoelectron studies of zinc, zinc oxide, gallium and gallium oxide. *Journal of Electron Spectroscopy and Related Phenomena*, 2(1):75–86, 1973.

[242] C. D. Wagner. *Handbook of x-ray photoelectron spectroscopy : a reference book of standard data for use in x-ray photoelectron spectroscopy*. Eden Prairie, Minn. : Physical Electronics Division, Perkin-Elmer Corp., 1979.

[243] W. A. M. Aarnink, A. Weishaupt, and A. van Silfhout. Angle-resolved X-ray photoelectron spectroscopy (ARXPS) and a modified Levenberg-Marquardt fit procedure: a new combination for modeling thin layers. *Applied Surface Science*, 45:37–48, 1990.

[244] Anderson Janotti and Chris G Van de Walle. Fundamentals of zinc oxide as a semiconductor. *Reports on Progress in Physics*, 72(12):126501, dec 2009.

[245] R. D. Shannon. Revised effective ionic radii and systematic studies of interatomic distances in halides and chalcogenides. *Acta Crystallographica Section A*, 32(5):751–767, 1976.

[246] A Janotti, J B Varley, J L Lyons, and C G Van De Walle. Controlling the Conductivity in Oxide Semiconductors. In Junqiao Wu, Jinbo Cao, Wei-Qiang Han, Anderson Janotti, and Ho-Cheol Kim, editors, *Functional Metal Oxide Nanostructures*, Springer Series in Materials Science, chapter 2, pages 23–35. Springer New York, New York, NY, 2012.

[247] C. Klingshirn. ZnO: From basics towards applications. *Physica Status Solidi (B)*, 244(9):3027–3073, sep 2007.

[248] Y. C. Lin, T. Y. Chen, L. C. Wang, and S. Y. Lien. Comparison of AZO, GZO, and AGZO Thin Films TCOs Applied for a-Si Solar Cells. *Journal of The Electrochemical Society*, 159(6):H599, 2012.

[249] Qingjun Jiang, Jianguo Lu, and Zhizhen Ye. Plasma-induced surface textures of ZnO:Al transparent conductive films. *Vacuum*, 111:42–47, jan 2015.

[250] Chaoying Liu, Zhiwei Xu, Yanfang Zhang, Jing Fu, Shuguang Zang, and Yan Zuo. Effect of annealing temperature on properties of ZnO:Al thin films prepared by pulsed DC reactive magnetron sputtering. *Materials Letters*, 139:279–283, jan 2015.

[251] Jin Hua Gu, Lu Long, Zhou Lu, and Zhi You Zhong. Optical, electrical and structural properties of aluminum-doped nano-zinc oxide thin films deposited by magnetron sputtering. *Journal of Materials Science: Materials in Electronics*, 26(2):734–741, nov 2015.

[252] E. G-Berasategui, C. Zubizarreta, R. Bayón, J. Barriga, R. Barros, R. Martins, and E. Fortunato. Study of the optical, electrical and corrosion resistance properties of AZO layers deposited by DC pulsed magnetron sputtering. *Surface and Coatings Technology*, 271:141–147, 2014.

[253] Jia Liu, Weijia Zhang, Dengyuan Song, Qiang Ma, Lei Zhang, Hui Zhang, Xiaobo Ma, and Haiyang Song. Comparative study of the sintering process and thin film sputtering of AZO, GZO and AGZO ceramics targets. *Ceramics International*, 40(8):12905–12915, sep 2014.

[254] Qinghu You, Hua Cai, Kun Gao, Zhigao Hu, Shuang Guo, Peipei Liang, Jian Sun, Ning Xu, and Jiada Wu. Highly transparent and conductive Al-doped ZnO films synthesized by pulsed laser co-ablation of Zn and Al targets assisted by oxygen plasma. *Journal of Alloys and Compounds*, 626:415–420, mar 2015.

[255] Yang Geng, Li Guo, Sai-Sheng Xu, Qing-Qing Sun, Shi-Jin Ding, Hong-Liang Lu, and David Wei Zhang. Influence of Al Doping on the Properties of ZnO Thin Films Grown by Atomic Layer Deposition. *The Journal of Physical Chemistry C*, 115(25):12317–12321, 2011.

[256] S Vunnam, K Ankireddy, J Kellar, and W Cross. Highly transparent and conductive Al-doped ZnO nanoparticulate thin films using direct write processing. *Nanotechnology*, 25(19):195301, 2014.

[257] Byung Ho Choi and Ho Bin Im. Electrical Properties of Gallium-Doped Zinc Oxide Films Prepared. *Journal of the American Ceramic Society*, 73(5):1347–1350, 1990.

[258] Eunkyoung Nam, Young-Hun Kang, Donggeun Jung, and Young Sung Kim. Anode material properties of Ga-doped ZnO thin films by pulsed DC magnetron sputtering method for organic light emitting diodes. *Thin Solid Films*, 518(22):6245–6248, sep 2010.

[259] Junjun Jia, Aya Yoshimura, Yukihiro Kagoya, Nobuto Oka, and Yuzo Shigesato. Transparent conductive Al and Ga doped ZnO films deposited using off-axis sputtering. *Thin Solid Films*, 559:69–77, may 2014.

[260] Ji Hun Park, Sang Ho Shin, Hyung Seok Yoon, Yongbae Jeon, Seunghun Lee, Yoongyu Lee, and Sangwon Yoon. Gallium codoping for high visible and near-infrared transmission in Al-doped ZnO thin films for industrial-scale applications. *Journal of Vacuum Science & Technology A: Vacuum, Surfaces, and Films*, 33(2):021508, mar 2015.

[261] J.-H. Kang, D.W. Kim, J.H. Kim, Y.S. Lim, M.-H. Lee, W.-S. Seo, H.J. Choi, K.H. Seo, and M.G. Park. Improved thermal stability of ZnO transparent conducting films with a ZnO overlayer. *Thin Solid Films*, 519(20):6840–6843, aug 2011.

[262] Tae Hoon Kim, Young-Gu Ju, Lee Soon Park, Sang Hern Lee, Jong Hyeob Baek, and Young Moon Yu. Enhanced Optical Output Power of Tunnel

Junction GaN-Based Light Emitting Diodes with Transparent Conducting Al and Ga-Codoped ZnO Thin Films. *Japanese Journal of Applied Physics*, 49(9):091002, sep 2010.

[263] Y. H. Son, S. H. Choi, J. J. Park, M. H. Jung, Y. Hyr, and I. S. Kim. Fabrication and Study of Transparent Conductive Films ZnO(Al) and ZnO(AlGa) by DC Magnetron Sputtering. *Journal of the Korean Vacuum Society*, 22(3):119–125, 2013.

[264] Frank C. Porter. *Zinc Handbook: Properties, Processing, and Use in Design (Mechanical Engineering Series).* CRC Press, 1st edition, 1991.

[265] Amir Moezzi, Andrew M. McDonagh, and Michael B. Cortie. Zinc oxide particles: Synthesis, properties and applications. *Chemical Engineering Journal*, 185-186:1–22, 2012.

[266] Fathi Habashi. *A Hundred Years of the Bayer Process for Alumina Production*, pages 85–93. Springer International Publishing, Cham, 2016.

[267] Normal N. Greenwood. The Chemistry of Gallium. *Advances in Inorganic Chemistry and Radiochemistry*, 5:91–134, 1963.

[268] G. A. Jenner, H. P. Longerich, S. E. Jackson, and B. J. Fryer. ICP-MS - A powerful tool for high-precision trace-element analysis in Earth sciences: Evidence from analysis of selected U.S.G.S. reference samples. *Chemical Geology*, 83(1-2):133–148, 1990.

[269] Gaurav Bajpai, Tulika Srivastava, Mohd Nasir, Saurabh Tiwari, Shubhra Bajpai, E G Rini, Sajal Biring, and Somaditya Sen. Scripta Materialia A comprehensive theoretical and experimental study on structural and mechanical properties of Si doped ZnO. *Scripta Materialia*, 135:1–4, 2017.

[270] Wolfgang Korner and Christian Elsasser. Density functional theory study for polycrystalline ZnO doped with Si or Nb. *Physical Review B*, 83(205306):1–6, 2011.

[271] Frederick K. Lutgens, Edward J. Tarbuck, and Dennis G. Tasa. *Essentials of Geology (12th Edition)*. Pearson, 12 edition, 2014.

[272] Mukesh Kumar, a.K. Sigdel, T. Gennett, J.J. Berry, J.D. Perkins, D.S. Ginley, and C.E. Packard. Optimizing amorphous indium zinc oxide film growth for low residual stress and high electrical conductivity. *Applied Surface Science*, 283:65–73, 2013.

[273] Z C Chang and S C Liang. The Microstructure of Aging ZnO , AZO , and GZO Films. *International Journal of Chemical, Molecular, Nuclear, Materials and Metallurgical Engineering*, 8(5):451–453, 2014.

[274] Hsuan-Chung Wu, Yen-Chun Peng, and Tsu-Ping Shen. Electronic and Optical Properties of Substitutional and Interstitial Si-Doped ZnO. *Materials*, 5(12):2088–2100, 2012.

[275] Dominic B Potter, Michael J Powell, Jawwad A Darr, Ivan P Parkin, and Claire J Carmalt. RSC Advances Transparent conducting oxide thin fi lms of Si- doped ZnO prepared by aerosol assisted CVD. *RSC Advances*, 7:10806–10814, 2017.

[276] Nazanin Rashidi, Vladimir L. Kuznetsov, Jonathan R. Dilworth, Michael Pepper, Peter J. Dobson, and Peter P. Edwards. Highly conducting and optically transparent Si-doped ZnO thin films prepared by spray pyrolysis. *Journal of Materials Chemistry C*, 1(42):6960, 2013.

[277] Nazanin Rashidi, Alex T. Vai, Vladimir L. Kuznetsov, Jonathan R. Dilworth, and Peter P. Edwards. Origins of conductivity improvement in fluoride-enhanced silicon doping of ZnO films. *Chem. Commun.*, 51(45):9280–9283, 2015.

[278] Vladimir L Kuznetsov, Alex T Vai, Malek Al-mamouri, J Stuart Abell, Michael Pepper, and Peter P Edwards. Electronic transport in highly conducting Si-doped ZnO thin films prepared by pulsed laser deposition Elec-

tronic transport in highly conducting Si-doped ZnO thin films prepared by pulsed laser deposition. *Applied Physics Letters*, 107(232103):1–5, 2015.

[279] R. E. Treharne, L. J. Phillips, K. Durose, a. Weerakkody, I. Z. Mitrovic, and S. Hall. Non-parabolicity and band gap re-normalisation in Si doped ZnO. *Journal of Applied Physics*, 115(6):063505, feb 2014.

[280] Normal N. Greenwood and Alan Earnshaw. *Chemistry of the Elements*. Butterworth-Heinemann, 1st edition, 1984.

[281] O. W. Flörke, H. A. Graetsch, F. Brunk, L. Benda, S. Paschen, H. E. Bergna, W. O. Roberts, W. A. Welsh, C. Libanati, M. Ettlinger, D. Kerner, M. Maier, W. Meon, R. Schmoll, H. Gies, and D. Schiffmann. Silica. In *Ullmann's Encyclopedia of Industrial Chemistry*, pages 422–507. Wiley-VCH Verlag GmbH & Co. KGaA, Weinheim, 2008.

[282] M. Buchanan, J. B. Webb, and D. F. Williams. Preparation of conducting and transparent thin films of tin-doped indium oxide by magnetron sputtering. *Applied Physics Letters*, 37(2):213–215, 1980.

[283] Mamoru Mizuhashi. Electrical Properties of Vacuum-Deposited Indium Oxide and Indium Tin Oxide Films. *Thin Solid Films*, 70(1):91–100, 1980.

[284] J. C. Manifacier, L. Szepessy, J. F. Bresse, and M. Perotin. In203 : (Sn) and SnO2: (F) Films - Application to Solar Energy Conversion Part II - Electrical and Optical Properties. *Materials Research Bulletin*, 14:163–175, 1979.

[285] R. Ota, S. Seki, M. Ogawa, T. Nishide, A. Shida, M. Ide, and Y. Sawada. Fabrication of indium-tin-oxide films by dip coating process using ethanol solution of chlorides and surfactants. *Thin Solid Films*, 411(1):42–45, 2002.

[286] Sung-Jei Hong, Yong-Hoon Kim, and Jeong-In Han. Development of Ultrafine Idium Tin Oxide (ITO) Nanoparticle for Ink-Jet Printing by Low-Temperature Synthetic Methods. *IEEE Trans. Nanotechnol*, 7(2):172–176, 2008.

[287] Ki-Won Seo, Hyun-Su Shin, Ju-Hyun Lee, Kwon-Bum Chung, and Han-Ki Kim. The effects of thickness on the electrical, optical, structural and morphological properties of Al and Ga co-doped ZnO films grown by linear facing target sputtering. *Vacuum*, 101:250–256, mar 2014.

[288] Dona S.Y. Jayathilake, T. A. Nirmal Peiris, Jagdeep Singh Sagu, Dominic B. Potter, K.G. Upul Wijayantha, Claire J. Carmalt, and Darren John Southee. Microwave Assisted Synthesis and Processing of Al, Ga and Al,Ga Co-doped ZnO for the Pursuit of Optimal Conductivity for Transparent Conducting Film Fabrication. *ACS Sustainable Chemistry & Engineering*, page acssuschemeng.7b00263, 2017.

[289] Rahul P. Bagwe, Lisa R. Hilliard, and Weihong Tan. Surface modification of silica nanoparticles to reduce aggregation and nonspecific binding. *Langmuir*, 22(9):4357–4362, 2006.

[290] Minori Taguchi, Naomi Yamamoto, Daisuke Hojo, Seiichi Takami, Tadafumi Adschiri, Toshitaka Funazukuri, and Takashi Naka. Synthesis of monocarboxylic acid-modified CeO2 nanoparticles using supercritical water. *RSC Adv.*, 4:49605–49613, 2014.

[291] Nguyen T.K. Thanh and Luke A.W. Green. Functionalisation of nanoparticles for biomedical applications. *Nano Today*, 5(3):213–230, 2010.

[292] Wei Wu, Quanguo He, and Changzhong Jiang. Magnetic iron oxide nanoparticles: Synthesis and surface functionalization strategies. *Nanoscale Research Letters*, 3(11):397–415, 2008.

[293] A. B. Bourlinos, R. Herrera, N. Chalkias, D. D. Jiang, Q. Zhang, L. A. Archer, and E. P. Giannelis. Surface-Functionalized Nanoparticles with Liquid-Like Behavior. *Advanced Materials*, 17(2):234–237, 2005.

[294] Imali A Mudunkotuwa and Vicki H Grassian. Citric Acid Adsorption on TiO 2 Nanoparticles in Aqueous Suspensions at Acidic and Circumneutral

pH : Surface Coverage , Surface Speciation , and Its Impact on Nanoparticle - Nanoparticle Interactions. *Jounal of American Chemical Society*, (132):14986–14994, 2010.

[295] Toshihiko Arita, Ken-ichi Moriya, Kimitaka Minami, Takashi Naka, and Tadafumi Adschiri. Supercritical Hydrothermal Synthesis of Carboxylic Acid-surface-functionalized TiO2 Nanocrystals: pH Sensitive Dispersion and Hybridization with Organic Compounds. *Chemistry Letters*, 39(9):961–963, 2010.

[296] Ameneh Sahraneshin, Shunsuke Asahina, Takanari Togashi, Varu Singh, Seiichi Takami, Daisuke Hojo, Toshihiko Arita, Kimitaka Minami, and Tadafumi Adschiri. Surfactant-Assisted Hydrothermal Synthesis of Water-Dispersible Hafnium Oxide Nanoparticles in Highly Alkaline Media. *Crystal Growth & Design*, 12:5219–5226, 2012.

[297] Minori Taguchi, Seiichi Takami, Tadafumi Adschiri, Takayuki Nakane, Koichi Sato, and Takashi Naka. Synthesis of surface-modified monoclinic ZrO2 nanoparticles using supercritical water. *CrystEngComm*, 14(6):2132, 2012.

[298] Shuwen Zeng, Ken-Tye Yong, Indrajit Roy, Xuan-Quyen Dinh, Xia Yu, and Feng Luan. A Review on Functionalized Gold Nanoparticles for Biosensing Applications. *Plasmonics*, 6:491–506, 2011.

[299] Junfeng Liu, Samuel Legros, Guibin Ma, Jonathan G C Veinot, Frank von der Kammer, and Thilo Hofmann. Influence of surface functionalization and particle size on the aggregation kinetics of engineered nanoparticles. *Chemosphere*, 87(8):918–924, 2012.

[300] Robert I. Gruar, Christopher J. Tighe, Paul Southern, Quentin A. Pankhurst, and Jawwad A. Darr. A Direct and Continuous Supercritical Water Process for the Synthesis of Surface-Functionalized Nanoparticles. *Industrial & Engineering Chemistry Research*, 54(30):7436–7451, 2015.

[301] Victor Khrenov, Markus Klapper, Mathias Koch, and Klaus M??llen. Surface functionalized ZnO particles designed for the use in transparent nanocomposites. *Macromolecular Chemistry and Physics*, 206(1):95–101, 2005.

[302] Sourav Bhattacharjee. DLS and zeta potential - What they are and what they are not? *Journal of Controlled Release*, 235:337–351, 2016.

[303] Malvern Instruments Ltd. Zeta potential: An Introduction in 30 minutes. *Zetasizer Nano Serles Technical Note. MRK654-01*, 2:1–6, 2011.

[304] Malvern Instruments Ltd. Zeta Potential Theory. In *Zetasizer Nano Series User Manual*, pages 1–12.

[305] A. N. Christensen, R. Gronbaek, and S. E. Rasmussen. The Crystal Structure of InOOH. *Acta Chemica Scandinavica*, 18:1261–1266, 1964.

[306] M. Marezio. Refinement of the crystal structure of In2O3 at two wavelengths. *Acta Crystallographica*, 20(6):723–728, 1966.

[307] Dougal P Howard, Peter Marchand, Tharan Gordon, and Jawwad A Darr. Sustainable Transparent Conducting Oxide Nanomaterials; Aluminium- and Gallium-Co-Doped Zinc Oxide (AGZO). *Journal of Nanoscience and Nanotechnology*, 16(9):10166–10171, 2016.